UNIVERSITÉ DE GENÈVE

FACULTÉ DES SCIENCES

Département de physique
nucléaire et corpusculaire

Professeur Maria Novella Kienzle Focacci

Cross sections measurement of $e^+e^- \rightarrow W^+W^-$ at $\sqrt{s} = 161$, 172 and 183 GeV and W mass determination with L3 at LEP.

THÈSE

présentée à la Faculté des Sciences de l'Université de Genève
pour obtenir le grade de Docteur ès Sciences, mention physique

par

Claudia PAUS-CECCHI

de Rome, Italie

Thèse N° 3006

GENÈVE
Atelier d'impression de la Section de physique
1998

La Faculté des sciences, sur le préavis de Madame M.-N. KIENZLE-FOCACCI, professeur titulaire et directeur de thèse (Département de physique nucléaire et corpusculaire), Messieurs U. AMALDI, professeur (CERN - Genève), G. COIGNET, professeur (LAPP - Annecy, France), F. FERRONI, professeur (Università "La Sapienza" - Roma, Italia) et M. MARTIN, professeur ordinaire (Département de physique nucléaire et corpusculaire), autorise l'impression de la présente thèse, sans exprimer d'opinion sur les propositions qui y sont énoncées.

Genève, le 7 juillet 1998

Thèse - 3006 -

Le Doyen, Eric DOELKER

QUANDO MORRÒ VOGLIO LE TUE MANI

Quando morrò voglio le tue mani sui miei occhi:
voglio la luce e il frumento delle tue mani amate,
passare una volta ancora su di me la loro freschezza,
sentire la soavità che cambiò il mio destino.

Voglio che tu viva mentr'io, addormentato, t'attendo,
voglio che le tue orecchie continuino a udire il vento,
che fiuti l'aroma del mare che amammo uniti
e che continui a calpestare l'arena che calpestammo

Voglio che ciò che amo continui a esser vivo
e te amai e cantai sopra tutte le cose,
per questo continua a fiorire, fiorita,

perché raggiunga tutto ciò che il mio amore ti ordina,
perché la mia ombra passeggi per la tua chioma,
perché così conoscano la ragione del mio canto.

Pablo Neruda

A te.

Remerciements

J'aimerais en premier lieu remercier sincèrement le Professeur M.N. Kienzle-Focacci pour la confiance qu'elle ma temoigné tout au long de ma thèse sourtout pour la liberté qu'elle m'a laissé dans la gestion de mon travail et de ma recherche ainsi que dans le choix du sujet, permettant ainsi mon développement professionnel.
Un grand merci aux Professeurs U. Amaldi, G. Coignet, F. Ferroni et M. Martin pour avoir accepté de faire partie de mon jury de thèse, ainsi pour leurs commentaires constructifs.
Je remercie les Professeurs P. Extermann et M. Bourquin pour m'avoir accueilli dans leur groupe, et pour m'avoir donné des responsabilité dans le groupe du BGO et sourtout pour m'avoir toujours soutenu dans mes initiatives.
Un remerciement particulier, dans le groupe de Genève, va au Dr. J.H. Field pour son fort soutien tout le long de mon travail et pour l'expérience partagée pour le projet de la diffusion Møller. Grace à lui j'ai eu la possibilité de développer un projet de recherche assez different de ce qu'est un travail d'analyse de données dans une grande expérience comme L3.
Je remercie tout les membres du groupe de Genève: P. Achard, B. Burger, P. Déglon, P. Emonet, L.Fredj, D. Goujon, H. Hoorani, F. Muheim, N. Produit, D. Sciarrino, pour la sympatie qu'il m'ont toujours montré et pour les commentaires très utile qu'ils m'ont donné pendant nos réunions hebdomadaire à l'Université; en particulier je remercie S. Braccini, G. Susinno et A. Teglia pour le bon temps qu'on a passé ensemble y compris en dehors du travail. Je remercie sincèrement D. Duchesneau pour m'avoir appris tous les secret pour le travail de calibration du BGO et aussi pour son cours intensif de français à mon arrivée.
Je remercie particulièrement, dans la collaboration L3, le Dr. J. Mnich pour ses précieux commentaires et conseils jusqu'à la fin de ma thèse. Je remercie tout le groupe BGO de L3 et en particulier A. Weber, pour tout ce que j'ai appris de lui pendant le temps où nous avons travaillé ensemble. Et, bien sûr, un grand remerciement va à tout le groupe W de L3, en particulier à M. Gruenewald et P. De Jong pour avoir suivi pas après pas le travail de ma thèse.
Un très profond remerciement va à ma famille sans laquelle tout ça n'aurait pas été possible, pour son soutien très fort surtout dans les moments les plus difficiles quand tout semble être impossible, en particulier je remercie ma grand-mère, ma soeur Cinzia et ma tante Laura; elles ne m'ont jamais abandonnée même lorsque j'etais tellement insupportable que je l'aurais mérité!
Je remercie aussi tous mes amis en particulier Cinzia, Massimo, Sabrina, Sonia, Luca,

Alessandro, Claudio, Francesca, Giampaolo, Marco, Mariagrazia, Maurizio, Mimmo, Riccardo, Stefano, Vincenzo pour tous le beaux moments qu'on a partagé ensemble, mais surtout pour m'avoir aidé chaque fois que nécessaire, même dans les moments les plus durs. Merci à tous!
Je remercie profondement Christoph pour le soutien qu'il m'a donné dans le travail et à côté.

Mais le plus grand merci, du fond du coeur, c'est pour Toi Maman!

Contents

Chapitre 1

Résumé

1.1 Introduction

La physique des particule élémentaires étudie les constituants fondamentaux de la matière et leurs intéractions. Les intéractions entre particules peuvent être de quatre types: intéraction gravitationelle, électromagnétique, faible et forte. En 1961 Glashow [2] a formulé une théorie dans laquelle l'intéraction électromagétique et l'intéraction faible sont unifiées, dans une théorie électrofaible, completée après par Weinberg et Salam [3]. Cette théorie est basée sur l'invariance locale de Jauge de la densité du Lagrangien et sur l'existence d'une particule scalaire, neutre, le boson de Higgs, qui, à travers le mécanisme de la brisure spontanée de symétrie, permet de generer les masses des particules. Dans le même temps une nouvelle théorie de Jauge fut introduite, qui décrivait les intéractions fortes entre quarks: la Chromodynamique Quantique (QCD). L'ensemble de la théorie électrofaible et de la théorie QCD forment aujourd'hui le Modèle Standard [3] des intéractions entre particules élementaires. Dans la théorie électrofaible, basée sur la symétrie de Jauge SU(2) $\times$ U(1), chaque intéraction est transmise par l'échange d'un boson de jauge médiateur de l'intéraction correspondante: les bosons $W^{\pm}$, le boson neutre Z et le photon γ. La Chromodynamique Quantique est basée sur la symétrie SU(3) de couleur et huit gluons colorées sont les médiateurs de l'intéraction forte. Les bosons $W^{\pm}$ et Z ont été découverts au collisioneur $p\bar{p}$ au CERN dans les expériences UA(1) et UA(2) en 1983.

Le collisioneur LEP (Large Electron Positron Collider) à été construit essentiellement pour effectuer une mesure précise des paramètres du Modèle Standard.

Dans une première phase, commencée en 1989, à une énergie dans le centre de masse $\sqrt{s}$ de collision $\sqrt{s} \simeq 91$ GeV, correspondant à la masse du Z, plusieurs millions de désintegrations du Z ont été enregistrés par chacune des expériences du LEP,

ALEPH, DELPHI, L3, OPAL. Ces données ont permis une mesure très precise des paramètres du Modèle Standard, comme la masse du boson Z, le nombre de générations à partir du comptage des neutrinos légers et l'angle de Weinberg. Le Modèle Standard reproduit avec une grande précision toutes les mesures effectuées, mais le boson de Higgs n'a pas encore été observé.
Après cette première phase, on est passé à LEP2 en 1995, pour explorer des plus hautes énergies jusqu'à environ 200 GeV d'énergie dans le centre de masse. L'un des objectifs fondamentaux de cette deuxième phase est la mesure de la masse du boson W. L'intérêt pour cette mesure est particulièrement dû au fait que les corrections radiatives du Modèle Standard dépendent de la masse du W et de la masse du boson de Higgs. Une mesure précise de M_W permettra de fixer une limite stricte sur la valeur de la masse du Higgs, s'il n'y a pas encore d'observation directe.
Dans cette thèse nous allons exposer les études sur la mesure de la section efficace de la réaction $e^+e^- \to W^+W^-$. Nous discuterons aussi la mesure de la masse du boson W à l'énergie dans le centre de masse $\sqrt{s} = 161$ GeV avec la méthode de la section efficace et à plus hautes énergies, $\sqrt{s} = 172$ GeV et $\sqrt{s} = 183$ GeV, avec la méthode de reconstruction dirècte du boson W.

1.2 Le LEP

Le LEP est actuellement le plus grand collisioneur e^+e^- du monde. Il a été construit avec une circonférence de $\sim$ 27 Km pour étudier les collisions e^+e^- à une énergie dans le centre de masse de $\sqrt{s} \simeq 90$ GeV jusqu'à $\simeq 200$ GeV. Les électrons et les positrons, circulant dans le LEP en direction opposée, sont d'abord accelerés à l'énergie voulue et après sont mis en collisions dans les quatre points d'interactions où se trouvent les quatre détecteurs: ALEPH [51], DELPHI [52], L3 [49] et OPAL [53]. De 1989 à 1995 LEP a tourné à une énergie dans le centre de masse autour du pic du Z. En 1995 pour la première fois LEP a atteint une énergie de $\sqrt{s} = 130 - 136$ GeV. En 1996 LEP a obtenu des énergies plus élévées du seuil de production de bosons W, $\sqrt{s}$=161 et $\sqrt{s}$ =172 GeV en 1996 et $\sqrt{s}$= 183 GeV en 1997, où les sections efficaces de production de paires de W sont plus élevées.

1.3 Le détecteur L3

Le détecteur L3 (Figure 5.3) est installé au point d'interactions n^0 2 à 50 m sous terre. Il est entouré par un aimant de 7800 t qui produit un champ magnétique de 0.5 T. A l'intérieur de l'aimant le détecteur est appuyé sur un tube de support de

240 t, avec un diamètre interne de 4.45 m et une longueur de 32 m.
Le spectromètre a été dessiné pour obtenir une bonne résolution en énergie dans la mésure des muons, des électrons et des photons. Pour le spectromètre à muons, le but était d'obtenir une résolution sur la mesure de l'impulsion $\Delta p/p \sim 2$ % à 50 GeV. Celà est obtenu en maximisant la longueur de la trajectoire du muon. De cette façon l'éspace disponible pour le reste du détecteur est réduit, ce qui impose le choix des calorimètres et d'une chambre centrale très compactes.
Le détecteur a une géométrie cylindrique, autour de l'axe du faisceau. En commençant par le centre il est composé par:

- le détecteur au silicium (Silicon Microvertex Detector, SMD) pour la mesure précise de traces et des vertex secondaires dûs à la désintegration des particules à long temps de vie, tels que le D^* ou K^0.

- le détecteur des traces central (Time Expansion Chamber, TEC);

- le calorimètre électromagnétique;

- les scintillateurs;

- le calorimètre hadronique;

- le spectrométre à muons.

1.3.1 Le détecteur au silicium.

Le SMD a été installé dans L3 en 1993 pour augmenter la précision de la reconstruction des traces. Il est constitué de deux couches d'échelles au silicium. Le SMD a une résolution de 7 μm dans le plan $R-\Phi$ et de 14 μm dans le plan $R-z$. Avec ce détecteur la résolution de l'impulsion mesurée avec la partie interne de la chambre centrale est ameliorée d'un facteur deux.

1.3.2 Le détecteur de traces central.

La chambre centrale est une chambre à dérive à symétrie cylindrique. Elle a un rayon d'environ 50 cm et une longueur de 1 m. Elle a été construite pour détecter les particules chargées. Elle mesure les coordonnées spatiales en 62 points de leurs trajectoires dans le champ magnétique. D'après la mesure des traces on reconstruit le point d'interaction et la multiplicité des particules chargées produites dans les interactions e^+e^-.
La position des fils dans la TEC est montrée dans la Figure 5.4.

1.3.3 Le calorimètre électromagnétique.

Le calorimètre électromagnétique est contitué de 10780 cristaux d'oxyde de germanate de bismuth (BGO). Le BGO est un scintillateur intrinsèque et il a une petite longueur de radiation telle qu'une gerbe électromagnétique de 50 GeV est complétement contenue dans le détecteur. Il est divisé en deux parties: un tonneau qui couvre la partie centrale ($42.3° \leq \theta \leq 137.7°$ pour une couverture de 74 % de l'angle solide) et deux bouchons qui couvrent les régions avant-arrière correspondant à $10.5° \leq \theta \leq 36.7°$ et $143.3° \leq \theta \leq 169.5°$. Dans le tonneau les cristaux sont dirigés vers le point d'interaction et ils ont la forme d'une pyramide tronquée de 24 cm de longueur ($\sim$ 21 longueurs de radiation). Une résolution de $\sim$ 1.4 % à 45 GeV a été obtenue grâce à une système de calibration relative de chaque cristal qui utilise la lumière produite par des lampes au Xenon.
Le calorimètre électromagnétique a été completé en 1995 par le nouveau détecteur EGAP, deux anneaux constitués par 24 modules avec une structure en plomb rempli par des fibres scintillantes. La lumière est collectée par des guides de lumière et lue par des phototriodes. Le détecteur peut être utilisé comme veto avec une éfficacité de 98% ou aussi comme détecteur pour la mesure des énergies des electrons et des photons.

1.3.4 Le calorimètre hadronique.

Le calorimètre hadronique est constitué d'un tonneau central et d'un système de bouchons qui couvrent les régions avant-arrière. Il couvre 99.6 % de l'angle solide total. C'est un calorimètre à échantillonage, constitué par des couches d'Uranium comme absorbeur, intercalées avec des chambres proportionnelles utilisant un mélange de Argon (80 %) et de CO_2 (20 %). Le calorimètre hadronique a une résolution en énergie de

$$\frac{\sigma}{E} = \frac{55\%}{\sqrt{E}(GeV)} \oplus 5\%. \tag{1.1}$$

1.3.5 Le déclenchement et l'acquisition des données.

A chaque croisement des faisceaux, les systèmes de déclenchement de L3 décident si l'événement doit être gardé ou pas. Si la réponse est affirmative toutes les informations relatives à l'événement sont lues et transférées sur bande magnétique. Le système de déclenchement est constitué de trois sous-système: le niveau-1, constitué par une logique électronique enregistre les informations en 500 μs; si la décision est positive; le niveau-2 enregistre environ 1 évenement sur 20 avec un facteur de rejection de $\sim$ 30 % et le niveau-3 qui a un facteur de rejection de $\sim$ 80-90 %. Une configuration de ce type minimise le temps mort et fournit un taux d'événements acceptées de l'ordre de 10 Hz.
L'acquisition des données est faite par un système FASTBUS.

1.4 Production des bosons W.

Au LEP les bosons W sont produits en paires dans la réaction d'annihilation $e^+e^- \to W^+W^-$. Chaque boson W peut se désintégrer en une paire quark-antiquark ($W \to q\bar{q}'$), ou dans une paire lepton neutrino ($W \to l\nu$); on observe ainsi trois types d' état final: $W^+W^- \to q\bar{q}'q''\bar{q}'''$ (hadronique), $W^+W^- \to q\bar{q}'l\nu$ (sémileptonique) et $W^+W^- \to l\nu l\nu$ (leptonique). Les rapports relatifs de chaque canal sont de 45.6 % pour le canal hadroniqe, 43.8 % (14.6 % pour chaque lepton) pour le canal sémileptonique, et 10.6 % pour le canal leptonique.

1.5 Sélection des événements WW et mesure de la section efficace.

1.5.1 Le canal hadronique $W^+W^- \to q\bar{q}'q''\bar{q}'''$.

Les événements hadroniques sont caracterisés par une haute multiplicité de traces et de clusters calorimétriques et par une valeur élevée de l'énergie visible due à la présence de quatre jets hadroniques.
Du point de vue expérimental un jet est le résultat de l'association des hadrons dans l' état final en un seul quadrivecteur qui donne l'énergie et la direction du quark

produit dans l'interaction e^+e^-. Un quark en effet ne peut pas être observé comme une particule libre, mais il subit un processus d'hadronisation, aussitôt qu'il est créé. Pour réconstruire un jet il y a différents algorithmes. L'algorithme utilisé pour cette analyse est celui de DURHAM [89].
Les événements hadroniques ont une symétrie sphérique et les énergies manquantes longitudinales et transversales sont très petites. Le bruit de fond le plus important vient du processus $e^+e^- \to q\bar{q}(\gamma)$. Ce processus d'annihilation a une section éfficace qui est deux ordres de grandeur plus grand que la section éfficace de production des W; la topologie de l' état final est très semblable parce-que plus que deux jets peuvent être présents à cause de la radiation de gluons par les quarks.

1.5.2 Le canal semileptonique $W^+W^- \to qql\nu$.

Dans ce canal un de deux W se désintègre en une paire de quarks et l'autre en un lepton avec son neutrino associé, où $l = e, \mu, \tau$ et $\nu = \nu_e, \nu_\mu, \nu_\tau$. La topologie caractéristique de ces événements est la présence d'un lepton isolé dans un environnement hadronique. Ces événements ont une haute multiplicité et une grande valeur de l'énergie visible mais il sont caractérisés par une énergie manquante différente de zéro due à la présence du neutrino. L'énergie manquante peut être réconstruite en imposant la conservation de la quadri-impulsion dans l'évenement mesuré. Les deux masses réconstruites, $M_{q\bar{q}}$ et $M_{l\nu}$, doivent se trouver à l'intérieur d'une fenêtre prédéfinie autour de la valeur de la masse du W. Dans ce canal on doit considérer séparemment le cas dans lequel le lepton est un τ. En ce cas, quand le τ se désintègre hadroniquement, l' état final est un état avec trois jets et la contamination qui vient du processus $e^+e^- \to q\bar{q}(\gamma)$ est grande. D'autre part, quand le τ se désintègre en un lepton, il y a un deuxième neutrino dans l'événement et donc la réconstruction de l'impulsion manquante est plus difficile et il faut utiliser un ajustement cinématique.

1.5.3 Le canal leptonique $W^+W^- \to l\nu l\nu$.

Ce canal est caracterisé par une basse multiplicité, une petite valeur de l'énergie visible et une très grande impulsion manquante due à la présence de deux neutrinos. Le bruit de fond le plus important vient des événements du type $e^+e^- \to l^+l^-(\gamma)$. Ils peuvent être rejetés en considérant l'acollinearité des deux leptons. Ici aussi, quand les leptons sont des τ qui se désintègrent hadroniquement, le bruit de fond qui vient du processus $e^+e^- \to q\bar{q}(\gamma)$ doit être consideré.

1.6 Mesure des sections efficaces à 161, 172 et 183 GeV et détermination de la masse du W à 161 GeV.

Les sections efficaces pour la production des bosons W ont été mesurées aux énergies dans le centre de masse de $\sqrt{s}$ = 161 GeV, $\sqrt{s}$ = 172 GeV et $\sqrt{s}$ = 183 GeV. Elles ont été mesurées pour les différents canaux de désintegrations. Pour obtenir la section efficace totale, σ_{WW}, tous le canaux sont combinés, avec leur rapport d'embranchement théorique, dans une fonction de maximum de vraisemblance, produit des probabilitées Poissonniennes $P(N_i, \mu_i)$.

$$L = \prod_i P(N_i, \mu_i) = \prod_i \frac{\mu_i^{N_i} e^{-\mu_i}}{N_i!} \tag{1.2}$$

où N_i est le nombre d'événements selectionés. Le nombre d'événements attendus, μ_i, est calculé comme

$$\mu_i = \left(\sum_{j=1}^{5} \epsilon_{ij} \sigma_j + \sigma_i^{fond} \right) \cdot \mathcal{L}_i \tag{1.3}$$

où ϵ_{ij} est l' élement de la matrice des éfficacités expérimentales. Il est défini comme la probabilité d'observer le processus j dans la sélection i. Il est determiné par une simulation complète de chaque processus à travers le détecteur L3. La section efficace de chaque canal est $\sigma_j = r_{SMj} \sigma_{WW}$, où r_{SMj} est la valeur du Modèle Standard du taux de branchement pour le processus j. La luminosité integrée, $\mathcal{L}$, varie légèrment pour chaque canal à cause de l'importance des différents détecteurs dans la sélection des événements.

La section efficace totale mesurée à $\sqrt{s} = 161$ GeV est :

$$\sigma_{W^+W^-} = \mathbf{2.89^{+0.81}_{-0.70}}(\boldsymbol{stat.}) \pm \mathbf{0.14}(\boldsymbol{syst.})\ \boldsymbol{pb}$$

à $\sqrt{s} = 172$ GeV:

$$\sigma_{W^+W^-} = \mathbf{12.27^{+1.41}_{-1.32}}(\boldsymbol{stat.}) \pm \mathbf{0.23}(\boldsymbol{syst.})\ \boldsymbol{pb}$$

à $\sqrt{s} = 183$ GeV:

$$\sigma_{W^+W^-} = \mathbf{16.66} \pm \mathbf{0.66}(\boldsymbol{stat.}) \pm \mathbf{0.30}(\boldsymbol{syst.})\ \boldsymbol{pb}.$$

Près du seuil de production des bosons W^+W^-, à une énergie dans le centre de masse de $\sqrt{s} = 161$ GeV, la section efficace augmente très rapidement. A cause de ça elle est très sensible à la valeur de la masse M_W (de laquelle elle dépend) $\sigma_{WW} = \sigma(\sqrt{s}, M_W)$ [38]. En utilisant les donées selectionnées, on peut faire un ajustement du maximum de vraisemblance, laissant comme paramètre libre la mass du W. Le résultat qu'on obtient en utilisant cette méthode est:

$$\boldsymbol{M_W = 80.80^{+0.48}_{-0.42}(exper.) \pm 0.03(LEP)\ GeV}.$$

1.7 Mesure de la masse du W à $\sqrt{s}$= 172 et 183 GeV.

1.7.1 Méthode de la réconstruction directe.

Pour des énergies plus élevées que $\sqrt{s} = 161$ GeV la section efficace varie peu en fonction de l' énergie et donc la dépendance de la section efficace de la masse du W devient plus faible, par conséquence la méthode du seuil devient inutilisable.
D'autre part, pour des plus hautes énergies il est possible de réconstruire directement la distribution de masse invariante des événements $d\sigma_{WW}/dm$ et de mesurer directement la masse M_W.
Malheureusement, bien que l'on utilise un ajustement cinématique, les effets éxperimentaux modifient la distribution théorique de la masse invariante. Il faut employer une simulation Monte Carlo où les quantités cinématiques de l'évènement sont convoluées avec les effets éxperimentaux. En utilisant toute l'information du Monte Carlo on peut réconstruire la distribution de masse originale par la méthode de la densité (box method) décrite dans cette thèse. Pour chaque événement des données on réconstruit la masse M et on considère tous les événements Monte Carlo qui ont une valeur similaire. Puisque, pour chacun des événements Monte Carlo on connait la masse "vraie", avant qu'elle soit modifiée par les effets éxperimentaux, on peut reconstruire une distribution des masses "vraies" utilisable pour la mesure de la masse et de la largeur du W.
A ce moment on construit une fonction de maximum de vraisemblance, produit des fonctions de probabilité de chaque événement, qui doit être maximisée par rapport au paramètre M_W.

$$\mathcal{L} = \prod_j \frac{1}{\sigma_{WW}(M_W) + \sigma_{fond}} \left[\frac{d\sigma_{WW}}{dm_j}(m_j, M_W) + \frac{d\sigma_{fond}}{dm_j}(m_j) \right]. \tag{1.4}$$

1.7.2 Résultats.

En utilisant la méthode décrite dans la section précedente, à une énergie dans le centre de masse de $\sqrt{s} = 172$ GeV on obtient pour la masse du W la valeur:

$$\boldsymbol{M_W = 80.71^{+0.34}_{-0.35}(stat.) \pm 0.09(syst.)\ GeV.}$$

Avec la même méthode à $\sqrt{s} = 183$ GeV on obtient:

$$\boldsymbol{M_W = 80.40 \pm 0.15(stat.) \pm 0.09(syst.)\ GeV.}$$

Si on combine les deux résultats éffectués à haute énergie avec la mesure faite à $\sqrt{s} = 161$ GeV dans un ajustement du maximum de vraisemblance le résultat qu'on obtient est:

$$\boldsymbol{M_W = 80.40 \pm 0.16(exper.) \pm 0.03(LEP)\ GeV}$$

où la première erreur exprime l'incertitude expérimentale de la mesure, combinaison des erreurs statistiques et systématiques. La deuxième erreur est dûe à l'incertitude sur la mesure de l'énergie du faisceau de LEP. Les résultats separés pour le canal hadronique et pour le canal semileptonique sont:

$$M_W(qql\nu) = 80.09 \pm 0.23(stat.) \pm 0.07(syst)\ GeV$$
$$M_W(qqqq) = 80.59 \pm 0.19(stat.) \pm 0.13(syst)\ GeV$$

Dans la précision statistique il n'y a pas une différence significative entre la masse du W obtenue avec le canal semileptonique et celle obtenue avec le canal hadronique. La contribution du processus d'hadronisation à l'erreur systematique est dûe au fait que la reconstruction de la masse du W est basée sur le principe que l'hadronisation de deux W est complétement independent et ça n'est pas tout à fait vrai. Des effets de recombinaison de couleurs et de corrélation de Bose-Einstein peuvent être présents dans le canal hadronique entre deux pions de même charge qui viennent de deux W différents.

Pour déterminer aussi la largeur total du boson W, Γ_W, cette quantité est traitée comme un paramètre indépendant au lieu de le fixer à la valeur du Modèle Standard. Pour tous les états finaux combinés ensemble cet ajustement donne:

$$M_W = 80.41 \pm 0.15(stat.) \pm 0.09(syst)\ GeV$$
$$\Gamma_W = 2.41 \pm 0.39(stat.) \pm 0.25(syst)\ GeV$$

Ces mesures de la masse et de la largeur du boson W sont en accord avec les mesures précedentes faites aux expériences $p\bar{p}$ avec une précision comparable ($M_W = 80.33 \pm 0.15$ GeV, $\Gamma_W = 2.07 \pm 0.06$ GeV) [18]. La masse du W est aussi obtenue indirectement à LEP1 puisque elle rentre dans le calcul des sections efficaces via les corrections radiatives électrofaibles. La valeur de $M_W = 80.329 \pm 0.041$ GeV, obtenue par un ajustement globale sur toutes les mesures éffectués au LEP est en très bon accord avec les mesures directes, ce qui montre q'on est aussi en accord avec les predictions du Modèle Standard.
Avec un ajustement globale qui contient aussi la masse du W mesurée à LEP2 à, $\sqrt{s} = 161$ GeV et $\sqrt{s} = 172$ GeV (résultats publiés) ($M_W = 80.75^{+0.26}_{-0.27}(exp.) \pm 0.03(LEP)$ GeV), et le résultat de la mesure de la masse du quark top [11, 12] on peut contraindre la masse du boson de Higgs du Modèle Standard à la valeur:

$$M_H = 115^{+116}_{-66}\ GeV$$

Avec les mêmes données une limite supérieure au 95 % de niveau de confidence est fixée pour la masse du Higgs à $M_H < 420$ GeV.
Des nouveaux résultats sont mainteinant disponible depuis quelques mois: la nouvelle mesure de la mass du W à 183 GeV (pas encore publiée), une grande amélioration vient de nouveaux calculs aux ordres supérieurs des corrections radiatives de la masse du quark top et pour finir la nouvelle mesure préliminaire de $sin^2\theta^{lept}_{eff} = 0.23084 \pm 0.00035$ de SLD [96]. En utilisant ces nouveaux résultats dans le fit la limite supérieure de la masse du Higgs au 95 % de niveau de confidence est fixée à $M_H < 215$ GeV (PRELIMINAIRE) [95]. Ce resultat est montré dans la Figure 9.13.

Chapter 2

Introduction

The Physics of Elementary Particles studies the point-like constituents of matter and their fundamental interactions. In the last twenty years, big progress has been made in the understanding and unification of the fundamental forces of the nature: gravitational, electromagnetic, weak and strong. The progress is related to the understanding of invariance properties of the interactions and a fundamental role is played by the local gauge invariance.

In 1961 Glashow suggested a scheme in which the electromagnetic and weak interactions were unified, the electroweak theory. This theory was completed by Weinberg and Salam in 1970. The theory is based on the local gauge invariance SU(2) $\otimes$ U(1) of the electroweak interactions and on the existence of a neutral, scalar particle, the Higgs boson, which with the spontaneous breaking of the symmetry mechanism, allows the generation of the masses of the particles.

At the same time gauge theories were extended to the strong interactions: the quarks are the elementary constituents of the hadrons and a new gauge theory describes the interactions between quarks. The quarks have a new "charge", the colour, which gave the name to the theory: Quantum Chromodinamics (QCD) built on the local gauge invariance of the strong interaction Lagrangian under the group $SU_C(3)$. The electroweak theory and QCD form together the Standard Model.

Many predictions of the Standard Model, in the electroweak field, have been verified by different experiments, for example the observation of neutral currents and by the discovery of the vector bosons $W^{\pm}$ and Z^0 in the UA1 and UA2 experiments at CERN. At LEP we have performed very precise measurements of the electroweak parameters.

Even if the agreement between experimental results and the predictions of the Standard Model theory is very good, this model is considered as an intermediate step towards a more complete theory. There is, in fact in the theory, a large number of

parameters, which must be determined experimentally.
For this reason several extensions of the model have been developed, which contain the Standard Model as a low energy approximation.
The high precision measurements obtained at LEP allow the determination of the Standard Model parameters and exclude for the moment new physics beyond it. The characteristic of LEP is in the fact that the e^+e^- annihilation is an interaction between elementary particles, quantum numbers and the centre-of-mass energy are known and there are no spectator particles which make the situation obscure. Therefore the electroweak processes can be studied in a very "clean" environment.
In the first phase, started in 1989, at the centre-of-mass-energy $\sqrt{s} = M_Z \sim 4$ millions of Z decays were collected by each of the four LEP experiments ALEPH, DELPHI, L3, OPAL, which has allowed the precise measurement of the mass of the Z and of its coupling to quarks and leptons and the determination of the number of generations by counting the number of light neutrinos.
After the first phase of LEP, the second phase LEP2 has started with the aim of exploring the higher centre-of mass energies until $\sqrt{s} \sim 200$ GeV. One of the most important goal of this second phase is the determination of the W mass. The interest in such a measurement is that the radiative corrections of the Standard Model depend on M_W and on the Higgs mass, not yet observed. A precise determination of the W mass would put a strong constraint on the Higgs mass. Moreover since with a global fit of the electroweak measurements an indirect measurement of the W mass is possible, a direct determination of this mass, not in agreement with the indirect measurement, could evidentiate possible deviations from the Standard Model.
At LEP the W bosons are produced in pair in the annihilation process $e^+e^- \rightarrow W^+W^-$; each pair can decay in a quark anti-quark pair ($W \rightarrow q\bar{q}'$), or in a lepton neutrino pair ($W \rightarrow l\nu$), with three possible final states: $W^+W^- \rightarrow q\bar{q}'q''\bar{q}'''$, $W^+W^- \rightarrow q\bar{q}'l\nu$, $W^+W^- \rightarrow l\nu l\nu$. The measurement of the W mass at LEP can be done in different ways, two are the most accurate: the direct reconstruction from the decay products or the measurement of the cross section at threshold which depends on M_W.
In this thesis the first Chapter is dedicated to a description of the Standard Model; the theory of the interaction $e^+e^- \rightarrow W^+W^-$ is presented in Chapter 2. In the third Chapter a detailed description of the L3 experiment is done and in the Chapter 4 we present the calibration of the electromagnetic L3 calorimeter. The Chapter 5 is devoted to a description of the analysis in particular to the selection for W events. Finally, in the Chapter 6 and 7 the results for the W cross sections and for the W mass and width with the two different methods, with the data collected at LEP in 1996

and 1997, are presented. Finally a global fit of all precise data on the electroweak sector will give the upper limit of the Higgs mass obtained today.

Chapter 3

The Standard Model.

3.1 Introduction.

Before the seventies the weak interactions were described by the Fermi Lagrangian as a current current interaction:

$$L_F = \frac{G}{\sqrt{2}} J^{\alpha}(x) J^{\dagger}_{\alpha}(x) \tag{3.1}$$

where G is the Fermi constant. The current has a V-A structure, for leptons it is

$$J^{\alpha}(x) = \bar{l}(x)\gamma^{\alpha}(1-\gamma^5)\nu_e(x). \tag{3.2}$$

This theory contained only charged currents and it is not renormalisable. Even the introduction of a massive vector boson, mediator of the interaction, in the propagator, could not solve the renormalisation problem.
In 1968 Weinberg and Salam constructed independently a theory of local gauge invariance [3]. By imposing to the Lagrangian a local gauge symmetry, relative to the groups $\mathrm{SU(2)_L} \otimes \mathrm{U(1)_Y}$, the electromagnetic and the weak interactions are unified. Today the strong, weak and electromagnetic interactions between particles are described by the gauge symmetries $SU(3)_C \otimes \mathrm{SU(2)_L} \otimes \mathrm{U(1)_Y}$ (Standard Model) [1]. This means that the Lagrangian is invariant under a local gauge transformation

$$\psi'(x) \to exp\{i\alpha_i(x)R^i\}\psi(x) \tag{3.3}$$

where $\alpha_i(x)$ are real numbers in space-time and R^i are the generators of the group. The group $SU(3)_C$ characterises the interactions between quarks which have a colour charge "C" (QCD Quantum ChromoDinamics). The SU(3) group is a non-Abelian group, it has eight generators which do not commute. The gauge fields responsible of the strong interaction are eight vector, coloured fields: the gluons. The gluons interact with the quarks and also between themselves, i.e. in QCD, because of the non-Abelian nature of the group, there exists a triple gluon vertex whereas there is no triple photon vertex in the Abelian QED theory.
The unified electroweak interactions have a more complicated group structure, $SU(2)_L \otimes U(1)_Y$. Only left-handed fermions interact with the gauge fields of SU(2) ($SU(2)_L$). This group has three generators, T_1, T_2, T_3, called weak isospin. The electromagnetic interaction is characterised by the Abelian group U(1) whose generator is the hypercharge Y.
The left-handed fermions form $SU(2)_L$ doublets while the right-handed fermions are represented by singlets. All the fermions, doublets or singlets, are eigenstates of the group $U(1)_Y$, where the weak hypercharge, Y, satisfies the relation:

$$Q = T_3 + \frac{1}{2}Y \tag{3.4}$$

We know three families of fermions described in table 3.1. In $SU(2)_L \otimes U(1)_Y$ there

	Symbol	Q	T_3	mass (GeV)
First family	ν_e	0	1/2	$< 1.8 \cdot 10^{-8}$
	e	-1	-1/2	0.000511
	u	2/3	1/2	~ 0.005
	d	-1/3	-1/2	~ 0.007
Second family	ν_μ	0	1/2	$< 2.5 \cdot 10^{-4}$
	μ	-1	-1/2	0.106
	c	2/3	1/2	~ 1.5
	s	-1/3	-1/2	~ 0.150
Third family	ν_τ	0	1/2	≤ 0.035
	τ	-1	-1/2	1.784
	t	2/3	1/2	~ 175
	b	-1/3	-1/2	~ 5

Table 3.1: **Known fermion families.**

are four gauge fields W^1_μ, W^2_μ, W^3_μ, B_μ, related to four vector bosons mediators of the electroweak interactions: the photon and the massive bosons $W^\pm$ and Z^0. The $W^\pm$ and Z acquire a mass by the Higgs mechanism [6].

The first success of the Glashow-Weinberg-Salam model was the observation of neutral currents in 1972 [4]. The $W^{\pm}$ and Z bosons have been discovered in 1982 at the CERN SPS operated as $p\bar{p}$ collider [5].

3.2 The Lagrangian of the SM and the Higgs mechanism.

The Lagrangian density of the Standard Model can be divided in the following parts:

$$\mathcal{L}_{SM} = \mathcal{L}_{fields} + \mathcal{L}_{fermions} + \mathcal{L}_{Yukawa} + \mathcal{L}_{Higgs} \tag{3.5}$$

$\mathcal{L}_{fields}$ introduce the kinetic energy and the interaction of the gauge fields. $\mathcal{L}_{fermions}$ accounts for the kinetic energy of the fermions and for their interaction with the gauge boson fields. The last two terms, $\mathcal{L}_{Yukawa}$ and $\mathcal{L}_{Higgs}$, are introduced to give masses to the fermions and to the bosons.
The term of the Lagrangian accounting for the scalar Higgs field Φ is written:

$$\mathcal{L}_{Higgs} = (D_\mu \Phi)^\dagger (D^\mu \Phi) - V(\Phi) \tag{3.6}$$

where D_μ is the covariant derivative, chosen to preserve the local gauge invariance by the introduction of gauge fields, B_μ and W^i_μ, associated respectively to the group $\mathrm{U(1)_Y}$ and $\mathrm{SU(2)_L}$:

$$D_\mu = \partial_\mu + igYB_\mu + ig'T_iW^i_\mu \tag{3.7}$$

There is one coupling constant for each group, g and g', for $\mathrm{SU(2)_L}$ and $\mathrm{U(1)_Y}$ respectively. The minimal choice for the Higgs field is a doublet complex field Φ of hypercharge Y=1,

$$\Phi(\vec{x}) = \begin{pmatrix} \Phi^+(\vec{x}) \\ \Phi^0(\vec{x}) \end{pmatrix}. \tag{3.8}$$

The potential of the interaction of the scalar field with itself, the Higgs potential, is written:

$$V(\Phi) = \frac{\lambda}{4}(\Phi^\dagger\Phi)^2 - \mu^2(\Phi^\dagger\Phi) \tag{3.9}$$

It is chosen such as to ensure the spontaneous symmetry breaking. In order to generate masses it is necessary to have minima of the potential different from zero, thus requiring $\lambda > 0$ and $\mu^2 > 0$. The minimum is

$$|\Phi|^2 = \frac{2\mu^2}{\lambda} = \frac{v^2}{2} \neq 0 \tag{3.10}$$

and represents the mean value $| < \Phi^2 > |^2$ of the field in the vacuum. In perturbation theory the fields are expanded around the mean value in the vacuum.

$$\Phi_0 =< \Phi >= \begin{pmatrix} 0 \\ v/\sqrt{2} \end{pmatrix} \tag{3.11}$$

and the field Φ is parametrised as:

$$\Phi(\vec{x}) = \begin{pmatrix} \Phi^+(\vec{x}) \\ \frac{1}{\sqrt{2}}(v + H(\vec{x}) + i\chi(\vec{x})) \end{pmatrix} \tag{3.12}$$

where the fields $\Phi(\vec{x})$, $H(\vec{x})$ and $\chi(\vec{x})$ are equal to zero in the vacuum. The three degrees of freedom associated to the complex field $\Phi^\dagger(\vec{x})$ and to the real one $\chi(\vec{x})$ (Goldstone bosons) are not physical and can be eliminated with a good choice of the gauge. The real scalar field $H(\vec{x})$ describe the physics degree of freedom associated to the Higgs boson.
By choosing a point for the expansion of the Higgs field the $\mathrm{SU(2)_L} \otimes \mathrm{U(1)_Y}$ symmetry breaks down. The only residual symmetry is the one associated to the subgroup $U(1)_{em}$ because its generator, the charge Q, is the only combination of the generators of the group $\mathrm{SU(2)_L} \otimes \mathrm{U(1)_Y}$ which cancel the mean value of the field in the vacuum:

$$Q < \Phi >= (T_3 + \frac{1}{2}Y) < \Phi >= 0. \tag{3.13}$$

The mean value of the scalar field $< \Phi >$ generates a mass for the gauge fields; when writing the expression of the scalar field Φ (Equation 3.12) in Equation 3.6, one mass term appears for the gauge bosons:

$$\begin{aligned} \mathcal{L}_{Higgs}^{M_W,M_Z} &= \frac{1}{2}\left(\frac{1}{2}gv\right)^2 \left((W_\mu^1)^2 + (W_\mu^2)^2\right) + \\ & \frac{1}{2}\left(\frac{1}{2}v\right)^2 (W^{3\mu}, B^\mu) \begin{pmatrix} g^2 & -gg' \\ -gg' & g'^2 \end{pmatrix} \begin{pmatrix} W_\mu^3 \\ B_\mu \end{pmatrix} \end{aligned} \tag{3.14}$$

This corresponds, after the diagonalization of the matrix, to the transformation of the fields $\vec{W}_\mu$ and B_μ into experimentally measurable particle fields, two charged ones

$$W^{\pm}_{\mu} = \frac{1}{\sqrt{2}}(W^1_{\mu} \mp iW^2_{\mu}) \tag{3.15}$$

$$\tag{3.16}$$

and two neutral ones

$$\begin{pmatrix} Z_{\mu} \\ A_{\mu} \end{pmatrix} = \begin{pmatrix} cos\theta_W & sin\theta_W \\ -sin\theta_W & cos\theta_W \end{pmatrix} \begin{pmatrix} W^3_{\mu} \\ B_{\mu} \end{pmatrix}. \tag{3.17}$$

The field A_{μ} is massless and is identified with the photon. The neutral gauge fields W^3_{μ} and B_{μ} are mixed by the electroweak mixing angle, θ_W, which satisfies the following relation:

$$cos\theta_W = \frac{g}{\sqrt{g^2 + g'^2}}. \tag{3.18}$$

By identifying the coupling of the photonic field A_{μ} with the electric charge e, one can write

$$e = \frac{gg'}{\sqrt{g^2 + g'^2}} \tag{3.19}$$

which means

$$gsin\theta_W = g'cos\theta_W = e. \tag{3.20}$$

The ratio of the W and Z boson masses is expressed as a function of the electroweak mixing angle:

$$\frac{M_W}{M_Z} = cos\theta_W. \tag{3.21}$$

The Equation 3.21 is valid only in the model described here, the so called minimal Standard Model, with only one doublet of scalar fields.

3.3 The parameters of the Standard Model.

The Standard Model depends on the following parameters:

- the fermion masses, m_f;
- the quark mixing angles defined by the Cabibbo-Kobayashi-Maskawa matrix [22];
- the gauge coupling constants, g and g' which can be measured by the boson masses M_W, M_Z and by the fine structure constant, α;
- the QCD coupling constant, $\alpha_s(M_Z)$;
- the Higgs boson mass, m_H.

The Z mass has been measured at LEP with a precision of 2×10^{-5} ($m_Z = 91.1867 \pm 0.0020$ GeV) and the fine structure constant α has been measured in the quantum Hall effect with a precision of 5×10^{-7} [7].

$$\frac{1}{\alpha} = \frac{4\pi\epsilon_0}{e^2} = 137.035989 \pm 0.000061 \tag{3.22}$$

The W mass is not known with high precision, therefore the parameters of the SM can be derived from a different measurement, the Fermi constant G_μ, accurately measured in the muon decay

$$G_\mu = \frac{\sqrt{2}g^2}{8M_W^2} = (1.16639 \pm 0.00002) \cdot 10^{-5}\ \mathrm{GeV}^{-2}. \tag{3.23}$$

The Higgs boson has not yet been observed. Direct searches exclude a mass lower than 87.6 GeV [8]. The theory requires an Higgs boson mass smaller than 1 TeV [9, 10].
The top quark has been discovered at Fermilab by CDF and DØ. The mass obtained averaging the results of the two experiments is [11, 12, 95]:

$$m_t = 174.1 \pm 5.4\ \mathrm{GeV}. \tag{3.24}$$

3.4 Radiative corrections.

To test the Standard Model we need not only the first order of perturbative calculations, the Born term, but also the higher orders. These calculations can be subdivided in:

1. The QED corrections: real and virtual photon emission and fermion loops in the photon propagator. These corrections are big at the LEP energies and contain diagrams with radiation of real bremsstrahlung photons which can be explicitly measured in the final state. The most important QED corrections diagrams, for the process $e^+e^- \to e^+e^-$, are illustrated in Figure 3.1.

2. The electroweak corrections. These include the one loop corrections on the Z propagator and vertex. They depend on the top and Higgs mass.

The QED corrections and the purely weak ones are treated separately since the purely weak corrections include only the one loop corrections leading only to two-body final states. These corrections can be separated into radiative corrections, propagator corrections, vertex corrections and box diagrams. The vertex and propagator corrections are shown in Figure 3.2. The propagator corrections can be absorbed in the electromagnetic and weak coupling constants which become running coupling constants as function of s, $\alpha(s)$, and $g_Z(s)$ where $g_Z = \sqrt{g^2 + g'^2}$. Around the Z pole, these modifications consist in

$$\alpha \to \alpha(M_Z^2) = \frac{\alpha}{1 - \Delta\alpha} \tag{3.25}$$

$$\left(\frac{g_Z}{2}\right)^2 \to \sqrt{2} G_\mu M_Z^2 r = \sqrt{2} G_\mu M_Z^2 \frac{1}{1 - \Delta r} \tag{3.26}$$

where Δr contains the contribution of the radiative corrections to the ratio between the amplitudes of neutral and charged current.

3.5 The cross section of $e^+e^- \to Z \to f\bar{f}$ at LEP1.

Around the Z peak the most important part of the radiative corrections, related to the process $e^+e^- \to f\bar{f}$, can be included in the so called Improved Born Approximation. One uses the Born matrix elements, but the following substitutions are introduced:

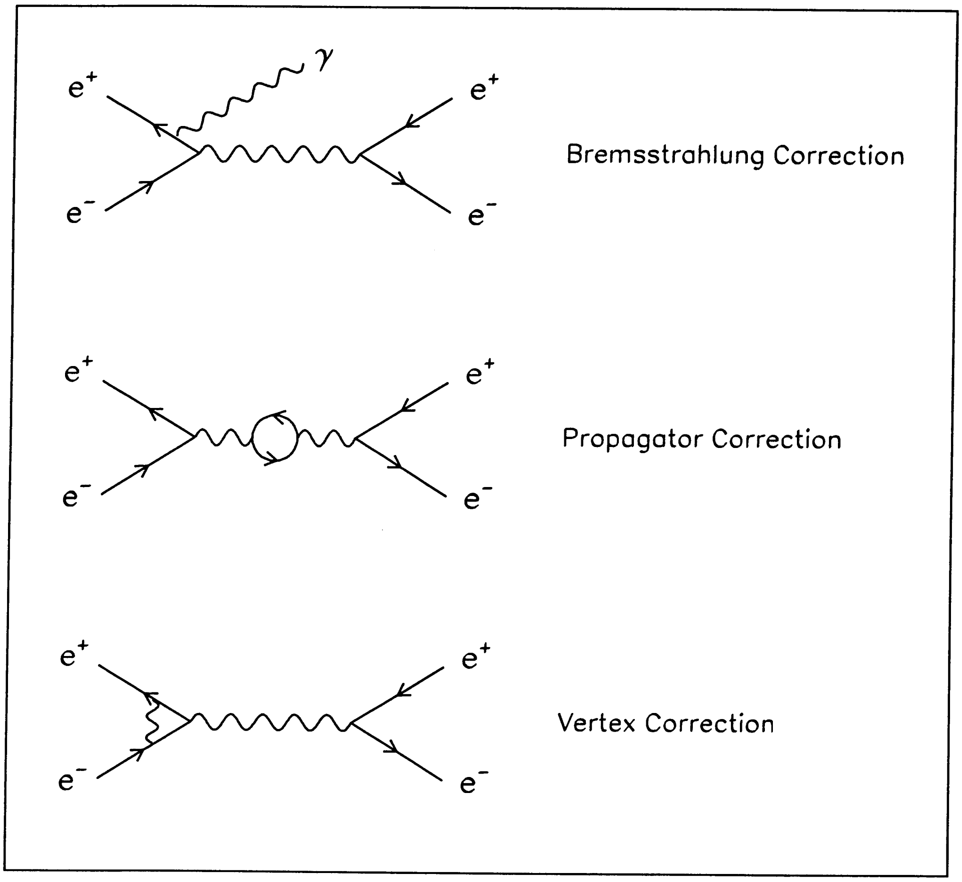

Figure 3.1: **The most important QED correction diagrams.**

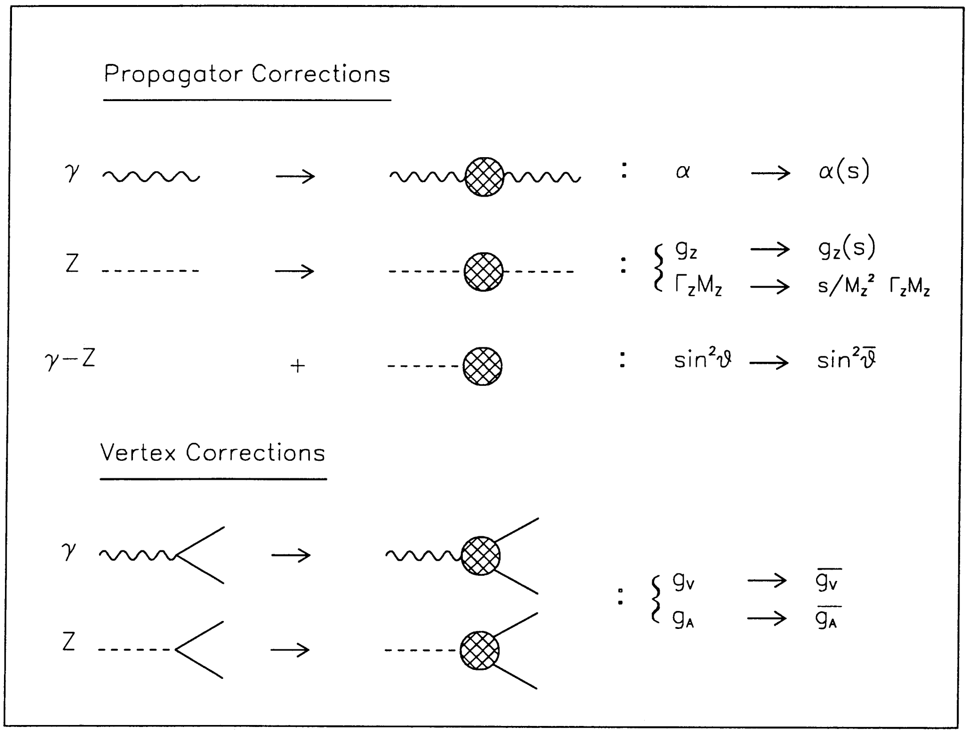

Figure 3.2: **The propagator electroweak corrections and vertex correction diagrams.**

$$\begin{aligned}\alpha &\rightarrow \alpha(M_Z)\\ v_f &\rightarrow \bar{v}_f\\ a_f &\rightarrow \bar{a}_f\\ M_Z\Gamma_Z &\rightarrow \tfrac{s}{M_Z^2}M_Z\Gamma_Z\end{aligned}$$

Where v_f and a_f are the axial and vector couplings describing the vertex between the Z and two fermions.

$$(v_f - a_f\gamma^5)\gamma^\mu \tag{3.27}$$

where $a_f = 2^{1/4}\sqrt{G_\mu}M_Z T_{3f} = \frac{g}{2cos\theta_W}T_{3f} = \frac{e}{2cos\theta_W sin\theta_W}T_{3f}$

and $v_f = \frac{e}{2cos\theta_W sin\theta_W}(T_{3f} - 2Qsin^2\theta_W)$.

The Z cross section at LEP: $e^+e^- \rightarrow Z \rightarrow f\bar{f}$, can be written in a form similar to the one obtained in the Born approximation.

$$\sigma_{tot}^{ff}(s) = \frac{12\pi}{M_Z^2}\frac{s\Gamma_{ff}\Gamma_{ee}}{(s-M_Z^2)^2 + \left(\frac{s}{M_Z}\right)^2\Gamma_Z^2} + \frac{4\pi\alpha^2(s)}{3s}N_c(1+ < \delta_{QCD}^f >) \tag{3.28}$$

$$\Gamma_{ff} = N_c\frac{M_Z}{12\pi}(\bar{a}_f^2 + \bar{v}_f^2)(1+\delta_{QCD}^q)(1+\delta_{QED}^f) \tag{3.29}$$

$$< \delta_{QCD}^q >= \frac{\alpha_s}{\pi} + 1.409\left(\frac{\alpha_s}{\pi}\right)^2 - 12.8\left(\frac{\alpha_s}{\pi}\right)^3 \simeq 0.041 \qquad with\ \alpha_s = 0.125 \tag{3.30}$$

$$\delta_{QED} = \frac{3\alpha}{4\pi} = 0.0017 \tag{3.31}$$

δ_{QED} and δ_{QCD} represent the QED and QCD corrections to the final state. The QCD factor has to be applied only for the quarks.

3.6 Forward-backward asymmetry at the Z peak.

In measuring the polar angle (θ) distribution of a fermion, in the channel $e^+e^- \rightarrow f\bar{f}$, the forward-backward asymmetry is defined as:

$$A_{fb} = \frac{\int_0^1 \frac{d\sigma}{dcos\theta}dcos\theta - \int_{-1}^0 \frac{d\sigma}{dcos\theta}dcos\theta}{\sigma_{tot}} \tag{3.32}$$

At the Z peak, without taking into account the contribution of the photon exchange we obtain:

$$A_{fb} = \frac{3v_e a_e v_f a_f}{(v_e^2 + a_e^2)(v_f^2 + a_f^2)} = \frac{3}{4} A_e A_f \tag{3.33}$$

$$A_f = \frac{2v_f a_f}{(v_f^2 + a_f^2)} \tag{3.34}$$

The measurement of A_{fb} allows to determine the ratio of the coupling constants while the partial width Γ_{ff} gives $a^2 + v^2$ (3.29).

3.7 Fit of the Standard Model parameters.

The electroweak parameters can be determined using measurements from different experiments. At LEP, we measure the cross sections for the charged lepton channels, $\sigma(e^+e^- \to l^+l^-)$ $(l = e, \mu, \tau)$ and for the hadronic final states $\sigma(e^+e^- \to q\bar{q})$. Forward-backward asymmetries are also measured separately for all charged leptons. The measurement of the helicity of the τ lepton allows also the determination of A_τ. For the b and c quarks, the ratios, $R_b = \Gamma_b/\Gamma_{had}$ and $R_c = \Gamma_c/\Gamma_{had}$, and the forward-backward asymmetry at the Z pole, $A_{FB}^{0,b}$, $A_{FB}^{0,c}$, are measured.
The SLD collaboration measure $e^+e^- \to Z \to f\bar{f}$ with polarised beams. They have similar measurements as LEP, but they measure also the left-right asymmetry which gives the single most accurate value of the effective electroweak mixing angle [13, 14]. In fact, because of the polarised electron beam, they can measure directly A_{LR} which is extremely sensitive to $sin^2\theta_W$ and insensitive to QED radiative corrections.
The electroweak mixing angle is also measured by νN experiments [15, 17].
Measurements of the W mass were performed at $p\bar{p}$ collider at CDF and DØ experiments ($M_W = 80.41 \pm 0.09$ GeV) [18] where they measure also the top quark mass ($m_{top} = 174.1 \pm 5.4$ GeV) [11, 12, 95].
We can perform a fit of the Standard Model, included in an analytical program ZFITTER [19]. Different kinds of fits can be done. We perform here, as an example, a fit to all the measurements listed in table 3.2 leaving as free parameters α_s, m_{top}, M_H and M_W. A fit can also be done fixing the value of the quark top mass to its measured value. The results of table 3.3 are obtained.
The value of the strong coupling constant obtained from the fit is in excellent agreement with the world average $\alpha_s(M_Z^2) = 0.118 \pm 0.003$ and is of similar precision.
The values of the W mass and of the top mass obtained from the fit are in excellent

agreement with the direct measurement from CDF and DØ. This constitutes a test of the validity of electroweak corrections of the Standard Model. From the fit of all the electroweak measurements listed in table 3.2, excluding M_W and m_{top}, the following W mass can be extracted:

$$M_W^{EW\ fit\ (1997)} = 80.329 \pm 0.041 \text{ GeV [21]}. \tag{3.35}$$

3.8 The W mass as a test of the Standard Model.

In the Standard Model the mass of the W is correlated to the top mass and to the Higgs mass. The values (1997) measured at $p\bar{p}$ colliders are compared with the predictions of the Standard Model. The Figure 3.3 shows the W mass as function of the top mass for different values of the Higgs mass. The width of the bands takes into account the uncertainty on $\alpha(M_Z^2)$.

The direct measurements are in agreement with the prediction of the Standard Model if the Higgs has a low value.
The Figure 3.4 shows $sin^2\theta_W^{eff}$ as function of the W mass, each variable with a scale corresponding to the precision achieved today. The plot shows the result of the Standard Model fit for 39% (1σ dashed line), 68 % (black line) and 95 % (grey line) probability. Looking at the band which represents the variation of the Higgs mass, one can see that $sin^2\theta_W^{eff}$ is more effective than the W mass for determining the Higgs mass. To obtain a constraint from M_W similar to the one of $sin^2\theta_W^{eff}$, the error on the W mass has to be reduced by a factor 3 or 4.
The measurements of $sin^2\theta_W^{eff}$ and M_W are two different measurements of the mixing angle of the electroweak interactions in the Standard Model, $sin^2\theta_W^{eff}$ measures the couplings ($\frac{g_v}{g_a} = 1 - 4sin^2\theta_W^{eff}$), while M_W the mixing of the masses ($cos\theta_W = \frac{M_W}{M_Z}$). The comparison of these two measurements allows to test the Standard Model and to discover a possible breaking of the symmetry. One could imagine that, with a smaller error on the W mass, the value of the mixing angle would be different from the one predicted by $sin^2\theta_W^{eff}$.
The precision on the measurement of the electroweak coupling constant $\alpha(M_Z^2)$ introduces also an error on the prediction of the Standard Model. Its order of magnitude is indicated by the arrow on the left of Figure 3.4. The arrow is almost parallel to the variation of the Higgs mass, indicating that the uncertainty on $\alpha(M_Z^2)$ has an influence on the Higgs mass prediction. The main contribution to the error on $\alpha(M_Z^2)$ comes from its calculation at a value $s = M_Z^2 \neq 0$. In particular the calculation needs the cross section at low energy of $e^+e^- \rightarrow hadrons$ which has a large experimental error. These measurements will be repeated at BES (Beijing).

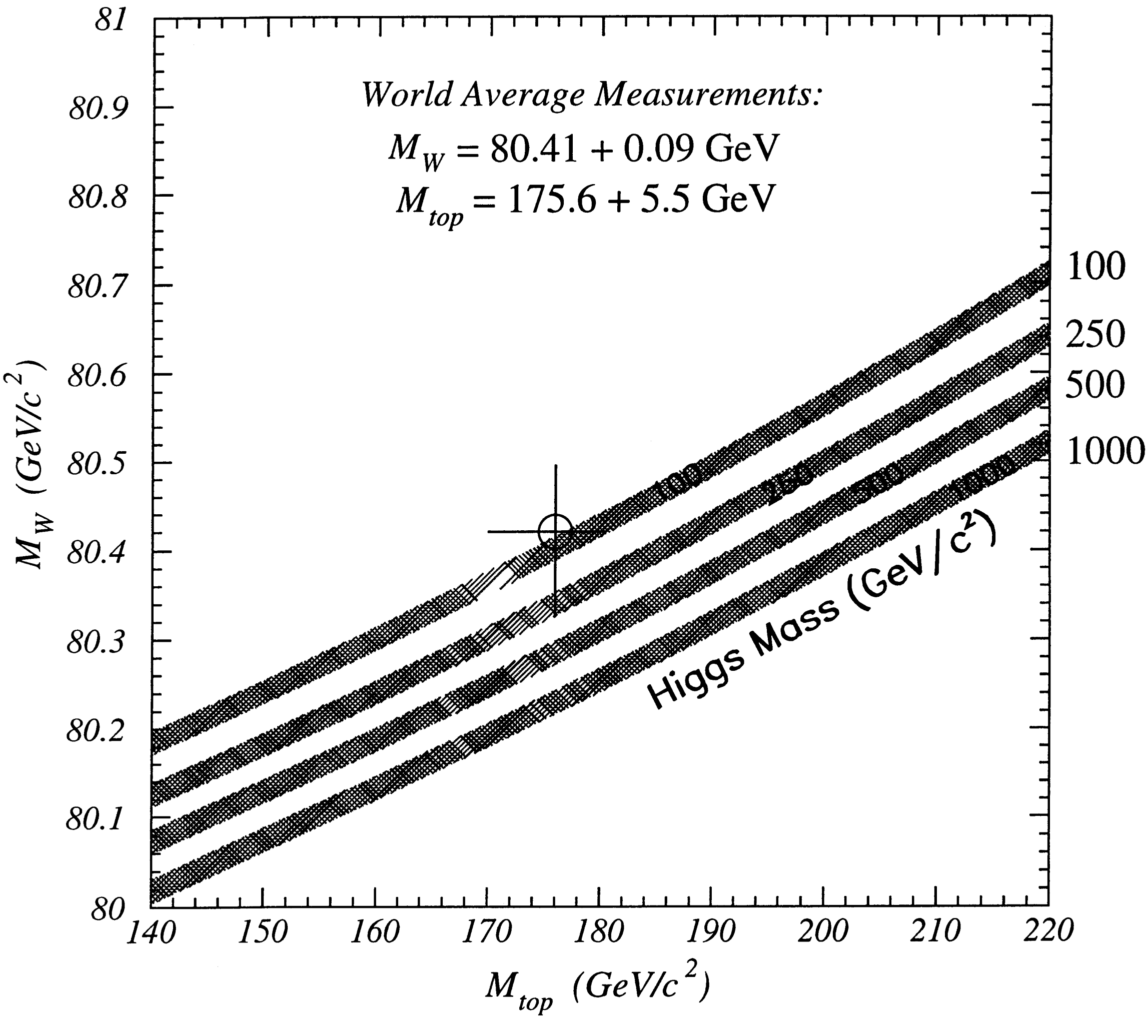

Figure 3.3: **Mass of the W as function as the top mass for different values of the Higgs mass.**

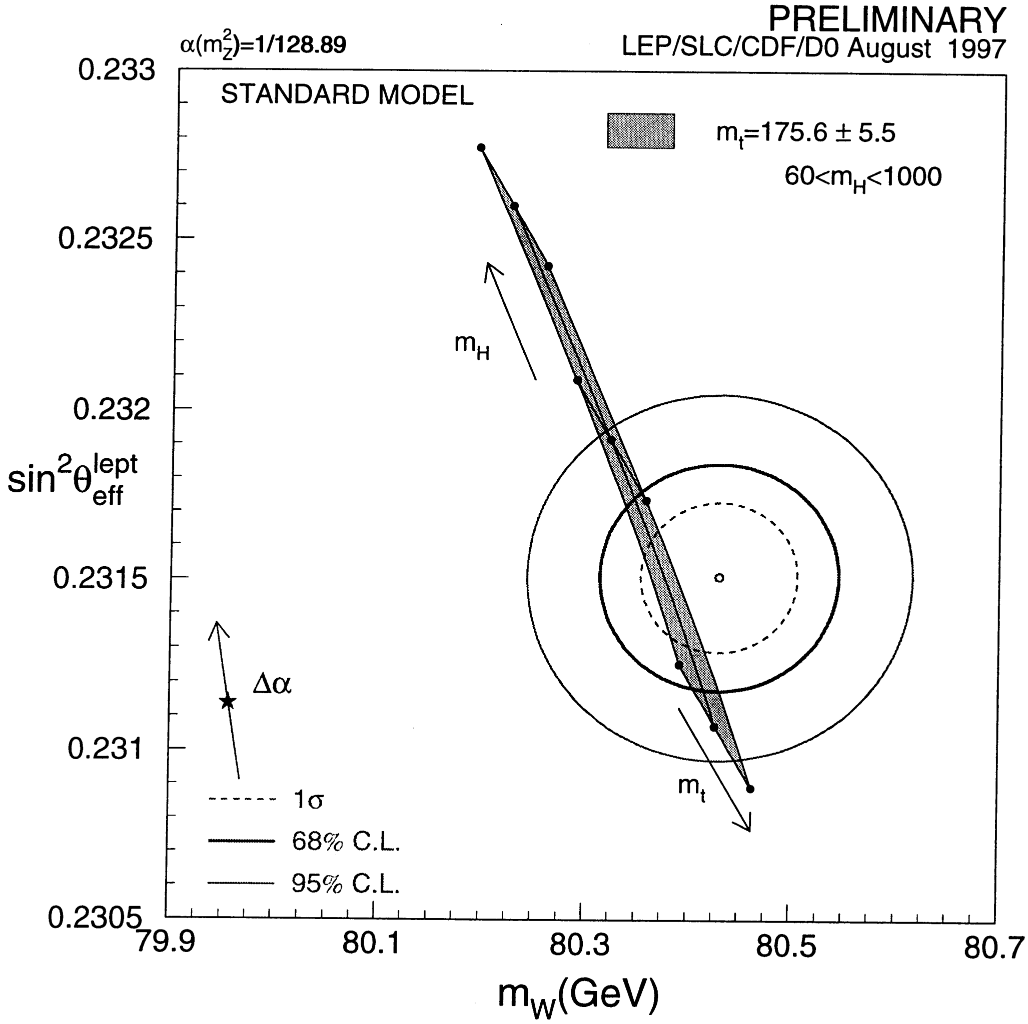

Figure 3.4: **Comparison of the measurements of $sin^2\theta_W^{eff}$ and M_W for different values of M_H and m_t. The value of the $M_W = 80.41 \pm 0.09$ GeV is the world average in 1997 of the measurements at the $p\bar{p}$ colliders.**

	Measurement with total error	Systematic error	Standard Model
$\alpha(M_Z^2)$	128.896 ± 0.090	0.083	128.898
a)**LEP**			
Z lineshape and			
lepton asymmetries			
M_Z(GeV)	91.1867 ± 0.0020	0.0015	91.1866
Γ_Z(GeV)	2.4948 ± 0.0025	0.0015	2.4966
σ^0_{had}(nb)	41.486 ± 0.053	0.052	41.467
R_l	20.775 ± 0.027	0.024	20.756
$A^{0,l}_{FB}$	0.0171 ± 0.0010	0.0007	0.0162
τ polarisation			
A_τ	0.1411 ± 0.0064	0.0040	0.1470
A_e	0.1399 ± 0.0073	0.0020	0.1470
b and c quark			
results R^0_b	0.2175 ± 0.0009	0.0007	0.2158
R^0_c	0.1727 ± 0.0050	0.0038	0.1723
$A^{0,b}_{FB}$	0.0997 ± 0.0022	0.0010	0.1031
$A^{0,c}_{FB}$	0.0739 ± 0.0048	0.0025	0.0736
$q\bar{q}$ charge asymmetry			
$sin^2\theta^{lept}_{eff}(Q_{FB})$	0.2322 ± 0.0010	0.0008	0.23152
b) **SLD**			
$sin^2\theta^{lept}_{eff}(A_{LR})$	0.23084 ± 0.00035	0.00014	0.23152
R^0_b	0.2158 ± 0.0029	0.0017	0.2158
R^0_c	0.1810 ± 0.0145	0.0079	0.1723
A_b	0.900 ± 0.050	0.031	0.935
A_c	0.650 ± 0.058	0.029	0.668
c)$p\bar{p}$ **and** νN			
M_W (GeV) ($p\bar{p}$)	80.41 ± 0.09	0.07	80.375
$1 - m_W^2/m_Z^2$ (νN)	0.2254 ± 0.0037	0.0023	0.2231
m_t (GeV) ($p\bar{p}$)	174.1 ± 5.4	4.2	173.1

Table 3.2: **The measurements included in the combined analysis of SM parameters. The total error in column 2 contains the systematic errors listed in column 3. The Standard Model predictions, in column 4, are calculated with the central values of the parameters α_s, m_t, M_H obtained by the fit. The systematic error on M_Z and Γ_Z contains the error arising from the uncertainty in the LEP energy.**

Parameters	Results of the fit
$\alpha_s(M_Z^2)$	0.120 ± 0.003
m_t	157^{+10}_{-9}
M_H	41^{+64}_{-21}
M_W(GeV)	80.329 ± 0.041
χ^2/DoF	14/12
	Derived quantities
$sin^2\theta_{eff}^{lept}$	0.23153 ± 0.00023
$1 - m_W^2/m_Z^2$	0.2240 ± 0.0008

Table 3.3: **Results for $\alpha_s(M_Z^2)$, m_t, M_H and M_W from the fit to the electroweak data. The results when excluding m_t and M_W are shown. The bottom part shows the results for $sin^2\theta_{eff}^{lept}$ and $1 - m_W^2/m_Z^2$. The value of α_s is in agreement with the world average $\alpha_s(M_Z^2) = 0.118 \pm 0.003$ [20]. The value of M_W and m_{top} are in agreement with the values measured at $p\bar{p}$ colliders $M_W = 80.41 \pm 0.09$ GeV and 174.1 ± 5.4 GeV respectively.**

Chapter 4

Physics of the W boson at LEP.

4.1 Introduction.

At LEP1 the measurements of the Z boson parameters (mass, total and partial widths) have been performed with high statistical precision and with very small systematic uncertainties. All the results were in excellent agreement with the predictions of the Standard Model.
One of the main goal of LEP2 is the measurement of the parameters of the W boson: its mass, width and its couplings to different quark flavours. Until 1996 the production of the W boson was studied only at hadron colliders (CERN in the eighties [23] and then TEVATRON [18]). The production of the W boson at $p\bar{p}$ colliders occurs via the reaction $p\bar{p} \rightarrow W^{\pm}X$. Because of the high background of multi-jets channels produced in the strong interactions, only the leptonic decays of the W are available for the measurement of its mass. But the high statistics of W events allows a measurement of the W mass which is at the moment the most precise. The aim of LEP2 is a measurement of the W mass with a precision of about 30-40 MeV which means a factor of 3 better than the precision obtained presently at $p\bar{p}$ colliders. This would put a stronger constraint on the Higgs boson mass. At LEP the situation is completely different: W's are produced in pairs in the reaction $e^+e^- \rightarrow W^+W^-$. All the final states of the W decays can be identified. The W events can be classified in three channels:

- $W^+W^- \rightarrow q\bar{q}'q''\bar{q}'''$ hadronic;

- $W^+W^- \rightarrow q\bar{q}'l\nu_l$ where $l = e, \mu, \tau$ semileptonic;

- $W^+W^- \to l\nu_l l\nu_l$ where $l = e, \mu, \tau$ leptonic.

From now on we will indicate the three decay channels simply as $qqqq$, $ql\nu$ and $l\nu l\nu$. From the decay products, the W can be reconstructed and the mass can be measured [24, 26]. The mass measurement needs high statistics which is possible only at energies where the cross section is high well above the threshold energy. There is also the possibility to determine the W mass from the measurement of the W cross section near the threshold energy ($\sqrt{s} \simeq 2M_W$) [24, 26, 27].
Another important aspect of W pair production at LEP2 is the information that can be obtained on the triple gauge-boson coupling characteristic of the non-Abelian $\mathrm{SU(2)_L \times U(1)_Y}$ group of the electroweak gauge theory. At LEP1 this coupling enters only as a loop correction while now it contributes directly to the tree-level cross section.
All possible four fermions ($e^+e^- \to 4f$) final states are divided in two classes:

1. Final states due to W^+W^-, as for example ($e^+e^- \to W^+W^- \to l^+\nu l^-\bar{\nu}$) are called charged current **CC**-type final states.

2. Final states produced via a pair of two virtual neutral vector bosons as for example ($e^+e^- \to ZZ \to l^+l^-\nu\bar{\nu}$) are called **NC**-type.

In this Chapter the phenomenology of W boson production will be described [38] starting from the lowest order calculations with the W's produced **on-shell** and a width equal to zero, then the **off-shell** production of W's with the normal width of 2.067 ± 0.021 GeV (Standard Model prediction) will be described. This consists in the study of the process $e^+e^- \to 4\ fermions$, at the lowest order, with two resonant W's, with only three diagrams contributing. Finally there will be a description of **all** the diagrams contributing to the $4f$ cross section always at the lowest order. At the end of the introduction of the radiative corrections will be described.

4.1.1 Lowest order on-shell W production.

The production of W boson via the process $e^+e^- \to W^+W^-$, neglecting the decay of the W's is calculated in the Standard Model. Three diagrams contribute at the lowest order as shown in Figure 4.1: the photon and Z boson exchange in the s channel and the neutrino exchange in the t channel. The t channel gives a contribution only

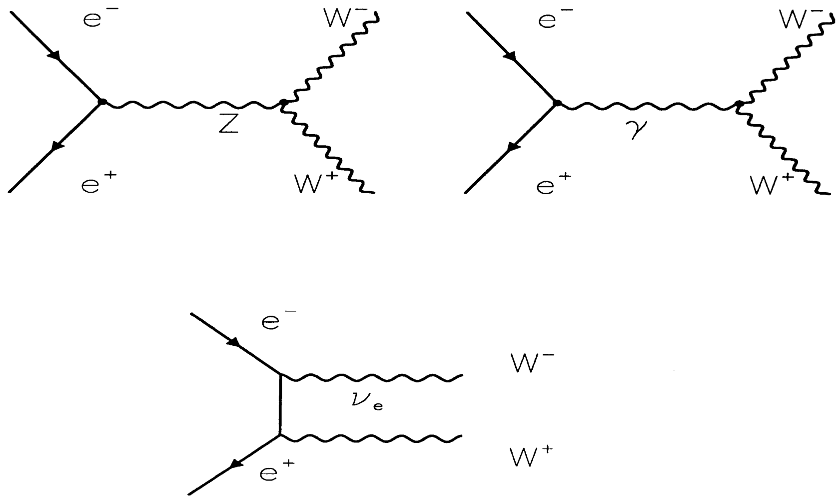

Figure 4.1: **Lowest order contributions to the process $e^+e^- \to W^+W^-$.**

for left-handed electrons, while the s channel, which contains the triple gauge-boson couplings, contributes for both electron helicities.
The helicity amplitudes for the W pair production is $\mathcal{M}(\kappa, \lambda_+, \lambda_-, s, t)$ where κ is the helicity of the electron, which is opposite to the helicity of the positron: $\kappa_- = \kappa_+ = \kappa$. λ are the helicities of the two W's and s and t are the Mandelstam variables

$$s = (p_+ + p_-)^2 = (k_+ + k_-)^2 = 4E^2_{beam}$$
$$t = (p_+ - k_+)^2 = (p_- - k_-)^2 = -E^2_{beam}(1 + \beta^2 - 2\beta cos\theta)$$

where p and k are the momenta of the electron and positron and of the W's, respectively, in the centre-of-mass system of the e^+e^- pair, θ is the scattering angle between e^+ and W^+ and β the velocity of the W boson $\beta = (1 - \frac{4m^2_W}{s})^{1/2}$.
The CP invariance implies that:

$$\mathcal{M}(\kappa, \lambda_+, \lambda_-, s, t) = \mathcal{M}(\kappa, -\lambda_-, -\lambda_+, s, t). \quad (4.1)$$

Therefore in the SM there are only 12 independent helicity matrix elements.
The differential cross section for unpolarised beams, and unpolarised W bosons is:

$$\left(\frac{d\sigma}{d\Omega}\right) = \frac{\beta}{64\pi^2 s}\sum_{\kappa,\lambda_+,\lambda_-}\frac{1}{4}\mid\mathcal{M}(\kappa,\lambda_+,\lambda_-,s,t)\mid^2 . \tag{4.2}$$

The matrix element for the **on-shell** W production, at the lowest order, is:

$$\mathcal{M}_{Born}(\kappa,\lambda_+,\lambda_-,s,t) = \frac{e^2}{2s_W^2}\frac{1}{t}\mathcal{M}_1^{\kappa}\delta_{\kappa^-} + e^2\left[\frac{1}{s} - \frac{c_W}{s_W}g^{\kappa}_{eeZ}\frac{1}{s-M_Z^2}\right]2(\mathcal{M}_3^{\kappa} - \mathcal{M}_2^{\kappa}) \tag{4.3}$$

where $\delta_{\kappa^-} = 1$ for left-handed electrons and $\delta_{\kappa^-} = 0$ for right-handed electrons, $g^{\kappa}_{eeZ} = \frac{s_W}{c_W} - \delta_{\kappa^-}\frac{1}{2s_W c_W}$ is the Z boson-fermion couplings and

$$\mathcal{M}_1^{\kappa} = \bar{v}(p_+)\epsilon_+(k_+,\lambda_+)(k_+ - p_+)\epsilon_-(k_-,\lambda_-)\omega_k u(p_-),$$

$$\mathcal{M}_2^{\kappa} = \bar{v}(p_+)\frac{k_+ - k_-}{2}[\epsilon_+(k_+,\lambda_+)\cdot\epsilon_-(k_-,\lambda_-)]\omega_k u(p_-),$$

$$\mathcal{M}_3^{\kappa} = \bar{v}(p_+)(\epsilon_+(k_+,\lambda_+)[\epsilon_-(k_-,\lambda_-)\cdot k_+] - \epsilon_-(k_-,\lambda_-)[\epsilon_+(k_+,\lambda_+)\cdot k_-])\omega_k u(p_-)$$

where $\epsilon_\pm$ are the polarisation vectors for the W^+ and W^- boson. The total cross section for the process $e^+e^- \to W^+W^-$ can be written as (Eq. 4.4):

$$\begin{aligned}\sigma \;=\; & \frac{\pi\alpha^2\beta}{2sin^4\theta_W s}\{[1 + \frac{2m_W^2}{s} + \frac{2m_W^4}{s^2}]\frac{1}{\beta}ln(\frac{1+\beta}{1-\beta}) - \frac{5}{4} + \\ & \frac{m_Z^2(1-2sin^2\theta_W)}{(s-m_Z^2)}[2(\frac{m_W^4}{s^2} + 2\frac{m_W^2}{s})\frac{1}{\beta}ln(\frac{1+\beta}{1-\beta}) - \frac{s}{12m_W^2} - \frac{5}{3} - \frac{m_W^2}{s}] + \\ & \frac{m_Z^4(8sin^4\theta_W - 4sin^2\theta_W + 1)\beta^2}{48(s-m_Z^2)^2}[\frac{s^2}{m_W^4} + 20\frac{s}{m_W^2} + 12]s\}.\end{aligned} \tag{4.4}$$

This cross section as function of the centre of mass energy is shown in Fig. 4.2 with a continuous line.

The cross section increases very rapidly at the threshold value $\sqrt{s} = 2M_W$ and reaches about 20 pb at its peak [38]. It is approximately constant in the high centre of mass energy region. The contribution of the t channel is dominant in the threshold region. Here the cross section is not sensitive to the triple gauge-boson coupling. The threshold behaviour determines the W mass from the measurement of the cross section at a single energy point near the threshold. At high energies the behaviour of the cross section as function of the centre of mass energy is obtained by gauge cancellations. In fact the contribution of the t channel grows rapidly with the energy

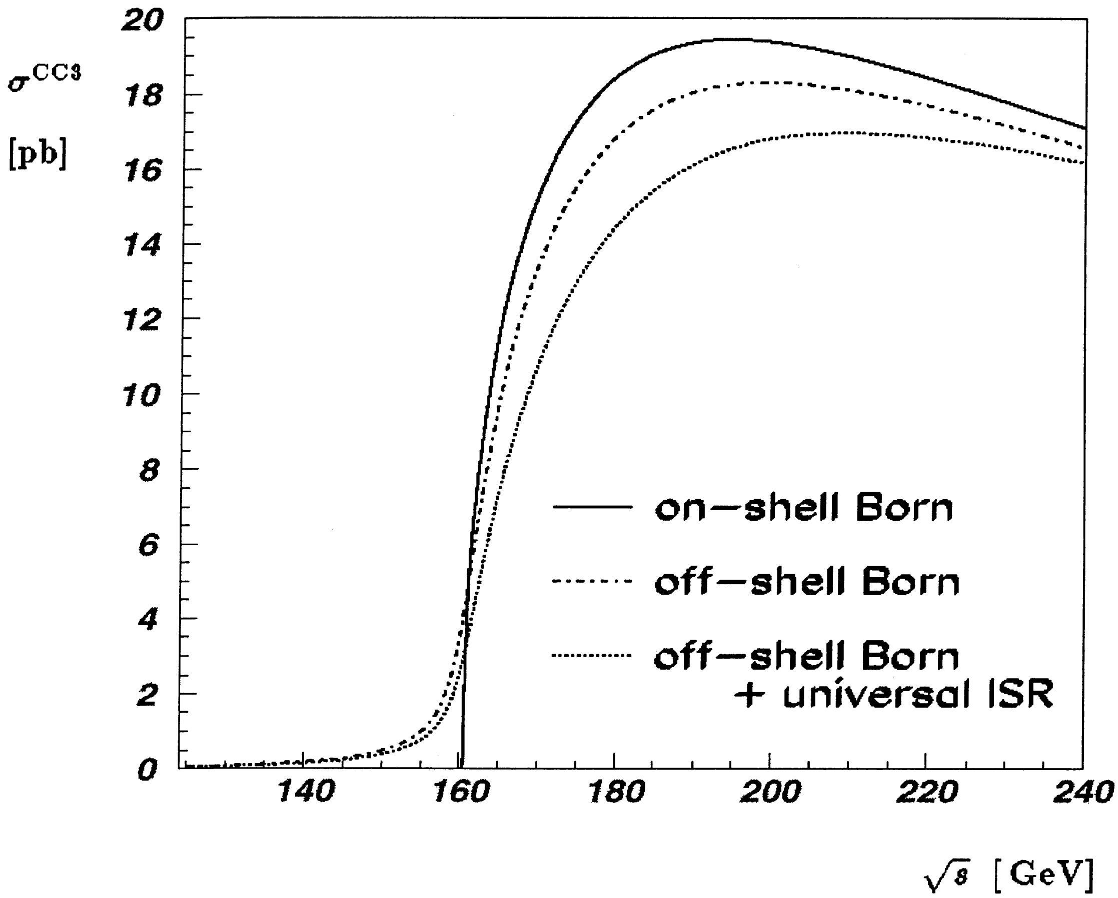

Figure 4.2: **Total cross section of the process $e^+e^- \to W^+W^-$ as function of $\sqrt{s}$. The index CC03 indicates that only the three lowest order diagrams are taken into account.**

and can violate the unitarity. In the Standard Model the t channel amplitude is compensated by the contributions of the γ and Z exchanges in the s channel whose coefficients are such that the cross section decreases with the energy.

4.1.2 Lowest order off-shell W production.

The production of two W bosons and their decay in two fermions, with non zero width, is described, at the lowest order ("CC03") by the three diagrams shown in Figure 4.1. To take into account the W width, in the calculation of the cross section, a semi-analytical approach or a Monte-Carlo method are necessary. In the semi-analytical method the total cross section at the lowest order is written as a double integral over the W masses [26, 28]:

$$\sigma_{WW}^{off-shell,Born}(s) = \int_0^s ds_1 \rho(s_1) \int_0^{(\sqrt{s}-\sqrt{s_1})^2} ds_2 \rho(s_2) \sigma_{WW}^0(s; s_1, s_2) \tag{4.5}$$

where $\sigma_{WW}^0(s; s_1, s_2)$ is the **on-shell** cross section, which can be calculated analytically, for the production of two W's, of mass s_1 and s_2, at the lowest order; and $\rho(s)$ is the Breit-Wigner function for the propagator of the resonant diagrams. The propagator is written as [26, 29]:

$$\rho(s) = \frac{1}{\pi} \frac{\Gamma_W}{M_W} \frac{s}{(s - M_W^2)^2 + s^2 \Gamma_W^2 / M_W^2} \tag{4.6}$$

The W width is a function of s

$$\Gamma_W(s) = \frac{s}{M_W^2} \Gamma_W(M_W^2) \tag{4.7}$$

the energy dependence can be approximated by

$$\bar{\rho} = \frac{1}{\pi} \frac{\bar{M_W} \bar{\Gamma_W}}{(s - \bar{M_W^2})^2 + \bar{M_W^2} \bar{\Gamma_W^2}} \tag{4.8}$$

where [26, 30]

$\bar{M_W} = M_W - \frac{1}{2} \frac{\Gamma_W^2}{M_W} = M_W - 26.9\ MeV$ and
$\bar{\Gamma_W} = \Gamma_W - \frac{1}{2} \frac{\Gamma_W^3}{M_W^2} = \Gamma_W - 0.7\ MeV$.

These relations are derived from the equivalence

$$(s - \bar{M}_W^2 + i\bar{M}_W\bar{\Gamma}_W) = (s - M_W^2 + is\Gamma_W/M_W)/(1 + i\Gamma_W/M_W). \quad (4.9)$$

In the second method, the cross section is calculated by a Monte Carlo integration. This allows the calculation of the differential and the total cross sections and gives the full kinematics for the particles in the final state. In this method one can also include the detector information and test different techniques of analysis. Two Monte Carlo programs have been chosen to perform the evaluation of the efficiency for the different channels: EXCALIBUR [32] and KORALW [31].

4.1.3 Four fermion production including diagrams beyond the "CC03" set.

The decay of two W produce a final state with four fermions. But more than hundred diagrams [33, 34], with the same initial and final state but different intermediate states, contribute to W boson **off-shell** production. For example for the channel $e^+e^- \to q\bar{q}e\nu$ twenty diagrams give a contribution (see Figure 4.3). These diagrams interfere with the CC03 contributions. The analysis of the events is done using the Monte Carlo programs, EXCALIBUR, which contains all the diagrams, and KORALW which contains only the CC03 graphs. Using EXCALIBUR one can switch on or off the contribution of the non resonant diagrams. The effect of the non resonant diagrams (graphs 4-20) is more important when, in the final state, there are one fermion and one anti-fermion with the same flavour, in this case diagrams with photons or with a Z resonant in the s channel are important. In the case in which one W decays into electron and neutrino it is necessary to introduce the diffusion diagrams in the t channel (graphs 11-20 Figure 4.3). The importance of the non resonant diagrams is more concentrated in certain regions of the phase-space so, for this reason their contribution to the cross section has to be calculated after the application of the selection cuts.

4.2 Radiative corrections.

The complete radiative electroweak $\mathcal{O}(\alpha)$ corrections, for the production of two W's **on-shell**, have been calculated independently by two groups: their results agree, for the unpolarised case, at the per-mill level [35, 36]. The calculation of the complete one loop radiative corrections to the **off-shell** case and to the four fermion process is very complicated and then it has not yet been done. The importance of the non calculated radiative correction to the **off-shell** case and to the four fermion production is estimated using the **on-shell** calculations.

4.2.1 Initial state radiation (ISR).

The most important correction to the cross section is initial state radiation, the radiation of one or more photons by the incoming electrons. The effective centre of mass energy is lowered by the photon emission and therefore the cross section is changed. The standard approach, for most of the analytical programs (for example GENTLE [39]), is to multiply the cross section by a radiation function $F(s')$:

$$\begin{aligned}\sigma_{WW}^{off-shell,ISR}(s) &= \int_0^s ds_1 \rho(s_1) \int_0^{(\sqrt{s}-\sqrt{s_1})^2} ds_2 \rho(s_2) \int_{(\sqrt{s_1}+\sqrt{s_2})^2}^{s} \frac{ds'}{s} \\ & F(1-\frac{s'}{s}, s)\sigma_0(s'; s_1, s_2) \end{aligned} \tag{4.10}$$

This multiplicative factor includes the leading log terms which take into account the emission of photons collinear to the incoming electrons. The multiplicative correction is only applicable to the diagrams in the s channel and not to the t channel diagrams because the t channel diagram involves a non-conserved charge flow in the initial state: to avoid the divergences it would be necessary to calculate also the emission of photons from the W's in the final state; these corrections have not been calculated. A way out is the approximation of the so called **current splitting technique** [37], which consists in the splitting of the neutral neutrino in the t channel into two oppositely flowing leptons of charge one. One of them is attributed to the initial state to build a continuous flow of charge, the other is attributed to the final state. Moreover this approximation does not take into account the non-leading photonic corrections, for example photons radiated by an intermediate state like a W. The order of magnitude of the non leading ISR corrections has been estimated, from the comparison between the **off-shell** case and the **on-shell** one, for which these corrections have been calculated, to be about 2% [38]. This is the major uncertainty coming from the theory for the cross section calculations.

Monte Carlo techniques adopts a different way to implement leading log corrections. One method, used for example in KORALW, is to solve the evolution equations for the structure functions numerically using techniques known from parton shower algorithms. In this way soft photon exponentiation and resummation of the leading logarithms from multiple hard-photon emission are automatically taken into account. The precision of this method is limited because the corrections of the order $\mathcal{O}(\alpha)$ are not totally present and it is estimated to be 2%, i.e. the same order of magnitude of the analytical calculation. The cross section calculated by KORALW is in fact in agreement with the one calculated by GENTLE within this limit.

4.2.2 Other radiative corrections.

The electroweak corrections to the cross section for W production are related to the value of the W mass. In the "G_μ scheme", which uses as parameters M_W, G_μ and M_Z, the dependence of the cross section on the mass of the top quark is very weak [43] because of the re-absorption of some radiative corrections into the value of the W mass. In this scheme the WW cross section and all the other observables are calculated in terms of the W mass which is predicted using G_μ as input.
The W cross section is sensitive to the value of the Higgs mass because of the radiative corrections associated to the Yukawa interaction between the two W's [44]. Because of the low velocity of the W's the effect is more important at the threshold energy, as for the Coulomb singularity. A change of the Higgs mass from 300 GeV to 60 GeV causes an increase of the W cross section of 0.9 %. For Higgs masses bigger than 300 GeV no variation of the W cross section are observed.
The QCD corrections are taken into account in calculating the W width:

$$\Gamma_W = \frac{9}{6\sqrt{2}\pi} G_\mu M_W^3 \left(1 + \frac{2\alpha_s(2M_W^2)}{3\pi}\right). \tag{4.11}$$

Another correction which can be important is the "colour reconnection" in the four jets final state $e^+e^- \to q\bar{q}q\bar{q}$. This effect has been studied with different models and can influence the mass distribution of the pairs of the two reconstructed jet, and therefore introduce systematic effects in the mass reconstruction. The effect of the colour reconnection on the cross section measurements is expected to be of the order of 10^{-3} [45, 46].
The total theoretical error on the calculation of the W total cross section is estimated to be around 2% at threshold. The most important contribution to this error comes from the $\mathcal{O}(\alpha)$ radiative corrections associated to the initial state radiation.

4.3 Coulomb singularity.

The interaction between the two W's in the final state must also be taken into account. This effect is important at the threshold energy, divergent in the **on-shell** case where the velocity of the W's is limited. In the **off-shell** case the divergence

is re-absorbed by the non zero width of the two W's. At the lowest order this correction increases the total WW cross section **off-shell** at threshold by 6% [40]. In comparison the higher orders give a contribution of only 0.2 % [41], and therefore can be neglected.
The Coulomb singularity has an effect also on the kinematics of the final state of the W decays [42], nevertheless the effect is small and can be neglected in the estimation of the selection efficiency.

4.4 Bose-Einstein effects.

During the hadronization of the two W's in the final state, some coherence effects can be present, between identical low momentum mesons coming from different W's. The resulting effect on the measurement of the W mass is not yet clear. Since the BE effect favours the production of identical bosons close together in phase-space, we expect the softest particles from each W to be closer to each other than in the absence of the BE effect. This reduces the momentum of the W's and therefore increases the measured W mass. An attempt to try to investigate this effect can be done using the algorithm LUBOEI implemented in JETSET. This algorithm is based on the assumption that BE effects are local in phase-space and do not change the multiplicity of the events. Therefore a re-weighting of the events, with a BE factor, is equivalent to a given shift of the momentum of the bosons produced in the hadronization. One problem with this algorithm is that it does not conserve energy and the momentum, so that this has to be done separately by rescaling all the momenta in the event. So when the events are W^+W^-, identical bosons within each W are shifted closer to each other in phase-space giving an artificial negative shift in the W mass. This shift has to be correct or shown to be negligible.

4.5 The angular distribution for $e^+e^- \to W^+W^-$.

In figure 4.4 the distribution of the differential cross-section as function of the W polar angle is shown:

As can be seen the distribution is forward peaked, in particular it is peaked along the initial charge direction, the W^+ is preferentially emitted along the initial e^+ direction. This is mainly due to the t channel neutrino exchange graph, in which the propagator of the neutrino leads the produced W along the direction of the initial charge. Another remark is that this pole is more pronounced at higher energies, thus the distribution become more and more peaked in the forward region when the energy increases. The study of the angular distribution of the produced W's allows for a separation of different states of helicity and can be used to measure the triple gauge boson couplings.

4.6 Helicity properties of the W pairs.

The helicity of the W pairs produced at LEP, derives from the V-A structure of the W coupling to leptons. The leptons are produced in pairs, and in the approximation m_l = 0 they are longitudinally polarised. As we are working with vector and axial-vector interactions, the scattering take place only if the helicity of the two interacting leptons are opposite: which means that $\sigma_{LL} = \sigma_{RR} = 0$. The vertex $e\nu W$ of Figure 4.1 has a V-A structure, and this graph gives a contribution only if the initial electron is left-handed and the initial positron right-handed. In fact what happens is the following: at high energies, the mass of Z boson plays no role, and thus instead of the exchange of the particles Z and γ, one can think in terms of the exchange of the W_3 and B, the gauge fields. Now, the W_3 cross section contributes only to σ_{LR} and cancels part of the contribution to this cross section coming from the neutrino exchange. The B cross section does not contribute at all because the gauge boson of U(1) does not couple to the W boson. So the graphs for γ and Z boson exchange nearly cancel and the result is that $\sigma_{RL} \sim 10^{-2}\sigma_{LR}$. Thus the dominant helicity configuration is the one shown in figure 4.5 (a). As the cross-section for W production is peaked in the forward region, the figure 4.5 (b) shows the helicity configuration in this region. Since the total spin of the two W's is one the two possible configurations are the following:

$$W^+(\lambda = +1), W^-(\lambda = 0) \qquad or \qquad W^+(\lambda = 0), W^-(\lambda = -1) \tag{4.12}$$

This means that a non negligible fraction of the produced W's are longitudinally polarised.

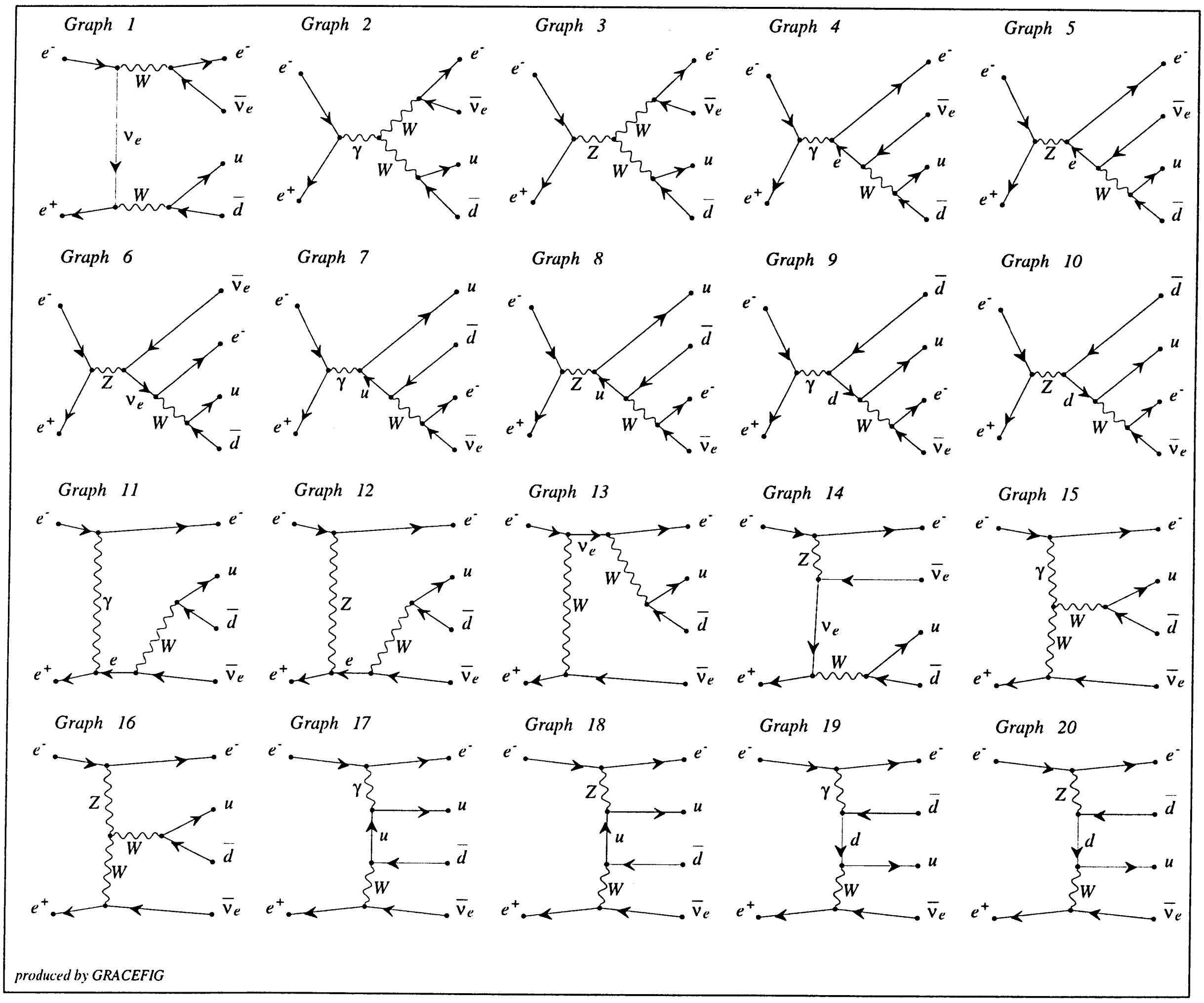

Figure 4.3: **The twenty diagrams contributing to the process $e^+e^- \to qqe\nu$. 1-3 double resonant diagrams as in Figure 4.1. 4-16 s channel single resonant W diagrams. 17-20 t channel (non-resonant). This Figure has been produced with the GRACE program [34].**

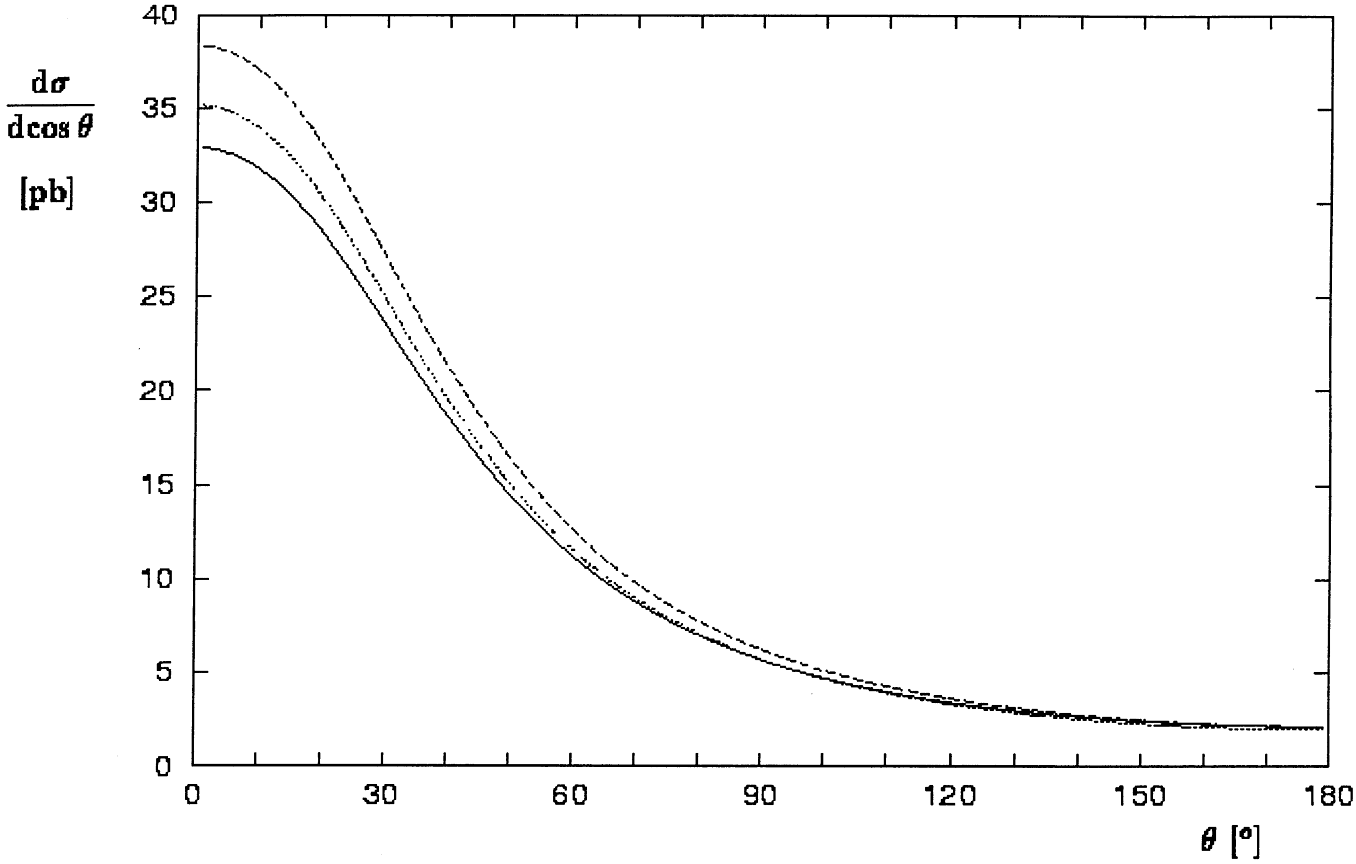

Figure 4.4: **Differential cross-section as function of the polar angle of the W^+ for $\sqrt{s} = 190$ GeV. The dotted line corresponds to Born level, the dashed one to G_μ-Born, and the solid line contains the full radiative electroweak $\mathcal{O}(\alpha)$ corrections.**

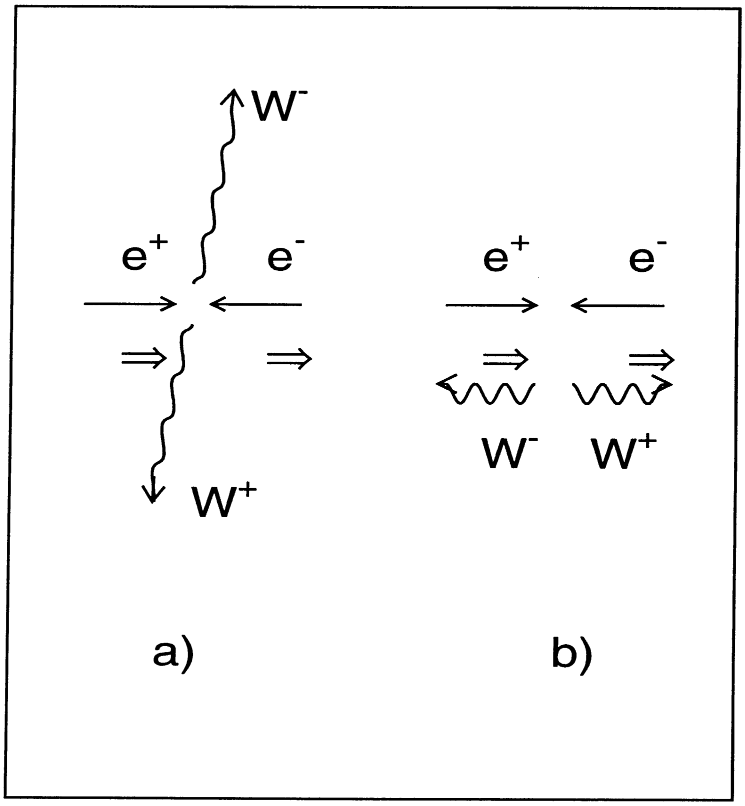

Figure 4.5: **Dominant helicity configuration for the process $e^+e^- \to W^+W^-$ (a). Helicity for the process $e^+e^- \to W^+W^-$ in the forward direction (b).**

Chapter 5

The L3 detector.

5.1 LEP: Introduction.

LEP [50], Large Electron Positron collider, is an accelerator for electrons and positrons built to study e^+e^- interactions at centre-of-mass energies between ~ 90 GeV and 200 GeV.
It has a circumference of about 27 Km. It has eight arcs and eight straight sections, four of which contains the experiments ALEPH [51], DELPHI [52], L3 [49], OPAL [53] (see Figure 5.1). From 1989 until 1995 LEP ran at energies around Z peak, producing about four million Z bosons per experiment. In 1995 LEP had the first high energy run at $\sqrt{s} = 130 - 136$ GeV. In 1996 it started to run at $\sqrt{s} = 161$ GeV the threshold of the W boson production. Since then LEP runs at energies above this threshold (at $\sqrt{s} = 172$ GeV in 1996 and at $\sqrt{s} = 183$ GeV in 1997) and has produced about 1500 pairs of W bosons per experiment.
In table 5.1 the most important parameters of LEP are shown (referring to the status of the accelerator in 1997).
A detailed description of the machine can be found in the reference [47].

5.1.1 Electron and positron beams and luminosity measurement.

Positrons and electrons are injected in the machine at the energy of ~ 20 GeV. They are grouped in four bunches circulating in opposite directions. When the ring is filled, with about $5 \cdot 10^{11}$ particle per bunch, the energy is increased to its final value. In the four arcs of LEP, quadrupole magnets produce the bending of the beam and maintain positrons and electrons on the orbit. Due to the bending, the particles

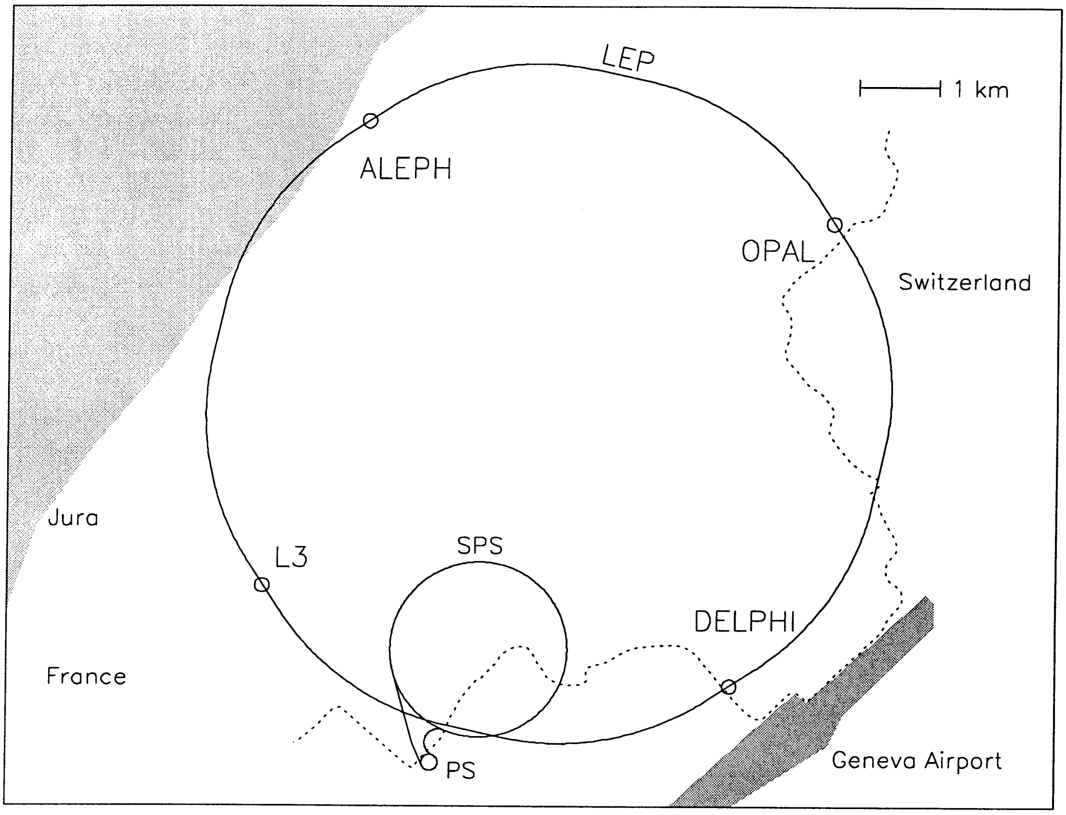

Figure 5.1: **The LEP collider and the four experimental points of LEP.**

loose a part of their energy by synchrotron radiation. The energy loss depends on the energy of the particles, E_{beam}, and on the radius of the curvature, ρ, being proportional to E_{beam}^4/ρ [54]. The typical energy loss for an electron of 45 GeV is 0.1 GeV per revolution [55]. The energy loss is compensated by the radio-frequency (RF) cavities, which accelerate the beams. When the beams are accelerated they are kept separated using electrostatic separators, and after reaching the design energy are placed on a common orbit. They are focused in the four interaction regions by the superconducting quadrupole magnets. This is very important to increase the luminosity.

The luminosity is the rate of interactions between electrons and positrons per unit of cross section σ. In terms of the machine's parameters the luminosity can be written as:

Circumference	26658.883 m
Frequency of the RF	352.20904 MHz
Total power of the RF	16 MW
Synchrotron radiation	260 MeV/turn
Time between two beam interactions	$\sim 11\mu s$
Maximum luminosity	$3 * 10^{31}\ cm^{-2}\ s^{-2}$
Number of bunches per beam	4
Number of particles per bunch	41.6×10^{10}
Mean life of the beams	8 hours
Error on the centre of mass energy	~ 50 MeV

Table 5.1: **LEP parameters.**

$$L_s = \frac{N_{e^-} N_{e^+}\ n_b\ f}{4\pi\sigma_x\sigma_y} \tag{5.1}$$

where $N_{e^\pm}$ is the number of particles per bunch, n_b the number of bunches per beam, f the frequency of revolution and $\sigma_{x,y}$ the semi-dispersions of the beams in the two transverse directions which define the effective area of interaction. In the design of LEP a luminosity of $1.7 \cdot 10^{31} cm^{-2} s^{-1}$ at m_Z was foreseen. $N = L \cdot \sigma$ relates the number of events observed in a given time, to the cross-section of the process.

At LEP the luminosity is measured, by the experiments themselves, using the Bhabha scattering $e^+e^- \to e^+e^-(\gamma)$. This process, at low scattering angles, is dominated by the photon exchange in the t channel and has a cross-section of about 88.5 nb. Since it is a pure QED process its cross-section can be calculated with high precision [56]. The actual theoretical uncertainty is 0.11% ($\sim$ 0.15% at LEP2). In L3 for example, the scattered $e^\pm$ are measured in two calorimeters, luminosity monitors, placed symmetrically with respect to the interaction point, covering the angular region $25 \simeq (\theta, \theta - \pi) \simeq 70$ mrad (Figure 5.2). A silicon tracker (SLUM) [57] is placed in front of each BGO calorimeter. Each calorimeter is a matrix of 340 BGO crystals. The energy resolution of the calorimeter is 2% at 45 GeV and the angular resolution is 0.4 mrad in θ and 0.5 mrad in ϕ. The silicon detector has three layers: two layers of strips concentric with the beam axis (r wafers $\pm$ 2610 mm and $\pm$ 2690 mm), to measure θ angle, and one layer with the strips perpendicular to beam axis (ϕ wafers $\pm$ 2650 mm) to measure the ϕ angle. The wafers have a very high intrinsic geometrical precision (1-2 μm).

To avoid radiation damages, the two monitors are each divided in two halves, which are separated during the filling of LEP and during the acceleration phase. They are

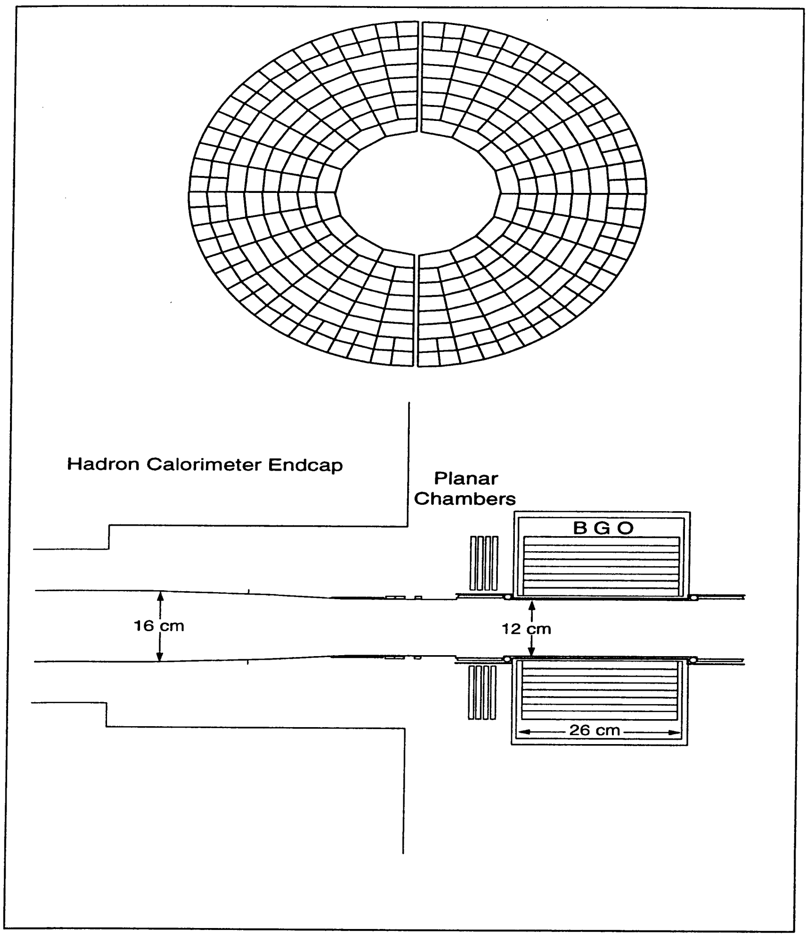

Figure 5.2: **View of the luminosity monitors and their position in the detector.**

closed, and their separation is controlled with a precision of 10 μm, when the beams are stable.

The differential cross section of the Bhabha scattering depends strongly on the angle θ (like θ^{-4}), therefore the measurement is sensitive to the definition of the minimum angle of acceptance. To reduce the systematic error on the acceptance, due to uncertainties on the position of the calorimeters and on the position of the interaction point, an asymmetric criteria on the selection of the Bhabha events is used. In at least one monitor the energy must be deposited at more than one crystal spacing from the edge of the calorimeter. The luminosity is obtained by taking the mean of the two samples of events obtained with the restriction of the fiducial volume in one or the other calorimeter. The total systematic error on this measurement is 0.6 % when using only the BGO calorimeter, and 0.15 % when using both the BGO and the SLUM detector.

5.1.2 Beam energy measurement.

Energy measurements.

One of the most important parameter to perform precise measurements of the W mass is the energy of the beam. Different methods to determine the energy of the beam are used at LEP [58].

- **field display**: this method uses a reference dipole magnet, containing a rotating coil to measure its field, put in series with the bending magnets. This magnet is kept in a controlled environment with stable conditions of temperature and humidity. The measurements are taken continuously with the advantage that they can be performed when the ring is filled. The reproducibility of the measurement is $2.5 \cdot 10^{-5}$. The energy measured with the field display system E_{FD} is related to the centre-of-mass energy by the relation: $E_{CM} = 2E_{FD} - 68$ MeV.

- **flux loop**: the flux loop is a system used to monitor the strength of the magnetic field in the bending dipoles of the ring. It allows the extrapolation of the field display over all the ring of LEP. It consists of eight electric loops passing in the ring through the dipoles. Their effect is to change the current in the dipoles, and then measuring the induced voltage one can extract the magnetic field.

- **proton calibration**: the LEP ring is filled with protons of 20 GeV of energy. Their momentum can be measured from the frequency of the RF acceleration voltage f_{RF_p}. Using the same magnetic setting of the protons, positrons are injected in the machine and after tuning the frequency of the RF, f_{RF_e}, the velocity of the protons and their momentum can be extracted from the following relation:

$$\frac{v_p}{v_e} = \frac{\beta_p c}{\beta_e c} = \frac{h_p f_{RF_e}}{h_e f_{RF_p}} \tag{5.2}$$

where $h_{p,e}$ represents the number of oscillations of the RF cavity per particle revolution of the ring. These numbers are integers and they have no errors (they are 31324 and 31358) because a change of 1 in one of them would mean a change of the circumference of LEP of 0.8 m, while it is measured with a precision of 2mm [59]. β_e for ultra-relativistic positrons is 1.

This method is used to calibrate the flux loop measurement. The calibration procedure has an accuracy of 10^{-4} at 20 GeV. This uncertainty has to be multiplied by a factor two due to the extrapolation, with the flux loop, from 20 GeV to the running energy of the machine.

- **resonant depolarisation**: the most precise measurement used at LEP to measure the beam energy is based on the resonant depolarisation of a transversally polarised beam [60]. The beam polarises itself under precise conditions due to the Sokolov-Ternov effect [61]. The maximal polarisation that can be obtained is 92.4 % [62]. In this method, the frequency of the spin precession of the electron or of the positrons in the polarised beam, is measured. This number is directly related to the momentum of the particles [59]. The relation between the spin tune, ν_s, which is the number of spin precession per revolution, and the beam energy, E_b, is the following:

$$\nu_s = \frac{g_e - 2}{2} \frac{E_b}{m_e c^2} \tag{5.3}$$

  where $(g_e - 2)/2$ is the anomalous magnetic moment of the electron. ν_s is determined by exploiting resonant depolarisation. An oscillating horizontal magnetic field is applied to the vertically polarised beam, then, from the frequency of the oscillating field when the beam depolarises one can derive the spin precession frequency. Some other corrections have to be applied: temperature corrections, aging of the magnets and tidal effects of the moon and the sun which can deform the surface of the earth so changing the circumference of LEP. The method reached in 1991 a precision of 1.6 MeV. In 1993, 24 calibrations of the energy, each better than 1 MeV, were performed [63].

In 1996 we studied a new method to measure the energy of the beam at LEP (which takes into account the new situation of the machine running at energies higher than 45 GeV). It consists on a new detector based on the principle of Møller scattering. It will be discussed in detail in appendix A.

Procedure.

All the methods mentioned in the previous section (except of course the Møller method) are used to determine the energy of the beam at LEP, and then combined together. The energy is evaluated as function of the time for each experiment. The total error on the centre-of-mass energy is also determined and the correlations of these errors for different energy points. At LEP2 the energy cannot be measured with the energy depolarisation method at the physics energy of 161 and 172 GeV because the maximum energy at which we have measured the beam polarisation is $\sim$ 55 GeV. Therefore the energy is measured using the resonant depolarisation at the maximum possible energy ($\sim$ 55 GeV) and then extrapolated using magnetic measurements with NMR probes in the dipoles magnets and flux loop measurement of the dipole field. The method used in 1996 can be summarised as follows:

- determine the absolute energy scale using the resonant depolarisation at the energy of 45 or 50 GeV: these are the references points, E_{ref}. These measurements were extrapolated to the physics energy, E_{ext}, using the 16 NMR probes installed in the dipole magnets.

- correct for known effects like earth tides, rise of the dipole field during the fill due to the temperature and train effect.

- correct for effects specific to each interaction point (IP) due to RF configuration and vertical collision offsets.

The error on the measurement was calculated as the difference between the result obtained with the NMR's, with the flux loop magnetic field and the resonant depolarisation at 45 and 50 GeV. Taking into account the fact that all these measurements were done during a single fill, we do not have to take into account the error coming from fill-to-fill changes. The difference between the NMR energy measurement and the flux-loop, at physics energy, has been measured to be about 10 MeV.
The extrapolation errors, estimated from NMR and flux-loop are of the order of 10-12 MeV. However the polarisation measurements were done only in one fill. Then, using the flux-loop energy scale would give a deviation of about 20 MeV compared to the energy derived from the linear extrapolation of the polarisation points. As there are only two points, no linearity check is possible. Taking into account all these contributions the systematic error coming from the extrapolation to the physics energy has been calculated to be $\sim$ 25 MeV. This is the major source of systematic error in the measurement of the beam energy at LEP in 1996. The total systematic error on $\sqrt{s}$ has been estimated to be $\sim$ 30 MeV.

5.2 General characteristics of the L3 detector.

The L3 detector is in the point 2 interaction region of LEP at a depth of 52 m. It is surrounded by a magnet of 7800 t which produces a magnetic field of 0.5 T. In table 5.2 characteristics of the magnet are shown.

Inside the magnet, the detector is hold up by a steel support tube of weight 240 t,

Internal radius of the coil	5390 mm
Thickness of the conductor	890 mm
Total length of the coil	11900 mm
Electric power dissipated	4.2 MW
Central field	0.5 T
Current circulating in the conductor	30 KA
Density of the current in the conductor	55.5 A/cm^2
Weight of the aluminium coil	1100 t
Weight of the filling iron	6700 t

Table 5.2: **Characteristic of the L3 magnet.**

with an internal diameter of 4.45 m and a length of 32 m.
The detector was designed to have a good energy resolution in the measurement of muons, electrons and photons. For the muon spectrometer the aim was to have a resolution in the momentum measurement of $\Delta p/p \sim 2\%$ at 50 GeV. This was obtained by maximising the length of the μ trajectory. In fact the momentum resolution is proportional to the sagitta s ($\Delta p/p \simeq \Delta s/s$). The sagitta can be written as:

$$s \simeq \frac{0.3}{8}\frac{L^2 B}{p_t} \tag{5.4}$$

where B is the intensity of the magnetic field, L the distance between the first and the last point measured on the muon trajectory and p_t the transverse momentum of the muon. But in this design the space available for the rest of the detector is reduced imposing the choice for very compact and high precision calorimeters and tracking chambers.
Starting from the central region nearest to the interaction point, the detector (Figure 5.3) is composed of:

- The Silicon Microvertex Detector (SMD), for precise measurements of charged tracks near the production point.

- The central chamber to detect the tracks of the charged particles (Time Expansion chamber, TEC).

- The high resolution electromagnetic calorimeter composed of 10780 crystals of bismuth germanate (BGO).

- The scintillator system to measure the time of flight.

- The hadronic calorimeter made of layers of uranium alternated with wire proportional chambers.

- The muon filter.

- The muon spectrometer made of three layers of drift chambers which is outside the support tube.

The reference system of L3 is defined with origin in the centre of the detector, at the interaction point. The z axis is parallel to the beam in the direction of the electron beam. The y axis is in the vertical direction and the x axis is in the horizontal direction pointing toward the centre of LEP.
The apparatus has a cylindrical symmetry with respect to the beam axis. The cylindrical coordinates are defined by the angle θ, the polar angle with respect to the z axis and the azimuthal angle ϕ in the $x-y$ plane (also called R-Φ plane), measured starting from the x axis.

5.3 The central tracking system.

5.3.1 The silicon microvertex detector (SMD).

The SMD [64] was installed in the L3 detector in the year 1993, to improve the track reconstruction capability. It is made of two layers of double-sided silicon microstrips.

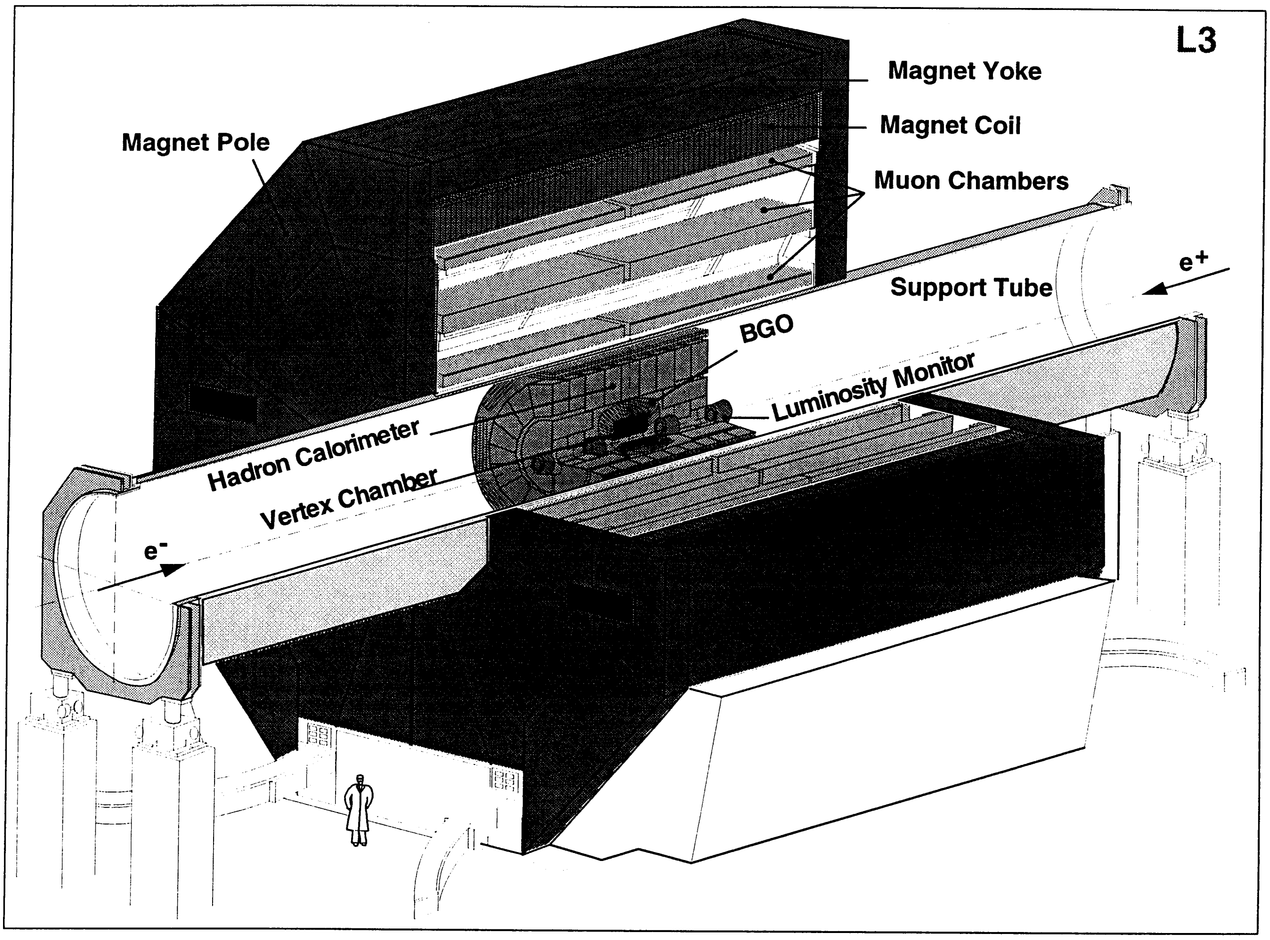

Figure 5.3: **Perspective of L3 detector.**

It has a resolution of 7 μm in the $R-\Phi$ plane and of 14 μm in the $R-z$ plane. This improves by a factor of two the momentum resolution of the inner tracking system independently on the alignment SMD-TEC, because of the longer lever arm, and the impact parameter can be improved by a factor of 5 if the alignment of the SMD with the TEC is controlled with a precision of 10 μm. Such improvements allow important progress in different fields of LEP1 and LEP2 physics. At the Z pole the SMD is important for the reconstruction of heavy quarks in hadronic events, it allows the measurement of secondary vertices for particles with a lifetime bigger than 10^{-13} s. At LEP2 the identification of the b quark is crucial in the searches of the Higgs boson. This detector is hermetic in Φ and covers the θ angular region between 22° and 158°.

5.3.2 The time expansion chamber (TEC).

The central chamber [65] is a drift chamber with a cylindrical symmetry, it has a radius of about 50 cm and a length of 1 m, the lever arm available for the measurements of the transverse momentum is 37 cm.
The TEC has been constructed to:

- detect charged particles and to measure the spatial coordinates of their trajectory in the magnetic field;
- measure the transverse momentum and the sign of the charged particles with an energy up to 50 GeV;
- reconstruct the interaction vertex;
- reconstruct the impact point and the direction of the charged particles at the beginning of the electromagnetic calorimeter.

It is made of two coaxial,cylindrical, drift chambers which cover the radial region from 90 to 457 mm.
In each of them the drift space is divided into two zones: the drift zone with a low electric field and the amplification zone with a high electric field.
The TEC works with a mixture of CO_2 (80%) and C_4H_{10} (20%) at the pressure of 2 bars, which guarantees a slow drift velocity (6 μ m/ns) (Time Expansion Chamber) [66].
In Figure 5.4 the positions of the wires in one TEC sector is shown. The inner chamber is divided in 12 sectors each of them containing 8 anode wires parallel to the beam axis, to measure the $R - \Phi$ coordinate to a precision of about $60\mu m$. Two of them have charge division readout to determine the z coordinate to a precision of 2.5 cm.
The external chamber is divided in 24 sectors with 54 anode wires which measure the track coordinate with a resolution per single track of 51 μm.
The two tracks separation power is 450 μm.
The stability of the electric field contributes to the spatial resolution, because the drift velocity depends on it, it has to be constant within 0.5 V/cm.

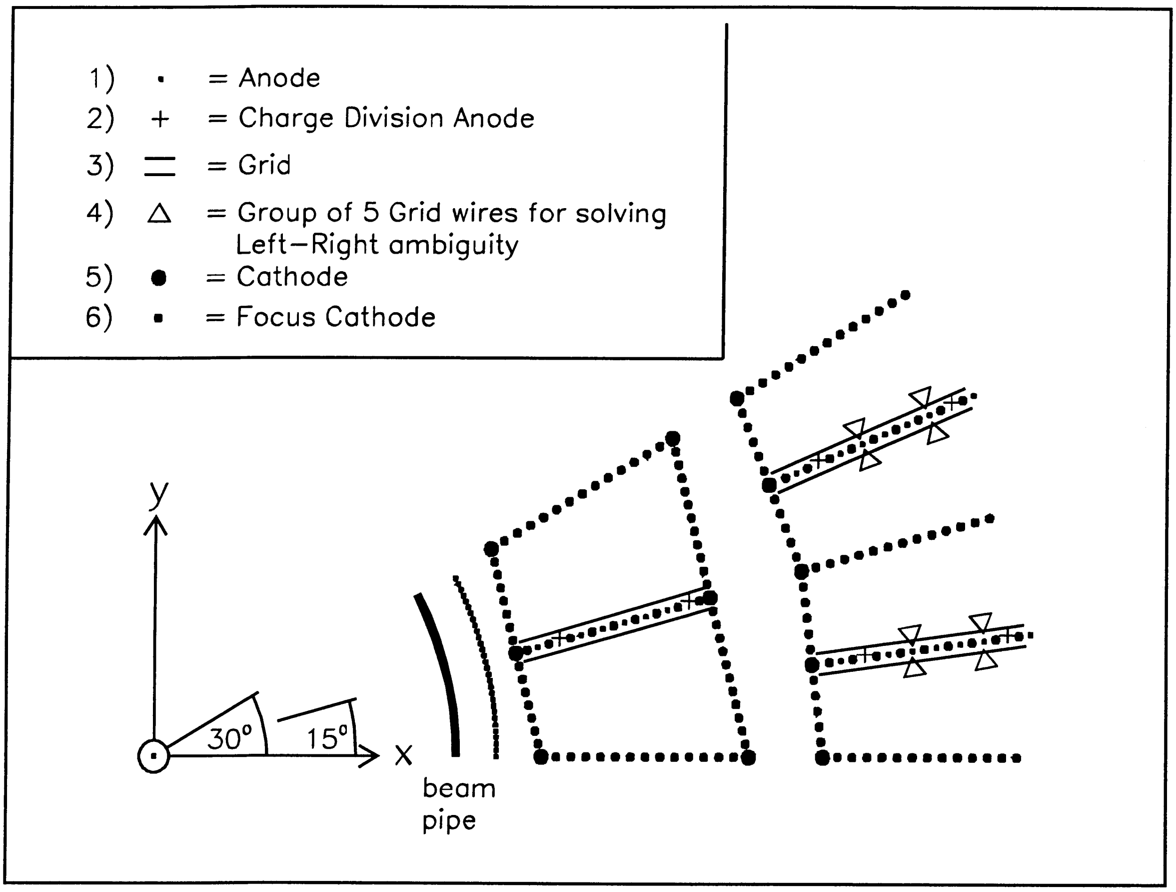

Figure 5.4: **Position of the wires in a TEC sector.**

The TEC is completed by two cylindric proportional chambers, with a cathode read-out to measure the z coordinate. The cathode strips are oriented at 90°, 70.1°, −70.1° and 0° with respect to the beam direction. The resolution of the z measurement in the region $45° \leq \theta \leq 135°$ is 300 μm.
For the analysis described in this thesis the TEC has been used to separate electrons from photons by associating a track to an electromagnetic bump in the BGO calorimeter.

5.4 The scintillator system.

The scintillators, placed in the barrel between the electromagnetic calorimeter and the hadronic calorimeter, are used to measure the time of flight of particles.
They are 2900 mm long and they cover the angular region $25° \leq \theta \leq 155°$.

They are made of 30 plastic scintillator bars, BICRON BC-412 with a thickness of 1 cm and of a length of 290 cm, read by Hamamatsu phototube R249-01.
Their time resolution is 1 ns which allows to distinguish a cosmic muon passing near the interaction point from a muon produced in the events, as for $e^+e^- \rightarrow \mu^+\mu^-$. A cosmic muon, takes 5.8 ns to cover the distance between two opposite counters.

5.5 The electromagnetic calorimeter.

The electromagnetic calorimeter(BGO) [68] is made of Bismuth-Ortogermanate crystals ($Bi_4Ge_3O_{12}$). It is an intrinsic scintillator, it has a small radiation length (1.12 cm) such that one electromagnetic shower, even of 50 GeV of energy, is contained in a compact detector. The small Molière radius, i.e. the small transverse development of electromagnetic showers, imposes an high granularity of the detector ($2 \times 2cm^2$), to allow for a good angular separation of near by particles.
The hadronic component of the event interacts rarely in the BGO because it has only one absorption length and this allows a good π/e separation.
In the table 5.3 the most important characteristics of the BGO are shown. The light

Density (g/cm^3)	7.13
Radiation length (cm)	1.12
Interaction length (cm)	22
Molière radius (cm)	2.3
dE/dx at minimum ionization (MeV/cm)	9.1
Relative production of light (%) with respect to NaI(Tl)	8-15
Wave length of emission at the peak (nm)	480
Decay time of the emission (ns)	300
Index of refraction	2.15
Temperature coefficient (%/degree C)	-1.55 (at 25°)
Intrinsic resolution $\sigma E/E$	$0.5\%/(E(GeV))^{1/2}$
Higroscopicity	No

Table 5.3: **BGO properties.**

yield depends on the temperature, which is kept at $\sim 18° \pm 0.1°$ by a special cooling system. A map of the temperature is obtained by sensors attached in the front and in the end surface of the crystals. This allows for the registration of the temperature of 1 crystal out of 12 and a possible correction of the energy according to the observed variation.
The calorimeter is divided in two parts: the barrel which covers the central region

(covering the angular region $42.3° \leq \theta \leq 137.7°$, corresponding to 74 % of the total solid angle), and two endcaps, which cover forward and backward the angular region in θ from 10.5° to 36.7° and from 143.3° to 169.5°.

In the barrel the crystals are pointing the interaction region, they have the form of a truncated pyramid with a front surface of $2 \times 2\ cm^2$ and the back surface of $3 \times 3\ cm^2$. The crystals are 24 cm long, which corresponds to $\sim$ 21 radiation lengths. In the Figure 5.5 the sections of the calorimeter showing the orientation of the crystals are reported. The crystals lie in a support structure made of two symmetric half barrels,

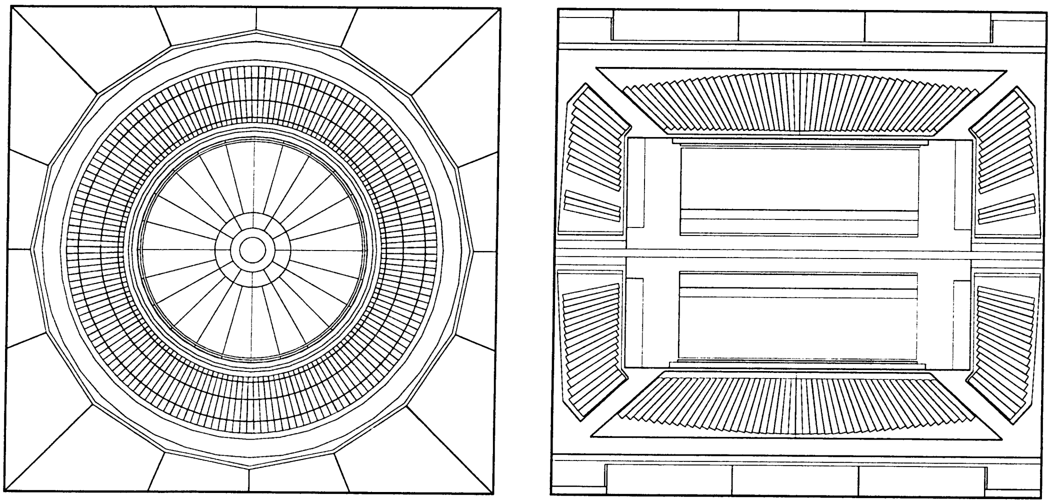

Figure 5.5: **Section in the R-Φ (a) and R-z (b) plane of the electromagnetic calorimeter.**

each of one containing 3840 crystals, 160 crystals in Φ and 24 in θ.

In the endcaps 3070 crystals are disposed in 17 rings in θ with a variable number of crystals per ring. Each endcap is subdivided in 16 sectors in ϕ (Fig. 5.6). All the crystals in the calorimeter are supported by a carbon fibre structure which creates a very thin separation between the crystals (200-250 μm). In front of the two endcaps there are two tracking chambers (Forward Tracking Chambers) to measure the position and the direction of charged particles at low angle. They have a spatial resolution $\leq$ 200 μm.

Since the TEC has been made longer with respect to the original design, they are moved behind, leaving an open region of about 5° between the barrel and the endcap. This hole has been covered in 1995 with a new calorimeter, EGAP, which will be described next in this Chapter.

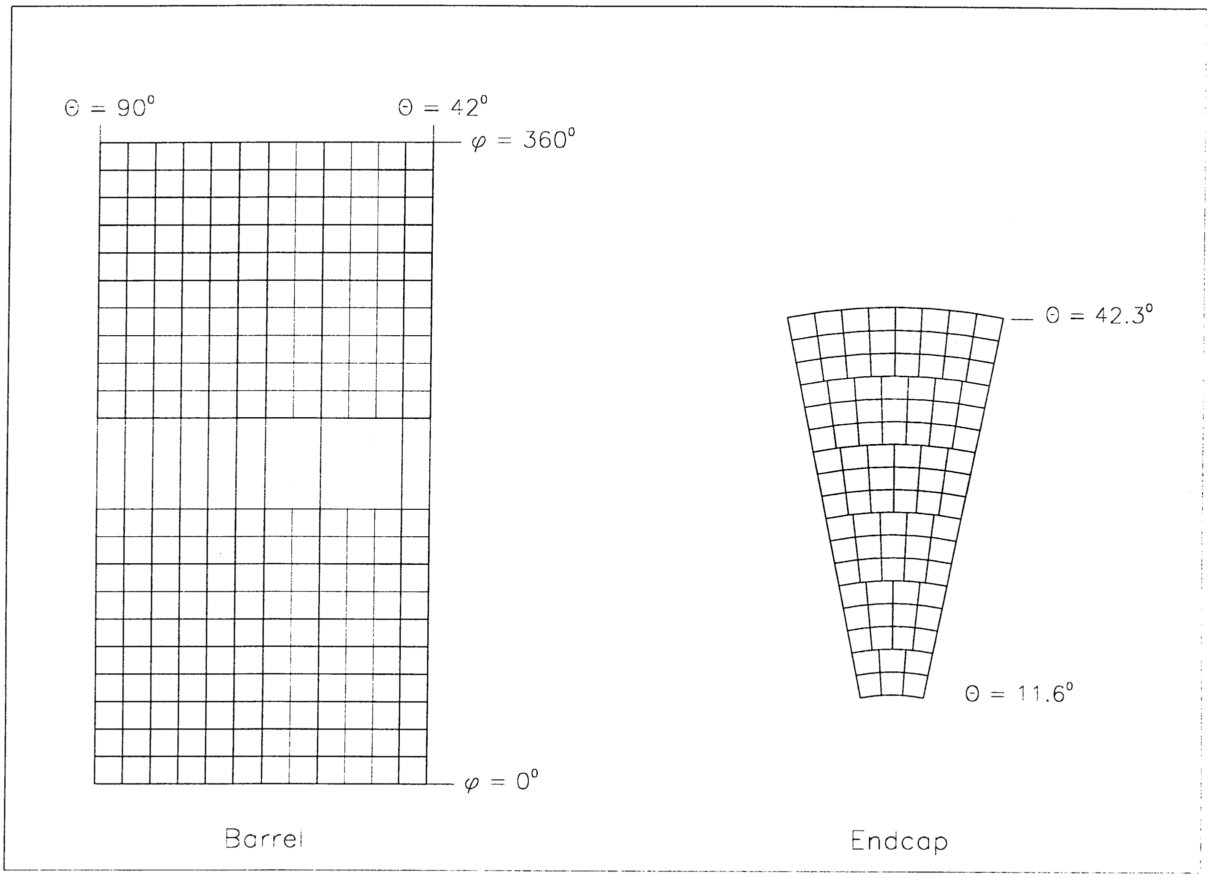

Figure 5.6: **Position of crystals in a half barrel and in a sector of the endcap.**

5.5.1 Electronics.

The scintillation light is collected by two Hamamatsu S-2662 photodiodes on the back surface of each crystal. These photodiodes have an efficiency of $\sim$ 70% around the emission peak of the BGO (480 nm). The photodiode produces $\sim$ 1200 electrons per MeV of deposited energy, which corresponds to a signal of $\sim$ 0.2 fC. This is only a fraction of the total produced light, which is reflected many times on the sides of the crystal before reaching the photodiodes. A uniform light collection is obtained by modifying the reflecting properties of the surfaces of the crystals: on each crystal a layer of white paint, with high diffusion power, of a thickness of $\sim$ 40-50 μm has been applied.

The first calibration of the crystals, was done by studying the response to muons, using the muon chambers as a telescope for cosmic rays [48]. The light collected for different impact points (x) in the BGO crystal can be written as:

$$Light \sim 1 + R\,\frac{L-x}{L} \tag{5.5}$$

where L is the length of the crystal and R a non uniformity parameter. In Figure 5.7 is shown the value of R ($\sim -10\%$) in the crystals and the energy variation for different values of R. For all energies bigger than 10 GeV, the corrections for the non

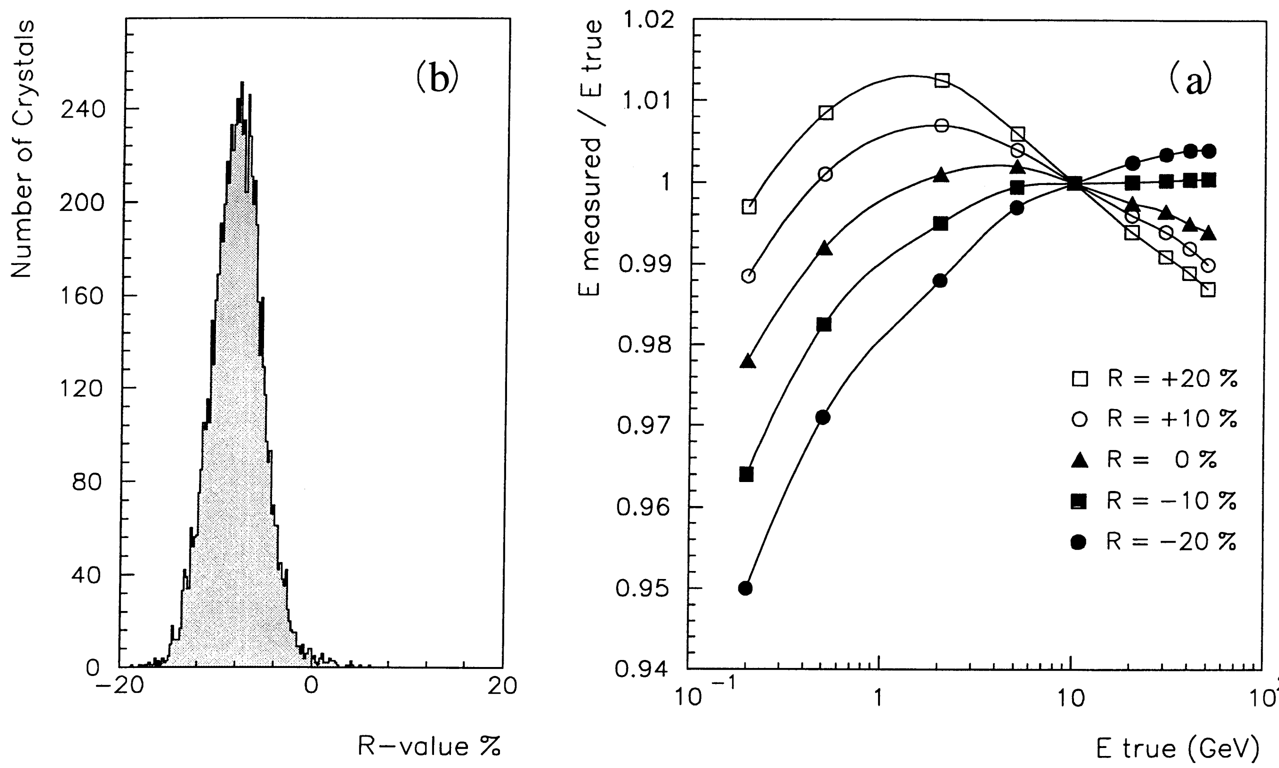

Figure 5.7: **Distribution of the non uniformity factor R and the measured energy normalised to the true value as function of the initial energy for different values of R.**

uniformity in the light collection are negligible (for $R = -10\%$ corresponding to the mean value of the distribution of R) while they are important at low energies: of the order of $\sim 1\%$ at 1 GeV for $R = -10\%$.

This signal coming from the photodiodes is amplified by a preamplifier, glued behind the crystal. The output signal has an amplitude of 50μV/MeV, proportional to the collected charge and therefore to the deposited energy, with a rise time of 300 ns and a decaying exponential time of 800 μs. The noise produced by the photodiode-preamplifier system is $\sim$ 1 MeV equivalent.

The first level of the electronics is given by analog-digital converters, near the crystals.

The analog signal of the preamplifier passes in a shaping circuit which reduces the exponential tail from 800 μs to 1.2 μs.
All information is here contained in the height of the signal, which is read by three channels:

- low energy.
- high energy.
- analog adder for the energy trigger.

In the low energy channel the signal is amplified by a factor 32 before integration. At each bunch crossing the signals are integrated for 5 μs and kept in a sample circuit. If the signal fulfils the requests of the trigger it is digitised, otherwise the integrators are cleared 2μs before the next bunch crossing. As output of the sample circuit three signals are available for the low and high energy channels, corresponding to three amplification factor 1, 4 and 16. A microprocessor MC6803 chooses the one with the best amplitude for the analog-digital conversion using 6 comparators and a DAC (digital-analog converter) with 12 bits. The range of the signals is from 5 μV (about 0.1 MeV) for a single count in the low energy channel amplified by 16, to 10 V (200 GeV) for the maximum of the high energy channel. In this interval the linearity of the energy measurement is better than 1%. The amplitude of the signal is proportional to the ADC counts, for each of the 6 channels a slope (s) and an offset (o) is measured:

$$V = s \cdot ADC + o \tag{5.6}$$

When no scintillation signal is present in the crystal, a pedestal signal, which should be subtracted from the measured value of V, is read. Each channel has two pedestals, one for the low energy and one for the high energy channels. They are measured in special runs at least once per day.

5.5.2 Measurement of the electromagnetic particles in the BGO.

In the BGO electromagnetic calorimeter, two objects can be reconstructed: the **clusters** and the **bumps**. A **cluster** is an isolated energy deposit, when in the adjacent crystals no energy is present. A **bump** is a local maximum of the energy distribution in a cluster. To measure the energy of a bump, the energy of the crystals which form the bump can be simply added; but for electromagnetic particles we use three different quantities:

1. **sum of one**, Σ_1, defined as the energy of the central crystal, which is the most energetic one.

2. **sum of nine**, Σ_9, obtained adding the sum of the energy of the central crystal to the energies of the 8 crystals in the ring around it.

3. **sum of twenty-five**, Σ_{25}, obtained adding to Σ_9 the energies of the 16 crystals in the ring around it.

These three objects are shown in Figure 5.8. For electromagnetic showers, most of the energy is deposited in the central crystal. The intrinsic resolution of the calorimeter

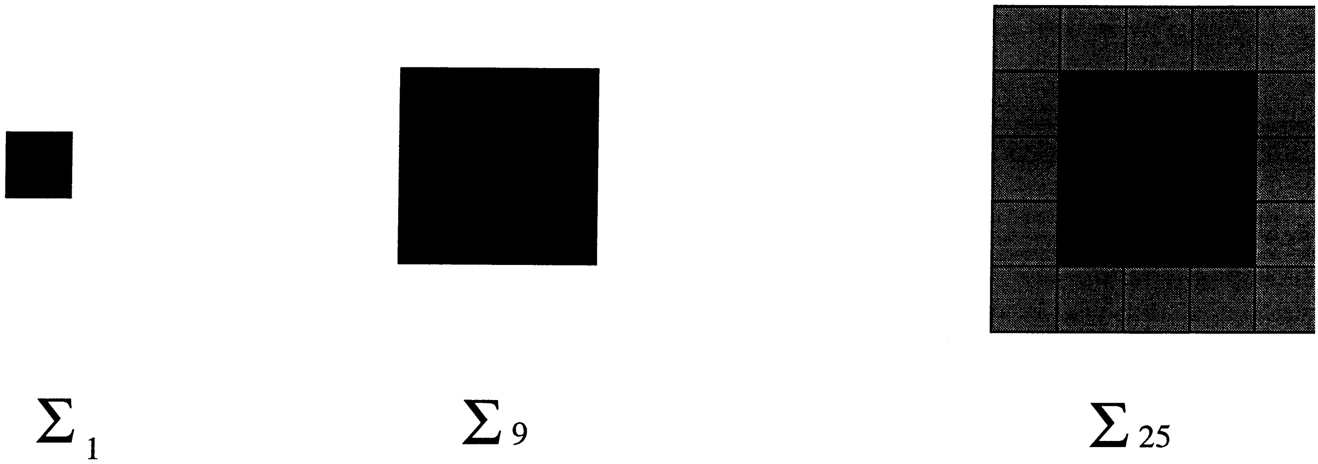

Figure 5.8: $\sum_1$, $\sum_9$ **and** $\sum_{25}$.

is related to the poissonian fluctuations of the number of the particles which compose the shower. Since the number of produced particles is proportional to the energy of the incoming particle the intrinsic resolution is:

$$\frac{\sigma_{intr}}{E} \propto \frac{1}{\sqrt{E}} \tag{5.7}$$

At high energies only one contribution is important for the resolution; it comes from the different response of the crystals. The Figure 5.9 shows the energy resolution of the BGO as function of the energy. The asymptotic behaviour at high energy

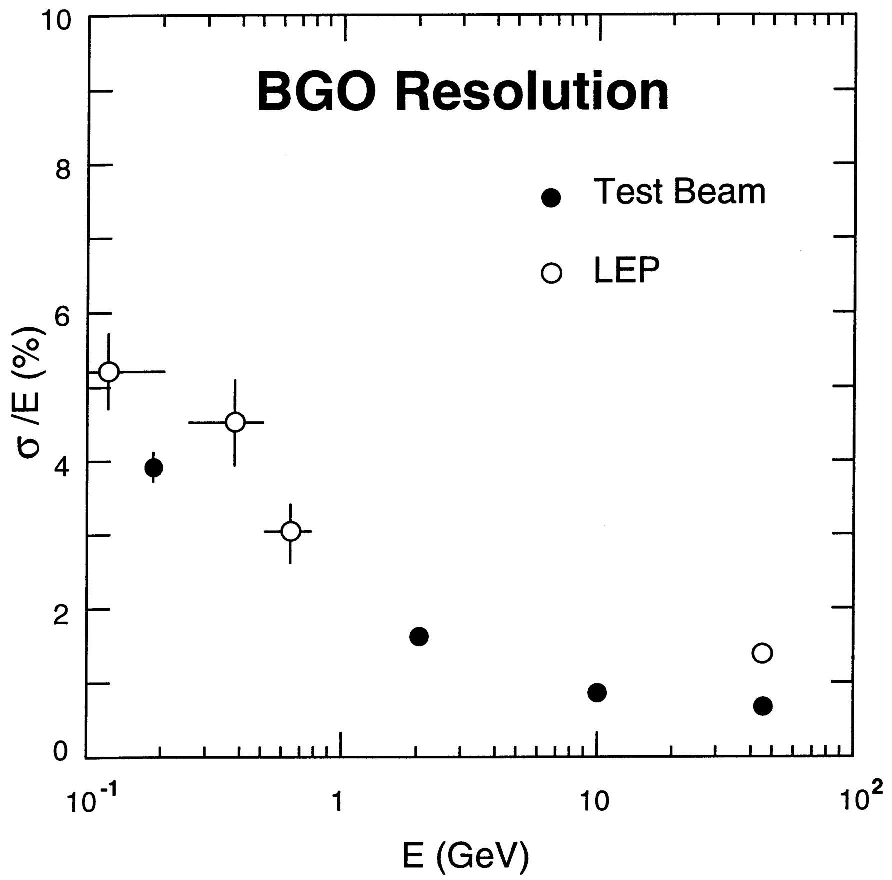

Figure 5.9: **Energy resolution of the BGO barrel as function of the energy, as measured during the test beam and at LEP.**

represents the constant term which takes into account the calibrations [67].
The impact point resolution of an electromagnetic shower, can be obtained, by comparing the impact point measured in the BGO with the one measured with the TEC in the $R-\Phi$ plane. The Figure 5.10 shows the Φ resolution as function of the energy. At high energy σ_Φ is 1.2 mrad (0.7 mm).

5.5.3 EGAP.

The new EGAP [69] detector is made of a lead structure filled with scintillating fibres SPACAL (Fig.5.11). There are two rings, one for each gap, of 24 modules of

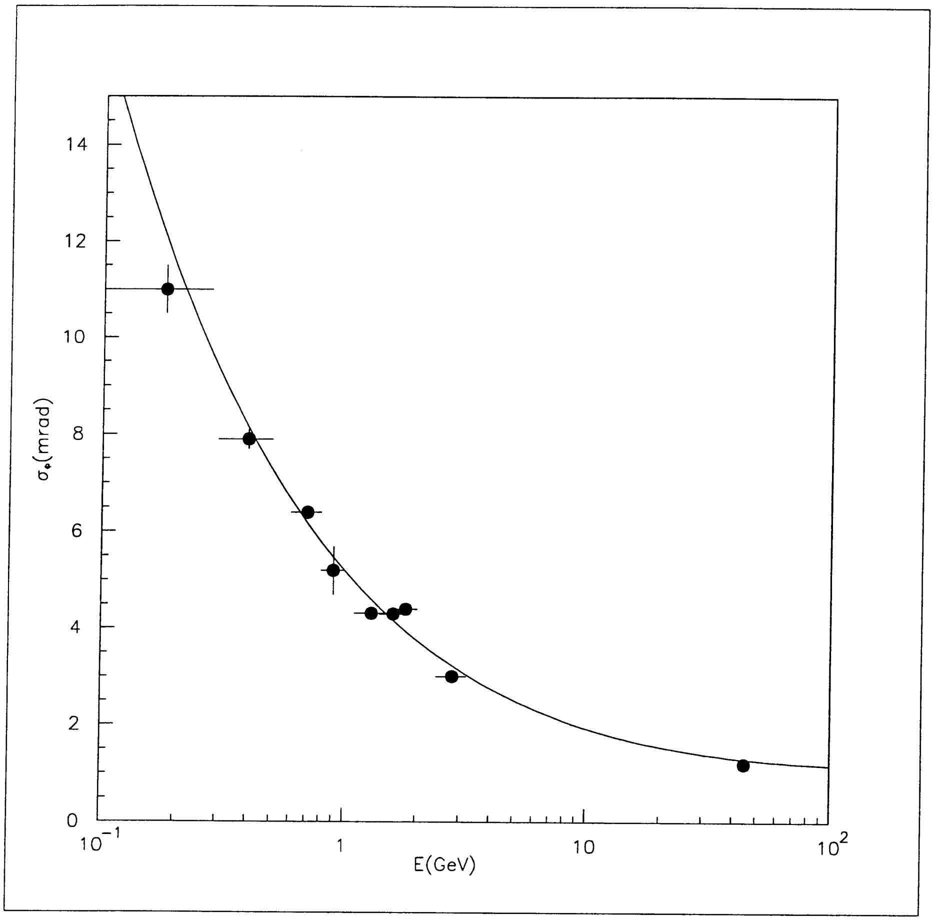

Figure 5.10: **Angular resolution of the BGO as function of the energy, in the R-Φ plane.**

trapezoidal form. The light is collected using two Plexiglas light guides per module plus two phototriodes. Some space is left between modules due to the presence of cables coming from the TEC. To reduce the inefficiencies caused by this dead space the modules are not pointing to the interaction point. The radiation length of the calorimeter is 0.72 cm which ensure a good shower containment ($21X_0$). The measured energy resolution, when the particle hits the centre of the brick, is [70]

$$\frac{\sigma(E)}{E} = (2.3 \pm 0.6)\% + \frac{(11.6 \pm 1.3)}{\sqrt{E(GeV)}}\%. \tag{5.8}$$

The efficiency of the detector used as a veto is 98%.

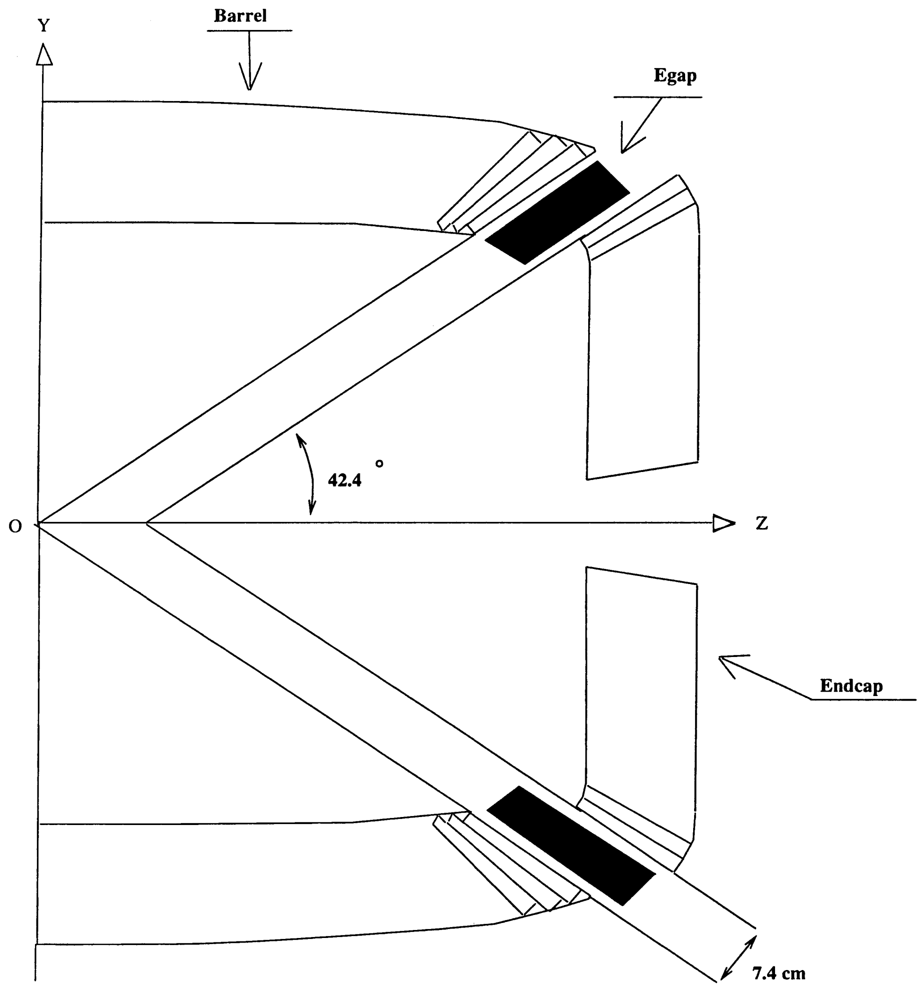

Figure 5.11: **Longitudinal view of the EGAP.**

5.6 Hadronic calorimeter and muon filter.

The hadronic calorimeter [68, 71] measures the energy and the direction of the hadron showers, and identifies the muons as minimum ionising particles. The hadronic calorimeter covers 99.6% of the solid angle; it is divided into a barrel, in the angular region $36° \leq \theta \leq 144°$, and two endcaps in $5° \leq \theta \leq 36°$ and $144° \leq \theta \leq 175°$. It is a sampling calorimeter made of layers of depleted Uranium, as absorber, and proportional chambers (PC), operating in a mixture of Argon (80%) and CO_2 (20%), as detectors. They are calibrated with cosmic rays and with γ rays emitted by the uranium. The uranium was chosen because of its small interaction length ($\sim$ 10.5 cm), which allows to have a very compact calorimeter. The signal of the chambers

is proportional to the number of the charged tracks of an hadronic shower, which is, in turn, proportional to the energy of the incoming particle.
The barrel is made of 9 rings (along z) each of them having 16 modules in ϕ. The external radius is 179.5 cm and the internal one is 88.5 cm for the "long" modules and 97.9 for the "short" modules (Fig. 5.12). The long modules are made of 60

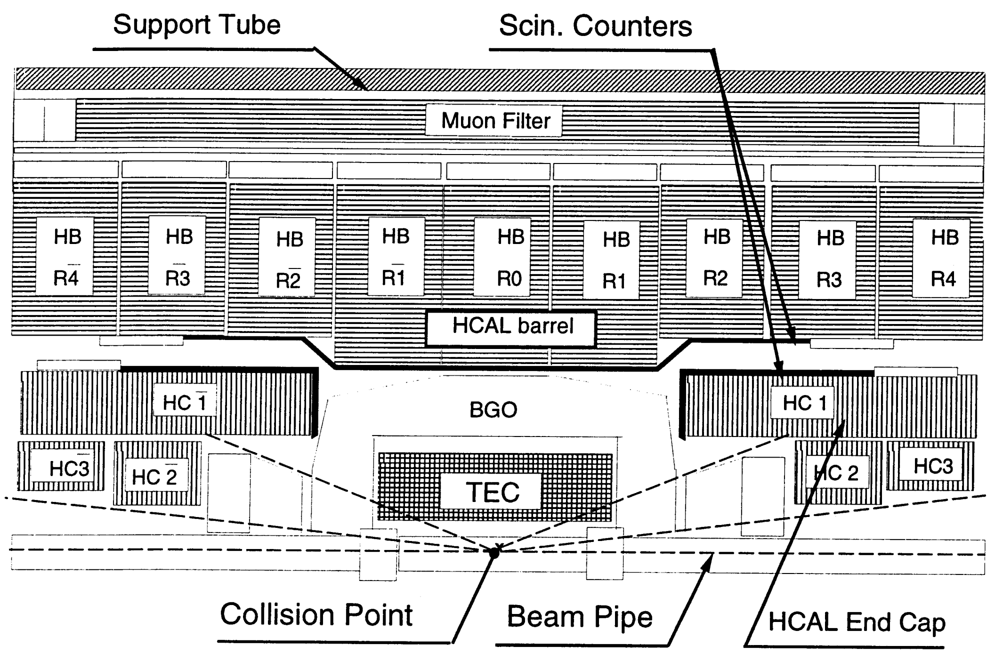

Figure 5.12: **Longitudinal section of the L3 detector. TEC, BGO and the segmentation of the hadronic calorimeter are shown.**

layers of PC and the short ones of 53.
The PC are, alternatively, chambers to measure the z coordinate (z chambers) in which the wires are perpendicular to the direction of the beam, and ϕ chambers in which the wires are parallel to the beam direction. For the read-out the wires of each module of the barrel are put together in "towers" with a number of sensitive wires varying from 3 to 28. Each tower covers a solid angle of about $2^\circ \times 2^\circ$. The resulting segmentation of a long module (short) is of 10 (8) radial layers, made each of 9 towers in θ and 9 towers in ϕ, for a total of 180 (144) towers per module.
The endcaps are made of three cylindrical boxes each of them divided in two semi-cylinders (Fig 5.12). The wires of the chambers are perpendicular to the beam direction, measuring directly the θ coordinate. They are also grouped in towers with

a total segmentation of 1° in θ, 22.5° in ϕ and 7 layers of chambers along z coordinate.
The resolution of the hadronic calorimeter, studied with beam of pions of momentum between 1 and 50 GeV/c can be written as:

$$\frac{\sigma}{E} = \frac{55\%}{\sqrt{E}(GeV)} \oplus 5\%. \tag{5.9}$$

The energy resolution of a $Z \to hadrons$ event, using only the electromagnetic and hadronic calorimeter information, is about 10%.
The hadronic calorimeter is completed by a muon filter, in the space between the barrel calorimeter and the support tube. It is divided in octants, each of them is made of 6 layers of brass (absorber) of 1 cm, alternated with 5 proportional chambers of 1.5 cm. The filter add one absorption length to the 4 of the hadronic calorimeter and to the one of the electromagnetic calorimeter for a total of 6 absorption lengths. The filter is used to identify hadrons which do not interact in the electromagnetic calorimeter and which can simulate a muon (punch-trough).

5.7 Muon spectrometer.

The central μ spectrometer covers about 73 % of the 4π solid angle, it is divided in octants. In each octant, of which the section R-ϕ is shown in Figure 5.13, three layers of drift chambers are present: the inner layer (MI), the intermediate layer (MM) and the outer one (MO). The intermediate layer is made of two chambers which sample the track of the muon 24 times in the R-Φ plane. The inner and outer layers sample the track only 16 times. The layers MI and MO are surrounded by z chambers, with wires perpendicular to the beam direction, that measure the track 8 times in the R-z plane.
The spectrometer is built to measure the momentum of a 50 GeV muon with a resolution Δ p/p of 2% which corresponds to a resolution of 1.4 % on the reconstruction of the invariant mass of muon pairs.
The chambers have a single wire resolution of 200 μm. The alignment of the chambers is controlled with a precision optomechanical system.
Since February 1995, the L3 experiment is fully equipped with forward-backward muon chambers in order to improve the momentum resolution between $36° \leq \theta \leq 44°$, and to allow the muon momentum resolution measurement down to 24° in θ. They are made of 96 drift chambers, divided into 16 sectors with three layers each on both sides of the detector [72].

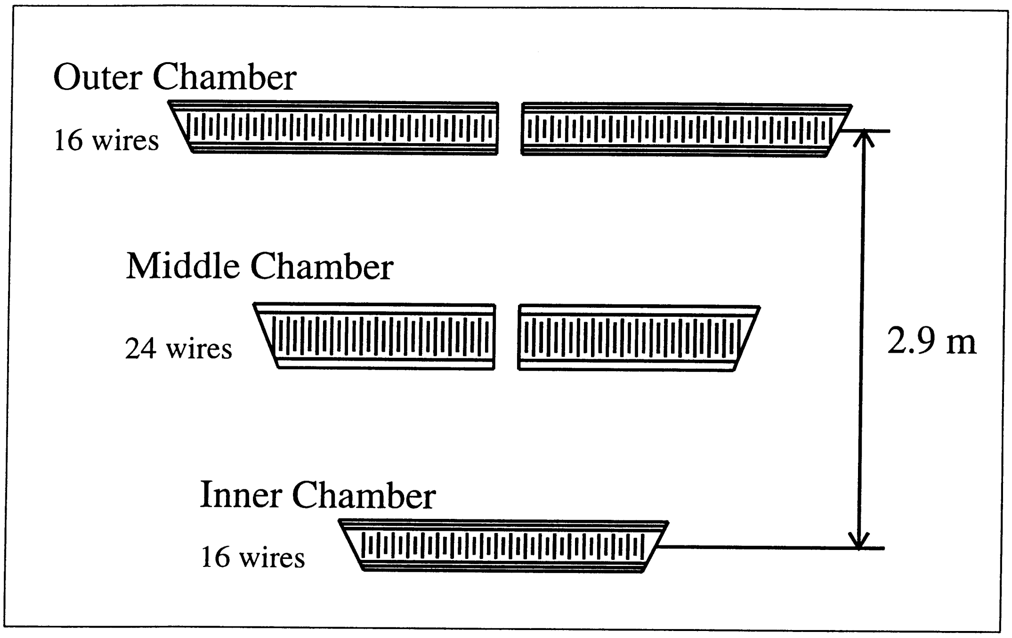

Figure 5.13: **Section in the R-Φ plane of one octant of the spectrometer.**

5.8 L3 Trigger.

LEP has a bunch crossing each 11 μs, which means a frequency of about 45 KHz. As it is not possible to digitise and to read the whole detector between two bunch crossings, a trigger system is necessary to separate the physics events from the background events, allowing the acquisition of the data with a low dead time.
The L3 trigger is separated in three different levels, level-1, level-2 and level-3.

5.8.1 Level-1 Trigger.

There are five sub-triggers:

- energy trigger;

- muon trigger;

- TEC trigger;

- scintillator trigger;

- luminosity trigger.

Energy Trigger.

The energy trigger [73] combines signals from the electromagnetic and the hadronic calorimeters. It has a rate of $\sim$ 5-6 Hz.
The 7680 crystals of the BGO barrel are put together in groups of 30 (5 in Φ and 6 in θ) to have 256 analog signals. The endcaps divided into 4 polar and 32 azimuthal segments, produce another 128 trigger signals each. To simplify the operations of the processor, the azimuthal segmentation is almost constant, therefore the grouping in θ and Φ of the crystals in the endcaps is not uniform (Fig.5.14). For the hadronic

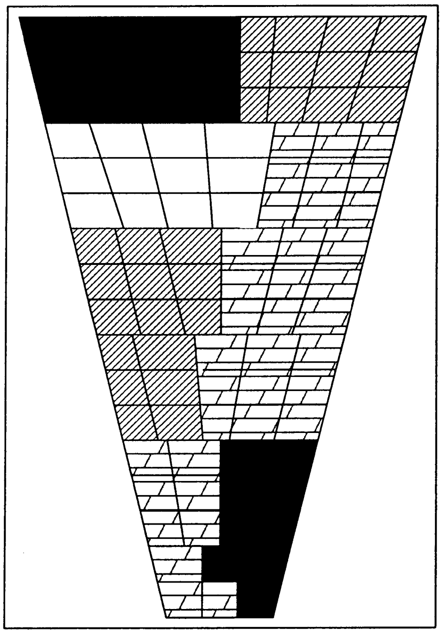

Figure 5.14: **Trigger segmentation of the crystals in one of the endcap.**

calorimeter the trigger gets two signals per module, one for the first interaction length of the detector (part A) one for the rest (part B). In total the calorimeter is segmented in 16 parts in Φ and of 11 (13) in θ for the part A (B). The total segmentation of the calorimeter is shown in Figure 5.15. Good events have to fulfil one of the following conditions:

- **A cluster trigger** (localised deposit of energy observed in different detector layers (BGO and HCAL at the same θ and Φ coordinates) searches for energy

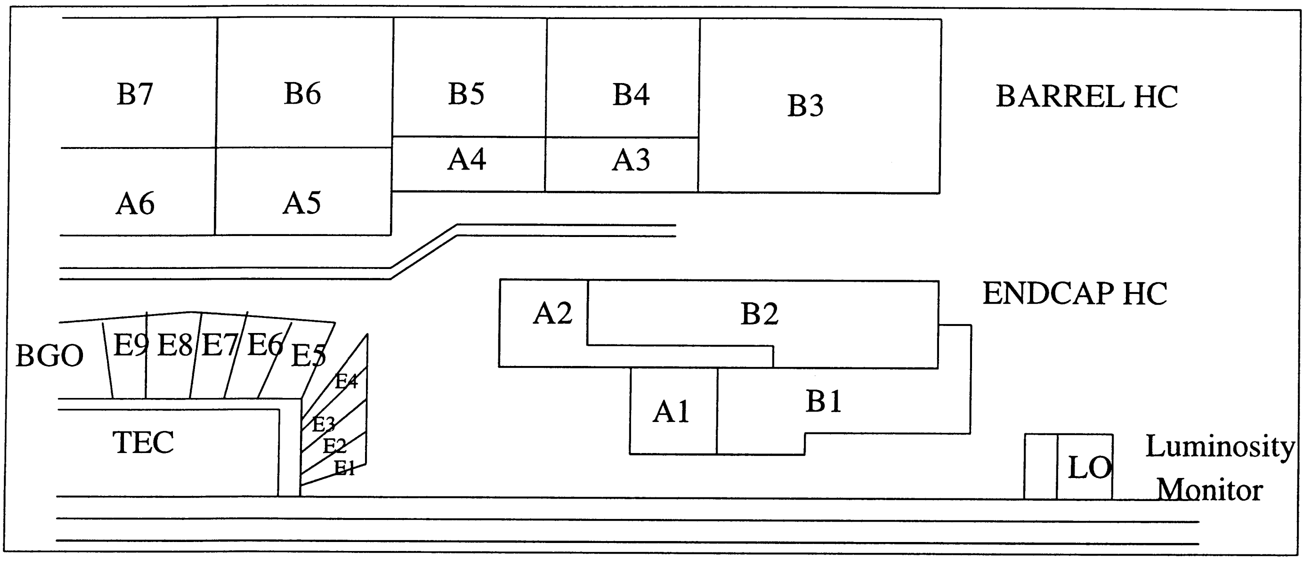

Figure 5.15: **Total segmentation of the energy trigger in the R-Φ plane.**

deposition which forms clusters in different detector layers. The threshold is 7 GeV if there is no TEC track and 3 GeV with a TEC track.

- **The total energy trigger** requires at least 10 GeV in the barrel BGO or 15 GeV in the BGO and HCAL barrel, or 20 GeV in all the calorimeters including the endcaps.

- **A single photon trigger** with a single isolated energy cluster in the BGO barrel of $E > 2$ GeV.

- **A hit counting trigger** asks for a minimum number of hits in the calorimeters: two trigger cells with more than 5 GeV.

- **Bhabha trigger** requires two back-to-back energy deposition ($E > 15$ GeV) in two opposite luminosity detectors.

TEC Trigger.

The TEC trigger [74] reads 14 anode wires for each of the 24 sectors of the outer TEC chamber. Each sector is divided in 4 intervals in Φ. The R-Φ plane is therefore divided in 96 intervals in Φ. An event is registered in a matrix of 96×14 bits. Software programmable masks recognise the tracks and count them. The trigger requires at least one back-to-back configuration inside 60°. As the background rate peaks at low transverse momentum, (P_T), the minimum P_T threshold is $\sim$ 150 MeV. It has a rate of $\sim$ 10 Hz which decreases with the luminosity.

Scintillator Multiplicity Trigger.

The scintillator multiplicity trigger [75] requires that at least 5 pairs of scintillators have an hit within ±15 ns of the bunch crossing.

Muon Trigger.

The muon trigger [76] accepts events with a transverse momentum larger than 1 GeV. It has a rate of $\sim$ 2-3 Hz which does not change with the luminosity because it is dominated by cosmic events. It consists in three sub-triggers.

1. **Single muon trigger**: two out of three P chambers are hit and three out of four Z chambers in the same octant in the angular region $44° \leq \theta \leq 136°$.
2. **Dimuon trigger**: two out of three P chambers are hit and one of the Z chambers in the same octant, together with two out of three P chambers hit in one of the five opposite chambers.
3. **Small angle muon trigger**: one P chamber hit and one Z chamber hit in the same octant, together with the same condition in one of the three opposite octants.

If the decision of the trigger is positive the information of each sub-detector is converted into digital signals and stored. This operation requires about 500μs and introduces a dead time of about 0.5 %. The rates of the different sub-triggers which composes the level-1 trigger, have to be lower than 20 Hz, otherwise the dead time is generated.

In the forward region there are three dimuons and three single muon triggers made using the following detectors: RPC (Resistive Plate Counters), endcap scintillators (ESCI) and forward-backward muon chambers (FB) [77].

5.8.2 Level-2 Trigger.

For an event triggered at level-1, the digitisation and the data transfer can start. The level-2 trigger [78] has two functions: it combines all the level-1 trigger information and rejects background events selected by only one level-1 trigger. The rejection factor of the level-2 trigger is $\sim$ 30 %. The following algorithms are employed:

1. The energy algorithm is based on a more precise energy estimation and reject events with energy smaller than a level-2 threshold.

2. The TEC algorithm rejects electronic noise, beam gas events and events with tracks not pointing to the interaction point.

3. The muon algorithm rejects muon events with a small number of hits in vertex chambers and with no scintillator in time.

If the event does not pass these requirements, the data transfer is stopped and the event is rejected. 1 rejected event out of 20 is kept in the data acquisition chain, to control the level-2 efficiency off-line.

5.8.3 Level-3 Trigger.

The level-3 trigger [79] starts when the event is fully digitised. Before writing the event on tape the level-3 checks whether it is a good physics event or not. It rejects background by using several algorithms with a rejection factor of $\sim$ 80-90 %.

The energy algorithm : it reconstructs energy in the electromagnetic and hadronic calorimeters using all the BGO crystals and HCAL information. As the calculations are based on a fine digitisation, the thresholds are more precise with respect to the level-2.

The muon algorithm : it requires a muon track to have a scintillator hit within a time of ± 10 ns with respect to the beam crossing.

The TEC algorithm : it reconstructs the TEC tracks and checks if they originate from the vertex. It checks also whether the tracks in the transverse plane are correlated with some energy deposit in the calorimeters or with hits in the scintillation counters.

5.9 The software of L3.

5.9.1 Reconstruction of L3 data: REL3.

The event reconstruction [80] builds, from the ADC and TDC signals and an accurate knowledge of the geometry, physics quantities like tracks, and energy deposits. The first time the events are reconstructed, in PASS1, the measured calibration constants are applied. Information from different sub-detectors are combined together to form a final reconstructed particle or a group of particles (jets).
The events have to fulfil some selection criteria (PASS1 selection) which ensure the interest of the event and in order classify them in different physics categories (STREAMS) defined by the analysis groups. The cuts applied in this first step are very loose to be sure that no interesting physics events are lost. The data after PASS1 are used only to produce more precise calibrations and to check the consistency of the data. Final physics analyses are done after a PASS2 reconstruction, where final calibrations are applied.

5.9.2 Database.

The L3 database has seven sections, one per each sub-detector. The informations come from different sources:

- General setups like the geometry of the detector, which are updated every year, especially when new sub-detectors are added.

- Data coming from the online monitoring system. For example BGO temperatures and pedestals, or TEC high voltage, etc.

- Off-line information. For example calibration constants: TEC calibrations of drift velocity and Lorentz angle, BGO energy calibrations and dead crystals.

5.9.3 Simulation of the Detector: SIL3.

The response of the detector is accurately simulated by SIL3. SIL3 is based on GEANT [81] which tracks the particles generated by a Monte Carlo event generator from the interaction vertex through all the detector materials in small steps. The structure of SIL3 can be described by three phases: the initialisation, the tracking and the digitisation.
The **initialisation** consists mainly in the description of the geometry and of the materials of the L3 detector, and in the definition of the ZEBRA banks which will register the event information.
The **tracking** of a particle is done integrating the equations of motion step by step. The particle is propagated according to the properties of the material encountered determining with random numbers if and which interaction process is present at each step.
When the energy of a particle becomes smaller than a predefined value the tracking is stopped. The value of this cut is chosen in function of the requested accuracy, and of the available CPU time.
In the **digitisation** phase, the response of each part of the detector is calculated, introducing all details, for example the saturation of the electronics, the fluctuations of the pedestals, the radioactivity of the uranium, are introduced.
To achieve such a detailed description, a good knowledge of the behaviour of the detector is necessary, obtained by a continuous comparison with real data.

5.10 Monte Carlo generators.

The L3 library, to generate Monte Carlo events, contains about 70 generators, which describe almost all possible e^+e^- reactions.
For the process $e^+e^- \to W^+W^-$, two different generators have been used: KORALW [31] and EXCALIBUR [32]. In addition the following not negligible backgrounds have been generated: $e^+e^- \to q\bar{q}(\gamma)$ (PYTHIA [82]), $e^+e^- \to ZZ$ (PYTHIA), $e^+e^- \to Zee$ (EXCALIBUR). GENTLE [39] has been used to calculate the differential cross section necessary for the fit of the W mass.
The general characteristics of these generators is now discussed.

5.10.1 KORALW [31].

KORALW generates all the W decay channels into pairs of leptons or quarks. This generator contains not only QED effects in the initial state, but also in leptonic decays of the W and in secondary decays, as in the case of the τ lepton. The hadronization of quarks is present. The matrix element for W pair production and decay into four fermions (CC03) with an appropriate W-spin treatment and with finite width are described. The τ polarisation is also taken into account.
The experimental cuts can be introduced rejecting some of the generated events.
The limitation of the program comes from the simplified matrix element for the QED photon emission, lack of the non QED electroweak corrections and a simplified colour arrangement for four quark jets.

5.10.2 EXCALIBUR [32].

EXCALIBUR calculates the cross section for the process $e^+e^- \to 4f$. All possible four fermion final states are included. A limit comes from the fact that the fermions are assumed massless so that Higgs exchange is not included. Then, because of the zero mass of the fermions, singularities can occur in the photon exchange channel. These can be avoided using well adapted cuts. For example, when there are one electron in the final state a cut on its scattering angle is necessary. For a calculation based on a restricted set of Feynman diagrams, without photon exchange (CC03), such cuts are not necessary.
It is a Monte Carlo program which generates events over a phase-space defined by some cuts (in many cases the whole phase-space is accessible). Each generated event has a weight, such that the mean weight for each event, gives the total cross section. A sample of unweighted events can be selected from the generated sample; the efficiency of this procedure is, in many cases, of the order of few percent depending on the final state on on the phase space cuts.
The ISR is implemented and the four fermions are generated in the reduced centre of mass energy. The FSR is not implemented in the program.

5.10.3 PYTHIA [82].

PYTHIA is an event generator for a multitude of processes in $\gamma\gamma$, e^+e^-, *ep* and *pp* physics. Major importance is given to the modelling of the hadronic final states, for example QCD parton showers, string fragmentation and secondary decays. The electroweak description is restricted to the improved Born-level, and therefore is not

competitive for high precision studies.
The ISR and FSR are implemented.

5.10.4 GENTLE [39].

The GENTLE package is designed to compute total four fermion production cross sections and final state fermion pair invariant mass distributions, for charged currents (CC) and neutral currents (NC). For the CC03 process the W production angular distribution is accessible. In the NC case, the production of the Standard Model Higgs is included.
The phase space integration is carried out by semi analytical technique. Without (with) ISR the phase space is parametrised by five (seven) angular variables and the final state fermion pair invariant masses. All angular variables are integrated analytically. The result of this calculation is the input for the package to integrate numerically the invariant masses. The method is numerically stable and in general very fast.
The FSR is not implemented and no hadronization interface is present.

Chapter 6

Calibration of the BGO calorimeter

6.1 Introduction

The excellent intrinsic resolution of the calorimeter can be spoiled if the response of the individual crystals is not continuously equalised. Sources of degradation can be the aging of the crystals, radiation damage, etc.. For example, Figure 6.1 shows the change of the response of the calorimeter as function of time in the barrel and the Figure 6.2 shows the same distribution in the inner and in the outer region of the endcaps. In the barrel, one can see the change in the gain of the calorimeter, due to a not yet understood source. Again in 1997 the gain of the detector was still decreasing with respect to the previous year.

In the endcap, in the inner part, one can clearly see the effect of a beam accident, which occurred in 1992, and the subsequent gain recovery. We notice also that during the data taking at $\sqrt{s} \simeq M_Z$ ($\leq$ 1995) several calibrations per year were performed. This is impossible at $\sqrt{s} > M_Z$ because of limited statistics for the Bhabha scattering process $e^+e^- \to e^+e^-$ used for absolute calibration. The evolution in time of the BGO response $R(t)$ can be parametrised as [83]:

$$R(t) = \frac{a}{t + t_0} + C_\infty \tag{6.1}$$

where t is the time starting from the beginning of LEP ,a, t_0 and C_∞ are constant values determined fitting the data points in the Figures 6.1 and 6.2 and listed in table6.1.

To control and correct for the evolution of the signals of the BGO crystals, a Xenon monitor was built by the L3 group of Geneva University and has been used throughout the LEP running. A detailed description of the Xenon monitor can be found in

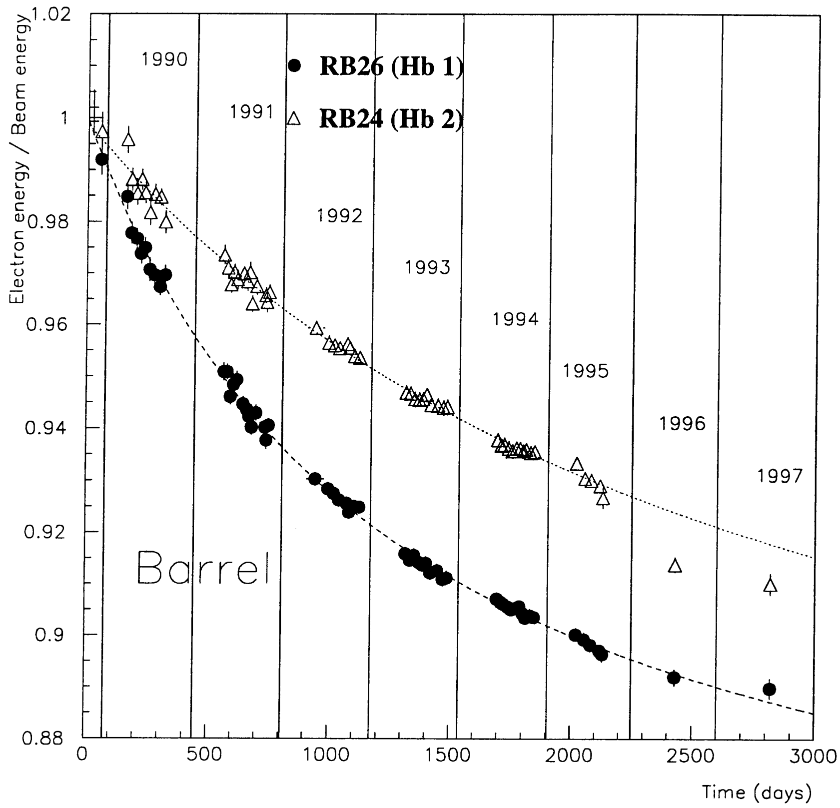

Figure 6.1: **Distribution of the electron energy normalised to the beam energy as function of the time for the barrel. The points are the mean value of the energy distribution in $e^+e^- \to e^+e^-$ events before the calibration.**

[83, 84]. Another system, the RFQ (Radio Frequency Quadrupole accelerator), was built in 1995 [88] and used since 1996.

The Xenon system, or alternatively the RFQ, allow to perform an inter-calibration of the crystals while the absolute energy calibration is done using "Bhabha events" ($e^+e^- \to e^+e^-$). In this channel the energy of the outgoing electrons is equal to the beam energy, if we exclude from the data sample the radiative events; therefore our calibration is in fact a "Xenon+Bhabha" or "RFQ+Bhabha" calibration.

The "Bhabha" cross section in the barrel region is dominated by Z formation in the s channel, this means that it drops by more than a factor ten when the energy increases above the Z resonance, as is shown in Figure 6.3. In the endcap region the cross section is dominated by the γ exchange in the t channel and then decreases with the energy as $1/s$. Monte Carlo simulations using the BHAGENE [86] generator

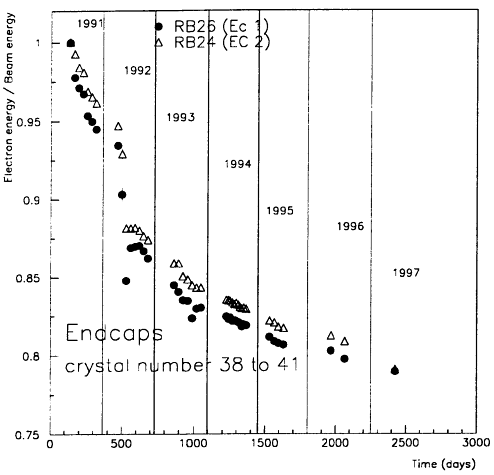

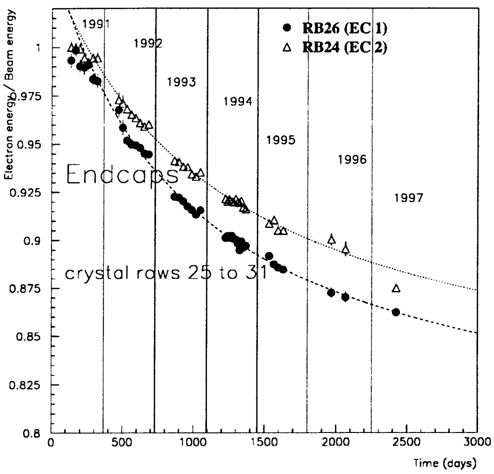

Figure 6.2: **Distribution of the electron energy normalised to the beam energy as function of the time and for the outer and for the inner region of the endcaps. The points are the mean value of the energy distribution in $e^+e^- \to e^+e^-$ before the calibration.**

Parameters	HB1 (RB26)	HB2 (RB24)	EC1 (RB26)	EC2 (RB24)
a (days)	209.6 ± 6.6	476.6 ± 12.0	256.7 ± 9.8	295.2 ± 11.0
t_0 (days)	1281.7 ± 33.7	2900.7 ± 52.4	991.7 ± 39.6	1264.3 ± 44.4
C_∞	0.836 ± 0.002	0.835 ± 0.002	0.787 ± 0.003	0.804 ± 0.003

Table 6.1: **Results of the fit of the response of the two half-barrel, and of the outer region of the endcaps.**

give a cross section, at $\sqrt{s}$ = 183 GeV, of 26.8 pb in the barrel and of 692 pb in the endcaps. The total luminosity of the high energy runs in 1996 and 1997 was not sufficient to perform an absolute calibration in the barrel region. At the beginning of these two years of data taking a dedicated LEP run at $\sqrt{s} = M_Z$ and L3 collected about 2.5 pb^{-1} each year to perform the TEC calibration. These data were used also to perform the calibration of the BGO electromagnetic calorimeter. This amount of luminosity is the minimum necessary to permit a good calibration of the detectors. A method to calibrate the BGO electromagnetic calorimeter by extrapolating the data of the previous years has been envisaged, if in future we will not have enough Bhabha events to perform the Xenon+Bhabha or the RFQ+Bhabha calibrations. The method consists in the evaluation of the xenon inter-calibration and then in the extrapolation of the absolute calibration using the evolution of the BGO with the

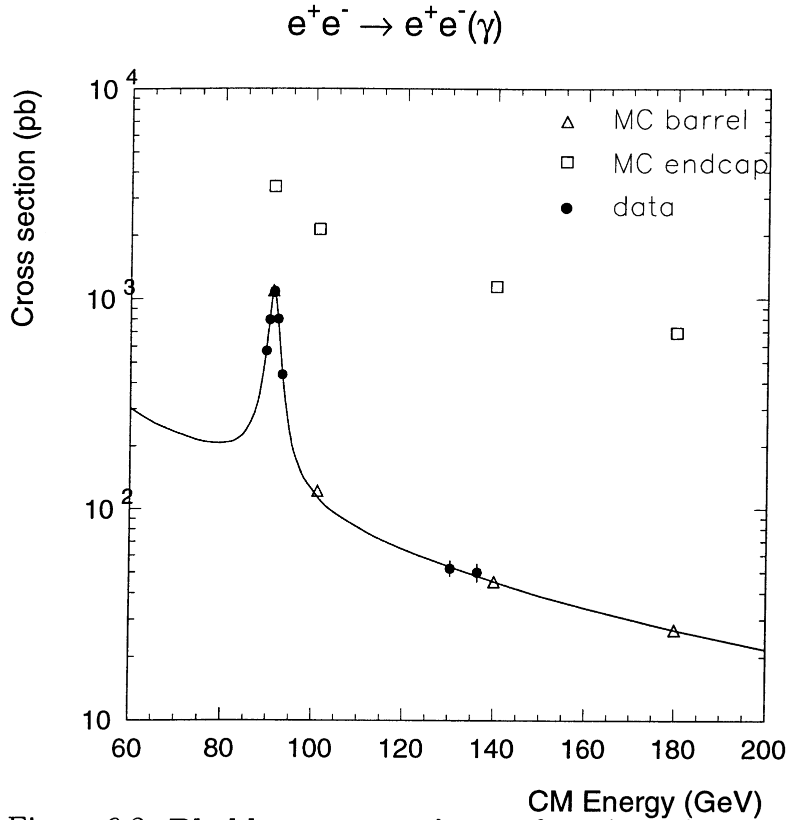

Figure 6.3: **Bhabha cross section as function of the centre-of-mass energy.**

time (see Figure 6.1). This procedure was studied in 1994 and is described in detail in the reference [87]. The results obtained with this method are comparable with the standard xenon calibration (table 6.2). This method has been proposed but it is not used. It has to be noticed that this method uses the assumption that the BGO calorimeter very stable during the time, in case of accident as is shown in Figure 6.1 for RB24 in 1997 the extrapolation become unusable.

	standard calibration	extrapolation
RB24	$1.47 \pm 0.01\%$	$1.55 \pm 0.01\%$
RB26	$1.33 \pm 0.01\%$	$1.41 \pm 0.01\%$

Table 6.2: **Resolution for Bhabha events in the barrel for the year 1994: comparison between the standard calibration and the extrapolation method studied to be applied at LEP2.**

6.2 The Xenon monitor [84]

There are 16 Xenon lamps for the barrel and 16 for the endcap, which simulate the scintillation light produced in the crystals. Their light is injected in the back of each crystal, using a beam of optical fibres. In Figure 6.4 the Xenon system is shown. Each beam of fibres illuminate a Plexiglas light mixer. A filter in between them,

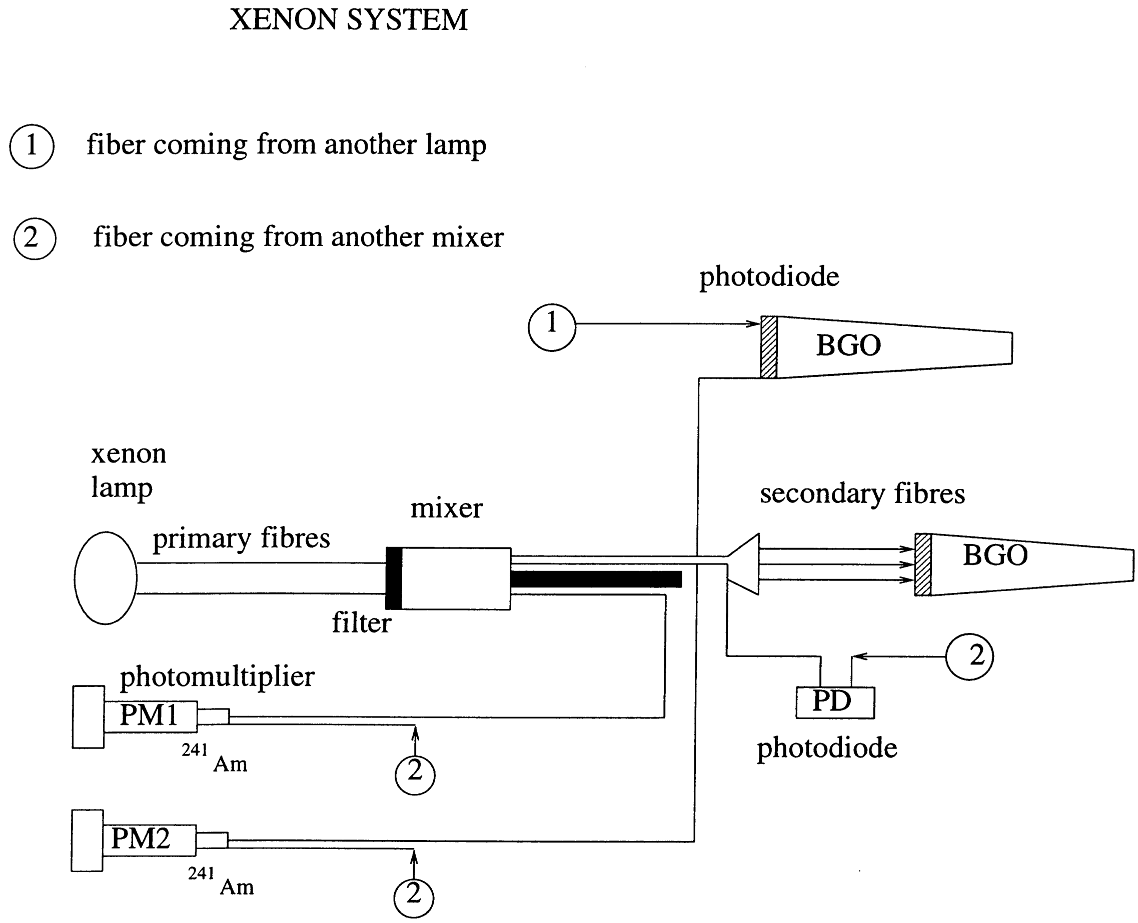

Figure 6.4: **Xenon system in the barrel.**

selects the spectrum of emission of the lamp corresponding to the BGO spectrum. The mixer transfers the light to a secondary beam of fibres which drives the light to the crystals, as well as to photomultipliers (PM) and photodiodes, (PD), used for the normalisation of the signal. The mixer makes the light uniform and stable at the level of the secondary fibres. With the PM and PD signals we correct event by event for the variation of the intensity of the light in the lamps. The gain of the PM and PD is controlled by americium sources.
In the barrel each crystal is connected to two secondary fibres for high and low intensity light corresponding to 30 GeV and 1.5 GeV respectively. In the endcap only one fibre is connected to the crystal, and an attenuation system can be used to set the intensity of the light. The most important characteristics of the Xenon

system are listed in table 6.3.

System	Barrel	Endcap
# of lamps	16	16
# of primary beams per lamp	4	1
# of fibres per secondary beam	240	192
# of fibres per crystal	2	1

Table 6.3: **Characteristics of the Xenon system.**

6.3 Xenon calibrations

The Xenon calibration runs are performed about every two days during data taking with an independent PC. The Xenon signals arrive with a frequency of about 20 Hz. The signal is registered by the BGO electronics. During the Xenon run calibration, ten events per lamp are taken for a total time of $\sim$ 5 minutes. Once the data taking in the BGO is completed, a run is initiated to read the reference PM. The analysis of the calibration data is done on line on the BGO VAX.
Off-line, first we equalise the signals of the crystals attached to the same mixer (inter-calibration). The inter-calibration is defined as the mean value over one run of the quantity x_i :

$$x_i = \frac{I_i/\xi_i}{\frac{1}{N}\sum_{j=1}^{N} I_j/\xi_j} \tag{6.2}$$

where N is the number of crystals per mixer, I_i is the xenon signal for the crystal i, ξ_i is the mean value of the I_i over the calibration period. As the inter-calibration is calculated over one mixer it is independent on the fluctuations of light of the lamp. The quantity x_i is calculated separately for the high intensity and low intensity systems. Adding the two informations the error is reduced by a factor $\sqrt{2}$. The fluctuations of x_i during one run are of the order of 0.12 % and the fluctuations of the mean value of the x_i are of the order 0.2 %, as measured during the initial test beam. In fact, the barrel calorimeter was calibrated on a test beam at CERN. Tests have been done on three matrices of 9, 25 and 100 crystals. The energy resolution obtained during these calibrations is shown in Figure 5.9 [85]. The results of these calibrations are used as a reference, providing a multiplicative correction factor for

the calibration performed each year. During the calibration with the electrons also Xenon runs were taken.
After the inter-calibration has been performed the absolute calibration with "Bhabha events", $e^+e^- \to e^+e^-$, is done.
The calibration method is somewhat different for the barrel and for the endcaps.

6.3.1 Barrel

An electronic card covers 24 crystals in θ and 5 in Φ, for a total of 60 crystals. The calibration regions are not defined following this geometry, to avoid that a problem in the electronic propagates over all the crystals belonging to this region. The inter-calibration is calculated for 64 regions defined by the topology of the mixers. The crystals attached to one mixer are not consecutive crystals there are some jumps: in particular we have a swap of 6 rings of crystals in ϕ and then we obtain one region with 144 crystals (24 in θ and 6 in ϕ) and one with 96 crystals (24 in θ and 4 in ϕ) alternatively (see Figure 6.5). We then equalise the 64 regions to the energy of the Bhabha events.
The absolute energy calibration per region has been chosen because it is impossible to have enough events to do a calibration crystal by crystal. The Bhabha cross section in the barrel region is $\simeq$ 1 nb at $\sqrt{s}$ = 45 GeV. The situation is even worse when we are working at LEP2 (see Figure 6.3). In the barrel we need to accumulate at least 2.5 pb^{-1} (at $\sqrt{s}$ = 45 GeV) per calibration period. In 1995, for example, with a total integrated luminosity of $\sim$ 30 pb^{-1} we did 5 calibrations.
The correction of the gain for the crystal i can be written as:

$$cor_i = \frac{1}{1/2 \cdot (x_i^{low} + x_i^{high})} \tag{6.3}$$

where the index "low" and "high" are referring to the inter-calibration with the low and the high intensity. When the difference between the low and the high intensity channel for one crystal is bigger than 5% the correction for this crystal is set to the mean value of the correction of the neighbouring crystals in θ and in ϕ. In general there are less than 1 % of the crystals which are noisy.
The calibration for the crystal i is written as:

$$cal_i = cor_i \times cal_{reg} \tag{6.4}$$

where cal_{reg} is the absolute correction in a given region, calculated with the Bhabha events. In the barrel the selection for Bhabha events requires:

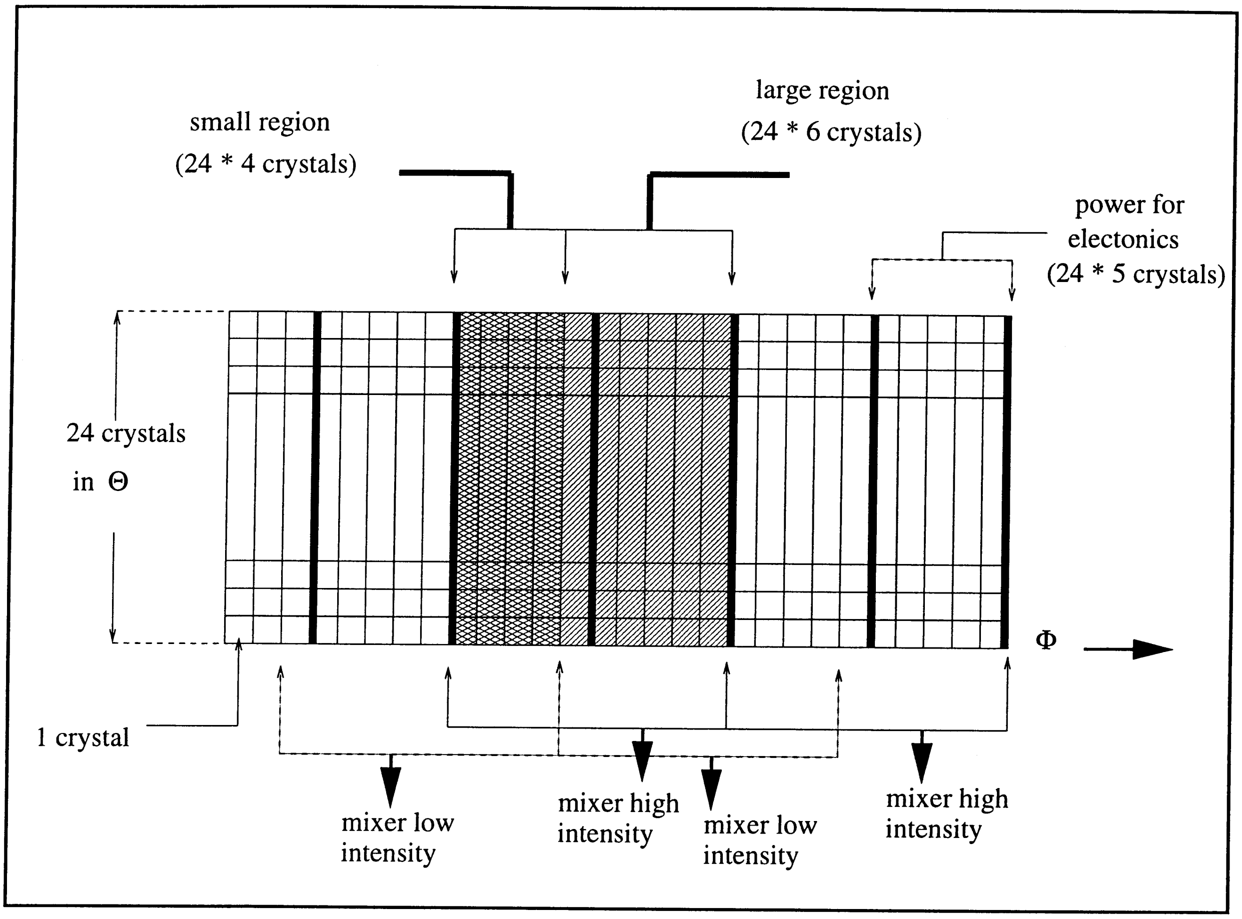

Figure 6.5: **Definition of the regions for the Xenon calibration. The limits for the electronics are indicated by the vertical black lines (5 crystals in Φ).**

1. at least 2 BGO bumps and less than 8;

2. the energy of the two most energetic bumps has to be greater than $0.5 \times E_{beam}$;

3. the number of the crystals in the bump has to be greater than 9;

4. the acollinearity between the two bumps has to be less than 4° to reject radiative events.

In Figure 6.6 and 6.7 the distributions of the energy in Bhabha events before and after the calibration for the years 1994 and 1997 is shown. The results for the barrel calibration from 1994 until 1997 are listed in table 6.4

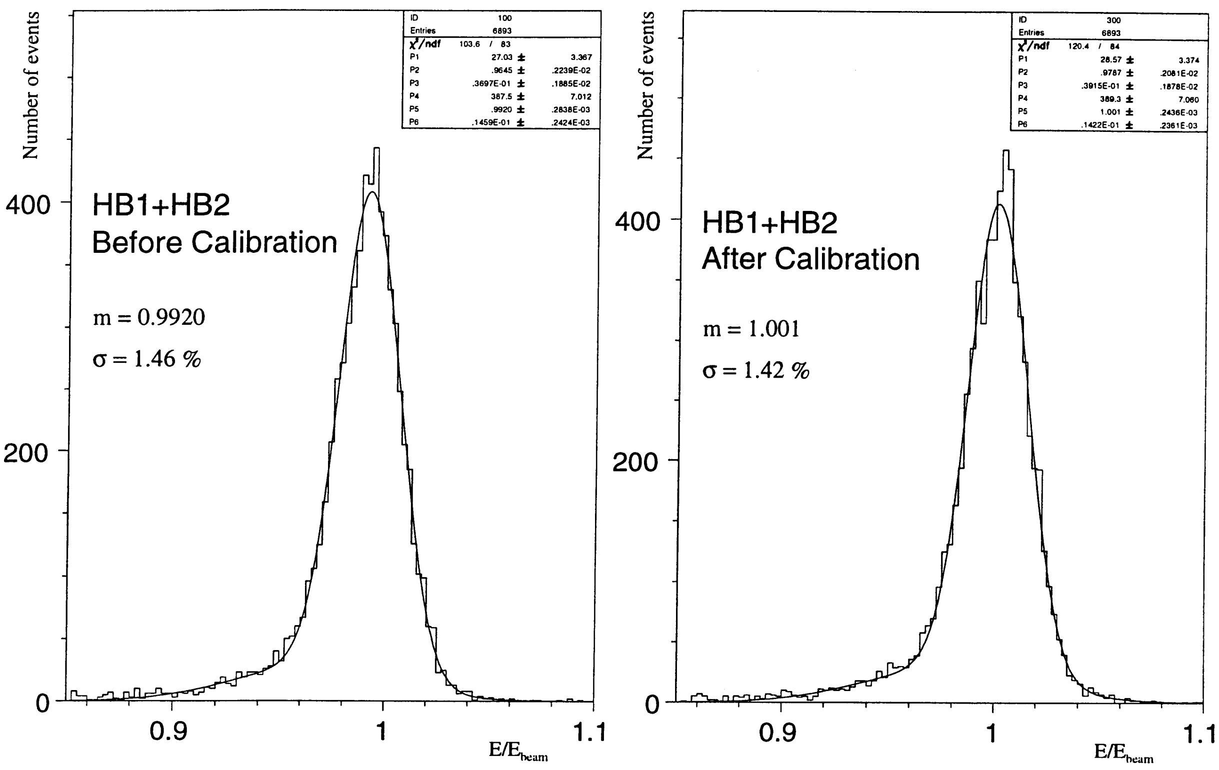

Figure 6.6: **Bhabha peak in the barrel region before and after Xenon calibration in the year 1994.**

As we can see from the Figures 6.6 and 6.7 in the barrel the most important difference

	1994	1995	1996	1997
RB26 (HB1)	$(1.35 \pm 0.02)\%$	$(1.38 \pm 0.02)\%$	$(1.39 \pm 0.02)\%$	$(1.56 \pm 0.02)\%$
RB24 (HB2)	$(1.51 \pm 0.02)\%$	$(1.54 \pm 0.02)\%$	$(1.56 \pm 0.02)\%$	$(1.65 \pm 0.02)\%$

Table 6.4: **Energy resolution for Bhabha events in the barrel after the calibration from 1994 until 1997.**

between before and after the calibration is in the mean value of the distribution and not on the resolution.

6.3.2 Endcaps

The endcaps of the BGO electromagnetic calorimeter have not been calibrated in a test beam, this results in the absence of reference calibrations. The statistics for Bhabha events in the endcaps is much bigger than in the barrel, because of

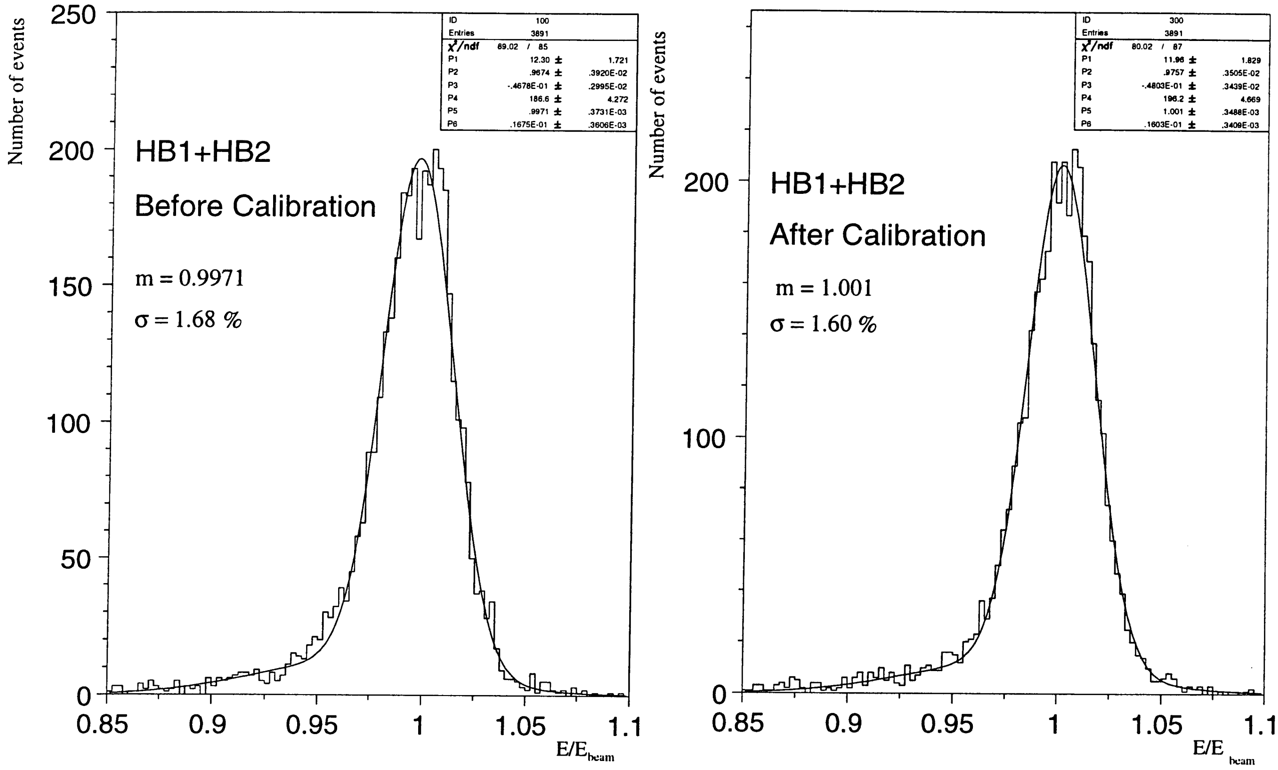

Figure 6.7: **Bhabha peak in the barrel region before and after the calibration in the year 1997.**

the predominance of the t channel in this angular region. This allows a Bhabha calibration crystal by crystal.
The endcaps are divided in three regions, the inner, the intermediate and the outer one (Figure 6.8). This separation avoids the propagation of problems related to beam accidents in a particular region to the whole detector. Each mixer is divided in 3 parts in θ and 2 in ϕ for a total of 6 parts. This gives a total of 48 regions per endcap. The subdivision in ϕ takes also into account the swap of the crystals in the mixers, in such a way that one region corresponds to one mixer.
The selection of Bhabha events in the endcaps requires:

1. the central crystal of the bump should not be a crystal at the edge of the detector, i.e. the outermost rings 41 and 25 are not calibrated;

2. the energy of the two most energetic bumps has to be greater than $0.5 \times E_{beam}$;

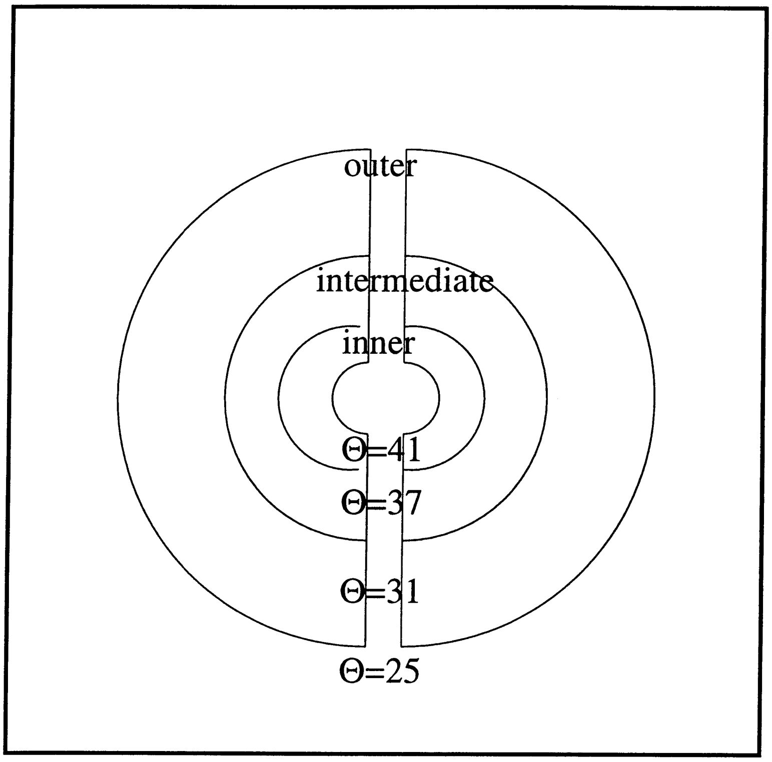

Figure 6.8: **Regions of θ in the endcap. Inner: 5 rings of crystals (41-37), intermediate 6 rings of crystals (36-31), outer 6 rings of crystals (30-25).**

3. the number of the crystals in the bump has to be greater than 9;

4. the sum of the energies of the third and the fourth most energetic bumps has to be smaller than 1 GeV;

5. the acollinearity between the two most energetic bumps has to be smaller than 2°.

Once the good Bhabha events are selected, the calibration procedure is an iterative procedure:

- we correct the energy of each crystal of the bump with the inter-calibration constants x_i (see Equation 6.2)

$$E_i' = (E_i/x_i)/E_{beam} \qquad i = 1,9 \tag{6.5}$$

i.e. the energies E_i are normalised to the beam energy;

- as in the barrel (Equation 6.4) a calibration constant cal_i is calculated and applied for the second iteration

$$E_i'' = E_i' \times cal_i; \tag{6.6}$$

- then we correct this energy for the leakage at the edges of a crystal due to the fact that if the electron does not hit the crystal in the centre we can loose some energy;

- we calculate the number of events per crystal and the energy deposited in each crystal N_{tot}^i, E_{tot}^i;

- we define the calibration constant for each crystal for the actual iteration as

$$cal_i' = cal_i \times \frac{N_{tot}^i}{E_{tot}^i} \qquad with\ N_{tot}^i \geq 2. \tag{6.7}$$

This procedure is repeated 5 times to allow the convergence of the algorithm and to obtain a resolution of the order of 1%.
When there is only one event to calibrate a crystal, the calibration constant is still calculated but with two more iterations using the mean value of the energy in the corresponding region:

- we calculate the mean value of the energy $\bar{E}^{reg}$ in all the regions which have at least one bump:

$$\bar{E}^{reg} = \Sigma_n E_n / n \tag{6.8}$$

where n are the bumps entering the considered region;

$$cal_i'' = cal_i' \times \bar{E}^{reg}. \tag{6.9}$$

To calculate the final calibration constants we need a set of inter-calibrations averaged over a given period of the time. For the outer and intermediate region this average is done over a longer period of Bhabha data taking because of the smaller statistics, for example over the five periods in 1995. The resolutions obtained in the endcaps after the calibration are listed in table 6.5. The bad resolution obtained in 1996 is

	1994	1995	1996	1997
RB26 (EC1)	$(1.23 \pm 0.01)\%$	$(1.22 \pm 0.01)\%$	$(1.46 \pm 0.02)\%$	$(1.17 \pm 0.02)\%$
RB24 (EC2)	$(1.21 \pm 0.01)\%$	$(1.19 \pm 0.01)\%$	$(1.43 \pm 0.02)\%$	$(1.30 \pm 0.02)\%$

Table 6.5: **Energy resolution for Bhabha events in the endcaps after Xenon calibrations from 1994 until 1997.**

due to the poor statistics with respect to the other years ($\sim$ 20 pb^{-1} to be compared with $\sim$ 30-50 pb^{-1}). It has to be noticed that in the endcap we use Bhabha events at 45 GeV but also the high energy data ($\sqrt{s}$ =161, 172, 183 GeV). In fact the Bhabha cross section is higher in the forward region for higher centre-of-mass energies so that we can have a bigger sample of events to do the calibration. This is not the case in the barrel region where the cross section decreases with the centre-of-mass energy, therefore the gain in using high energy data for the calibration is completely negligible.

Figures 6.9 and 6.10 show the distribution of the energy in the Bhabha events after calibration in 1995, 1996 and in 1997 for the endcaps. In 1996 a long tail in the high energy region is present, even after the calibration, in the energy distribution. This is due to 14 crystals with bad channels.

6.3.3 RFQ calibrations.

The RFQ calibration [87] uses a pulsed H^- beam, from a Radio Frequency Quadrupole accelerator. Afer focusing, the beam is neutralised to allow it to pass in the magnetic field of L3. Then the beam hits a target of lithium installed in the BGO calorimeter. The reaction which occurs is

$$p + Li_3^7 \to Be_4^8 + \gamma \tag{6.10}$$

The photons have an energy of 17.6 MeV. The calibration of the whole detector requires about one day. The photon spectrum in one crystal is shown in Figure 6.11.

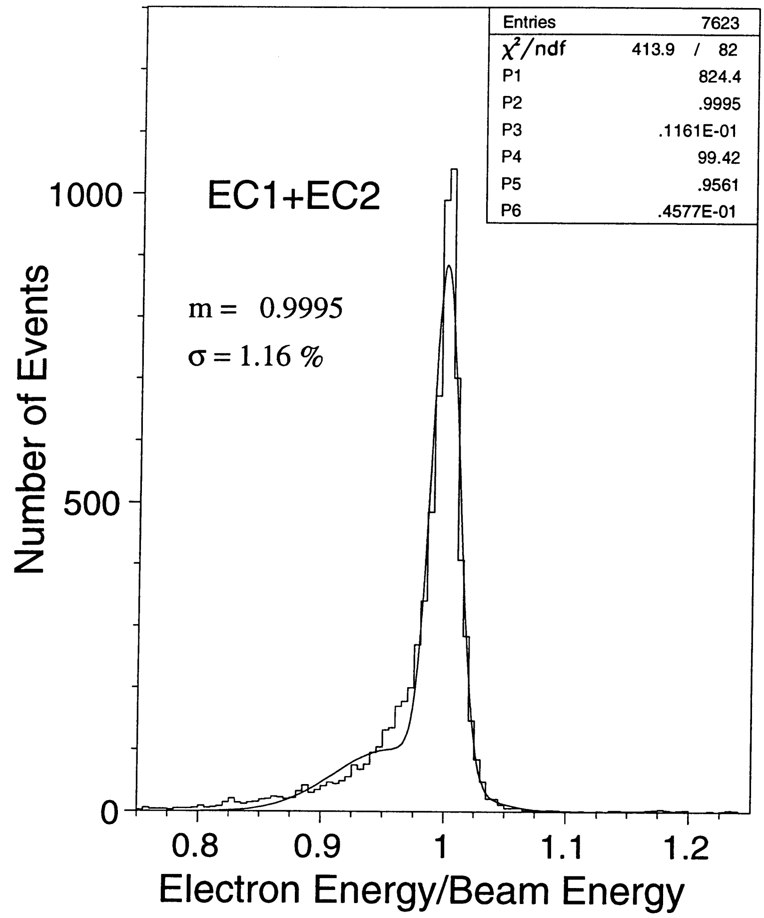

Figure 6.9: **Bhabha energy spectrum normalised to the beam energy for 1995 data, in the endcaps, after Xenon calibration.**

The calibration point is taken at the half maximum to the right of the signal peak. Two set of calibration constants can be calculated: one using only the RFQ and the other using also Bhabha events. The "RFQ only" calibrations, provide a set of constants, one per crystal, equating all the signals to 17.6 MeV. Once this calibration is done it is necessary to extrapolate from the 17.6 MeV measurement to the beam energy. The "RFQ+Bhabha" uses the calibration at 17.6 MeV only for an inter-calibration between adjacent crystals and the Bhabha events to provide the absolute calibration at 45 GeV, as in the Xenon calibration. The first RFQ run was taken in 1995. The results of this calibration for the "RFQ only" and for the "RFQ+ Bhabha" are shown in Figures 6.12 and 6.13. One can compare this first result with the one obtained in the last calibration in 1997, the results are listed in table 6.6. The better resolution achieved with the RFQ+Bhabha calibration, with respect to the Xenon+Bhabha one, for the year 1997, in the barrel region, is mainly due

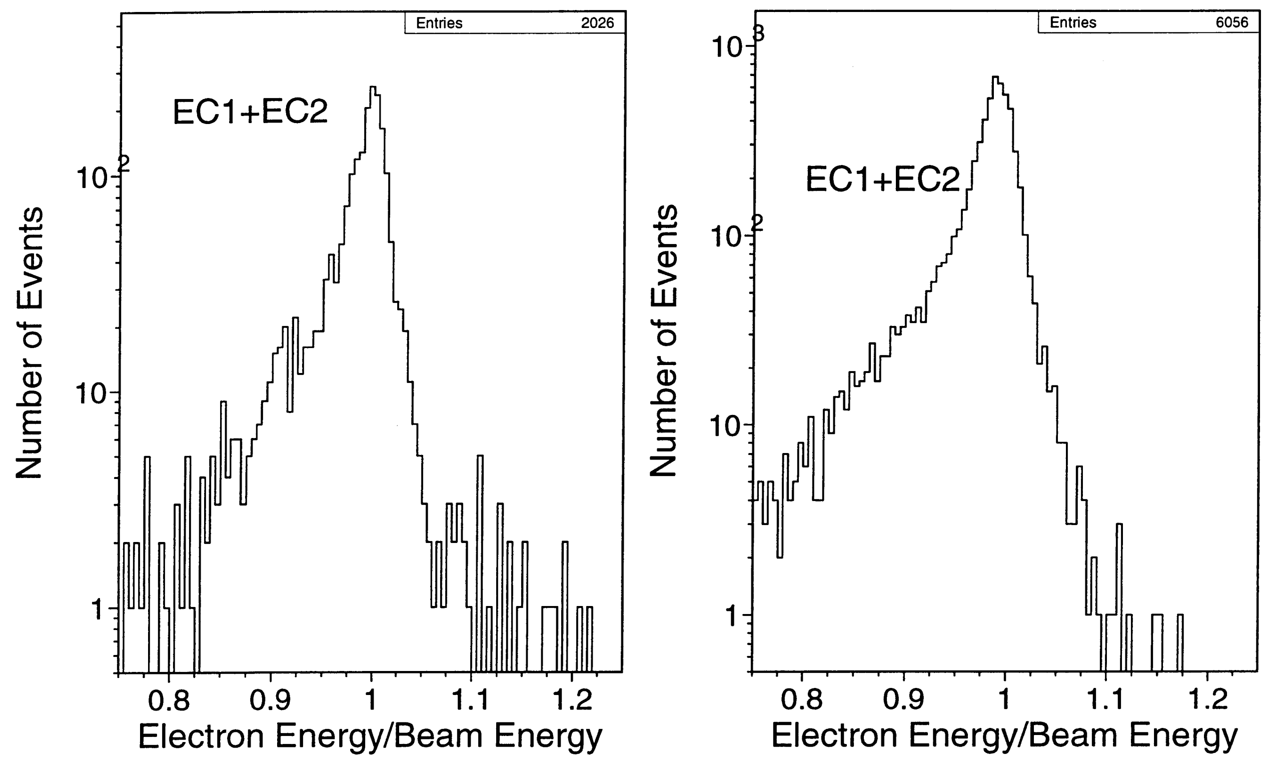

Figure 6.10: **Bhabha energy spectrum normalised to the beam energy for 1996 and 1997 data, in the endcaps, after Xenon calibration.**

to the fact that for the RFQ the starting point of the calibration is now the values obtained in 1995 with a large sample of Bhabha at the Z peak (30 pb^{-1}). In the Xenon+Bhabha calibration the sample of Bhabha events used is the one of the year itself, at $\sqrt{s} = M_Z$, because this allow to follow the behaviour of the detector during the time.

	Barrel(1995)	Endcaps(1995)	Barrel(1997)	Endcap(1997)
RB26 (HB1, EC1)	$(1.08 \pm 0.01)\%$	$(1.39 \pm 0.01)\%$	$(1.1 \pm 0.01)\%$	$(1.2 \pm 0.01)\%$
RB24 (HB2, EC2)	$(1.01 \pm 0.01)\%$	$(1.59 \pm 0.01)\%$	$(1.0 \pm 0.01)\%$	$(1.3 \pm 0.01)\%$

Table 6.6: **Resolution for Bhabha events in the barrel and in the endcap for the years 1995 and 1997 using RFQ calibrations.**

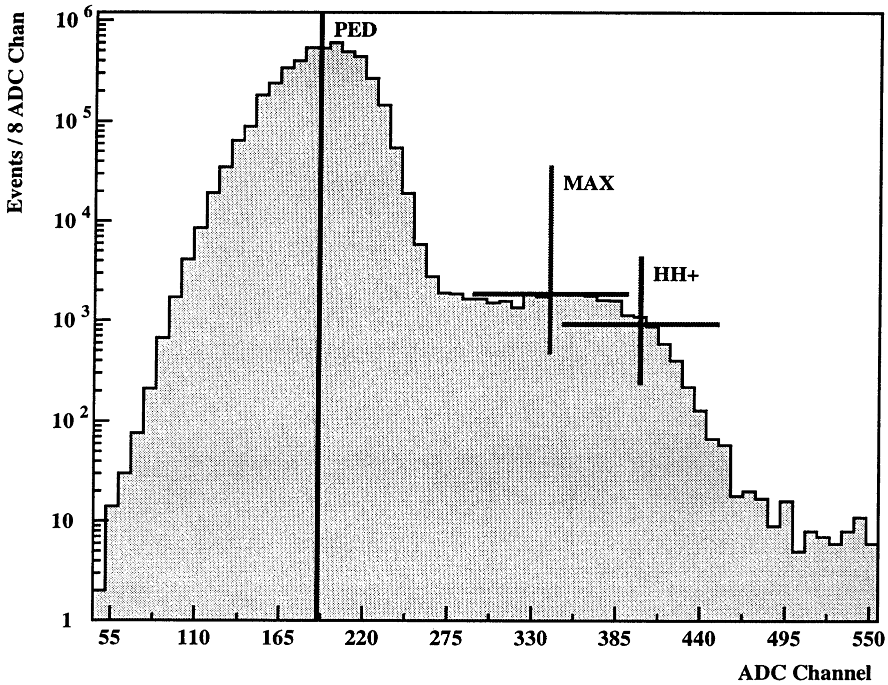

Figure 6.11: **Definition of the calibration point, HH^+, the pedestal value and the maximum of the signal of the 17.6 MeV photons are indicated.**

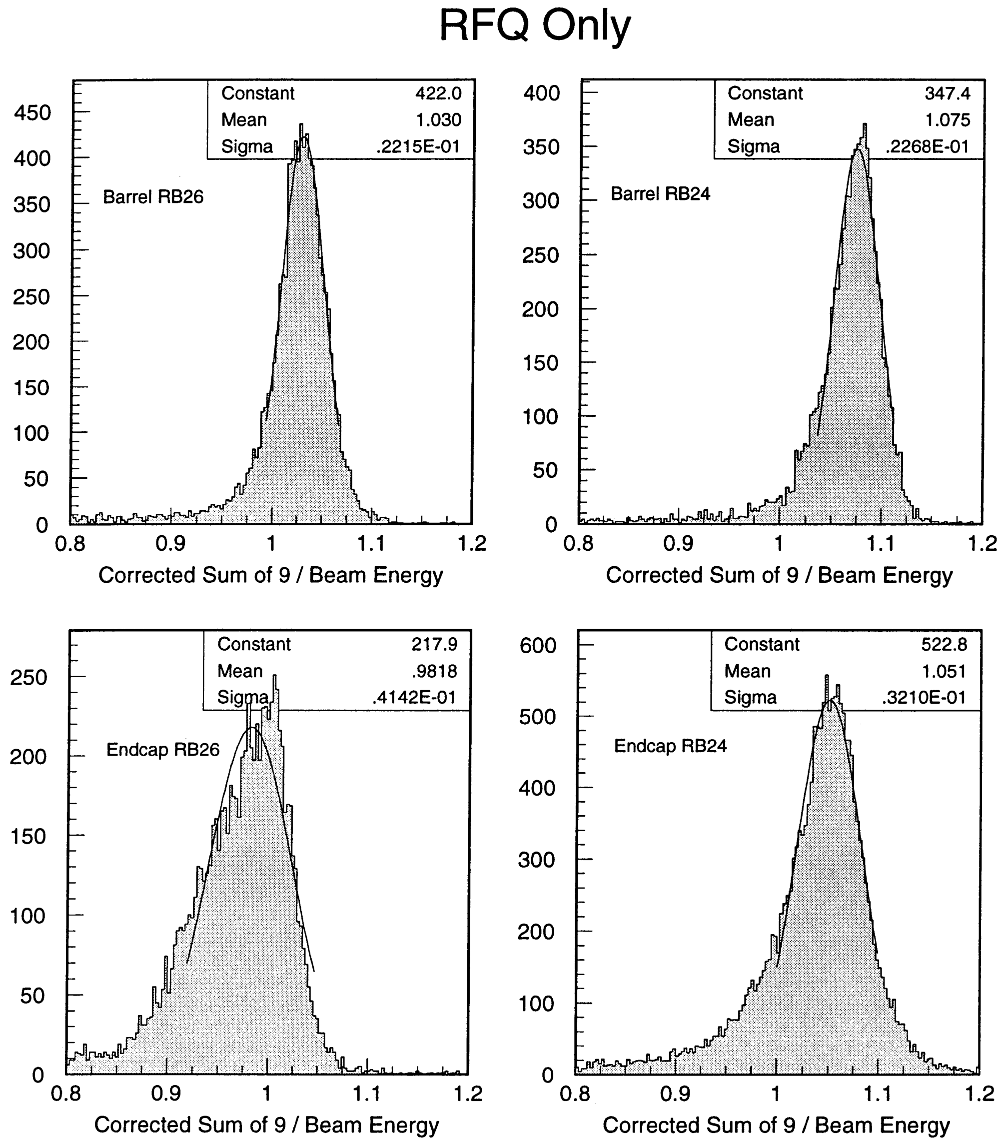

Figure 6.12: **Distribution of "Bhabha" electron energy using only RFQ calibration.**

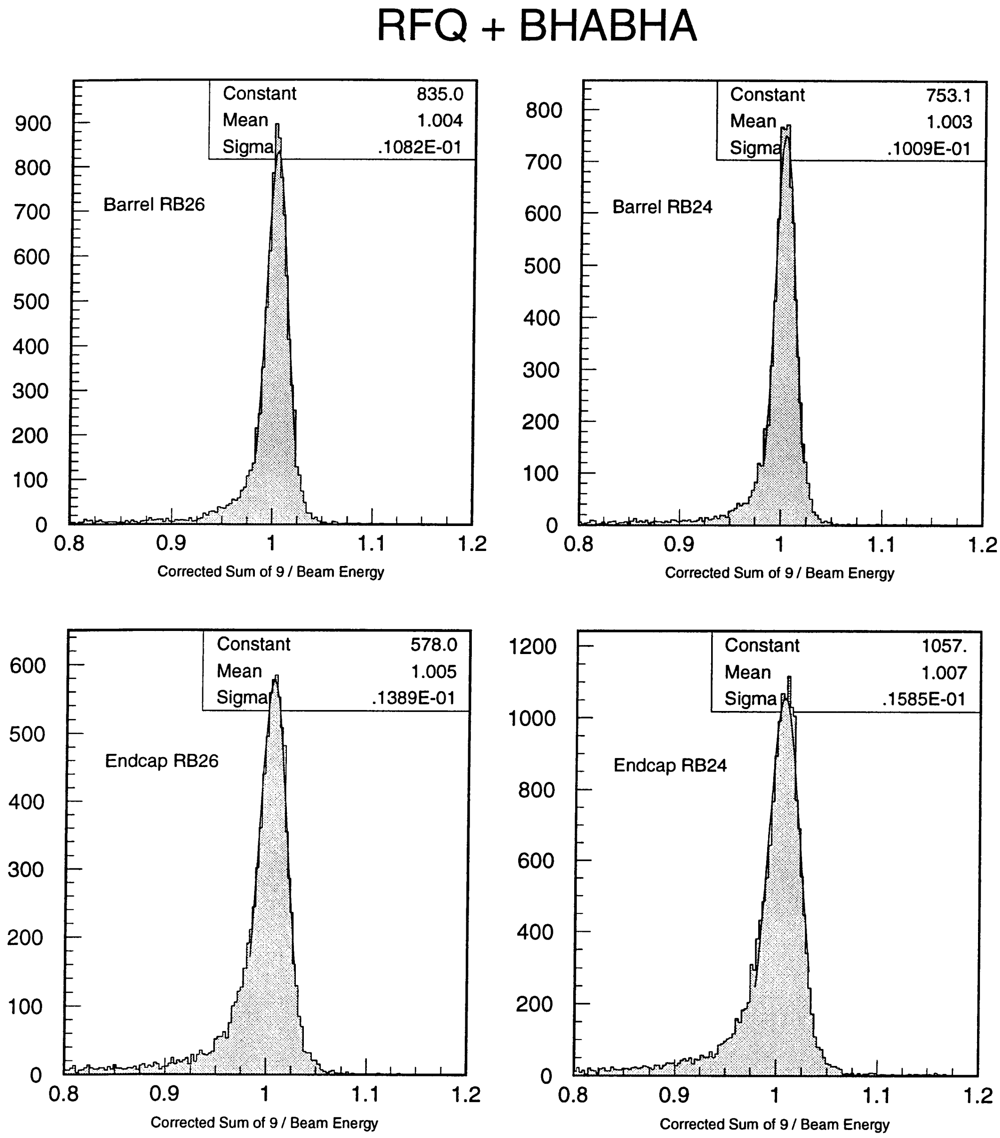

Figure 6.13: **Distribution of "Bhabha" electron energy using only RFQ+Bhabha calibration.**

Chapter 7

Analysis.

7.1 Introduction.

In this Chapter the details of the analysis for the W production measurement will be described. The data analysed in this thesis have been taken at LEP, with the L3 experiment, during the year 1996 and 1997 at centre of mass energy of $\sqrt{s}$=161.34 GeV and $\sqrt{s}$=172.13 GeV and 1997 at $\sqrt{s}$=182.69 GeV. About 10 pb^{-1} have been collected at 161 GeV, $\sim$ 10 pb^{-1} at 172 GeV and $\sim$ 55 pb^{-1} at 183 GeV.
The WW Monte Carlo events, relevant for this analysis, have been produced using EXCALIBUR as generator.
We will start with the description of the different decay channels of the W, then the description of the selection criteria is done. The different background channels have been generated with the PYTHIA generator.

7.2 Experimental topologies of the W decays and their signatures.

7.2.1 The hadronic channel: $W^+W^- \to qqqq$.

The two W's produced via $e^+e^- \to W^+W^-$ decay, 45.6 % of the cases, in two pairs of quarks-antiquarks $W^+W^- \to qqqq$. The events are characterised by a high track and calorimetric cluster multiplicity and a high visible energy, in the calorimeters, due to the presence of the four hadronic jets.
From the experimental point of view a jet is the result of the association of the hadrons in the final state after the hadronization of the produced quarks. To reconstruct a jet different algorithms can be used. They are iterative procedure: for

each pair of clusters, i and j, for which the four momentum vector $p_i = (E_i, \vec{p_i})$ has been calculated, a function, $y_{i,j} = f(p_i, p_j)$, is calculated and the two clusters with maximum $y_{i,j}$ are associated by adding their four momenta. The process is stopped when the association has a value of y greater than a predefined value, y_{cut}. For the DURHAM algorithm used, [89] the function $y_{i,j}$ is defined as:

$$y_{i,j} = \frac{2min(E_i^2, E_j^2)(1 - cos\theta_{ij})}{E^2_{visible}} \tag{7.1}$$

The events have a spherical symmetry, therefore the longitudinal or transversal energy imbalance is very small. The most important contamination for this channel comes from the process $e^+e^- \to q\bar{q}(\gamma)$ which has a cross section $\sim$ 2 orders of magnitude bigger than the cross section for W production; the topology of the final state can be similar because more than two hadronic jets can be present due to gluon radiation.

7.2.2 The semileptonic channel: $W^+W^- \to qql\nu$.

In this channel one of the two W's decays into a pair of quark-antiquark and the other in one lepton (l) and its associated neutrino, where $l = e, \mu, \tau$. The characteristic topology of these events is the presence of one isolated lepton in an hadronic environment. The events have high multiplicity and high visible energy, but they are characterised by a non zero missing energy due to the presence of the neutrino. This missing energy can be reconstructed by imposing four momentum conservation. The two reconstructed masses, M_{qq} and $M_{l\nu}$, have to be in a predefined window around the value of the W mass.
In this channel we have to separately consider the case in which the lepton is a τ. In this case, when the τ decays hadronically, the final state has three jets and the contamination coming from the process $e^+e^- \to q\bar{q}(\gamma g)$ is significantly higher. On the other hand, when the τ decays into a lepton there are extra neutrino-antineutrino in the event and the reconstruction of the missing energy is more difficult and the use of a kinematic fit is necessary.

7.2.3 The leptonic channel: $W^+W^- \to l\nu l\nu$.

This channel is characterised by a low multiplicity, a low visible energy and a very high missing momentum due to the presence of the two neutrinos. The most important background comes from events like $e^+e^- \to l^+l^-(\gamma)$, which can be rejected by taking into account the collinearity of the two leptons. Here also, when the two leptons are τ's decaying hadronically, the background coming from $e^+e^- \to q\bar{q}(\gamma)$ events has to be taken into account.

7.3 Backgrounds.

Potential background sources for $e^+e^- \to W^+W^-$ analysis are the following:

1. each decay channel of the W is a potential background for the others. The purely leptonic decays of the W are well separated by a cut on the number of clusters, since they have a low multiplicity.

2. The reaction $e^+e^- \to Z/\gamma \to q\bar{q}(\gamma g)$ is the dominant background. It has a cross section of 107 pb at $\sqrt{s} = 183$ GeV to be compared to 15.5 pb for the WW production. The Feynman diagrams corresponding to these events are shown in Figure 7.1. The energy of the photons in the final state changes with

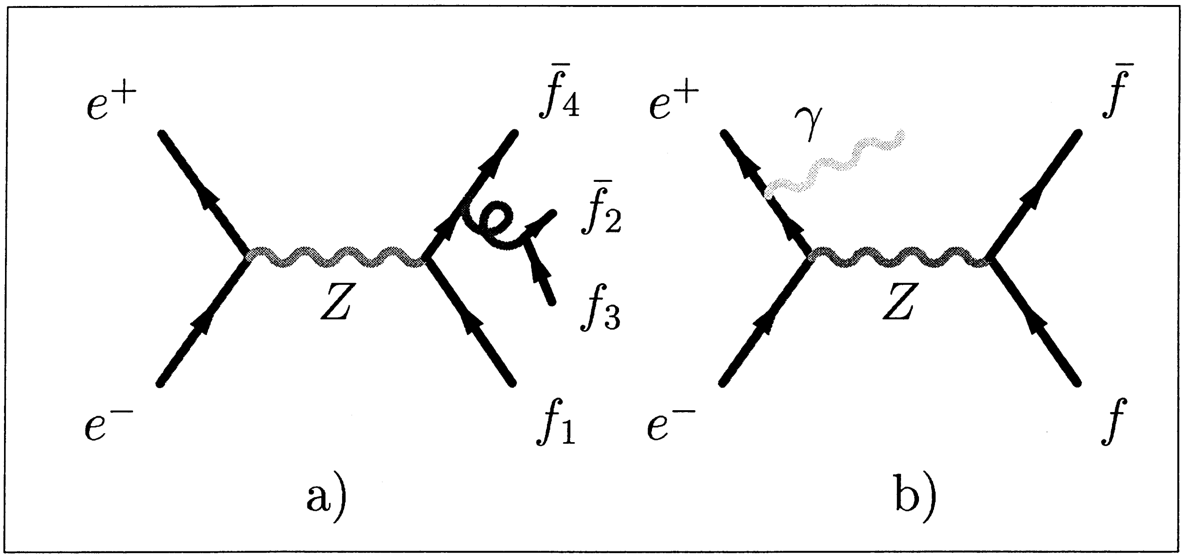

Figure 7.1: **Feynman diagrams for the process $e^+e^- \to Z/\gamma \to q\bar{q}(\gamma g)$.**

the virtuality of the Z. We can have initial or final state radiation of photons which converts into a fermion pair (a), when the two fermions are quarks the topology of the final state is the same as $W^+W^- \to qqqq$. We can have initial state radiation of photons of $E_\gamma \geq 50$ GeV which go along the beam pipe and are not detected (b). In this case the effective centre of mass energy is lowered

to the Z peak (return to the Z).
During the hadronization of the jets high energy leptons can be present mainly due to $c \to l$ and $b \to l$ decays. They represents the highest background for the semileptonic channel which can be reduced by isolation criteria.
When the two fermions, f_2, f_3, of Figure 7.1 (a) in the final state are leptons, they are a background for the leptonic channel. But the fermion from the W's are acoplanar because they come from different particles, which is not the case for $e^+e^- \to f\bar{f}f\bar{f}$.

3. The reaction $\boldsymbol{e^+e^- \to ZZ}$ has a small cross section, 0.59 *pb* at 183 GeV, and therefore it has not a major effect on the analysis. The corresponding Feynman diagram is shown in Figure 7.2. The final state has four fermions as in

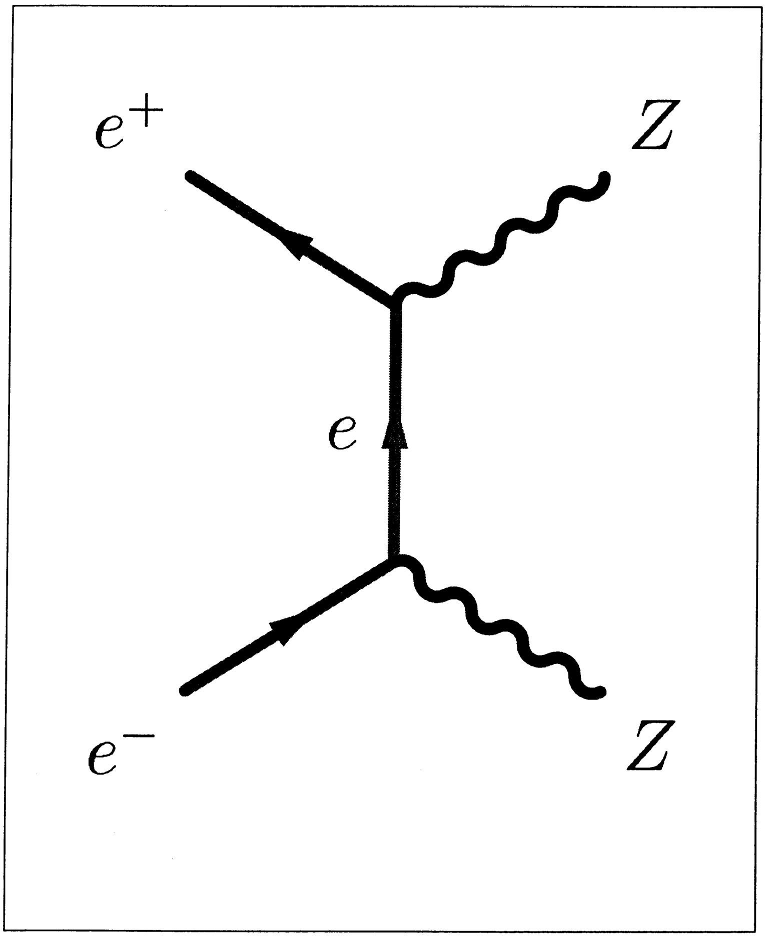

Figure 7.2: **Feynman diagrams for the process $ZZ \to all$.**

the case of the signal. The difference between signal and background is that

in the hadronic decays of the W, the quark-antiquark in the final state have a different flavour to conserve the charge of the W (for example $W^+ \to u\bar{d}$), in the decay of the Z boson they have the same flavour (for example $Z \to u\bar{u}$). But very often the charge of the jets is not correctly measured, in these case we cannot distinguish between $W^+W^- \to qqqq$ and $ZZ \to q\bar{q}q\bar{q}$ decays.
In the semileptonic decays of the W, the final state is $l\nu_l$ while the Z has a pair l^+l^-. The ZZ events are t channel processes, therefore the produced Z bosons are going mainly in the forward direction. In the final state $ZZ \to q\bar{q}l^+l^-$ when a lepton goes in the beam pipe and is not detected, these events have the same topology as a semileptonic W decay. This background can be suppressed requiring that the direction of the missing energy points inside the detector.

4. The reaction $\boldsymbol{e^+e^- \to e^+e^-Z \to e^+e^-hadrons}$ is important when the W decays into an electron. The cross section of this process at $\sqrt{s} = 183$ GeV is 3.3 *pb*. The Feynman diagrams for this process is shown in Figure 7.3. In this case also, the most important contribution, comes from the t channel diagrams, in which one of the particles in the final state goes along the beam pipe simulating a $W^+W^- \to qqe\nu_e$ event. By requiring the missing momentum to be inside the detector this background is substantially reduced.

7.4 Event selection.

7.4.1 $W^+W^- \to qqe\nu$ selection.

The channel $W^+W^- \to qqe\nu_e$ was under my direct responsibility in the L3 analysis group, therefore this analysis will be described in more detail than the other channels. The study of the selection started in 1996, before the beginning of the data taking, with Monte Carlo events.
A preselection has been studied and since then it is used in the PASS1 selection for the production of L3 data. A $qqe\nu$ event is shown in Figure 7.4. The selection cuts may vary slightly with the beam energy, they are summarised in Table 7.1.
The generators used to determine the selection efficiencies are $e^+e^- \to W^+W^-$ (CC03) KORALW [31] and $e^+e^- \to W^+W^-$ (CC20) EXCALIBUR [32].
The selection of the semileptonic events starts with the identification of an high energy isolated electron. The electron is characterised by an electromagnetic bump in the BGO electromagnetic calorimeter with $E_e > 20$ GeV, $\Sigma_9/\Sigma_{25} > 0.95$ and a cor-

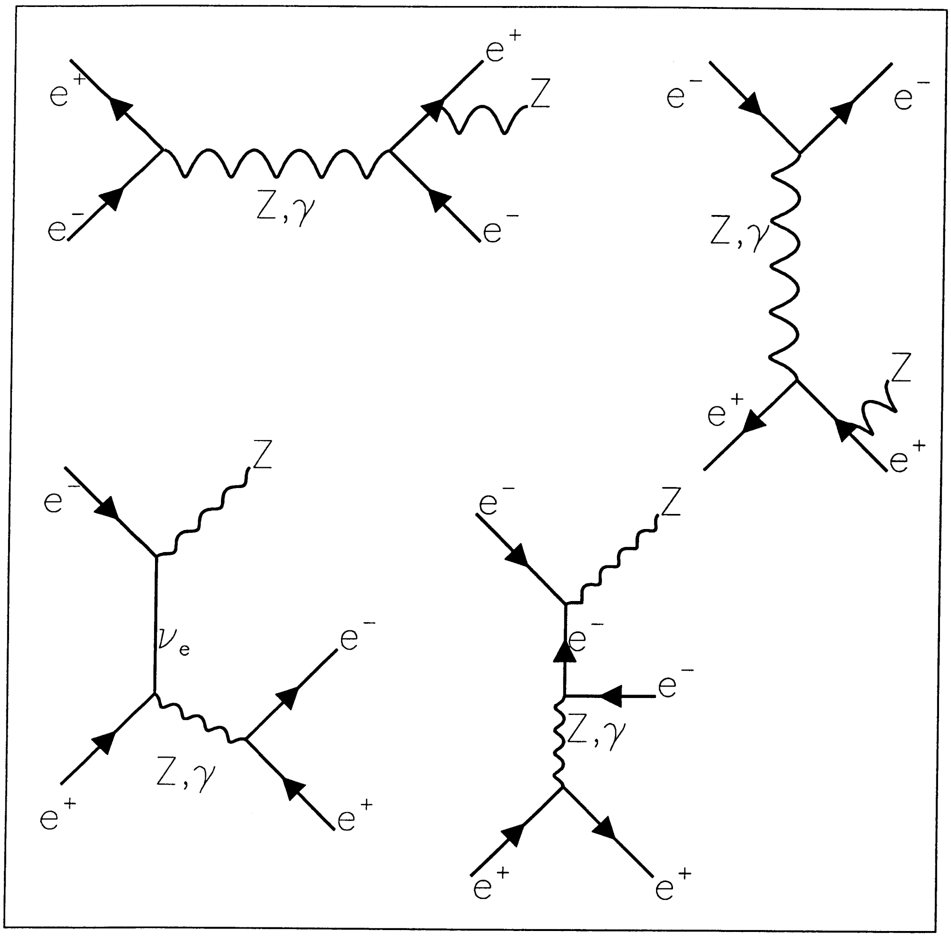

Figure 7.3: **Feynman diagram for the process $e^+e^- \to Zee \to all$.**

responding track in the central tracking chamber inside an azimuthal window $\Delta\Phi$. The energy of the electron is shown in Figure 7.5. Depending on the polar angle θ the $\Delta\Phi$ window varies from 10 to 42 mrad to account for geometrical and resolution effects.

The electrons from the decay of hadrons are rejected by requiring the electron to be isolated from the hadronic system. The isolation is imposed either by a cut on the total calorimetric energy deposited in a cone of half opening angle of 10 degrees around the electron direction, either with a cut on the angular distance between the electron and the nearest jet.

In the 1997 analysis, at $\sqrt{s} = 183$ GeV, the EGAP detector has been included. The improvement in the selection efficiency is $\sim 5\%$. A distribution of $\mid cos\theta_e \mid$ with and without EGAP is shown in Figure 7.6. Once the lepton has been identified, the rest of the event is clusterised in two hadronic jets, using the DURHAM algorithm [89].

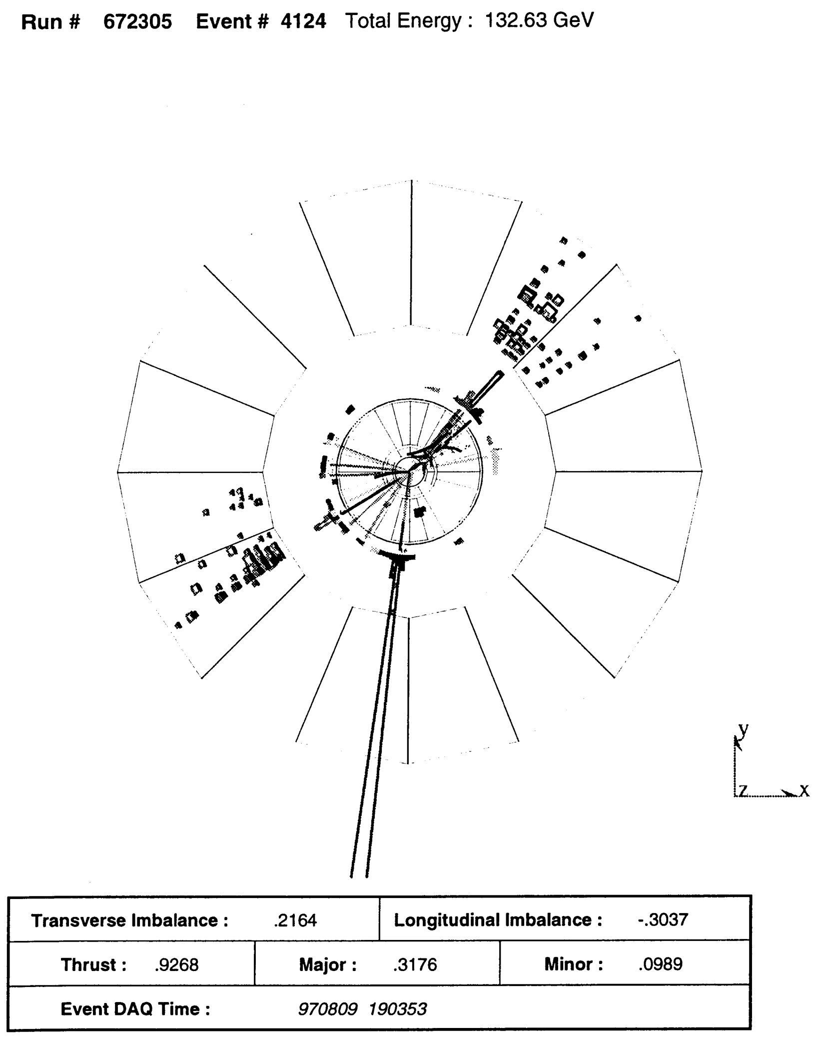

Figure 7.4: **Example of a *qqeν* event at 172 GeV.**

The track and cluster multiplicity of the event, due to the hadronization of the quarks, is a good variable to separate the signal from low multiplicity events like Bhabha, muon pairs, and purely leptonic decays of the W. The track multiplicity for purely hadronic and for semileptonic events is shown in Figure 7.7. From the lepton and the two jets four-vectors we can calculate the missing momentum due to the presence of the neutrino (Figure 7.8). In order to reject radiative $q\bar{q}(\gamma)$ events, where the photon escapes along the beam pipe, the polar angle of the missing momentum vector must point well inside the detector and the neutrino energy must be larger than 20 GeV. The Figure 7.9 shows the angular distribution of the neutrino $(cos\theta_{\nu})$.

The masses of the two W bosons are calculated as the invariant mass of the electron-neutrino system, $M_{e\nu}$, and the mass of the jet jet system, M_{qq}. The invariant mass

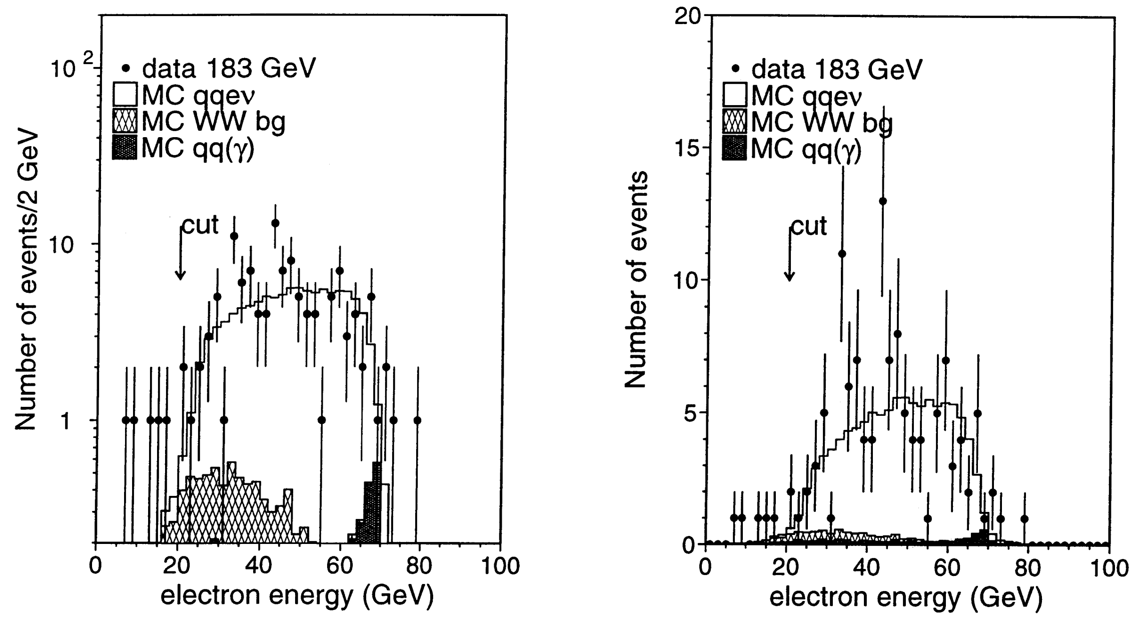

Figure 7.5: **Energy of the electron for $qqe\nu$ events at $\sqrt{s}$=183 GeV, in logarithmic and linear scale. The WW Monte Carlo background indicates the background from the other decay channels.**

electron neutrino and the invariant mass of the jet jet system are shown in Figure 7.10.

All the cuts are summarised in table 7.1.

In the $W^+W^- \to qqe\nu_e$ channel, the high selection efficiency and small background contamination allows a clean event selection which gives in a measurement of the cross section and of the W mass with a small systematic error. This will become more and more important in the future when the high statistics accumulated will induce an error reduction.

The number of selected events, the selection efficiency, the integrated luminosity and the background contamination (for the other decay channels of the W we quote the efficiency), for the channel $qqe\nu$ are listed in table 7.2. Since at present the statistics of the individual channels is limited we have decided to add all the leptonic decay channels together to measure the mass of the W boson. We summarise briefly in the following the analysis of the other decay channels. The approach is similar to the $qqe\nu$ selection, a detailed description of the analysis can be found in [90, 91].

Cut	$\sqrt{s} = 161$ GeV	$\sqrt{s} = 172$ GeV	$\sqrt{s} = 183$ GeV
# of clusters	≥ 15	≥ 15	≥ 15
# of tracks	≥ 5	≥ 5	≥ 5
Σ_9/Σ_{25}	≥ 0.95	≥ 0.95	≥ 0.95
E_e	≥ 25 GeV	≥ 20 GeV	≥ 20 GeV
E_ν	≥ 25 GeV	≥ 20 GeV	≥ 20 GeV
$\mid cos\theta_e \mid$	≤ 0.90	≤ 0.95	≤ 0.95
$\mid cos\theta_\nu \mid$	≤ 0.90	≤ 0.95	≤ 0.95
$\Delta\Phi_{TEC-BGO}$	≥ 10 mrad	≥ 10 *to* 42 mrad	≥ 10 *to* 42 mrad
θ_{e-jet}	-	$\geq 10°$	$\geq 10°$
$E_e/Econe_{15°}$	≥ 0.7	-	-
$M_{q\bar{q}}$	≥ 50 GeV	≥ 45 GeV	≥ 45 GeV
$M_{e\nu}$	≥ 50 GeV	≥ 55 GeV	≥ 55 GeV

Table 7.1: **Cuts used for the selection in the semileptonic channel with an electron in the final state at different centre-of-mass energies.**

	$\sqrt{s} = 161$ GeV	$\sqrt{s} = 172$ GeV	$\sqrt{s} = 183$ GeV
Luminosity (pb^{-1})	10.20	10.25	55.40
Signal efficiency (%)	76.3	79.3	85.5
Efficiency for $qq\mu\nu$ (%)	-	0.16	0.2
Efficiency for $qq\tau\nu$ (%)	1.4	1.74	1.7
Non W background (# of events)	0.16	0.65	6.54
# of events	4	19	119

Table 7.2: **Results for the $qqe\nu$ channel.**

7.4.2 $W^+W^- \to qq\mu\nu$ selection.

The event selection for the process $e^+e^- \to qq\mu\nu$ requires a good identification of the muon in the muon spectrometer. A muon can be identified as the highest momentum track pointing to the interaction vertex, matched with a track in the muon chambers and with a momentum p_μ larger than a predefined cut. Muons arising from decays of hadrons are rejected by requiring an angular separation between the muon and both hadronic jets. The distributions of the angle between the muon and the nearest jet multiplied by $\sqrt{1- \mid cos\theta_\nu \mid}$ is shown in Figure 7.11. The isolation cut is tighter as much as the missing energy is pointing along the beam pipe.

In order to reject $q\bar{q}\mu^+\mu^-$ events, any additional muon reconstructed in the muon chambers must have a small momentum or the invariant mass of the two muons has

to be smaller that 30 GeV.
The invariant mass of the muon-neutrino system and the polar angle of the neutrino are shown in Figure 7.12 and in Figure 7.13 respectively.

The selection is improved by including also muons identified as minimum ionising particles (MIP) in the calorimeters. In this case muons are identified as a track in the central tracking chamber with momentum larger than 10 GeV associated with an energy deposition in the calorimeters compatible with a MIP. For MIP muons the muon-neutrino invariant mass cut is lower than for well reconstructed muons, because the momentum measurement is not as accurate. The inclusion of the MIP muon identification increases the efficiency by 10 % because of the lower efficiency in the forward region.
The complete list of the cuts used in the analysis at the different centre of mass energies are listed in table 7.3. The luminosity used, the selection efficiency, the

Cut	$\sqrt{s} = 161$ GeV	$\sqrt{s} = 172$ GeV	$\sqrt{s} = 183$ GeV
# of clusters	≥ 15	≥ 15	≥ 15
# of tracks	≥ 5	≥ 5	≥ 5
P_μ	≥ 20 GeV	≥ 15 GeV	≥ 15 GeV
P_μ second	≤ 20 GeV	-	-
$M_{\mu\mu}$	-	≤ 30 GeV	≤ 30 GeV
$\mid cos\theta_\nu \mid$	≤ 0.95	≤ 0.95	-
$\theta_{\mu-jet}$	≥ 15	≥ 10	-
$\sqrt{1- \mid cos\theta_\nu \mid}\alpha(\mu, jet)$	-	-	1.8°
$M_{q\bar{q}}$	$\geq 40 \leq 120$ GeV	$\geq 30 \leq 120$ GeV	$\geq 30 \leq 120$ GeV
$M_{\mu\nu}$	≥ 55 GeV	≥ 55 GeV	≥ 55 GeV
MIP			
P_{track}	≥ 10 GeV	≥ 10 GeV	≥ 10 GeV
$\theta_{MIP-jet}$	≥ 15	≥ 15	≥ 15
$M_{q\bar{q}}$	$\geq 40 \leq 110$ GeV	$\geq 40 \leq 110$ GeV	$\geq 40 \leq 110$ GeV
$M_{MIP\nu}$	≥ 20 GeV	≥ 20 GeV	≥ 20 GeV

Table 7.3: **Cuts used for the selection in the semileptonic channel with a muon in the final state at different centre-of-mass energies.**

accepted background and the number of selected events, after applying this selection, are listed in table 7.4.

	$\sqrt{s} = 161$ GeV	$\sqrt{s} = 172$ GeV	$\sqrt{s} = 183$ GeV
Luminosity (pb^{-1})	10.90	10.25	55.40
Signal efficiency (%)	66.0	74.1	77.1
Efficiency for $qqe\nu$ (%)	-	0.11	0.1
Efficiency for $qq\tau\nu$ (%)	2.1	3.50	4.2
Accepted background (# of events)	0.17	0.38	3.16
# of events	4	9	108

Table 7.4: **Results for the $qq\mu\nu$ channel.**

7.4.3 Selection of $qq\tau\nu$.

The selection is based on the identification of a τ jet and of the missing energy associated to the two neutrinos. In the case of a leptonic τ decay, $\tau \to l\nu_e\nu_\tau$, the lepton, with an energy larger than 5 GeV, is identified as in the $W \to l\nu$ selection. The sum of the lepton energy and the missing energy has to be larger than 65 GeV. If a lepton is not identified, the clusters are grouped to form jets with energies larger than 10 GeV. Between the three most energetic jets, the two which show a back-to-back configuration are associated to the decay of a W ($W \to qq$), the third one is a candidate for a τ jet. The visible energy of the τ jet is shown in Figure 7.14. The τ must be isolated from the nearest hadronic jet by at least 25 degrees. The missing momentum of the decay $W \to \tau\nu_\tau$ is reconstructed performing a 4C kinematical fit of the two hadronic jets and the identified lepton.
The invariant mass of the τ-neutrino system has to be larger than 55 GeV and the mass of the jet-jet system has to be larger than 60 GeV and smaller than 100 GeV. To reduce the background from $e^+e^- \to q\bar{q}(\gamma)$, and from $W^+W^- \to qqqq$, the difference between the visible energy and the missing energy has to be smaller than 120 GeV. The results of this selection are shown in table 7.5.

7.4.4 Selection of $qqqq$.

In this channel the background from $q\bar{q}(\gamma)$ events is so high that it is necessary to use a neural network approach to reach reasonable purities. The neural networks are trained with Monte Carlo events for signal and background events and then they are applied to the data. A loose preselection is applied to Monte Carlo events before the training, asking for high multiplicity events with no missing energy. A cut on the resolution parameter, which separates 4 jets from 3 jets ($y_{34} \geq 0.0025$), is applied. A feed-forward three level neural network is used: the first level is formed by 10

	$\sqrt{s} = 161$GeV	$\sqrt{s} = 172$GeV	$\sqrt{s} = 183$GeV
Luminosity (pb^{-1})	10.2	10.3	55.4
Signal efficiency (%)	37.5	46.6	51.3
Efficiency for $qqe\nu$ (%)	4.7	5.62	7.2
Efficiency for $qq\mu\nu$ (%)	4.8	6.89	6.6
Efficiency for $qqqq$ (%)	0.1	0.14	0.2
Accepted background (# of events)	1.6	2.1	11.2
# of events	2	12	84

Table 7.5: **Results for the $qq\tau\nu$ channel.**

nodes in input, an intermediate (hidden) level with 15 nodes, and the third with only one node as output, which gives a value whose distribution is peaked at 1 for the signal and at 0 for the background. The 10 input variables are chosen according to the topology of the four jet events. They are: y_{34}, the sphericity, the minimal and maximal jet energies, the minimal jet cluster multiplicity, the sum and the difference of the two W masses, the maximal acollinearity between jets belonging to the same W, the minimal jet-jet angle, the minimal mass of jets when the event is reconstructed as two-jet event. The neural network output distribution for data events is fitted by a linear combination of neural network output distributions derived from Monte Carlo simulations for signal and background. The Figure 7.15 shows a distribution of the neural network output. The result of the selection are listed in table 7.6.

	$\sqrt{s} = 161$GeV	$\sqrt{s} = 172$GeV	$\sqrt{s} = 183$GeV
Luminosity (pb^{-1})	10.2	10.3	55.4
Signal efficiency (%)	67.0	84.1	88.0
Efficiency for $qqe\nu$ (%)	-	0.08	0.5
Efficiency for $qq\mu\nu$ (%)	-	0.04	0.1
Efficiency for $qq\tau\nu$ (%)	0.6	2.14	2.2
Accepted background (# of events)	5.2	12.7	86.4
# of events	8.9	61	475

Table 7.6: **Results for the $qqqq$ channel.**

7.4.5 Selection of $l\nu l\nu$.

On the $e^+e^- \to W^+W^- \to l\nu l\nu$ channel we require the presence of two leptons, a low multiplicity and the high missing energy due to two neutrinos. The number of tracks must be between 2 and 6 and the visible energy must be between 2 % and 80 % of $\sqrt{s}$. Electrons and muons are identified as in the semileptonic selection, in a polar angle range $|\ cos\theta\ | \leq 0.92$. Two categories are possible: lepton-lepton events or lepton-jet events when the τ is present. In the lepton-jet class the jet must have at least 8 GeV of energy. To reduce the $e^+e^- \to l^+l^-$ contamination, the acoplanarity has to be larger than 8 degrees and the missing momentum must not point along the beam pipe, $cos\theta_{p_\nu} \leq 0.96$. For the lepton-jet class the acoplanarity condition is applied not only between the lepton and the jet, but also between the lepton and all other tracks. The acoplanarity distribution is shown in Figure 7.16. The results of this selection are listed in table 7.7.

	$\sqrt{s} = 161$GeV	$\sqrt{s} = 172$GeV	$\sqrt{s} = 183$GeV
Luminosity (pb^{-1})	9.6	10.3	55.4
Efficiency (%)	39.8	45.1	42.8
Accepted background (# of events)	0.39	0.34	1.39
# of events	2	9	54

Table 7.7: **Results for the $l\nu l\nu$ channel The background from the other W decay channels is negligible, below 10^{-4}, and then is not reported in the table.**

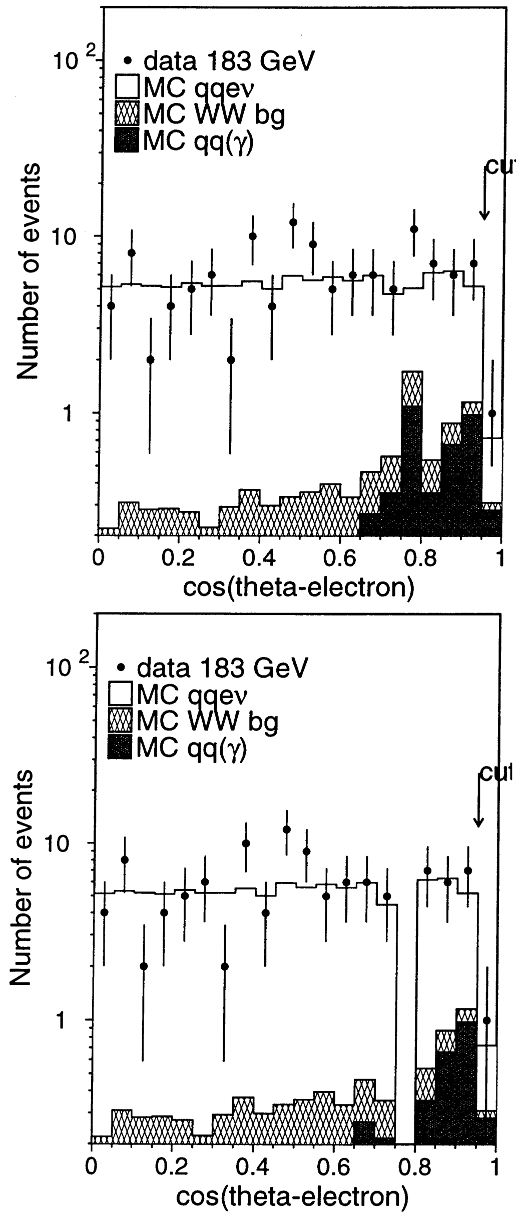

Figure 7.6: **Distribution of the polar angle | $cos\theta_e$ | of the electron, with and without EGAP, for $qqe\nu$ events at $\sqrt{s}$ = 183 GeV.**

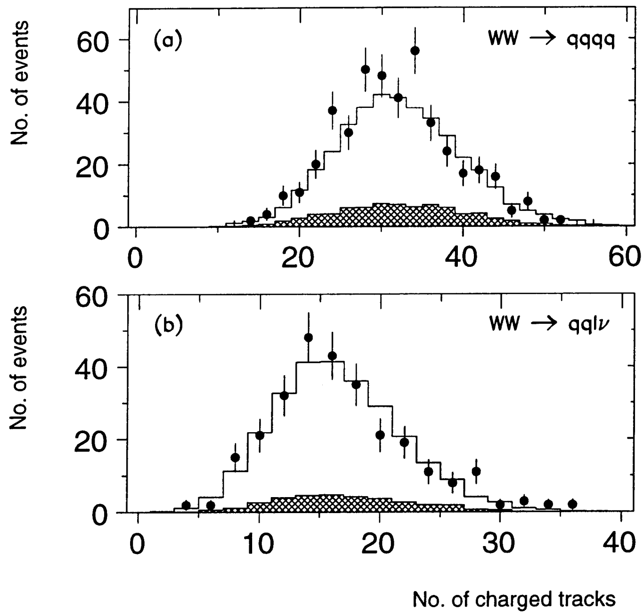

Figure 7.7: **Track multiplicity for $W^+W^- \to qqqq$ and $W^+W^- \to qql\nu$ events.**

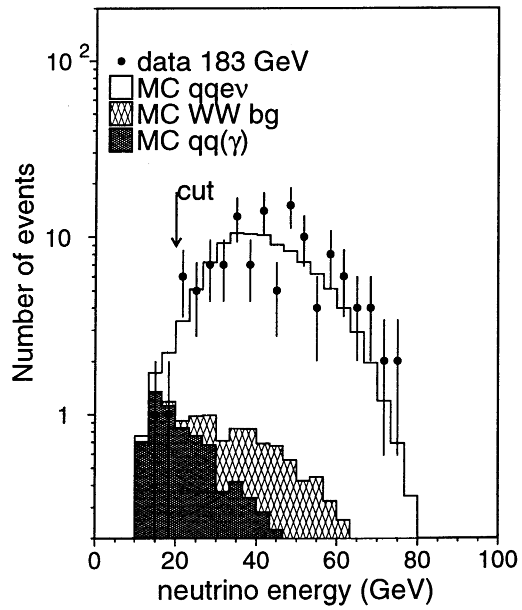

Figure 7.8: **Distribution of the missing momentum, i.e. the neutrino energy for $qqe\nu$ events at $\sqrt{s}$=183 GeV.**

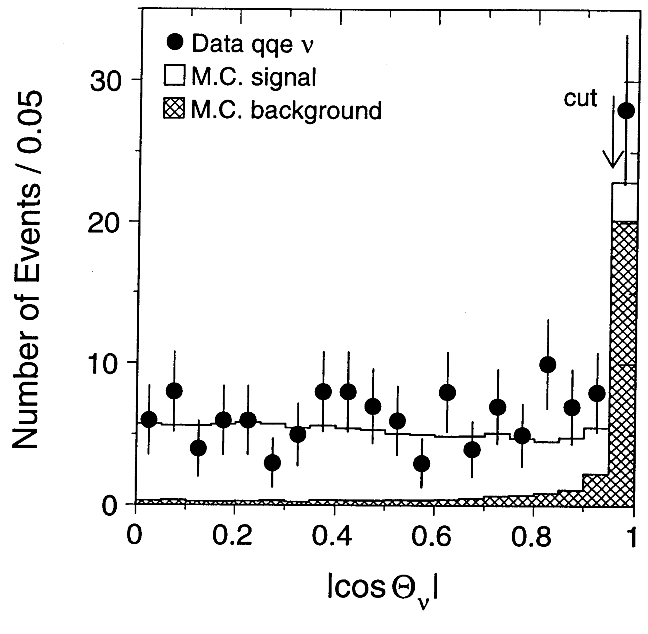

Figure 7.9: **Polar angle distribution of the missing energy, i.e. | $cos\theta_\nu$ | for $qqe\nu$ events at $\sqrt{s}$=183 GeV.**

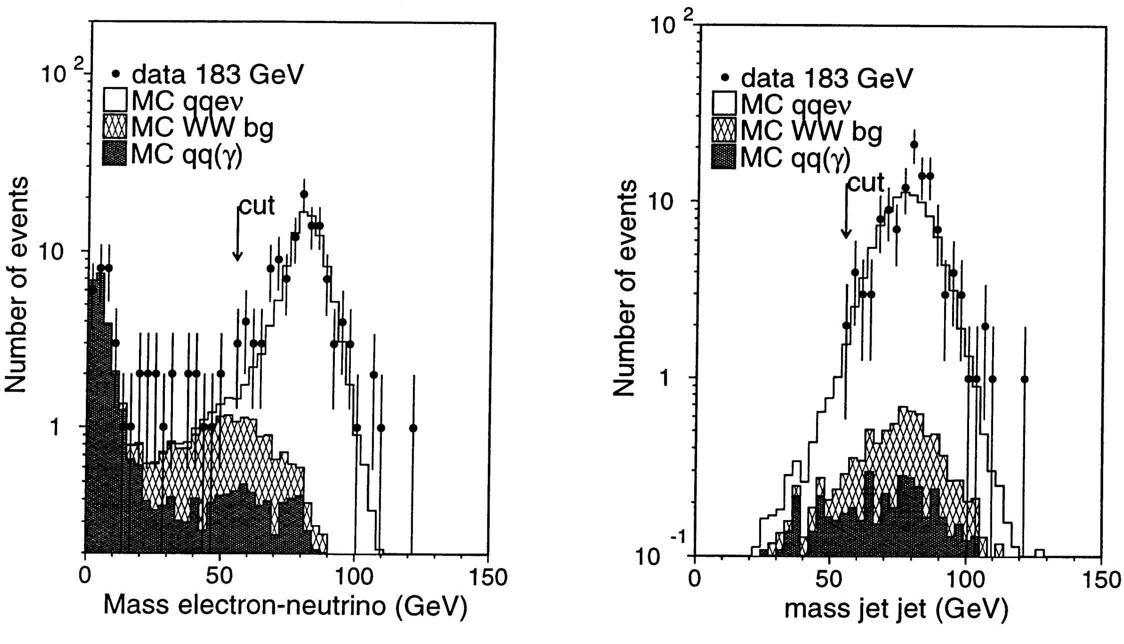

Figure 7.10: **Distribution of the mass of the electron neutrino system and of the jet jet system for $qqe\nu$ events at $\sqrt{s}$=183 GeV.**

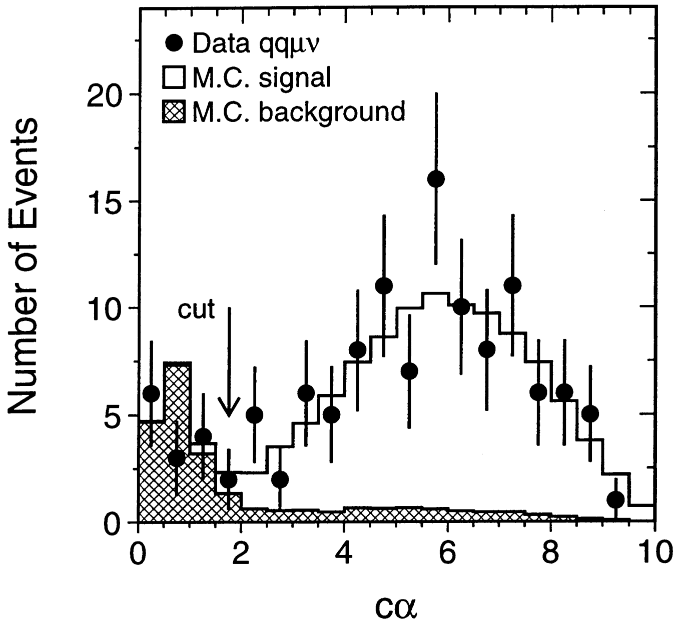

Figure 7.11: **Distribution of the angle α(in degrees) between the muon and the nearest jet for $qq\mu\nu$ events at $\sqrt{s}$=183 GeV multiplied by $\sqrt{1-\mid cos\theta_\nu \mid}$.**

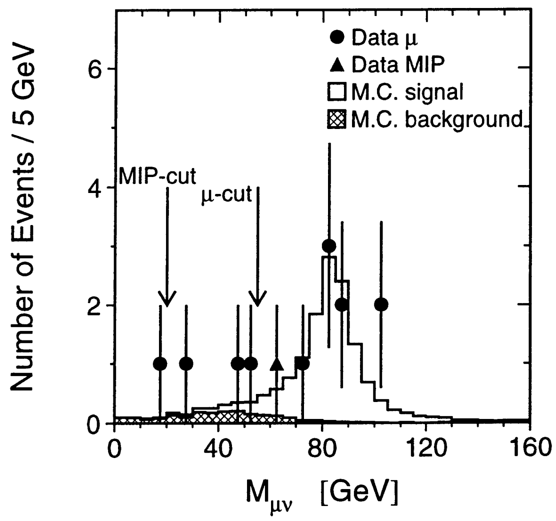

Figure 7.12: **Distribution of the invariant mass muon-neutrino ν for $qq\mu\nu$ events at $\sqrt{s}$=172 GeV.**

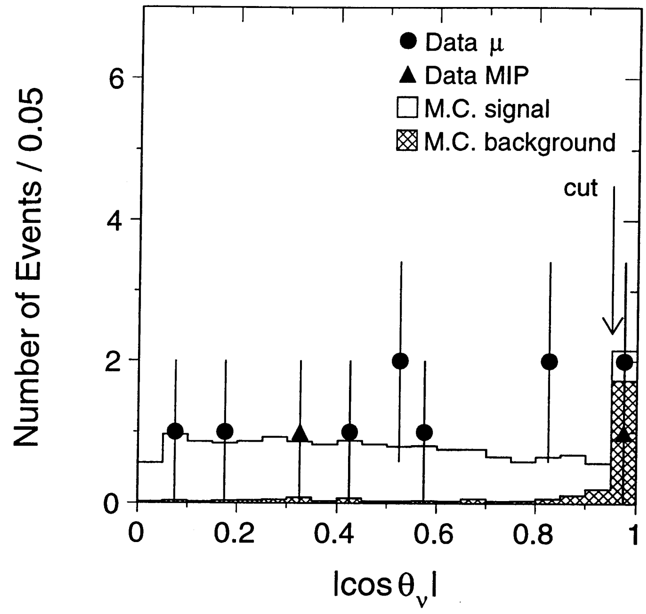

Figure 7.13: **Distribution of the polar angle of the neutrino, | $cos\theta_\nu$ | for $qq\mu\nu$ events at $\sqrt{s}$=172 GeV.**

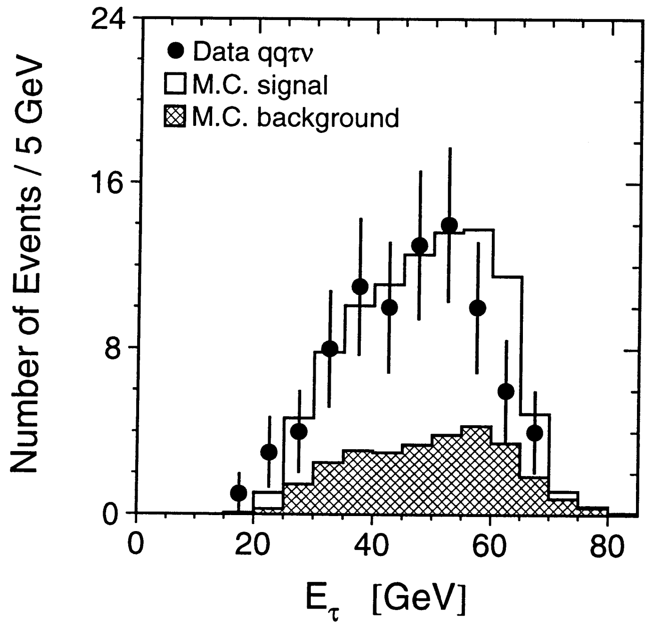

Figure 7.14: **distribution of the visible energy of the τ jet, E_τ, as observed in selected $qq\tau\nu$ events at $\sqrt{s}$=183 GeV.**

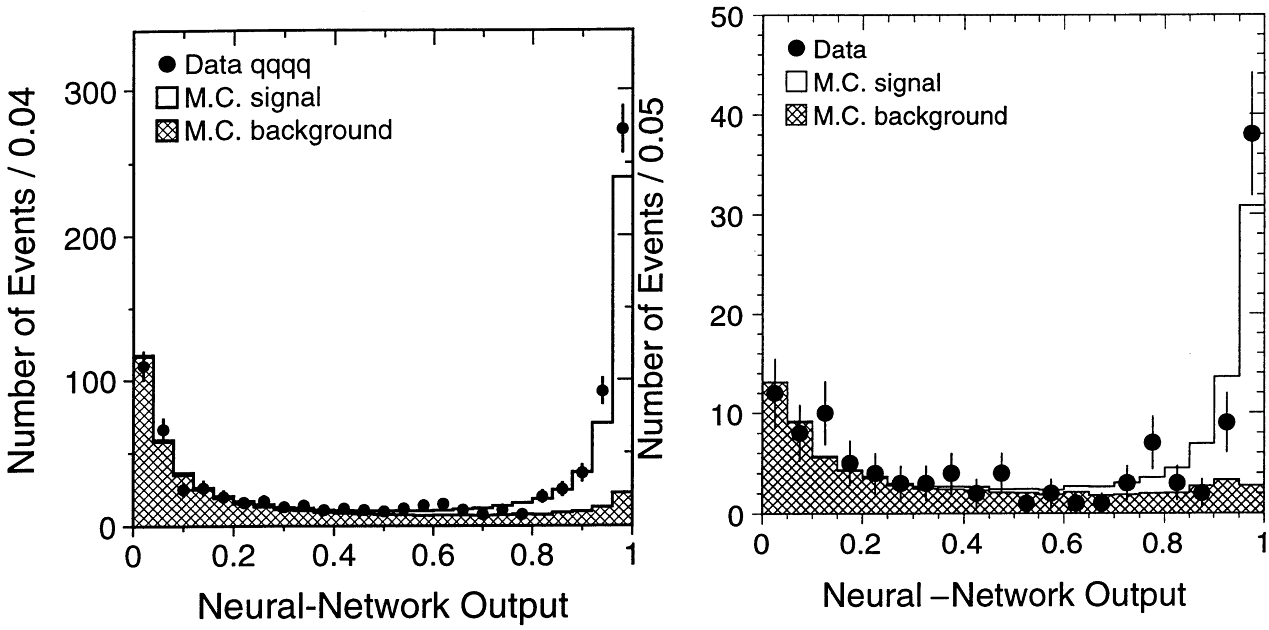

Figure 7.15: **Output of the neural network for $qqqq$ events at $\sqrt{s}$=183 GeV and $\sqrt{s}$=172. The disagreement between data and Monte Carlo in the distribution at 183 GeV is most probably due to a statistical fluctuation.**

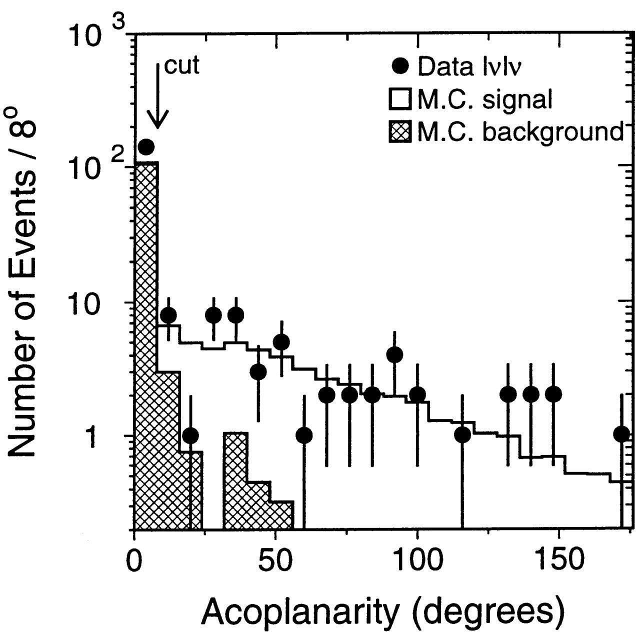

Figure 7.16: **Distribution of the acoplanarity between the two charged leptons for $l\nu l\nu$ events at 183 GeV.**

Chapter 8

Cross sections for W^+W^- production. W mass determination at $\sqrt{s}$=161 GeV.

8.1 Introduction.

In this Chapter the $e^+e^- \to W^+W^-$ cross sections measured at $\sqrt{s}$=161, $\sqrt{s}$=172 and $\sqrt{s}$=183 GeV will be presented with a description of the different contributions to the systematic error.
Then we will present the results on the W mass measurement at threshold ($\sqrt{s} = 161$ GeV) with the cross section method and we will discuss its systematic error.

8.2 Cross section measurement.

The cross section for a given class of events is given by

$$\sigma = \frac{N_{signal} - N_{background}}{\epsilon \mathcal{L}} \tag{8.1}$$

where

- N_{signal} is the number of selected events;

- $N_{background}$ the number of background events;

- ϵ is the selection efficiency, due to the acceptance and the efficiency of the detector and to the selection cuts;

- $\mathcal{L}$ is the integrated luminosity.

One important point, in the measurement of the cross section for the W production, is the contribution of the diagrams other than the "CC03" ones. The measured cross section is composed of all possible four fermion contributions, and so in the theoretical calculation we have to include all diagrams relative to the process $e^+e^- \to 4\ fermions$. The rapid growth of the $e^+e^- \to W^+W^-$ cross section around the threshold energy is a characteristic of this process. In fact, at the Born level, $\sigma_{WW} \propto \beta = \sqrt{1 - 4M_W^2/s}$. This kind of effect is present in none of the other diagrams of four fermion production. On the other hand the total cross section $\sigma(e^+e^- \to 4\ fermions)$ is neither easily measurable nor easily calculable and depends on the cuts applied. In fact we use a "CC03" Monte Carlo to evaluate the selection efficiency and we apply a correction to take into account the contributions of the four fermion diagrams. The correction is estimated by Monte Carlo simulation. Due to the long time necessary to generate the events when all the diagrams are taken into account, the selection has been tuned on CC03 events, then a small sample of CC20 events has been produced to evaluate the correction.
A preselection is used to generate the CC20 sample, the cuts are applied at the generator level and they are listed in table 8.1 for the three centre of mass energies:
We can calculate the number of events CC03 contained in the CC20 sample, then

	$\sqrt{s} = 161$GeV	$\sqrt{s} = 172$GeV	$\sqrt{s} = 183$GeV
$E_e \geq$ (GeV)	25	20	20
$E_\nu \geq$ (GeV)	25	20	20
$\mid cos\theta_e \mid <$	0.90	0.95	0.95
$\mid cos\theta_\nu \mid <$	0.90	0.95	0.95
$M_{e\nu} \geq$ (GeV)	50	45	45
$M_{q\bar{q}} \geq$ (GeV)	50	45	45

Table 8.1: **Phase-space cuts in which the signal efficiency and cross section are determined for the electron channel.**

the ratio $f_i = \frac{\sigma_{CC03}}{\sigma^{cuts}_{CC20}}$ is used to calculate the efficiency and to correct the cross section. The "CC03" cross section, taking into account this factor, is:

$$\sigma_{CC03} = \frac{N_{signal} - N_{background}}{\epsilon_{CC03}\mathcal{L}} \times f_i. \tag{8.2}$$

The correction factor f_i is 1.27 ± 0.05 at $\sqrt{s} = 161$ GeV, 1.10 ± 0.05 at $\sqrt{s} = 172$ GeV and 1.09 ± 0.05 at $\sqrt{s} = 183$ GeV for the $qqe\nu$ channel.
The cross sections are measured for the individual channels. To get σ_{WW} the results of the five measured channels are combined with a maximum likelihood function which is the product of the Poissonian probability $P(N_i, \mu_i)$:

$$L = \prod_i P(N_i, \mu_i) = \prod_i \frac{\mu_i^{N_i} e^{-\mu_i}}{N_i!} \tag{8.3}$$

where N_i is the number of selected events. The number of expected events, μ_i, is calculated as:

$$\mu_i = \left(\sum_{j=1}^{5} \epsilon_{ij}\sigma_j + \sigma_i^{bg} \right) \cdot \mathcal{L}_i \tag{8.4}$$

where ϵ_{ij} is the element of the matrix of the efficiencies and it is defined as the efficiency for the process j in the selection i. $\sigma_j = r_{SMj}\sigma_{WW}$ where r_{SMj} is the Standard Model branching fraction for the process j. $\mathcal{L}_i$ is the integrated luminosity for each channel. The luminosity is different for each channel because the selections are done using different sub-detectors (for example BGO calorimeter for the $qqe\nu$ channel or muon chambers for the $qq\mu\nu$ channel). A list of bad runs is produced for each sub-detectors, and then these runs are not used for the analysis.
Using the branching fractions (r_{SM}) predicted by the Standard Model the total cross section can be measured. The details for the cross section measurements are listed in table 8.2 for the $qqe\nu$ channel. The cross sections measured for the other channels are listed in table 8.3. The total cross section for W production measured at $\sqrt{s} =$ 161 GeV [90] is:

$$\sigma_{\mathrm{W^+W^-}} = \mathbf{2.89^{+0.81}_{-0.70}(stat.) \pm 0.14(syst.)} \ \ \mathbf{(pb)}. \tag{8.5}$$

At 172 GeV [91] the total cross section has been measured to be

$$\sigma_{\mathrm{W^+W^-}} = \mathbf{12.27^{+1.41}_{-1.32}(stat.) \pm 0.23(syst.)} \ \ \mathbf{(pb)} \tag{8.6}$$

and finally at 183 GeV the result is:

$$\sigma_{\mathrm{W^+W^-}} = \mathbf{16.66 \pm 0.66(stat.) \pm 0.30(syst.)} \ \ \mathbf{(pb)}. \tag{8.7}$$

	N_{data}	N_{bg}	$\sigma(CC03)$ (pb)	r_{SM}	σ_{SM} (pb)
$\sqrt{s} = 161$GeV	4	0.16	$0.62^{+0.38}_{-0.27}$	14.6	0.56
$\sqrt{s} = 172$GeV	19	0.64	$2.44^{+0.64}_{-0.55} \pm 0.07$	14.6	1.81
$\sqrt{s} = 183$GeV	119	6.6	$2.46^{+0.26}_{-0.24} \pm 0.06$	14.6	2.30

Table 8.2: **Number of selected events, N_{data}, number of expected non-W background events, N_{bg}, and CC03 cross section for the reaction $e^+e^- \to qqe\nu$. The first error is statistical the second, when reported, is systematic. Also shown are the CC03 ratio, r_{SM}, and the CC03 cross section, σ_{SM}, as expected in the Standard Model.**

Process	σ^{161}_{CC03} (pb)	σ^{172}_{CC03} (pb)	σ^{183}_{CC03} (pb)
$e^+e^- \to qq\mu\nu$	$0.53^{+0.33}_{-0.24}$	$1.06^{+0.44}_{-0.36}$	$2.34^{+0.25}_{-0.24}$
$e^+e^- \to qq\tau\nu$	$0.22^{+0.55}_{-0.38}$	$1.60^{+0.81}_{-0.67}$	$1.87^{+0.34}_{-0.32}$
$e^+e^- \to qqqq$	$0.98^{+0.51}_{-0.40}$	$5.48^{+0.92}_{-0.85}$	$8.25^{+0.46}_{-0.45}$
$e^+e^- \to l\nu_l l\nu_l$	$0.39^{+0.43}_{-0.27}$	$1.93^{+0.74}_{-0.60}$	$1.53^{+0.25}_{-0.23}$

Table 8.3: **Cross sections of the processes $qq\mu\nu$, $qq\tau\nu$, $qqqq$ and $l\nu l\nu$ measured at centre of mass energies of 161, 172 and 183 GeV. The errors are statistical only.**

The statistical error on the cross section measurement is the Poissonian statistical error on the number of selected events. The results for the cross section measurements are compared in Figure 8.1 with the Standard Model expectations. The data confirm the Standard Model calculation. The values obtained by excluding the triple gauge vertices ZWW and γWW or the ν_e t channel diagram are clearly too high.

8.2.1 Systematic errors on the cross section measurement.

The systematic errors on the measurement of the cross section are related to the selection efficiency and to the background contamination. For example in the cuts using the energies we have to take into account the calibrations of the detector, in the reconstruction of the W mass we have to consider the real value of M_W. The most important source of systematic error comes from the selection. At $\sqrt{s} = 183$ GeV the statistics is big enough to permit a calculation of this error by varying the cuts applied around their nominal value to evaluate the difference in the measured cross section as function of the variation of the cuts. Some examples of the variation of the cuts are shown in Figure 8.2. This error is added in quadrature to the other sources of systematic errors listed in table 8.4. For $\sqrt{s} = 161$ GeV, 172 GeV data,

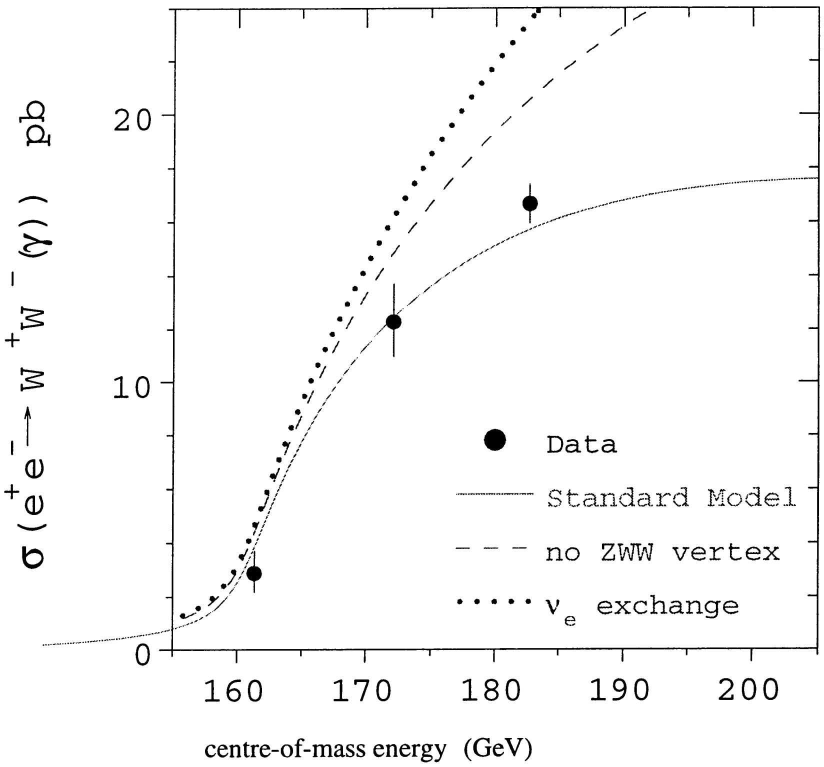

Figure 8.1: **The cross section, σ_{WW}, for the process $W^+W^- \to 4f$, as function of the centre-of-mass energy $\sqrt{s}$. The errors on the measurements are the combination of the statistical and systematic error, added in quadrature. The solid curve shows the Standard Model expectations. The dashed curve shows the expectations if there was no ZWW coupling. The dotted curve shows the expectations if only the t channel, ν_e exchange in W pair production is considered.**

due to the small statistics other methods have been used. For example systematics errors in the electron identification are derived from a comparison of data versus Monte Carlo using $e^+e^- \to e^+e^-(\gamma)$ as a control sample. Systematics errors on efficiency and accepted background cross sections are derived by comparing different Monte Carlo event generators and Monte Carlo samples with different W masses and detector energy scales. The Figure 8.3 shows the distribution of the neutrino energy when only loose cuts are applied. A total systematic error of 5 % has been quoted for the cross section measurement at $\sqrt{s} = 161$ GeV for the semileptonic channels, at $\sqrt{s} = 172$ GeV the total systematic error for the same two channels has been estimated to be 3 %. Finally at $\sqrt{s} = 183$ GeV the total systematic error has been estimated to be 2 %. It has to be noticed that at all the three energies the systematic errors are negligible compared to the statistical ones.

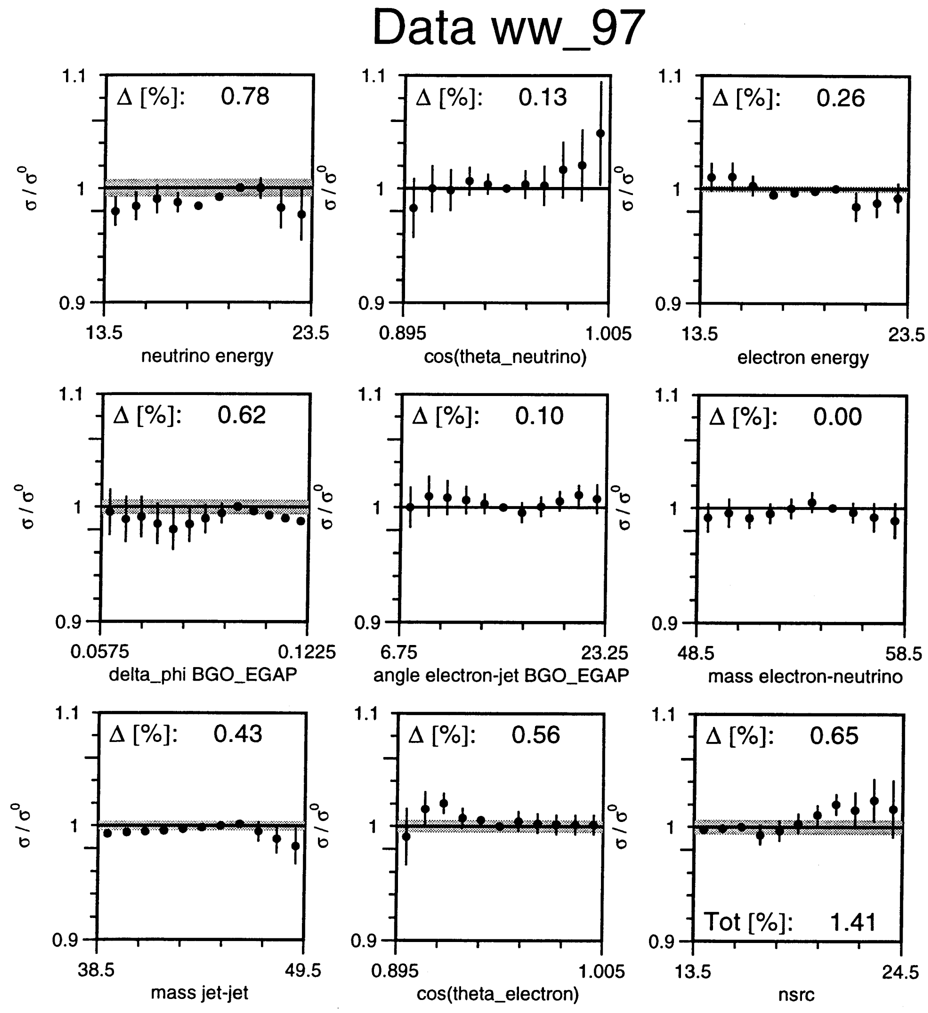

Figure 8.2: **Systematic errors due to the variation of the selection cuts. The y axis shows the ratio of the cross section calculated at the new value of the cut over the cross section calculated with the cut fixed at the nominal value.**

8.3 W mass measurement at $\sqrt{s}$ = 161 GeV from the cross section measurement.

As shown in Figure 4.2, the cross section $\sigma(e^+e^- \rightarrow W^+W^-)$ grows rapidly in the energy region just above threshold, therefore here it is sensitive to the value of the W mass. The measurement error on the W mass can be written as:

$$\Delta M_W = \left| \frac{dM_W}{d\sigma_{WW}} \right| \Delta\sigma_{WW} \tag{8.8}$$

which is obtained on the W mass from the measurement of the cross section as function of $\sqrt{s} - 2M_W$ (Figure 8.4) [26].

Sources	Systematic error (%)
$\Delta\phi_{TEC-BGO}$	0.8
TEC efficiency	0.1
BE correlation	0.4
ΔM_W	0.5
E_{jet} smearing 5 %	0.2
E_e smearing 2 %	0.05
Angle jets smearing 2°	0.5
MC statistics	0.25
EGAP efficiency	0.05
cut variation	1.41
total	2

Table 8.4: **Different contributions to the systematic error on the W cross section measurement at 183 GeV for $e^+e^- \to W^+W^- \to qqe\nu$.**

The errors in the cross section measurement are the statistical errors on the number of selected events (signal and background) and the systematic errors on the evaluation of the selection efficiency and on the evaluation of the background cross section. These errors propagate on the W mass precision as:

$$\begin{aligned}
\Delta M_W &= \left(\mid \frac{dM_{WW}}{d\sigma_{WW}} \mid\right) \left[\frac{\sigma_{bkg}}{\epsilon\sqrt{\mathcal{L}}} \oplus \frac{\Delta\sigma_{bkg}}{\epsilon}\right] && (a) \\
&\oplus \left(\sqrt{\sigma_{WW}} \mid \frac{dM_W}{d\sigma_{WW}} \mid\right) \frac{1}{\sqrt{\epsilon\mathcal{L}}} && (b) \\
&\oplus \left(\sigma_{WW} \mid \frac{dM_W}{d\sigma_{WW}} \mid\right) \frac{\Delta\epsilon}{\epsilon} && (c) \qquad (8.9)
\end{aligned}$$

where the sign $\oplus$ indicates the sum in quadrature of the different independent contributions. The statistical error from the number of signal events, $\sqrt{\epsilon\mathcal{L}}$, has been separated from the statistical error from the background events $\sigma_{bkg}/\epsilon\sqrt{\mathcal{L}}$. With a luminosity of 10 pb^{-1}, collected at $\sqrt{s} = 161$ and $\sqrt{s} = 172$ GeV, the most important contribution to the error on the W mass comes from the statistical error on the number of signal events. The corresponding sensitivity factor is shown in Figure 8.4, curve (b), which has a minimum of 0.89 $GeVpb^{-1/2}$ at $(\sqrt{s})^{opt} = 2M_W + 0.5$ GeV, therefore to minimise this error LEP did the measurement at $\sqrt{s} = 161.0$ GeV, the value calculated using the world average of the W mass available in 1996. To minimise the contribution from the background the minimum value of the derivative $\mid \frac{dM_W}{d\sigma_{WW}} \mid$ has to be calculated, it is 0.45 $GeV\ pb^{-1}$ (curve a) for $\sqrt{s} \sim 2M_W + 1.2$ GeV.

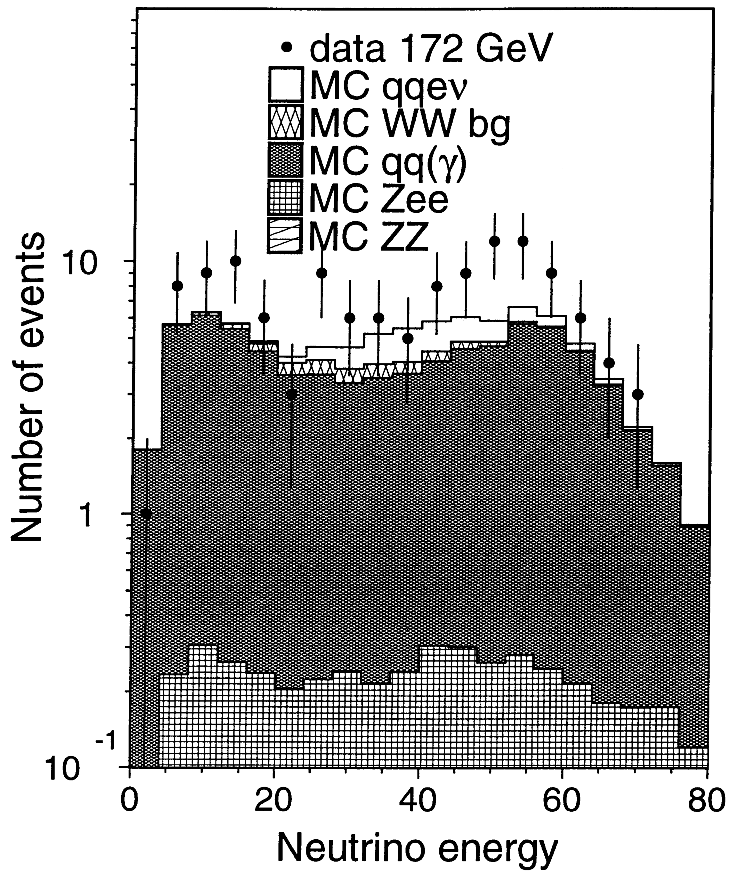

Figure 8.3: **Distribution of the neutrino energy in the $qqe\nu$ channel at $\sqrt{s} = 172$ GeV when only loose cuts are applied, to compare data and Monte Carlo background distributions.**

The error on M_W introduced by an uncertainty in the W width Γ_W is

$$\Delta M_W = \left| \frac{dM_W}{d\sigma} \right| \left| \frac{d\sigma}{d\Gamma_W} \right| \Delta\Gamma_W \simeq 0.16\Delta\Gamma_W \tag{8.10}$$

where the value of the derivative corresponds to $\sqrt{s} = 161$ GeV. In the Standard Model

$$\Gamma_W = 2.080 \left(\frac{M_W}{80.26GeV}\right)^3 . \tag{8.11}$$

If we use the world average value of the W mass, $M_W = 80.33 \pm 0.15$ GeV, the $\Delta\Gamma_W = 12$ MeV. In contrast the value of the width measured at the Tevatron is $\Gamma_W = 2.07 \pm 0.06$ GeV consistent with the Standard Model calculation but with a much larger error. If we use the Standard Model value of the width then the contribution (2 MeV) to ΔM_W is negligible.

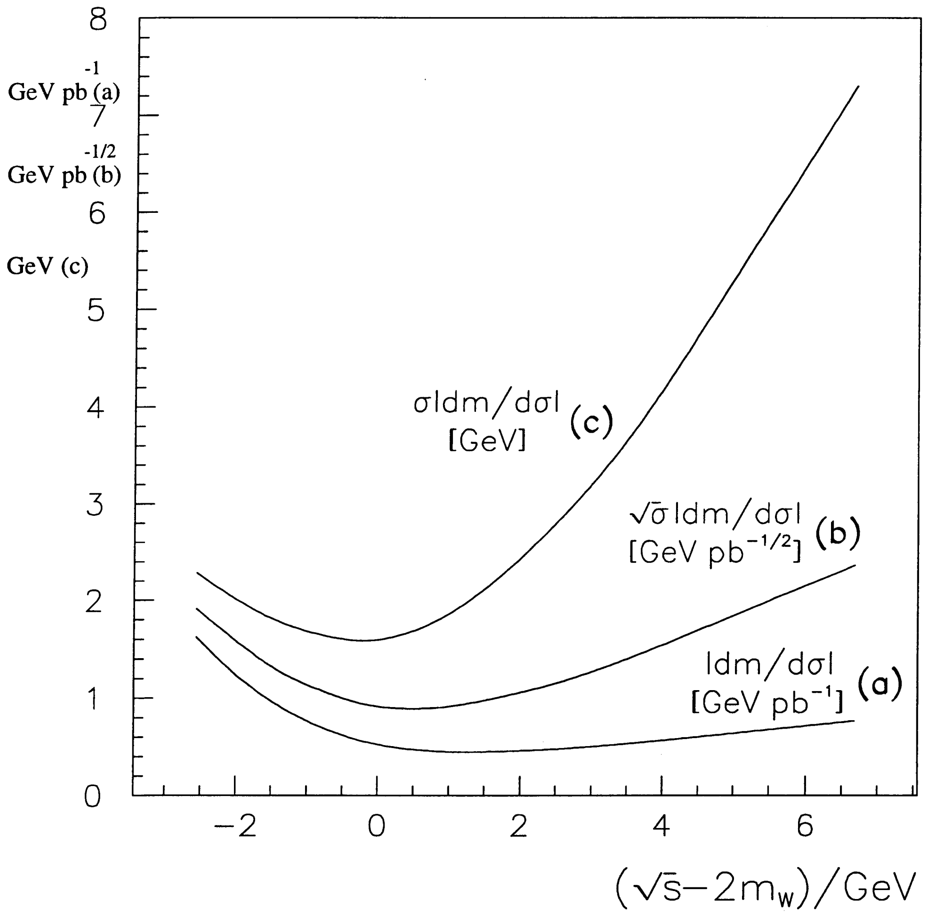

Figure 8.4: **Different contribution to the M_W error (Eq. 8.9). The curve (a) shows the contribution of the uncertainty on the cross section due to the background contamination. The curve (b) shows the uncertainty on the number of selected events. The curve (c) shows the contribution coming from the uncertainty on the selection efficiency. The errors have been estimated for an integrated luminosity of 100 pb^{-1} at $\sqrt{s} = 161$ GeV.**

8.3.1 Results.

To measure M_W the cross section fit to the data taken at $\sqrt{s}$ =161 GeV, is repeated with the cross section σ_j of the Equation 8.4 replaced by the function $\sigma_i(\sqrt{s}, M_W)$ leaving the W mass as the only free parameter. The semianalitical program GENTLE [39] has been used for the channels $qq\mu\nu$, $qq\tau\nu$ and $qqqq$ for which only the CC03 diagrams are important. For the channels $qqe\nu$ and $l\nu l\nu$ for which we have to consider also the other diagrams, we have used the program EXCALIBUR [32]. The measured W mass at $\sqrt{s}$ = 161 GeV is:

$$\mathbf{M_W = 80.80^{+0.48}_{-0.42}(exp.) \pm 0.03(LEP) \ \ GeV} \tag{8.12}$$

The experimental error contains the systematic (±0.08) and statistical (+0.47 -0.41) errors coming from the cross section measurement. The LEP error indicates the systematic error on the measurement of the beam energy [92]. The Figure 8.5 shows the cross section with the measured errors and the Standard Model expectations as function of the W mass, which allows the measurement of M_W.

8.3.2 Systematic error on the W mass measurement.

The total systematic error on the W mass measurement is given by

1. the selection efficiency and the background contamination described in 8.2.1;

2. the theoretical uncertainty on the σ_{WW}, calculated with the program GENTLE [39], which has a precision of the order of 2%. This corresponds to an error of 35 MeV on the W mass;

3. the measurement of the energy of the beams. The beam energy is measured near threshold with an error of 27 MeV.
   The contribution to the error on the W mass coming from the LEP energy measurement is expressed by the relation:

$$\Delta M_W = \left(-2\frac{dM_W}{d\sigma_{WW}} \frac{d\sigma_{WW}}{d\sqrt{s}} \right) \Delta E_b. \tag{8.13}$$

   The terms in the parentheses is about 1 at threshold energy. In the Appendix A a detailed discussion on the importance of the beam energy measurement at LEP, and its impact on the W mass measurement, will be given.

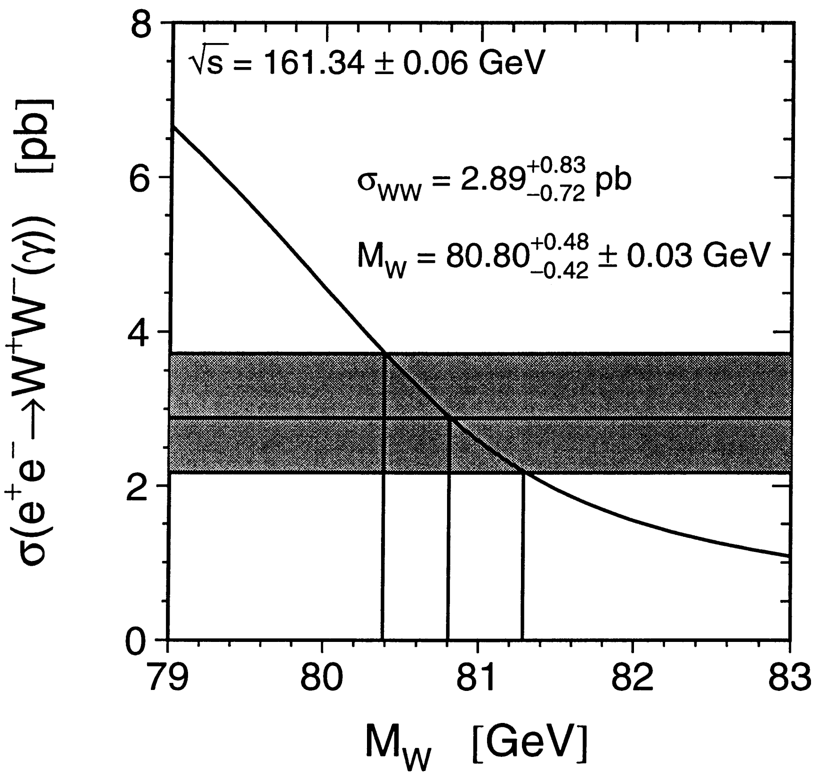

Figure 8.5: **The cross section, σ_{WW}, for the process $W^+W^- \to 4f$, as a function of the W mass, M_W. The curve shows the Standard Model expectation. The horizontal band shows the cross section measurement with its total error.**

Chapter 9

Measurement of the W mass at $\sqrt{s} = 172$ and 183 GeV.

9.1 Introduction

In this Chapter we present a short description of the kinematical fit, the method used to measure the mass and the width of the W boson and finally the results obtained at energies above the threshold.

9.2 The kinematical fit.

At energies above the threshold of the W production, the W boson mass is obtained by reconstructing the four-vectors of the two fermions in which the W decays and by calculating the W effective mass. The distribution of the reconstructed W mass at this level has not the correct W width because of the experimental resolution. Therefore it is necessary to perform a kinematic fit to improve the resolution of the W mass.

The function which describes the W mass distribution is a Breit-Wigner which, smeared by the finite resolution on the energy and momentum measurements, acquires in the experiment a gaussian profile.

The fit of the hypothesis $e^+e^- \to W^+W^-$ is done imposing the energy-momentum conservation on the event and the constraint that there are two equal masses, a "5C" fit. The constraint of the two equal masses, can be exact or can take into account the width of the two W's. The constraint of two equal masses improves dramatically the resolution on the W mass and plays a role in background rejection. In fact, if this condition is not applied the reconstructed mass of the two particles are strongly

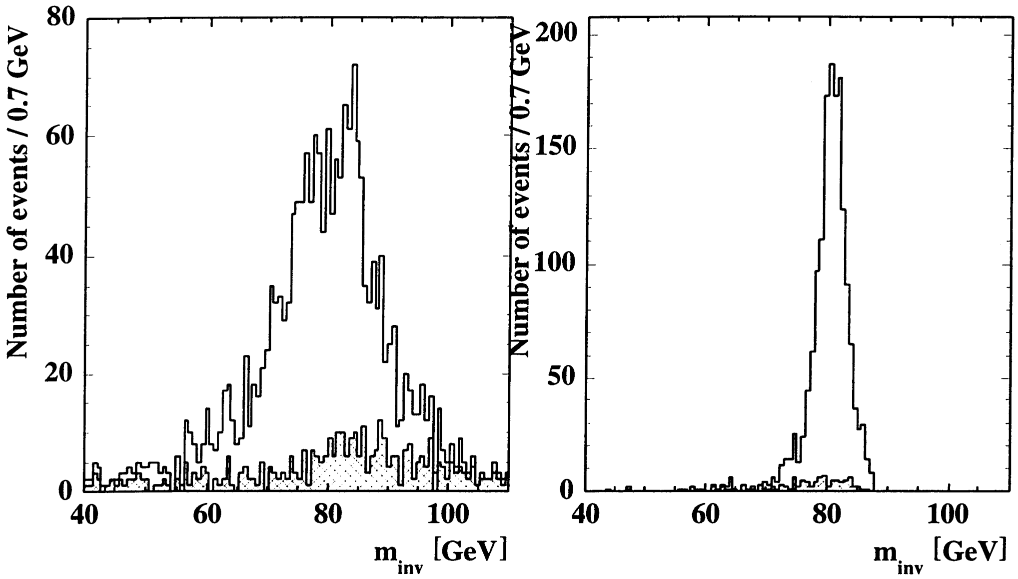

Figure 9.1: **Distribution of the invariant mass before and after the kinematic fit for $qqe\nu_l$ events.**

anti-correlated, especially in the semileptonic channel, where part of the energy of the hadrons can escape the detection and therefore be assigned to the neutrino. In this case, the invariant mass of the $q\bar{q}$ system is systematically underestimated and the mass $l\nu_l$ systematically overestimated. The fit is performed by minimising χ^2:

$$\chi^2 = \sum^{n}(x_i - \mu_i)^2/\sigma_i^2 \tag{9.1}$$

where in our case x_i represent the four-vectors energy-momentum, the azimuthal angle ϕ and the polar angle θ for the four particles in the final state. The errors on the jet four-vectors are extracted from the data or from the Monte Carlo under the hypothesis that they are uncorrelated, and that the error matrix is diagonal. This assumption is a bit too simple, because the fragmentation, the detector effects, and the way in which the particles are associated in a jets, introduce some correlations. The estimate of the non-diagonal elements is too complicated to be justified at the actual level of statistical precision. The error on the lepton parameters can be extracted from data or from Monte Carlo and can depend on the energy and on the position, these errors are uncorrelated therefore they give a diagonal matrix. These correlations are till now considered as systematic uncertainties.

In Figure 9.1 the invariant mass distribution for the semileptonic channel with an electron is shown, before and after the kinematic fit.

From the two distributions we can see that the mass resolution improves from $\sim$

10 GeV to a value which corresponds almost to the width of the W boson. In the purely hadronic channel $W^+W^- \to q\bar{q}q\bar{q}$, there are three possible combinations to make the pairing of the jets. For this reason the kinematic fit is done on the three possible combinations and, if the constraint on the two masses is used, the χ^2 of the three possibilities is different and then can be used as a discriminator. We have chosen the pairing for which the kinematic fit has the lowest χ^2. This criterion is correct in 60 % of the cases. In 25 % of the cases the correct pairing is the one with the second best χ^2.

9.3 Fit for M_W and Γ_W using the box method.

The distribution of Figure 9.1b cannot be used directly to extract the W parameters, M_W and Γ_W, because in between the measurement and the theory there are still detector effects. The observed distribution of the invariant mass is the differential cross section:

$$\frac{d\sigma}{dm}(s; M_W, \Gamma_W) = \int dm' G(s; m', m) \frac{d\sigma}{dm'}(s; M_W, \Gamma_W) \tag{9.2}$$

where m is the mass obtained by the kinematic fit and G contains the detector effects.

It is too difficult to calculate analytically the function G. We use Monte Carlo programs to generate events with a given mass distribution, we pass them through the full chain of simulation and reconstruction programs to obtain the experimental distribution. One method to extract M_W and Γ_W from Equation 9.2 is the so called box method [93].

The Monte Carlo contains all the necessary information to establish a relation between generated $m_{(gen)}$ and reconstructed quantities $m_{(rec)}$ (Figure 9.2). The probability density to reconstruct from the decay products of the two W's a value of the mass m_{rec} is $dP = w dm_{rec}$:

$$\begin{aligned} w(m_{rec}, M_W) \quad &= \quad \frac{1}{\sigma_{WW}(M_W) + \sigma_{background}} \times \\ &\quad \left[\frac{d\sigma_{WW}}{dm_{rec}}(m_{rec}, M_W) + \frac{d\sigma_{background}}{dm_{rec}}(m_{rec}) \right] \end{aligned} \tag{9.3}$$

where M_W is the mass we want to measure, σ_{WW} and $\sigma_{background}$ are the cross sections for the signal and for the background respectively. To take into account the selection effects the cross sections have to be measured within the selection cuts.

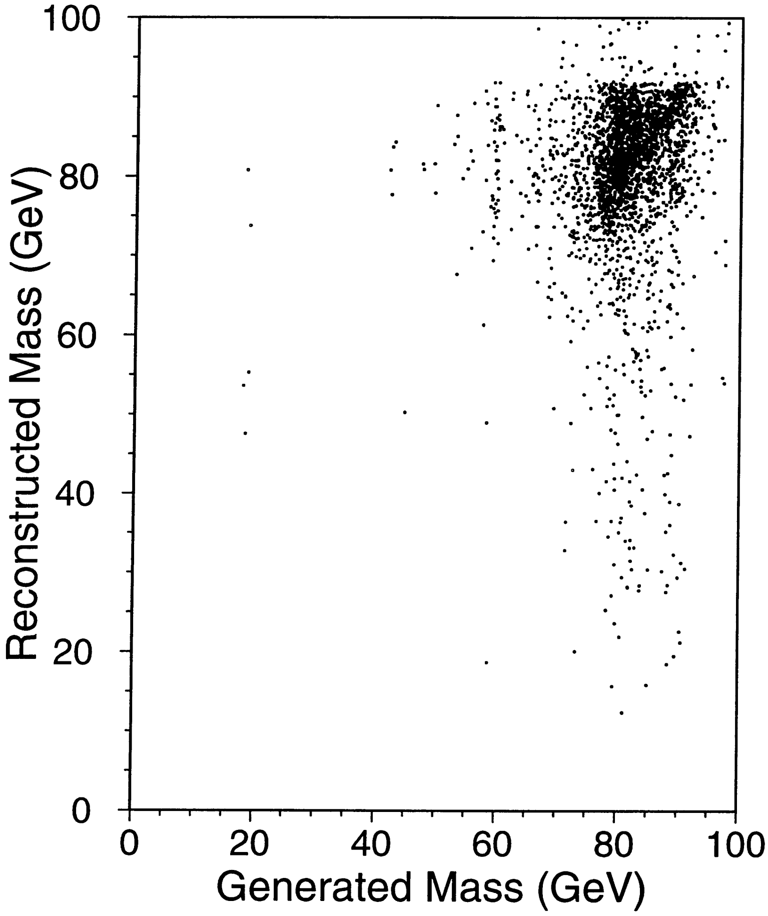

Figure 9.2: M_W **reconstructed mass as function of generated mass.**

Using this probability density, we write a maximum likelihood function:

$$L(M_W) = \Pi_j w(m_{rec}^{data}(j), M_W) \tag{9.4}$$

where $m_{rec}^{data}(j)$ is the value of the reconstructed mass of the event j.
The value $d\sigma_{WW}/dm_{rec}$ is obtained by counting the number of Monte Carlo events which are in a box, in the plane (m_{gen}, m_{rec}), around the value $m_{rec}^{data}(j)$:

$$\frac{d\sigma_{WW}}{dm_{rec}}(m_{rec}^{data}(j)) \sim \frac{1}{\mathcal{L}_{MC}} \times \frac{n_{box}^j}{V_{box}^j} \tag{9.5}$$

where

- $\mathcal{L}_{MC} = integrated\ Monte\ Carlo\ luminosity = \frac{Number\ of\ total\ Monte\ Carlo\ events}{total\ Monte\ Carlo\ cross\ section}$
- $V_{box}^j = volume\ around\ m_{rec}^{data}(j)\ (box)$
- $n_{box}^j = number\ of\ Monte\ Carlo\ events\ within\ V_j$

The total cross section, is the sum over all the volumes:

$$\sigma_{WW} = \Sigma_j \frac{n_{box}^j}{\mathcal{L}_{MC}} \tag{9.6}$$

The way to choose the volume is very important, in fact the volume has to be small enough to see the structure of the function $d\sigma_{WW}/dm_{rec}$; but it has to be big enough to contain a statistically significant number of events. The simplest way is to choose volumes with constant dimensions symmetric with respect to the measured value of the $m_{rec}(j)$. In this way, for volumes far from the peak of the distribution, the number of Monte Carlo events is small. A solution is the choice of asymmetric volumes, of fixed dimension, in such a way that the integral of the function, on the left and on the right side of m_{rec} is constant. Alternatively, one can use volumes with variable dimensions, but such that the integral of the function is the same per each volume. The advantage, in this case, is that the number of events is the same in each volume, but on the tails of the distribution the volumes become too big.
Once the dimension of the volume is fixed, we can construct $d\sigma_{WW}/dm_{rec}$ using the Equation 9.5.
To perform a fit with M_W as parameter we should be able to calculate $d\sigma_{WW}/dm_{rec}$

for each value of the W mass. This would mean to have one Monte Carlo fully simulated and reconstructed per each value of the M_W with a reasonable number of events. This is practically impossible, but a way out is to use the technique of Weighted Monte Carlo events.

The most important hypothesis for this method is that the differential cross section has always the same behaviour with respect to M_W, then once it is calculated for a given value of the W mass, M_W^0, the distribution can be shifted to a new value of M_W'.

The Monte Carlo contains information on the generated quantities therefore it is possible to obtain a new Monte Carlo with mass M_W' re-weighting the events of the original one. At the end we have to generate and reconstruct only one Monte Carlo and all the others used to extract the weight are only generated. Then we define:

$$\frac{d\sigma_{WW}}{dm_{rec}}(m_{rec}^{data}(j), M_W) = \frac{1}{\mathcal{L}_{MC}} \times \frac{1}{V^j} \Sigma_k \frac{w_k(M_W)}{w_k(M_W^0)} \tag{9.7}$$

where w_k is the weight of each Monte Carlo event.

The weight can represent different quantities:

- the double differential cross section with respect to the two W's

$$w_k = \frac{d^2\sigma(m_1^k, m_2^k)}{dm_1 dm_2} \tag{9.8}$$

- the differential cross section with respect to the mean value of the mass

$$w_k = \frac{d\sigma}{dm_{rec}}(m_{rec}^j) \tag{9.9}$$

- the matrix elements of the invariant amplitude $\mid \mathcal{M} \mid^2$

In the first two cases, the calculation can be done using the semianalytical program GENTLE [39]; in the last case the matrix elements can be obtained directly from generators like KORALW [31] or EXCALIBUR [32].

To summarise the procedure we start using the maximum likelihood function defined in Equation 9.4 to perform a fit of the parameter M_W. With the box method we reconstruct the function $d\sigma_{WW}/dm_{rec}$, as in Equation 9.5. Then varying the parameter M_W we recalculate $d\sigma_{WW}/dm_{rec}$, but this can be done directly using the Monte Carlo. With Monte Carlo programs the probability density as function of M_W is defined, for each experimental event. This is done for all Monte Carlo events with known generated mass and with a reconstructed mass within a fixed interval around each data event. With such density the maximum likelihood function is maximised as function of the free parameter M_W. For each selected event the value of the W mass used in the fit is the one obtained from the kinematic fit imposing the constraint of two equal masses. The interval is chosen in such a way to have an almost constant number of events ($\sim$ 1000 events) per interval. For this reason the variation of the reconstructed mass has been fixed in intervals from $\pm$ 35 MeV, in the peak region, to $\pm$ 250 MeV, in the tail regions.

9.3.1 Results for M_W and Γ_W.

Using the data obtained at $\sqrt{s}$ = 172 and $\sqrt{s}$ = 183 GeV, the W mass has been determined for each of the decay channels; then a combined fit has been performed to obtain the W mass in the $qql\nu$ channel, and for all the channels together. In the combined fits, the maximum likelihood function is the product of the functions for the single channel. The results of the fit at 172 GeV are listed in table 9.1. The same

Process	M_W(GeV)
$e^+e^- \to qqe\nu$	$80.25^{+0.68}_{-0.70} \pm 0.09$
$e^+e^- \to qq\mu\nu$	$80.94^{+1.15}_{-1.33} \pm 0.08$
$e^+e^- \to qq\tau\nu$	$80.43^{+1.07}_{-1.06} \pm 0.09$
$e^+e^- \to qql\nu$	$80.42^{+0.53}_{-0.55} \pm 0.07$
$e^+e^- \to qqqq$	$80.91^{+0.41}_{-0.44} \pm 0.13$
$e^+e^- \to 4f$	$80.71^{+0.34}_{-0.35} \pm 0.09$

Table 9.1: **Values of the W mass, with the direct reconstruction method, for all the decay channels, at 172 GeV. The first error is the statistical, the second is the systematic.**

results for the semileptonic channels are also shown in Figure 9.3. In the Figure 9.4 the reconstructed W masses for the first two pairings in the $qqqq$ channel are shown. The two values of M_W obtained in the semileptonic channel ($qql\nu$) and the hadronic one ($qqqq$), are in agreement with each other.
With all the channels combined together the value of the W mass is

$$\mathbf{M_W = 80.71^{+0.34}_{-0.35}(stat.) \pm 0.09(syst.)\ \ GeV.} \tag{9.10}$$

The systematic errors are listed in table 9.2.

The initial state radiation (ISR) is a source of systematic error because it is not taken into account in the box fit.

Source	$qqe\nu$	$qq\mu\nu$	$qq\tau\nu$	$qqqq$
Beam energy	30 MeV	30 MeV	30 Mev	30 MeV
ISR	10 MeV	10 MeV	10 MeV	10 MeV
Hadronization	40 MeV	40 MeV	40 MeV	40 MeV
Fit method	55 MeV	30 MeV	30 MeV	30 MeV
FSI(CR+BE)	-	-	-	100 MeV
Background	25 MeV	15 MeV	50 MeV	15 MeV
Calibrations	30 MeV	20 MeV	-	10 MeV
Monte Carlo statistics	40 MeV	40 MeV	40 MeV	40 MeV
Total	**90 MeV**	**80 MeV**	**90 MeV**	**130 MeV**

Table 9.2: **Systematic errors for the determination of the W mass, for the different final states. The contributions in the top part have been considered correlated in the combined fit between different channels at $\sqrt{s} = 172$ GeV.**

The fit can be done at the same time for the mass of the W and for its width (Figure 9.5). The results of this fit, for the leptonic and the hadronic channel and for their combination, are listed in table 9.3 and the systematic errors are listed in table 9.4:

Process	M_W	Γ_W	Correlation coefficient
$e^+e^- \to qql\nu_l$	$80.43^{+0.64}_{-0.58} \pm 0.07$	$2.76^{+1.93}_{-1.46} \pm 0.28$	+0.33
$e^+e^- \to qqqq$	$80.94^{+0.35}_{-0.36} \pm 0.13$	$1.21^{+0.77}_{-1.20} \pm 0.33$	+0.11
$e^+e^- \to 4f$	$80.72^{+0.31}_{-0.33} \pm 0.09$	$1.74^{+0.88}_{-0.78} \pm 0.25$	+0.27

Table 9.3: **Results of the fit to the mass of the W boson and to its width, in the last column the correlation coefficient at $\sqrt{s} = 172$ GeV is reported.**

$$M_W = 80.72^{+0.31}_{-0.33}(stat.) \pm 0.09(syst.)\ GeV \tag{9.11}$$

$$\Gamma_W = 1.74^{+0.88}_{-0.78}(stat.) \pm 0.25(syst.)\ GeV. \tag{9.12}$$

The W mass is in agreement with the previous one obtained with the threshold method. Combining the 161 and the 172 GeV measurements we obtain the value:

$$\mathbf{M_W = 80.75^{+0.26}_{-0.27}(exp.) \pm 0.03(LEP)\ \ GeV.} \tag{9.13}$$

The results for the W mass measurement, at 183 GeV are listed in table 9.5 and the systematic errors are listed in table 9.6. The Figure 9.6 shows the invariant mass

Source	$qql\nu_l$	$qqqq$
Fit method	200 MeV	200 MeV
Background	90 MeV	200 MeV
Calibrations	50 MeV	50 MeV
Resolutions	150 MeV	150 MeV
Monte Carlo statistics	60 MeV	60 MeV
Total	**280 MeV**	**330 MeV**

Table 9.4: **Systematic errors on the determination of Γ_W for the different final states at $\sqrt{s} = 172$ GeV. The error coming from the method used is considered correlated in the combination of the different final states. The other contributions are taken as not correlated.**

Process	M_W(GeV)
$e^+e^- \to qqe\nu$	80.01 ± 0.32
$e^+e^- \to qq\mu\nu$	80.23 ± 0.41
$e^+e^- \to qq\tau\nu$	80.50 ± 0.51
$e^+e^- \to qql\nu$	80.09 ± 0.23
$e^+e^- \to qqqq$	80.59 ± 0.19
$e^+e^- \to 4f$	80.40 ± 0.15

Table 9.5: **Values of the W mass, with the direct reconstruction method, for all the decay channels, at 172 and 183 GeV. The error is statistical.**

distribution after the fit for all the decay channels combined together. The results of the fit of the W mass together with his width are listed in table 9.7. The combined fit of the W mass and width give the following result

$$M_W = 80.41 \pm 0.15(stat.) \pm 0.09(syst.)\ GeV \tag{9.14}$$

$$\Gamma_W = 2.41 \pm 0.39(stat.) \pm 0.25(syst.)\ GeV \tag{9.15}$$

with a correlation coefficient of +14% between M_W and Γ_W. Combining the measurement at 172 GeV with the measurement at 183 GeV we obtain for the W mass:

$$\mathbf{M_W(qql\nu) = 80.09 \pm 0.23(stat.) \pm 0.07(syst.)\ \ GeV} \tag{9.16}$$

$$\mathbf{M_W(qqqq) = 80.59 \pm 0.19(stat.) \pm 0.13(syst.)\ \ GeV} \tag{9.17}$$

Within the statistical accuracy there is no significant difference between M_W from the semileptonic decay channel and from the purely hadronic one. The contribution

Source	$qql\nu$	$qqqq$	$4f$
Beam energy	30 MeV	30 MeV	30 MeV
ISR	10 MeV	10 MeV	10 MeV
Hadronization	40 MeV	40 MeV	40 MeV
Fit method	30 MeV	30 MeV	30 MeV
FSI(CR+BE)	-	100 MeV	60 MeV
Uncorrelated	40 MeV	60 MeV	35 MeV
Total	**70 MeV**	**130 MeV**	**90 MeV**

Table 9.6: **Systematic errors for the determination of the W mass at $\sqrt{s} = 183$ GeV, for the different final states. The contributions in the top part have been considered correlated in the combined fit between different channels.**

Process	M_W	Γ_W	Correlation coefficient
$e^+e^- \to qql\nu_l$	$80.16 \pm 0.26 \pm 0.07$	$3.12 \pm 0.69 \pm 0.28$	+0.30
$e^+e^- \to qqqq$	$80.58 \pm 0.18 \pm 0.13$	$1.85 \pm 0.46 \pm 0.33$	+0.12
$e^+e^- \to 4f$	$80.41 \pm 0.15 \pm 0.09$	$2.41 \pm 0.39 \pm 0.25$	+0.14

Table 9.7: **Results of the fit to the mass of the W boson and to its width, in the last column the correlation coefficient at $\sqrt{s} = 183$ GeV is reported.**

to the systematic error from the hadronization is due to the fact that the reconstruction of the W mass is based on the principle that the hadronization of the two W's is completely independent and this is not true in the real life. Effect of Bose-Einstein (BE) [94] correlations can be present for the hadronic channel between two pions of the same charge coming from two different W's. It has been suggested also that the hadronization time can be long enough to make possible the strong interaction between the two different hadronic system (colour reconnection, CR [45, 46]). This effect is not completely described by the perturbative QCD, there are different models trying to describe it, but it is not known at the moment which one is the best. The Figure 9.7 shows the 68 % and 95 % C.L. contours in the plane M_W, Γ_W, for the combined results at 172 and 183 GeV data. Combining all the channels together

$$\mathbf{M_W = 80.40 \pm 0.15(stat.) \pm 0.09(syst.)\ \ GeV.} \tag{9.18}$$

In order to determine also the total decay width of the W boson, Γ_W is treated as an independent parameter instead of imposing the Standard Model value. For all final states combined the result is:

$$\mathbf{M_W = 80.41 \pm 0.15(stat.) \pm 0.09(syst.)\ \ GeV} \tag{9.19}$$

$$\mathbf{\Gamma_W = 2.41 \pm 0.39(stat.) \pm 0.25(syst.)\ \ GeV.} \tag{9.20}$$

Our results on M_W and Γ_W are in agreement with the measurements obtained at $p\bar{p}$ colliders ($M_W = 80.33 \pm 0.15$ GeV, $\Gamma_W = 2.07 \pm 0.06$ GeV [5, 18]) and with the indirect measurement obtained at LEP1 at the Z peak ($M_W = 80.329 \pm 0.041$ GeV) and with the Standard Model expectations. The precision we obtain for the W mass is similar to the one obtained at $p\bar{p}$ colliders.

9.3.2 Results on colour reconnection and Bose-Einstein correlation.

The small difference between the W mass measured using only the semileptonic channel or only the hadronic one (Equations 9.16, 9.17), can come from effects like the colour reconnection or Bose-Einstein correlations (FSI). Such effects can increase the W mass by up to 100 MeV, a value obtained from studying Monte Carlo generators with different implementations of these effects [26, 38].

Bose-Einstein correlation.

At LEP energies the typical separation between W^+ and W^- in $e^+e^- \to W^+W^-$ events is smaller than 0.1 fm, which is much smaller than the source radii of 0.5 fm. Therefore one can expect that pions from different W's can be subject to Bose-Einstein correlations.
The BE correlations can be described in terms of a correlation function

$$C(k_1, k_2) = \frac{\rho(k_1, k_2)}{\rho_0(k_1, k_2)} \tag{9.21}$$

where k_1 and K_2 are the four-momenta of the two pions, ρ is the measured density for two identical bosons and ρ_0 is the two particle density in the absence of BE correlations. Experimentally this can be expressed in terms of

$$Q^2 \equiv (k_1 - k_2)^2 = M^2_{(\pi\pi)} - 4M^2_W \tag{9.22}$$

where M is the invariant mass of the two pions.
The correlation function can be written as:

$$C(Q) = \frac{\rho(Q)}{\rho_0(Q)}. \tag{9.23}$$

If the pion source is assumed to have a Gaussian shape in the rest frame of the pion pair, $C(Q)$ can be parametrised as:

$$C(Q) = 1 + \lambda e^{-Q^2R^2} \tag{9.24}$$

where λ represents the strength of the correlations and its value is between 0 and 1. R is related to the size of the pion.

The correlation $C(Q)$ is determined as the ratio between the differential cross section for pairs of like-charged pions and the differential cross section for pairs in a 'reference sample' which should not contain BE correlations and would have a differential cross section equal to that of the like-charged pairs.

The data collected at $\sqrt{s} = 183$ GeV are analysed. The like and unlike sign pairs are formed taking all the combinations for different jets in an events in which the two W's decay hadronically. Then using events generated with PYTHIA Monte Carlo the fraction of pairs coming from the same W is estimated in each bin of Q. The ratio of like-sign pairs to unlike-sign pairs is shown in figure 9.8. The solid line represents the fit to the data and the result of this fit is

$$\lambda = 0.88 \pm 1.14.$$

The value obtained is compatible with zero correlation strength λ. With the present statistics we can not conclude whether there is Bose-Einstein correlation in like-sign pion pairs originating from different W's or it is absent.

Colour reconnection.

To study the effects of colour reconnection, the charged particle multiplicity in the hadronic final state of $qql\nu$ channel and $qqqq$ channel are studied. The tracks are reconstructed in the central tracking chamber, then corrections for selection and acceptance effects, detector inefficiencies and ISR are applied. In $qql\nu$ events the lepton is subtracted in order to calculate the track multiplicity for the hadronic system only.

The selection criteria for the tracks are the following:

- at least one reconstructed track is requested;

- transverse momentum of the tracks greater than 100 MeV;
- radial distance of closest approach to the interaction point, DCA, lower than 10 mm;
- number of hits greater than 25.

The background is subtracted using the track multiplicities predicted by Monte Carlo for the background events. The Figure 9.9 shows the track multiplicity for hadronic and semileptonic events compared to KORALW predictions where there is no special QCD effect. The track multiplicity distribution is transformed in charged particle multiplicity distribution by unfolding it with the matrix $P(N_p, N_t)$, obtained form Monte Carlo events. $P(N_p, N_t)$ represents the probability to select N_t tracks when N_p charged particles were generated. Charged particles are considered stable hadrons if they have a lifetime bigger than 3.3×10^{-10} s , otherwise they can decay. The average charged particle multiplicity is found to be: 36.4 ± 0.4 for $qqqq$ events and 18.8 ± 0.3 for $qql\nu$ events to be compared to KORALW predictions of 37.2 ± 0.03 and 18.6 ± 0.02 respectively.
Another approach is to study the distribution of the scaled track momentum $x_p = 2p/\sqrt{s}$ of each track corrected for acceptance, selection effects and ISR. The Figure 9.10 shows the average charged multiplicity as function of x_p. By integrating the x_p distribution the following results are obtained 35.9 ± 0.4 for $qqqq$ events and 18.8 ± 0.3 for $qql\nu$ events.
A result on the average charged particle multiplicity is obtained from the two methods:

$$< N_{ch}^{qqqq} >= 36.1 \pm 0.4(stat.) \pm 0.8(syst.) \tag{9.25}$$

$$< N_{ch}^{qql\nu} >= 18.8 \pm 0.4(stat.) \pm 0.4(syst.) \tag{9.26}$$

Systematic errors arise from track selection and Monte Carlo simulation of the reconstructed tracks.
The difference between the charged particle multiplicity measured in $qqqq$ and twice the multiplicity of $qql\nu$ events is

$$\Delta < N_{ch} >= -1.5 \pm 0.8(stat.) \pm 0.5(syst.). \tag{9.27}$$

This result is statistically consistent with 0, as expected if the two W bosons in $qqqq$ events fragment and hadronize independently of each other.

9.3.3 Fit of the Standard Model.

The value of the W mass obtained from LEP1 (table 3.2) can be compared with the value of the direct measurements. Figure 9.11 shows that the prediction of the Standard Model are well in agreement with the direct measurements. As can be seen the indirect measurements prefer low values for m_{top} and M_H. The value of the W mass measured at LEP2 can be included in the fit described in Chapter 1 together with the measured top quark mass, to constrain the value of the Higgs mass.
The following W mass is extracted when using in the fit the W mass measured at LEP combining the result at $\sqrt{s} = 161$ GeV and the result at $\sqrt{s} = 172$ GeV (both already published):

$$M^{EW\ fit} = 80.375 \pm 0.030 GeV \tag{9.28}$$

The Higgs boson mass obtained is:

$$M_H = 115^{+116}_{-66}\ GeV \tag{9.29}$$

The results of this fit are listed in table 9.8, including the measurement of the m_{top} and M_W. In Figure 9.12 $\Delta\chi^2 \equiv \chi^2 - \chi^2_{min}$ is plotted as function of M_H. The lower

Parameters	Results of the fit
$\alpha_s(M_Z^2)$	0.120 ± 0.003
m_t	173.1 ± 5.4
M_H	115^{+116}_{-66}
M_W(GeV)	80.375 ± 0.030
χ^2/DoF	14/12
	Derived quantities
$sin^2\theta^{lept}_{eff}$	0.23152 ± 0.00022
$1 - m_W^2/m_Z^2$	0.2231 ± 0.0005

Table 9.8: **Results for $\alpha_s(M_Z^2)$, m_t, M_H and M_W from the fit to the electroweak data including m_t and M_W. The bottom part shows the results for $sin^2\theta^{lept}_{eff}$ and $1 - m_W^2/m_Z^2$. The values of α_s and of m_{top} are in agreement with the world average $\alpha_s(M_Z^2) = 0.118 \pm 0.003$ [20], $m_{top} = 174.1 \pm 5.4$ [11, 12, 95].**

limit on the Higgs mass from direct searches has not been used in this fit. New results on direct searches for the Higgs mass give a limit at 87.6 GeV [8]. The region excluded by the Higgs searches is indicated in Figure 9.12 by the vertical band. The shaded band show the uncertainty due to the missing high order corrections. Taking this error into account yields the one sided 95 % C.L. upper limit of $M_H < 420$ GeV. Some improvements have been done in the last months; first of all we can include in the fit the W mass measured at LEP2 at $\sqrt{s} = 183$ GeV (not yet published); then a big improvement comes from higher order radiative correction calculations on the mass of the top quark. Finally a new preliminary result of $sin^2\theta_{eff}^{lept} = 0.23084 \pm 0.00035$ from SLD [96], combining data from 1992 to 1997 is available. Including all this in the fit gives a 95 % C.L. upper limit of $M_H < 215$ GeV (PRELIMINARY) [95]. This result is shown in Figure 9.13.

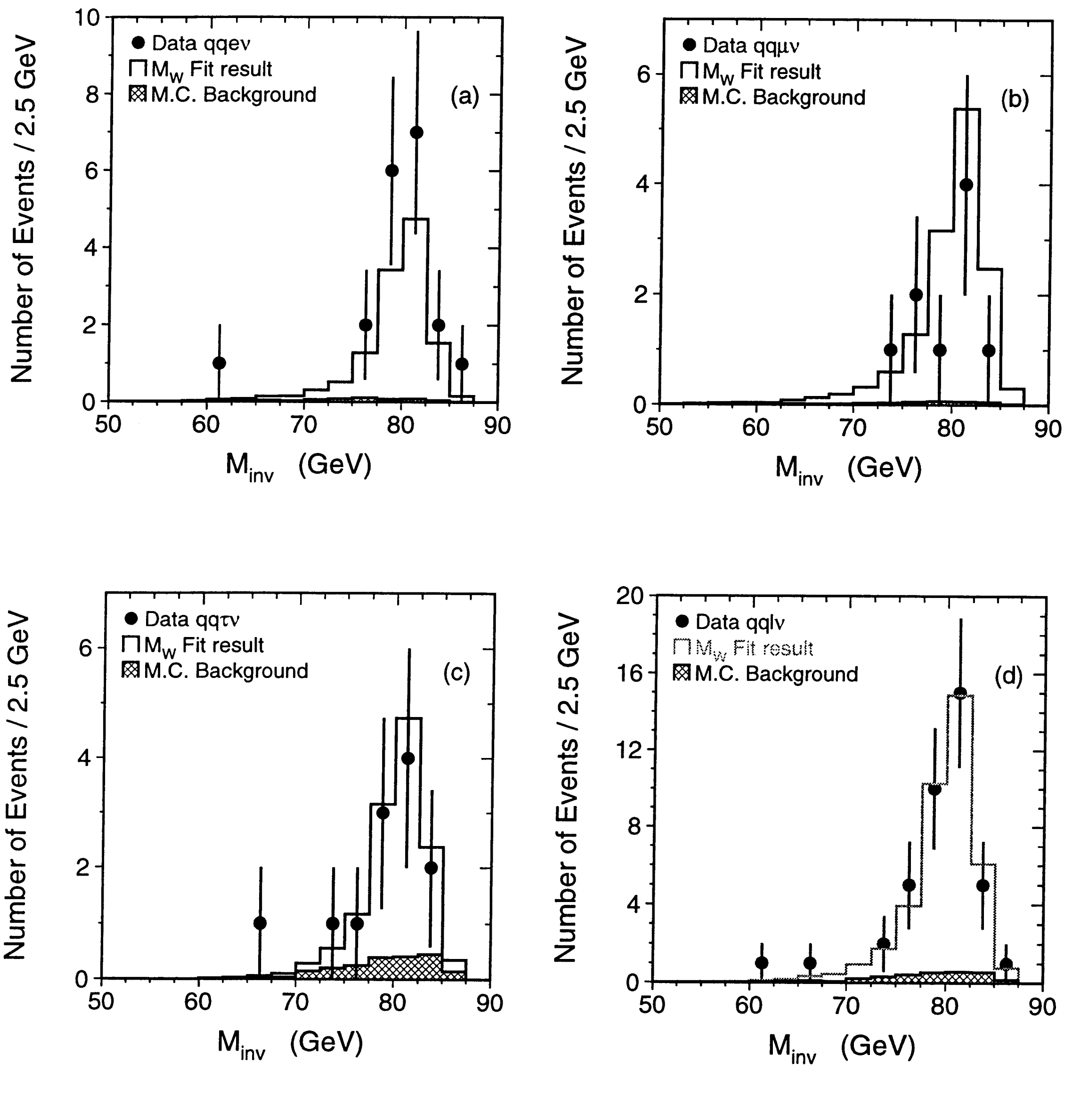

Figure 9.3: **Distribution of the invariant mass of a fermion pair for the $qqe\nu$, $qq\mu\nu$, $qq\tau\nu$ channels and for the combination of the three. The invariant mass is obtained by a kinematic fit using the equal-mass constraint. The solid lines show the results of the combined fit on M_W at 172 GeV.**

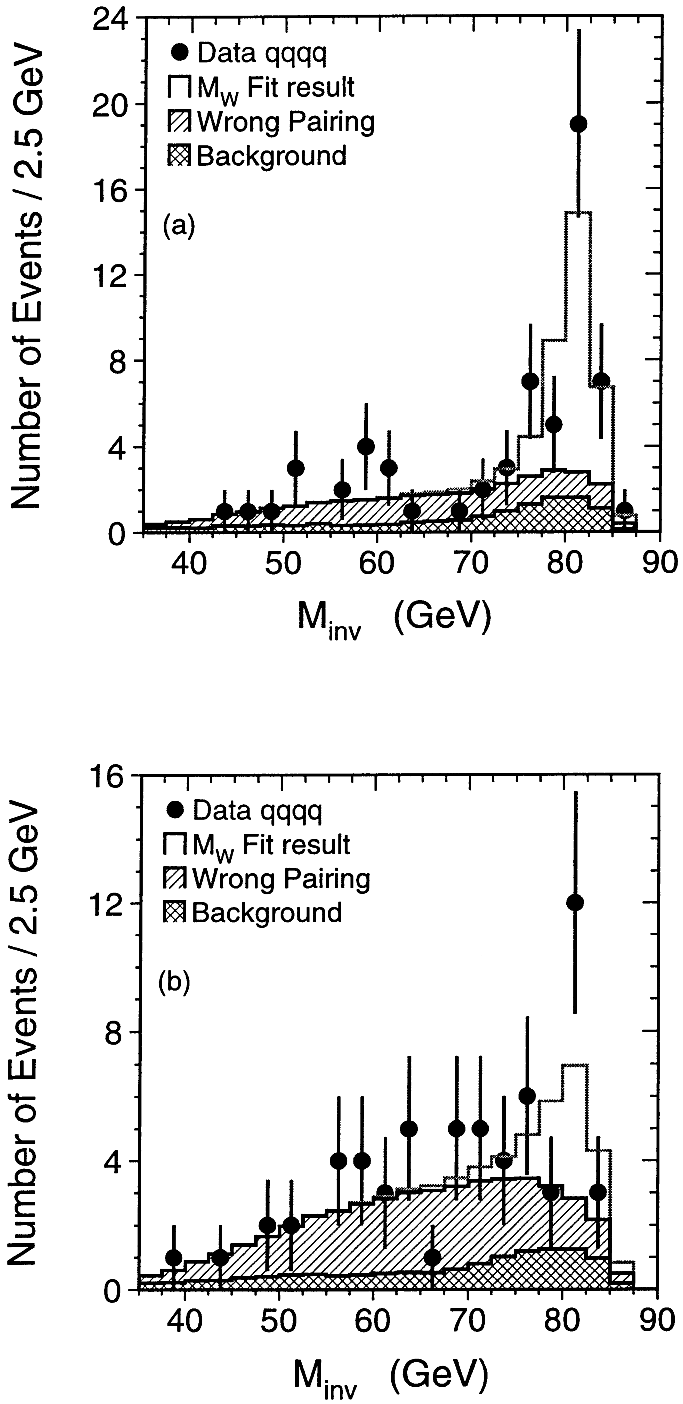

Figure 9.4: **The invariant mass obtained in** $qqqq$ **events by a kinematic fit, is shown for the jet pairing which gives the best** χ^2 **(a) and the second best jet pairing (b). The solid line represents the result of the fit at** $\sqrt{s} = 172$ **GeV.**

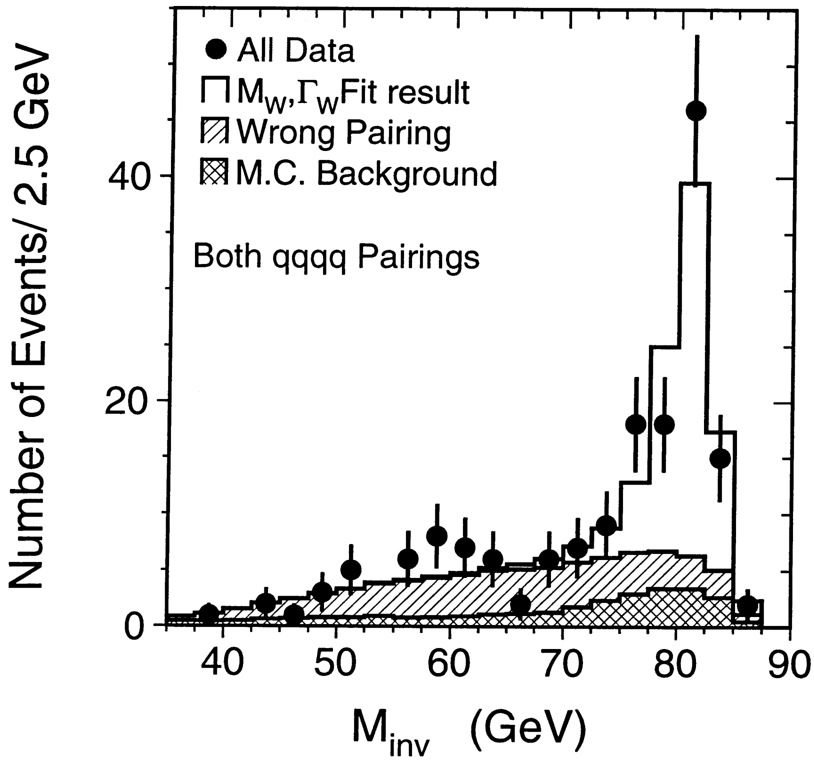

Figure 9.5: **Result of the fit of the W mass, M_W, and of its width Γ_W together at 172 GeV for all the channels combined together.**

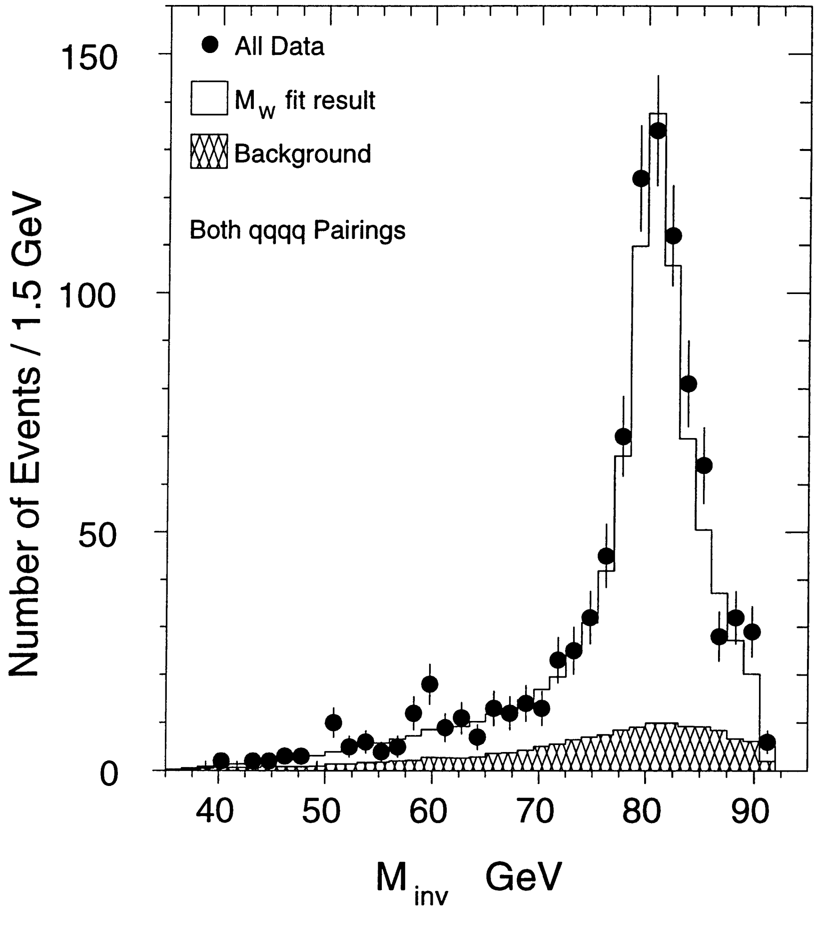

Figure 9.6: **Result of the fit of the W mass, M_W at 183 GeV for all the decay channels combined together. For the $qqqq$ channel the first and the second pairing are used.**

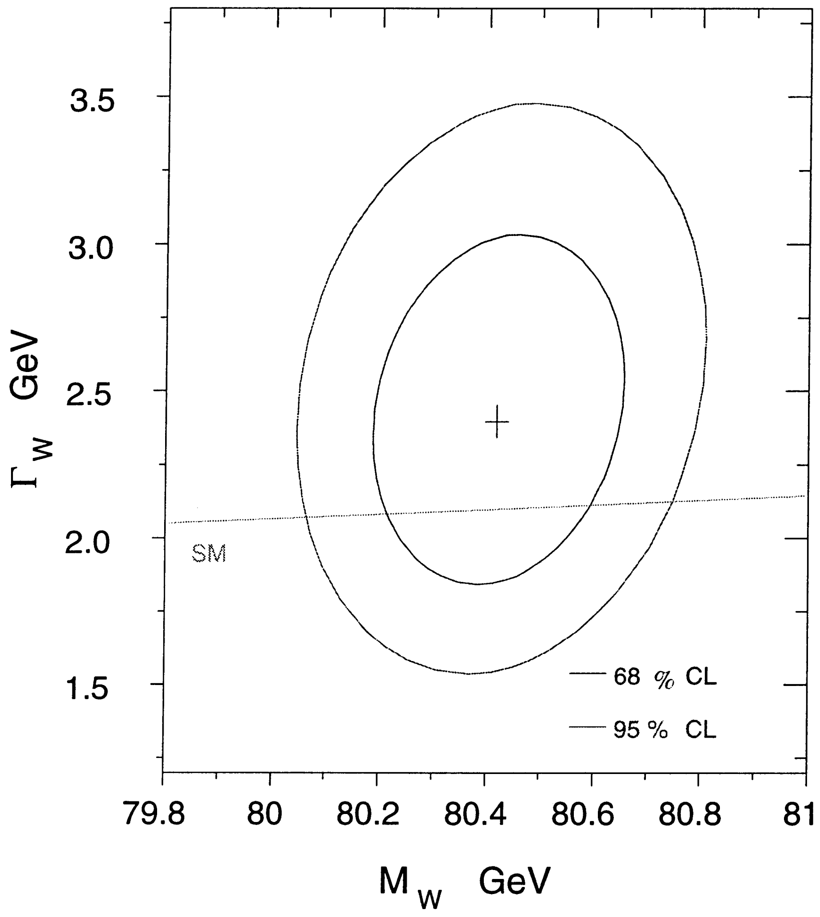

Figure 9.7: **Contour curves of 68 % and 95 % probability in the (M_W,Γ_W) plane from a fit to the combined 172 and 183 GeV data. The Standard Model dependence of Γ_W on M_W is shown as the line.**

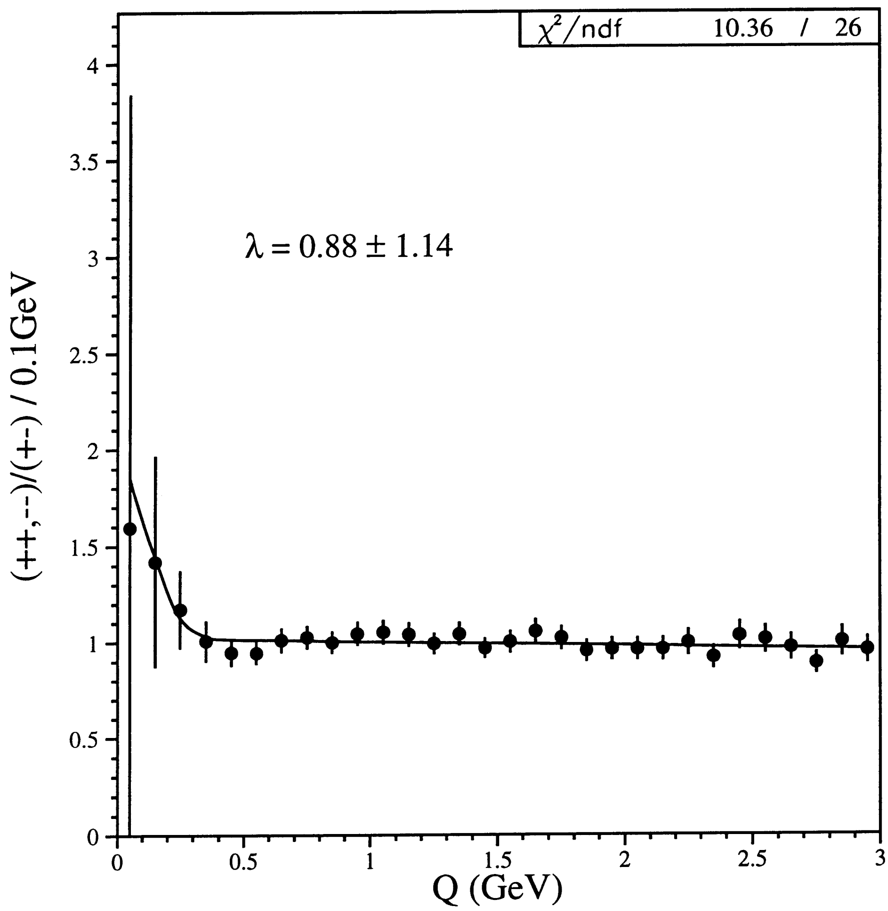

Figure 9.8: **Ratio of the like-sign pion pairs to unlike sign pion pairs. The solid curve represents the result of the fit.**

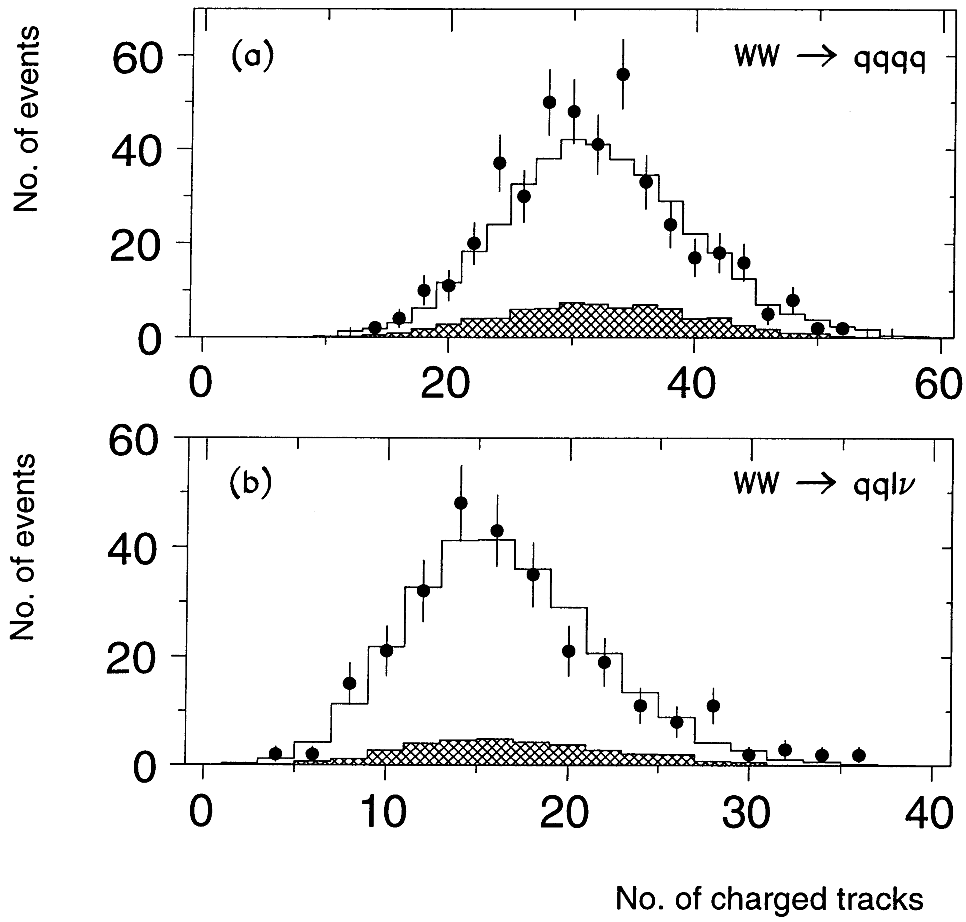

Figure 9.9: **Uncorrelated charged track multiplicity for $W^+W^- \to qqqq$ and $W^+W^- \to qql\nu$ events at $\sqrt{s} = 183$ GeV.**

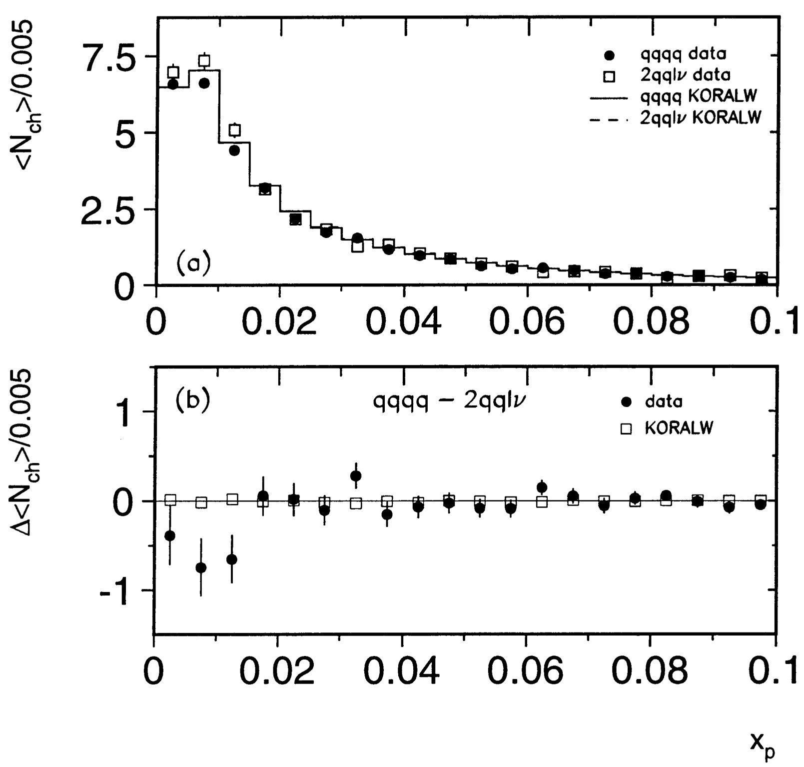

Figure 9.10: **Average charged particle multiplicity as function of a scaled particle momentum x_p, for $qqqq$ and $ql\nu$ events at 183 GeV (a). Difference in average charged particle multiplicity between $qqqq$ and $qql\nu$ events as function of x_p. The $qql\nu$ data and Monte Carlo are scaled by a factor of 2.**

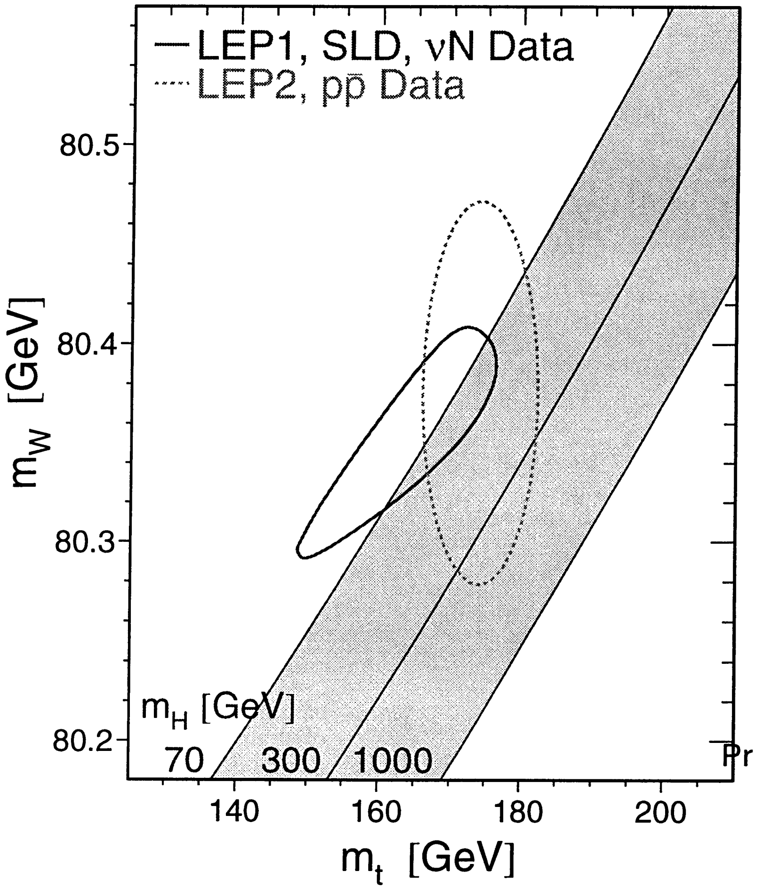

Figure 9.11: **Mass of the W as function of the top mass. Comparison of the indirect measurements (LEP + SLD + νN data) and the direct measurements (TEVATRON + LEPII data). In both cases 68 % CL contours are plotted. The bands indicates the variation of the Higgs mass from 70 to 1000 GeV.**

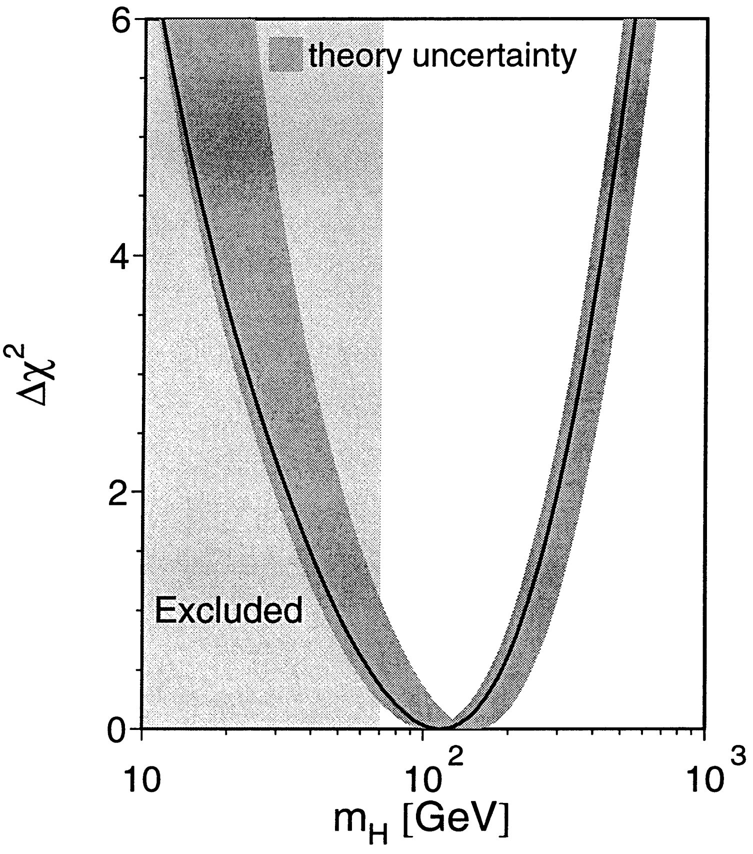

Figure 9.12: $\Delta\chi^2 \equiv \chi^2 - \chi^2_{min}$ **as function of** M_H. **The line is the result of the fit using all data. The band represents an estimate of the theoretical error due to the missing higher order corrections.**

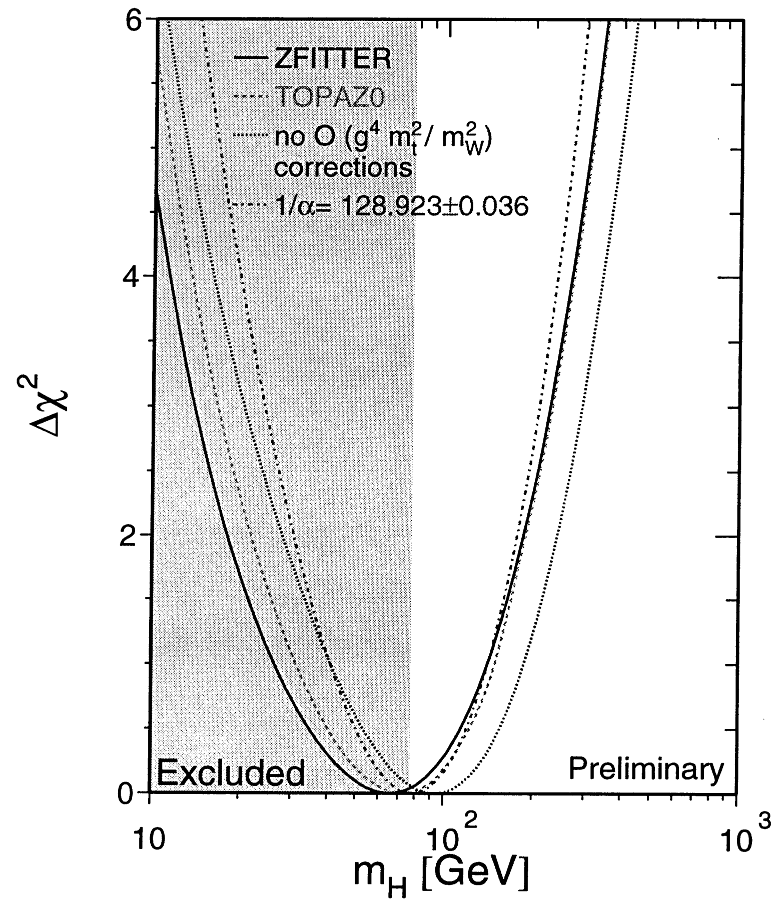

Figure 9.13: $\Delta\chi^2 \equiv \chi^2 - \chi^2_{min}$ **as function of** M_H**. The line is the result of the fit using all data. We can clearly see the improvement when using the new version of the ZFITTER program (continuous line) including the higher order corrections to the top mass and the old result (pointed line).**

Chapter 10

Conclusions

For the first time at LEP, in e^+e^- collisions, the threshold for the W production has been passed, allowing the observation of $W^\pm$ pairs and the measurement of the W mass and width.

In this thesis we have reported on the measurement of the W mass obtained by analysing the data collected by the L3 experiment at centre-of-mass energies of $\sqrt{s} = 161$ GeV, $\sqrt{s} = 172$ GeV and $\sqrt{s} = 183$ GeV. At LEP the $W^\pm$ bosons are produced via the process $e^+e^- \rightarrow W^+W^-$; the W's decay into quark anti-quark pair ($W \rightarrow q\bar{q}'$), or in a lepton neutrino pair ($W \rightarrow l\nu_l$).

The identification of the decay products of the W's is not easy because of the complicated nature of the hadronisation of the quarks in a jet, and in the case of semileptonic events because of the presence of the neutrino.

In this thesis we have described the selection of the all possible W decays, with particular attention to the semileptonic channel with an electron/positron in the final state ($W^+W^- \rightarrow qqe\nu$). In this channel, 4 events have been selected at $\sqrt{s} = 161$ GeV, 19 at $\sqrt{s} = 172$ GeV and 119 at $\sqrt{s} = 183$ GeV.

Near the threshold of W^+W^- production, which corresponds to a centre-of-mass energy of $\sqrt{s} = 161$ GeV, the cross section grows very rapidly: this makes it very sensitive to the value of the W mass on which it depends ($\sigma_{WW} = \sigma(\sqrt{s}, M_W)$). Using the events selected it is possible to make a likelihood fit of the cross section leaving as a free parameter the mass of the W. The result obtained with this method, for M_W is:

$$\boldsymbol{M_W = 80.80^{+0.48}_{-0.42}(exp.) \pm 0.03(LEP)\ \mathrm{GeV}.}$$

At energies higher than 161 GeV the cross section as function of the energy is rather constant and the the sensitivity to the W mass is reduced, making this method unusable.

At higher energies the mass of the W is reconstructed directly from the W decay products. The invariant mass distribution, $d\sigma_{WW}/dm$, allows a direct measurement of M_W and Γ_W.
Using this method with the data collected at 172 GeV, we obtain a value of the W mass of:

$$\boldsymbol{M_W = 80.71^{+0.34}_{-0.35}(stat.) \pm 0.09(syst.)\ \mathrm{GeV}.}$$

With the same method used at $\sqrt{s} = 183$ GeV we obtain:

$$\boldsymbol{M_W = 80.40 \pm 0.15(stat.) \pm 0.09(syst.)\ \mathrm{GeV}.}$$

Combining the high energy measurements with the $\sqrt{s} = 161$ GeV result in an extended maximum likelihood fit the result is:

$$\boldsymbol{M_W = 80.40 \pm 0.16(exp.) \pm 0.03(LEP)\ \mathrm{GeV}.}$$

The results obtained fitting the mass distributions separately for the hadronic and for the leptonic channel are:

$$\begin{aligned} \boldsymbol{M_W(ql\nu)} &= \boldsymbol{80.09 \pm 0.23(stat.) \pm 0.07(syst.)\ \mathrm{GeV}.} \\ \boldsymbol{M_W(qqqq)} &= \boldsymbol{80.59 \pm 0.19(stat.) \pm 0.13(syst.)\ \mathrm{GeV}.} \end{aligned}$$

Within the statistical accuracy there is no significant difference between M_W from the semileptonic decay channel and from the purely hadronic one. The contribution to the systematic error from the hadronization is due to the fact that the reconstruction of the W mass is based on the principle that the hadronisation of the two W's is completely independent and this is not true in the real life. Effects of Bose-Einstein (BE) [94] correlation can be present for the hadronic channel between two pions of the same charge coming from two different W's and also effect of colour reconnection [45].
In order to determine also the total decay width of the W boson, Γ_W is treated as an independent parameter instead of imposing the Standard Model value. For all final states combined the result is:

$$\begin{aligned} \boldsymbol{M_W} &= \boldsymbol{80.41 \pm 0.15(stat.) \pm 0.09(syst.)\ \mathrm{GeV}} \\ \boldsymbol{\Gamma_W} &= \boldsymbol{2.41 \pm 0.39(stat.) \pm 0.25(syst.)\ \mathrm{GeV}\ .} \end{aligned}$$

Our results on M_W and Γ_W are in agreement with the measurements obtained at $p\bar{p}$ colliders ($M_W = 80.41 \pm 0.09$ GeV, $\Gamma_W = 2.07 \pm 0.06$ GeV [5, 18]) and with the indirect measurement obtained at LEPI at the Z peak ($M_W = 80.329 \pm 0.041$GeV) and with the Standard Model expectations. The precision we obtain for the W mass is similar to the one obtained at $p\bar{p}$ colliders.
The value of the W mass measured at LEP2 can be included in the global fit of all electroweak measurements together with the measured quark top mass, to constrain the value of the Higgs mass.
The following W mass is extracted when using the measured W mass at LEP2 at $\sqrt{s} = 161$ GeV and at $\sqrt{s} = 172$ GeV (published results):

$$\boldsymbol{M^{EW\ fit} = 80.375 \pm 0.030\ \mathbf{GeV}}$$

The Higgs boson mass obtained is:

$$\boldsymbol{M_H = 115^{+116}_{-66}}\ \mathrm{GeV}$$

A 95 % C.L. upper limit of $M_H < 420$ GeV on the Higgs mass is also obtained.
Some improvements have been done in the last months; first of all we can include in the fit the W mass measured at LEP2 at $\sqrt{s} = 183$ GeV (not yet published), then a big improvement comes from higher order radiative correction calculations on the mass of the quark top. Finally a new preliminary result of $sin^2\theta^{lept}_{eff} = 0.23084 \pm 0.00035$ form SLD [96], combining data from 1992 to 1997 is available. Including all this in the fit gives a 95 % C.L. upper limit of $M_H < 215$ GeV (PRELIMINARY) [95]. This result is shown in Figure 9.13.

Appendix A

Appendix A: measurement of the LEP beam energy with the Møller scattering.

A.1 Introduction.

In this Appendix, we will describe the study we have done [97] on the Møller Scattering as a method to measure the beam energy at LEP2. At LEP1, the beam energy has been measured, with the Resonant Depolarization (RDP) [98] method with a precision of $\sim$ 1 MeV. This method is still used at LEP2, but the beam energy spread of 150 MeV at E_{beam} =90 GeV (compared to 37 MeV at E_{beam} = 45 GeV) is comparable to the separation of 440 MeV between two adjacent linear depolarising resonances, therefore the precision achieved is worse. In the absence of RDP at high energy, one possibility is to use the RDP up to the possible highest energy ($\sim$ 60 GeV) and then to extrapolate this measurement with the flux loop method [99]. With this procedure the error on the beam energy has been measured $\sim$ 30 MeV in 1996.

The error on the beam energy measurement is of course very important at LEP2 because it has an impact on the error on the W mass measurement. Different sources of errors propagating into the W mass uncertainty:

- systematic error due to theoretical and detector uncertainties, ΔM_W^{TD}, has been estimated to be 24 MeV.

- the combined statistical error of the four LEP experiments, is expected to be 25 MeV for an integrated luminosity of 500 pb^{-1}.

The systematic error on m_W from the flux loop extrapolation and from theoretical and detector effects are comparable so that the combined systematic error on the W mass is greater or of the order of the statistical error. If a big improvement on ΔE_{beam} ($\Delta E_{beam} \simeq$ 1-2 MeV) could be possible, its systematic contribution to the W mass error would be negligible.
One possibility to reduce the error on the measurement of the beam energy is the Møller Scattering method. We propose to cross calibrate the measurement with the flux loop method at lower energy and to perform a continuous monitoring of the electron beam with the Møller technique. The measurement is done in one interaction point of the machine, so that an extrapolation to the four interaction regions is necessary. However the same procedure is followed with the RDP method.

A.2 Description of the Møller scattering method.

The method is based on the elastic scattering of a beam of electrons or positrons of energy E_{beam} on an electron target. From the two body kinematics the following relation can be extracted:

$$E_{beam} = \frac{8m_e}{\theta_o^2} \cdot \frac{1}{1-k^2} - m_e \tag{A.1}$$

where m_e is the electron mass, θ_o is the opening angle between the two scattered electrons in the laboratory frame (A.1):

$$\theta_o \equiv tan\theta_1 + tan\theta_2 \tag{A.2}$$

θ_1 and θ_2 are the scattering angles of the two electrons with respect to the beam direction. The parameter k is the cosinus of the scattering angle of the electron in the centre of mass system ($k = cos\theta^*$), which can be written as:

$$k = \frac{tan\theta_1 - tan\theta_2}{tan\theta_1 + tan\theta_2} \tag{A.3}$$

$$k = \frac{E_{beam} + m_e}{E_{beam} - m_e} \cdot \frac{E_1 - E_2}{E_1 + E_2} \simeq \frac{E_1 - E_2}{E_1 + E_2} \tag{A.4}$$

where E_1, E_2 are the energies of the scattered electrons. The principle is to measure θ_0 and k and determine E_{beam} from the Equation A.1.

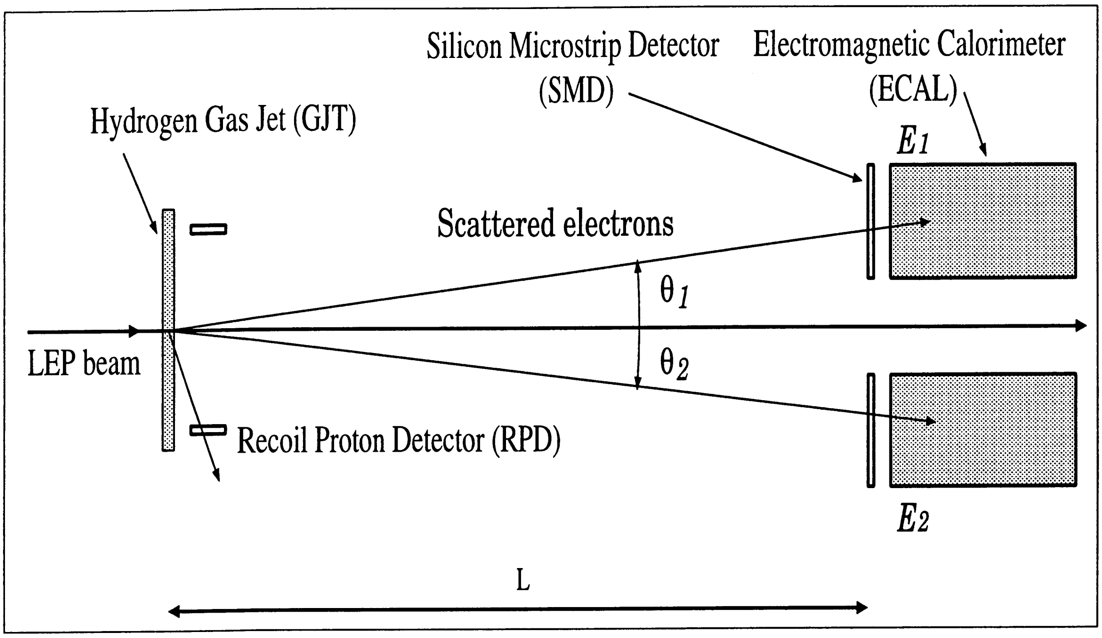

Figure A.1: **The Møller detector.**

The proposed detector is shown in Figure A.1. It consists of:

1. a hydrogen gas jet target (GJT) similar to the one used in the UA6 experiment [100]. The bound electrons of the atoms are the target;

2. a silicon microstrip detector (SMD) which cover the full azimuthal angle and the polar region from 2 to 10 mrad. It measures the (r, Φ) coordinates, of the two scattered electrons, in the plane transverse to the beams;

3. a high resolution electromagnetic calorimeter (ECAL) with a similar angular coverage of the SMD;

4. a recoil proton detector (RPD) consisting of a small planar silicon microstrip detector in vacuum, close to the GJT, to detect the recoil proton from the $e-p$ elastic scattering.

From the Figure A.1 one can see that the two electrons are detected in a almost symmetric configuration with $E_1 \simeq E_2 \sim E_{beam}/2$ and $\theta_1 \simeq \theta_2$. Two measurements are possible, depending on how the parameter k is determined. From now on the two methods will be indicated with A and B.

$$E_{beam} = E_A : \qquad k_A \equiv \frac{E_1 - E_2}{E_1 + E_2} \tag{A.5}$$

$$E_{beam} = E_B : \qquad k_B \equiv \frac{tan\theta_1 - tan\theta_2}{\theta} \tag{A.6}$$

where

$$tan\theta \equiv \frac{\sqrt{(x_1-x_2)^2+(y_1-y_2)^2}}{L} = \frac{l}{L}.$$

Indicating with (x_i, y_i) the coordinates of the impact points of the two electrons in the plane of the SMD and L the distance from the target to the SMD plane

$$tan\theta_i \equiv \frac{\sqrt{(x_i - x_0)^2 + (y_i - y_0)^2}}{L} = \frac{l_i}{L} \tag{A.7}$$

with (i= 1,2), where (x_0, y_0) is the position of the beam in the SMD coordinate system.
In the method A the beam energy is obtained using angle and energy measurements, and its determination is independent of the transverse beam position. The method B uses only angular information but the transverse beam position has to be known. The parameters of our model detector are listed in table A.1
From now on, we will indicate with SX a shift of the quantity X, due to some

L	30 m
SMD acceptance	2.00-6.00 mrad
ECAL acceptance	1.67-6.33 mrad
ECAL resolution	$\sigma_E/E = 3.37/E(GeV)^{1/4}\%$
Beam size	$\sigma_x = 1.54$, $\sigma_y = 0.34$ mm
Divergence	$\sigma'_x = 28.5$, $\sigma'_y = 5.0$ μrad
Energy spread	$\sigma_E = 145$ MeV (at $E_0 = 90$ GeV)

Table A.1: **Parameters of the model detector.**

systematic effect. It has a direct influence on the precision ΔX with which X can be measured. SX depends on measurable or calculable parameters, as for example the resolution of the ECAL, or the Fermi momentum of the electrons in the hydrogen atom. The aim of the simulation presented in the following sections is to measure the shift SX in terms of these parameters. From the Equation A.1 we can write

$$\frac{SE_{beam}}{E_{beam}} = -2\frac{S\theta}{\theta} + 2k_{obs}Sk - (Sk)^2 \qquad (A.8)$$

where k_{obs} is the measured k (k_A or K_B), $K_{obs} = K + S_K$.
From this relation we derive that to have a precision of 1 MeV for $E_{beam} = 90$ GeV, θ has to be known to 5 parts in 10^{-6}. This can be done taking under control the variation of l and L within some tolerances. The contributions to Sk are different for the two methods A and B. In the Method A the most important effects come from the finite energy resolution of the calorimeter and from the calibration gain error. In the method B the finite beam size and the uncertainty in the beam position are the major sources.

A.2.1 Statistical error.

The accepted Møller cross section, inside the considered solid angle, at 90 GeV, is 15.5 μb. With a LEP luminosity of $4 \times 10^{31} cm^{-2} s^{-1}$ the Møller event rate is 620 events per second. In two hours we can collect 4.5×10^6 events. The statistical error is determined by the spread of the reconstructed E_{beam} distribution. From Monte Carlo simulation this spread has been found to be $\sigma_E = 390$ MeV. For the number of events recorded in two hours the statistical error would be 0.18 MeV, which is sufficiently small compared to the 1-2 MeV of precision we want to reach with this method.
In order to quantify the contribution from statistical and systematic effects, a Monte Carlo study with realistic assumptions has been carried out. The following systematic effects have been studied: radiative corrections, Fermi motion, beam energy spread, beam size, beam angular divergence and ECAL resolution. The simulation has been done using the generator BHAGENE [86], in which the modification necessary for this study have been implemented.

A.2.2 Radiative corrections.

The effects of photon radiations have been investigated, Figure A.2 shows the Møller scattering Feynman diagram with the initial (ISR) and final state (FSR) radiations.

In the program BHAGENE there are up to two initial state photons generated and up to three final state photons. This is done using an improved soft photon approximation in the full angular phase space.

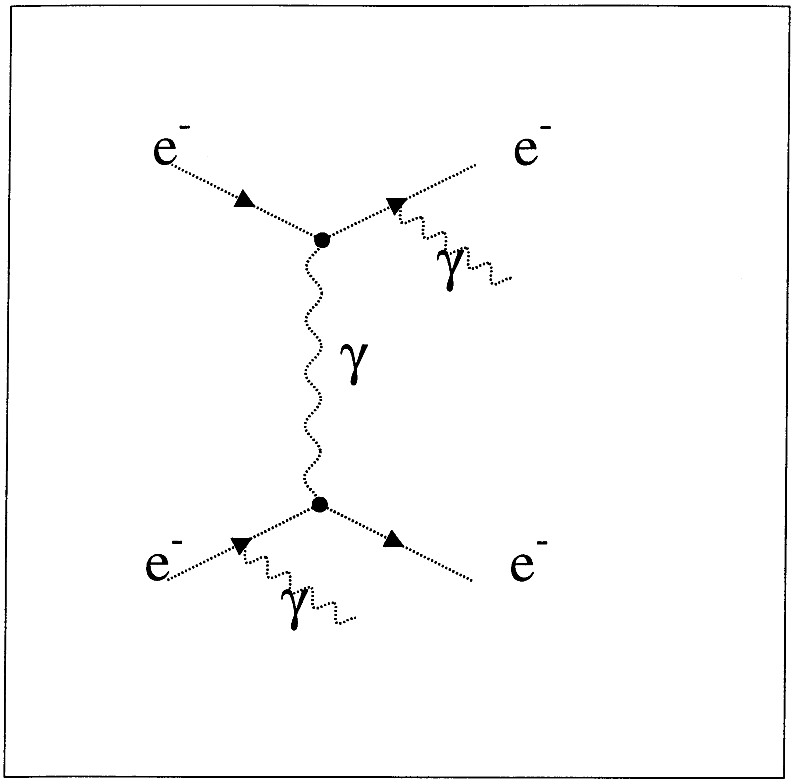

Figure A.2: **Møller scattering diagram with initial and final state radiation.**

The most important effects of the photon radiation are the following:

1. **ISR** collinear photons radiated from the beam or from the target are not observed in the detector and the reconstructed energy is lower than the beam energy. For the non collinear photons we have as a consequence that the angle between the plane defined by the scattered electrons and the beam direction is not zero, therefore $\theta \neq \theta_0$;

2. **FSR** collinear photons are detected in ECAL together with the scattered electrons, therefore the measurement of the energies E_1 and E_2 is not affected. Non collinear photons can lead to the same effect as for the ISR, if they are not detected the energy measurement is affected. The energies of the detected photons are added to the energy of the nearest electron.

A.2.3 Binding effects.

If a bound electron has Fermi momentum p_f, then the centre-of-mass energy is changed according to the relation

$$s' = s\left[1 - \frac{p_f}{m_e} cos\chi\right] \tag{A.9}$$

where χ is the angle between p_f and the beam direction. The modification of $\sqrt{s}$ causes the change of the opening angle θ. For a typical value of $p_f = 1/a_0 = 3.73$ KeV (a_0 is the Bohr radius), the shift on the beam energy is $\delta Ebeam/E_{beam} = \pm 3.6 \times 10^{-3}$. The increase in the width of the E_{beam} distribution is significant, but this shift averages to zero when integrated over $cos\chi$ and then the net shift, due to high order terms, is small.

A.2.4 ECAL resolution.

In the method A, the ECAL resolution σ_E propagates on the resolution of k_A as $\sigma_k = \sigma_E/\sqrt{2}$. The relative gain calibration error between different modules of the calorimeter corresponds to a shift of the parameter k. From Equation A.8, in particular from the third term ($S\bar{E}_{beam}/E_{beam} \simeq -S\bar{k}^2$) a good calorimeter is important to reduce the contribution from $S\bar{k}^2$. Today, in a BGO calorimeter, at 45 GeV a resolution of the order of 1% has been achieved. With such a resolution the shift due to the quadratic term in Sk of about 4.5 MeV would be present in the measurement of the beam energy. To correct for this effect with a precision of 1 MeV the ECAL resolution should be known with a relative accuracy of 10-20 %. The resolution can be controlled using the $e-p$ elastic scattering as described in next section. The gain calibration can be controlled using monitoring system, or again using the electrons from the $e-p$ elastic scattering.

A.2.5 Beam size and divergence.

In the method B the parameter k is defined by the Equation A.6. The main source of its shift are the uncertainties in the beam position and the finite transverse beam size. In the worst case, when the scattering plane is horizontal and the collision point is also displaced horizontally from its mean position, the shift in the beam energy is estimated to be 20 MeV at E_0= 90 GeV. To correct for this effect, in order to have a shift of 1 MeV, the beam size should be known with a relative precision of 5%. The way to achieve this precision is discussed in the following section.

A.2.6 Results of the simulation.

The reconstructed beam energy with the two methods, containing all the effects discussed above, is shown in Figure A.3. The shift due to each considered effect

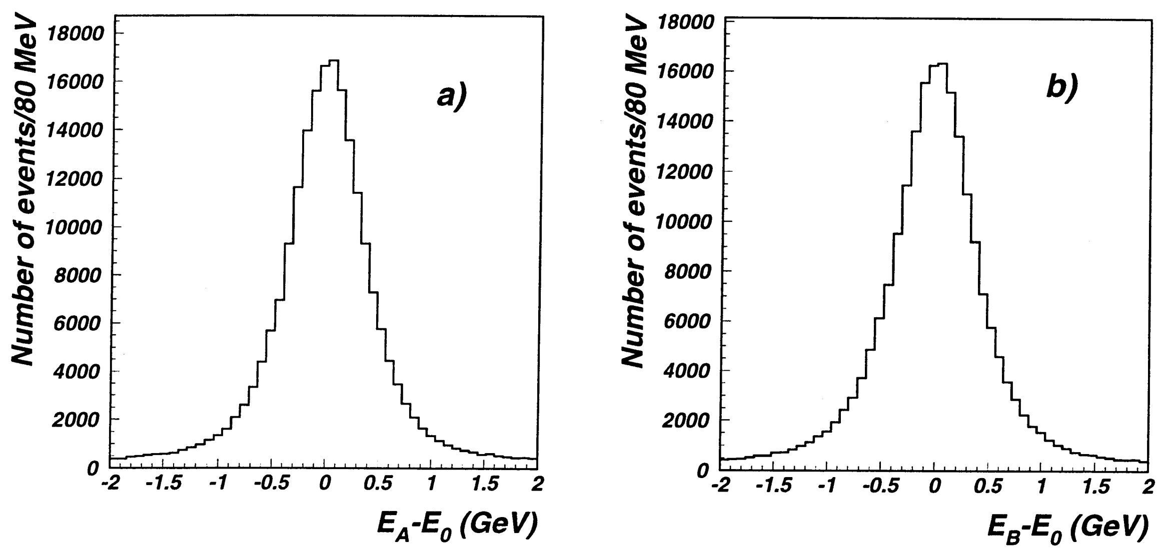

Figure A.3: **Effect of all systematic effects on E_A (a) and E_B (b) for $E_0 = 90$ GeV.**

has been estimated from the mean value of the corresponding distribution. The estimator used to evaluate the mean value is a mean of a truncated distribution, inside a window of 90 % or 95 % of the events. The systematics shifts due to the individual contributions for both methods A and B for E_0 =90 and 50 GeV are listed in table A.2. The results are shown for a sample of 2×10^6 simulated events, which corresponds, for a luminosity of $4 \times 10^{31} cm^{-2}s^{-1}$, to one hour of data taking. For the method A the most important contributions come from the ECAL resolution and from the Fermi motion, whereas for the method B the dominant effect is the finite beam size. The stability of the chosen procedure is shown in Figure A.4.

The changes in the mean energy for a different choice of window are $\simeq$ 1 MeV for the method A and $\simeq$ 2 MeV for the method B.

A.3 Calibration of important parameters.

Two important quantities have to be controlled: the distance L and the transverse beam size and position relevant for the method B.

Parameter	E_A 90 GeV	E_B 90 GeV	E_A 50 GeV	E_B 50 GeV
Radiative corrections	-0.2 ± 0.9	-0.03 ± 0.1	-0.1 ± 0.9	-0.05 ± 0.1
Fermi motion	-1.8 ± 0.3	-1.7 ± 0.3	-0.2 ± 0.1	-0.1 ± 0.1
Beam size	-0.2 ± 0.2	-8.8 ± 0.4	-0.06 ± 0.05	-0.8 ± 0.1
Beam divergence	-0.2 ± 0.2	-3.5 ± 0.2	0.06 ± 0.05	-0.2 ± 0.5
ECAL resolution	2.2 ± 0.3	-	0.3 ± 0.1	-
All effects	1.4 ± 0.4	-6.1 ± 0.4	2.2 ± 0.3	-2.9 ± 0.3

Table A.2: **Systematic shifts of the energy measurement $SE_i = \bar{E}_i - E_0$ in MeV where i is A or B for $E_0 = 90$ GeV and for $E_0 = 50$ GeV. The errors are statistical for a sample of 2×10^6 simulated events.**

A.3.1 Monitoring of the distance between the target and the detector, L, using the $e - p$ elastic scattering.

For a distance L of 30 m the accuracy on this parameter to achieve a precision of 1 MeV has to be 150 μm. It is possible to monitor continuously the mean value of the distance L using $e-p$ elastic scattering. The recoil proton is detected in coincidence with the scattered electron in the RDP. This can be done event by event, and the coordinate parallel to the beam direction of the proton hit in the RDP, z, can be measured with a precision of a fraction of a millimetre. The accuracy with which the mean value of z can be measured is completely dominated by the statistics. From the cross section of the $e - p$ elastic scattering, and from the number of events recorded in one hour we obtain a statistical error of 4.8 μm, which is an order of magnitude better than what we need for 1 MeV precision in the measurement of E_{beam}.

A.3.2 Monitoring of transverse beam profile using Møller events.

The monitoring of the transverse beam profile is important for the method B. The idea to monitor this parameter with the Møller events is the following: most of the electron pairs are coplanar with the beam direction, in the transverse plane the vertex position of an event lies on a straight line between the position of the electron in the SMD plane (Figure A.5). We can use this in two ways:

1. for a fast on-line monitoring. The intersection of the line between the two hit positions of the electrons with the nominal Y axis and X axis gives, to a good

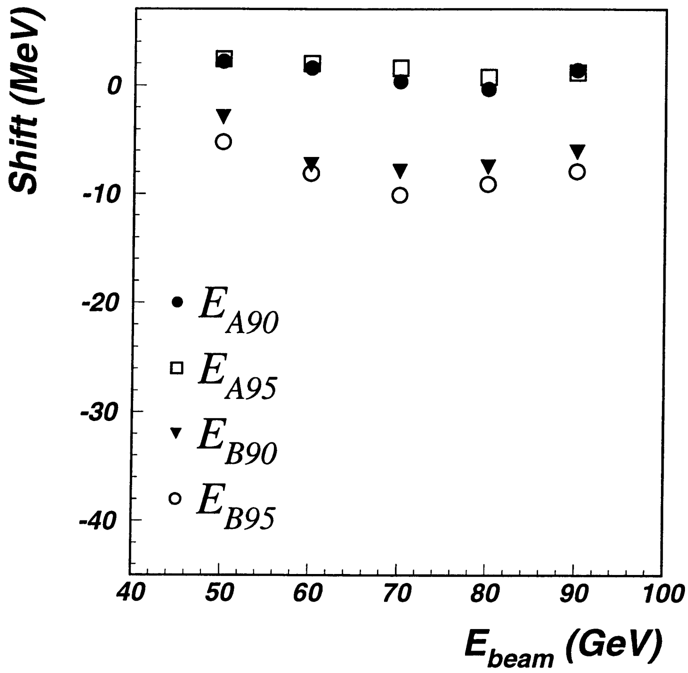

Figure A.4: **Energy shift of E_A and E_B as function of the beam energy.**

approximation, the vertex position. An example of Monte Carlo simulation is shown in Figure A.6;

2. the second method consists in a maximum likelihood fit of the distribution of the luminous region. The line between the two electrons recorded in the SMD has a high probability to pass near the mean beam position (Figure A.7). The probability to find an electron in the SMD at a given point can be calculated event by event for a certain model of the beam profile function.

A.4 Conclusions.

The precision on the beam energy measurement depends on the accuracy with which the changes of the systematic shifts with E_{beam} is simulated. If a simulation is accurate to $\pm 20\%$ the corresponding error on E_{beam} is a fraction of an MeV for the method A and about 2 MeV for the method B. The error coming from the extrapolation of this measurement to the interaction points is of the order of 5-7 MeV. An

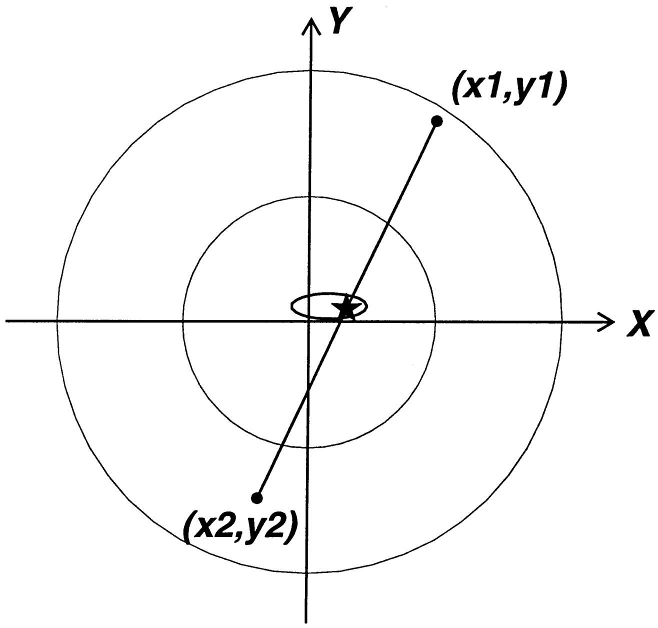

Figure A.5: **Beam profile and Møller event in the transverse view.**

improved measurement of E_{beam} can have two effects on the W mass measurement at LEP2:

1. for a given integrated luminosity the error on M_W is reduced;

2. less integrated luminosity is required to obtain a given accuracy on M_W.

In summary, the impact of the Møller method is an improvement on the total W mass error that can vary from 2% to 20 % depending on the values of ΔM_W^{TD} and of the flux-loop extrapolation. In all cases the improvement on the error using this method is equivalent to a reduction of the statistical error that would require a substantial larger integrated luminosity.

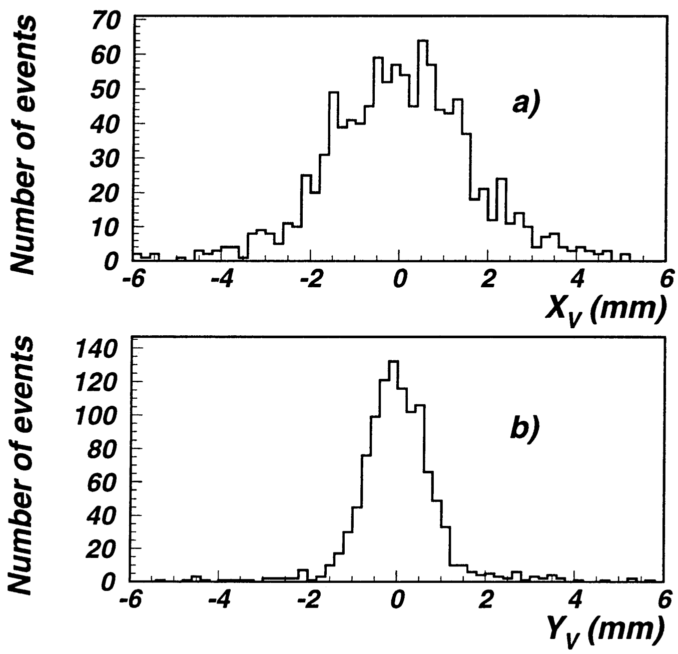

Figure A.6: **The reconstructed beam profile, the X-projection and the Y-projection.**

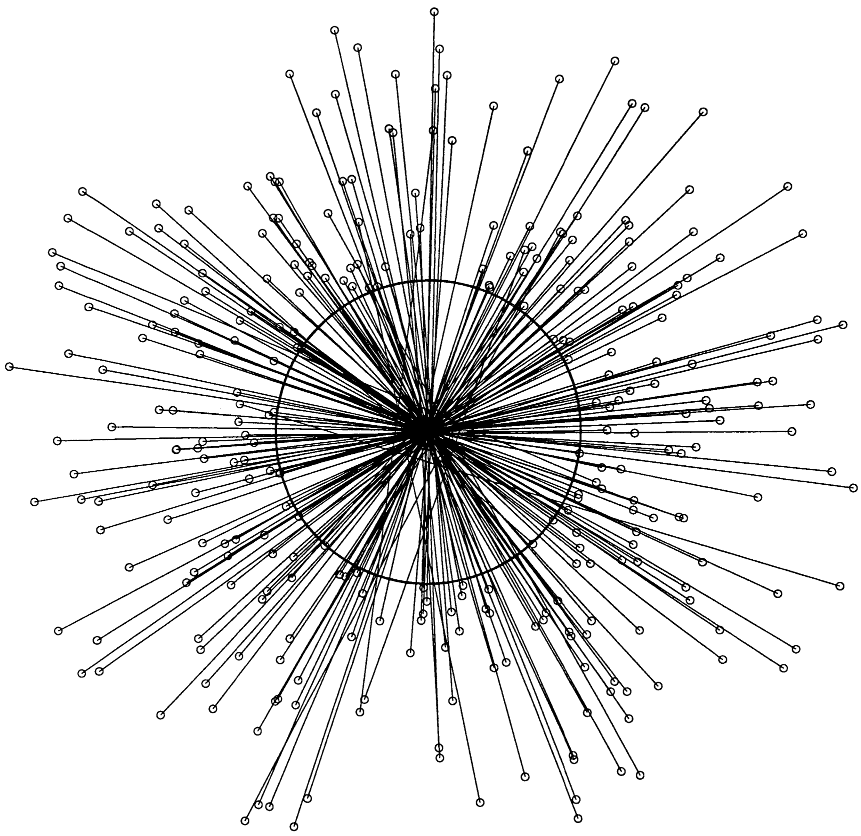

Figure A.7: **Distribution of lines joining electron hits in the SMD.**

Bibliography

[1] **E.Leader, E.Predazzi**, "An introduction to Gauge theories and the New Physics"
Cambridge University Press (1985)
R.Kleiss CERN academic training lectures, CERN (1990).

[2] **S.L. Glashow**, Nucl.Phys. **22** (1961) 168.

[3] **S. Winberg**, Phys.Rev.Lett. **19** (1967) 1264
A.Salam, "Elementary Particle Theory: Relativistic Groups and Analyticity" ed. N. Svartholm, Stockholm (1968) 367.

[4] **J.F. Hasert at al.**, Phys.Lett. **46B** (1973) 138.
J.F. Hasert at al., Nucl.Phys. **B73** (1974) 1.

[5] **UA1 Coll.**, Phys.Lett. **122B** (1983) 103.
UA2 Coll., Phys.Lett. **122B** (1983) 476.

[6] **P.W. Higgs** Phys.Lett. **12** (1964) 132.

[7] **R.M. Barnett at al.** (The Particle Data Group).
Review of Particle Properties, Phys. Rev. **D54** (1996) 1.

[8] **L3 Collaboration, M.Acciarri et al.**
CERN-EP/98-52 (L3 1997).

[9] **P.Giacomelli** 2^{nd} Conference on Recent Developments in the Phenomenology of Particle Physics, Italy, Trieste (1992).

[10] **G.Schwindling** International Europhysics Conference on High Energy Physics, France, Marseille (1993).

[11] **CDF Collaboration, J. Lys**, talk presented at ICHEP96, Warsaw, 25-31 July 1996.

[12] **DØ Collaboration, S.Protopopescu**, talk presented at ICHEP96, Warsaw, 25-31 July 1996.

[13] **LEP electroweak Working Group and the SLD Heavy Flavour Group, D. Abbaneo et al.**, A Combination of Preliminary LEP and SLD electroweak Measurements and Constraints on the Standard Model, Preprint LEPEWWG/96-01 and ALEPH 96-043 PHYSICS 96-039 and DELPHI 96-36 PHY 609 and L3 note 1927 and OPAL Technical Note TN 360 and SLD Physics Note 47, CERN, 1996.

[14] **LEP Heavy Flavour Group, D. Abbano et al.** Combining Heavy Flavour Electroweak Measurements at LEP, Preprint CERN PPE/96-017, CERN, 1996.

[15] **CDHS Collaboration, H. Abramowicz, at al.**Phys. Rev. Lett. **57** (1986) 298.
CDHS Collaboration, A. Blondel, at al.Z. Phys. **C45** (1990) 361.

[16] **CHARM Collaboration, J.V. Allaby, at al.**Z. Phys. **C36** (1987) 611.
CHARM Collaboration, J.V. Allaby, at al. Phys. Lett. **B177** (1986) 446.

[17] **CCFR Collaboration, K. McFarland**, A Precision Measurement of Electroweak Parameters in Neutrino-Nucleon Scattering, FERMILAB-Pub-97/001-E, January 1997, submitted to Phys. Rev. Lett..

[18] **CDF Collaboration**, CDF Electroweak Physics: Blessed Analysis. WWW http: //www-cdf.fnal.gov/physics/ewk/ewk.html (April 1997); CDF W Mass Measurement. WWW http: //www-cdf.fnal.gov/physics/ewk/wmass.html (April 1997). The results have been presented at the 1997 winter conferences.
M. Rijssenbeek, W Mass from the Tevatron. Contributed talk to ICHEP96, Warsaw (July 1996), on behalf of the DØ and CDF Collaborations. FERMILAB-Conf-96/365-E. See also the references therein.
Y.K. Kim, talk presented al the Lepton-Photon Symposium 1997, Hamburg, 28 July - 1 Aug, 1997.

[19] **D. Bardin et al.**, "ZFITTER An Analytical Program for Fermion Pair Production in e^+e^- Annihilation",
CERN-TH **6443** (1992).

[20] **R.M. Barnett at al.**, Phys. Rev. **D54** (1996) 1.

[21] **LEP Electroweak Working Group and the SLD Heavy Flavour Group**, A Combination of Preliminary Electroweak Measurements and Constraints on the Standard Model, Preprint LEPEWWG/97-02 and ALEPH 97-085 PHYSICS 97-075 and DELPHI 97-141 PHYS 726 and L3 Note 2153 and OPAL Technical Note TN 504 and SLD Physics Note 63, CERN, 1997.

[22] **N. Cabibbo**, Phys. Rev. Lett., **10**, (1963) 531.
M. Kobayashi and **T. Maskawa**, Prog. Theor. Phys., **49** (1973) 652.

[23] **UA1 Collaboration, G. Arnison et al.**, Phys. Lett., **B122**, (1983) 103.
UA2 Collaboration, M. Banner at al., Phys. Lett,, **B122**, (1983) 476.
UA2 Collaboration, J. Alitti at al., Phys. Lett,, **B276**, (1992) 354.

[24] **P. Roudeau at al.**, Measurement of the W mass at LEP200, in Proceedings of the ECFA Workshop on LEP200, Aachen 1986 (Vol. 1). CERN 87-08, ECFA 87/108.

[25] **A. Trabelsi, P.Perez** and **J. Schwindling**, W mass reconstruction in the $WW \to l\bar{\nu}q_1\bar{q}_2$ channel. ALEPH 95-048 (1995).
P. Perez on behalf of the W Mass Group. Contribution to the Plenary meeting of the CERN Workshop on Physics at LEP2. (June 1995).
P. Perez W Mass Measurement at LEP2 Contribution to the International Europhysics Conference on High Energy Physics, Brussels (August 1995).

[26] **Z. Kunszt et al.**, Determination of the Mass of the W Boson, in Physics at LEP2, eds. G. Altarelli at al. CERN Yellow Report 96-01 (1996) Vol. 1.

[27] **M. L. Swartz**, Measurement of the W^+W^- Threshold. SLAC-PUB-5258 (1990).
H.S. Chen and **G.J. Zhou**, Phys. Lett., **B331**, (1994) 441.

[28] **T. Muta, R. Najima** and **S. Wakaizumi**, Mod. Phys. Lett., **A1** (1986) 203.

[29] **M. Consoli** and **A. Sirlin**, The role of the one-loop electroweak effects in $e^+e^- \to \mu^+\mu^-$. CERN Yellow Report 86-02 (1986) 63.

[30] **F.A. Berends, G. Burgers, W. Hollik** and **W.L. van Neerven**, Phys. Lett. **B203** (1988) 177.
D. Berends, A. Leike, T. Riemann and **M. Sachwitz**, Phys. Lett. **B206**, (1988) 539.

[31] **M. Skrzypek, S. Jadach, W. Placzek** and **Z. Was**, Monte Carlo program Koralw-1.02 for W pair production at LEP2/NLC energies with Yenni-Frautschi-Suura exponentiation, in Comp. Phys. Comm., **94**, (1996) 216.
T. Ishikawa, Y. Kurihara, M. Skrzypek and **Z. Was**, Four quark final state in W pair production: case of signal and background. CERN-TH/97-11 (Feb 1997).

[32] **F.A. Berends, R. Pittau** and **R.Kleiss**, EXCALIBUR-a Monte Carlo program to evaluate all four fermion processes at LEP200 and beyond. INLO-PUB-12/94 (1994).

[33] **F.A. Berends, R. Pittau** and **R.Kleiss**, Nucl. Phys., **B424**, (1994) 308.
D. Bardin et al., Events Generators for WW Physics, in Physics at LEP2, eds. G. Altarelli et al. CERN Yellow Report 96-01 (1996) Vol. 2.

[34] **Minami-Tateya collaboration**, GRACE manual ver 1.0, KEK report **92-19**, 1993,
Minami-Tateya collaboration, Brief Manual of GRACE system ver $2.0/\beta$, 1995.

[35] **M. Bohm et al.**, Nucl. Phys., **B304**, (1988) 463.
W. Beenakker, K. Kolodziej and **T. Sack**, Phys. Lett., **B258**, (1991) 469.
W. Beenakker, F.A. Berends and **T. Sack**, Phys. Lett., **B367**, (1991) 287.

[36] **J. Fleischer, F. Jegerlehner** and **M. Zralek**, Zeit. Phys., **C42**, (1989) 409.
K. Kolodziej and **M. Zralek**, Phys. Rev., **D43**, (1991) 3619.
J. Fleischer, F. Jegerlehner and **K. Kolodziej**, Phys. Rev., **D47**, (1993) 830.

[37] **D. Bardin, M. Bilenky, A. Olchevski** and **T. Riemann**, Phys. Lett. **B308**, (1993) 403.
D. Bardin, T.Lehner and **T. Riemann**, Complete Initial State QED Corrections to Off-Shell Gauge Boson Pair Production in e^+e^- Annihilation. DESY 96-028 (Feb. 1996).

[38] **W. Beenakker et al.**, WW Cross Section and Distributions, in Physics at LEP2, eds. G. Altarelli et al. Yellow Report 96-01 (1996) Vol. 1.

[39] **D. Bardin et al.**, Semi-Analytical Approach to Four Fermion Production in e^+e^- Annihilation. CERN-TH-7295-94 (1994).
D. Bardin et al., GENTLE/4fan: a package of Fortran programs for the description of e^+e^- annihilation into four fermions. DESY-ZEUTHEN-96-05 (March 1996).

[40] **V.S. Fadin, V.A. Khoze** and **A.D. Martin**, Phys. Lett., **B311**, (1993) 311.
D. Bardin, W. Beenakker and **A. Denner**, Phys. Lett., **B317**, (1993) 213.
V.S. Fadin, V.A. Khoze, A.D. Martin and **A. Chapovsky**, Phys. Rev., **D52**, (1995) 1377.

[41] **V.S. Fadin, V.A. Khoze, A.D. Martin** and **W.J. Stirling**, Higher order Coulomb corrections to the threshold $e^+e^- \to W^+W^-$ cross section. University of Durham, DTP/95/64.

[42] **V.A. Khoze** and **T. Sjöstrand**, QED Interconnection Effects on W Momentum Distributions at LEP2. University of Durham, DTP/95/68

[43] **J. Fleischer, F. Jegerlehner** and **M. Zralek**, Zeit. Phys., **C42**, (1989) 409.
F. Jegerlehner, Radiative Corrections to W Pair Production at LEP, in Proc. Rinberg Workshop on Electroweak Radiative Corrections. Paul Sherrer Institut Preprint PR-89-09 (1989).
F. Jegerlehner, Renormalisation Scheme Dependence of Electroweak Radiative Corrections, in Proc. NATO Workshop on Radiative Corrections. Paul Sherrer Institut Preprint PR-89-23 (1989).

[44] **W. Beenakker** and **G.J. van Oldenborg**, The effect of the Higgs boson mass on the threshold cross-section in WW production. INLO-PUB-02/96, hep-ph/9603411 (March 1996).

[45] **T. Sjöstrand** and **V.A. Khoze**, Zeit. Phys., **C62**, (1994) 281. **T. Sjöstrand** and **V.A. Khoze**, Phys. Rev. Lett., **72**, (1994) 28.

[46] **G. Gustafson, U. Pettersson** and **P.M. Zerwas**, Phys. Lett., **B209**, (1988) 90.
E. Accomando, A. Ballestrero and **E. Maina**, Phys. Lett., **B362**, (1995) 141.

[47] LEP Design report Vol. 1, "The LEP injector chain", CERN-LEP/TH 83-29 (1983).
LEP Design report Vol. 2, "The LEP main ring", CERN-LEP/TH 84-01 (1984).
S. Meyers, The LEP collider, from design to approval and commissioning, CERN-91-08 (1991).

[48] **M. Chemarin, M. ElKacimi**, CERN-L3 88-621 (1988).

[49] **L3 Collaboration, B. Adeva et al.**, Nucl. Inst. Meth., **A289**, (1990) 35.

[50] **L. Camilleri et al.**, Physics with Very High Energy e^+e^- Colliding Beams, Preprint CERN 76-18, (1976). **J.B. Adams et al.**, Design Study of a 22 to 130 GeV e^+e^- Colliding Beam Machine (LEP), Preprint CERN/ISR-LEP/79-33 (1979).

[51] **ALEPH Collaboration, D. Decamp et al.**, Nucl. Inst. Meth., **A294**, (1990) 127.

[52] **DELPHI Collaboration, P. Aarnio et al.**, Nucl. Inst. Meth., **A303**, (1991) 233.

[53] **OPAL Collaboration, K. Ahmet et al.**, Nucl. Inst. Meth., **A305**, (1991) 275.

[54] **J.D. Jackson**, "Classical Electrodynamics", John Wiley & Sons, 1975.

[55] **S. Meyers**, The LEP collider, from design to approval and commissioning, CERN-91-08 (1991).

[56] **M. Bohm, A. Denner** and **W. Hollik**, Nucl. Phys., **B304**, (1988) 687.
F.A. Berends, R. Kleiss and **W. Hollik**, Nucl. Phys., **B304**, (1988) 712.
S. Jadach et al., CERN-TH 6118, CERN-TH 6230.

[57] **M. Merk**, in XXIX Rencontre de Moriond, France, Moriond (1994).

[58] **L. Arnaudon et al.**, The Energy Calibration of LEP in 1991, Preprint CERN-SL/92-37(DI) and CERN-PPE/92-125, (1992).
L. Arnaudon et al., The Energy Calibration of LEP in 1992, Preprint CERN-SL/93-21(DI), (1993).
L. Arnaudon et al., Phys. Lett., **B307**, (1993) 187.

[59] **L. Arnaudon et al.**, The Energy Calibration of LEP in 1991, Preprint CERN-SL/92-37(DI) and CERN-PPE/92-125, (1992).

[60] **A.A. Zholentz et al.**, Phys. Lett., **B96**, (1980) 214.
A.S. Artamonov et al., Phys. Lett., **B118**, (1982) 225.
A.N. Skrinskii and **Yu.M. Shatunov**, Sov. Phys. Usp., **32(6)**, (1989) 548.
ARGUS Collaboration, D.P. Barber et al., Phys. Lett., **B135**, (1984) 498.
CUSB Collaboration, W.W. McKay et al., Phys. Rev., **D29**, (1984) 2483.

[61] **A.A. Sokolov** and **I.M. Ternov**, Sov. Phys. Dokl., **8**, (1964) 1203.

[62] **L. Knudsen et al.**, Phys. Lett., **B270**, (1991) 97.

[63] **L. Arnaudon et al.**, Accurate Determination of the LEP Beam Energy by Resonant Depolarization, Preprint CERN-SL/94-71(BI), (1994).

[64] **M. Acciarri et al.**, The L3 Silicon Microvertex Detector, Preprint CERN-PPE/94-122, (1994).

[65] **B.Beissel at al.**, Nucl. Inst. Meth., **A332**, (1993) 33.

[66] **A.H. Walenta**, IEEE Trans. Nucl. Sci., **NS-26, No. 1**, (1979) 73.

[67] **1987-1988 L3 BGO Collaboration**, Calibration of the L3 electromagnetic calorimeter in electron beam, Internal Report L3 Note 1712, CERN, (1995).

[68] **L3 Collaboration B. Adeva et al.**, Nucl. Inst. Meth., **A289**, (1990) 35.

[69] **G. Basti et al.**, Nucl. Inst. Meth., **A374**, (1996) 293.

[70] **A. Boucham et al.**, Results from the 1995 Test-Beam for the SPACAL, Internal Report L3 Note 1776, CERN, (1995).

[71] **O. Adriani et al.**, Nucl. Inst. Meth., **A302**, (1991) 53.
O. Adriani et al., Phys. Rep., **236**, (1993) 1.

[72] **The L3 Forward-Backward Muon Group**, The Forward Muon Detector of L3, Internal Report L3 Note 1984, CERN, (1996).

[73] **R. Bizzarri et al.**, Nucl. Inst. Meth., **A317**, (1992) 463.

[74] **P. Béné et al.**, Nucl. Inst. Meth., **A306**, (1991) 150.

[75] **U. Uwer**, The L3 Scintillation Counter System, Internal Report L3 Note 1400, CERN, (1993).

[76] **M. Fukushima**, L3 Level I Muon Trigger, Internal Report L3 Note 515, CERN, (1987).
T.S. Dai and **M. Fukushima**, Level I Muon Trigger schematics, Internal Report L3 Note 668, CERN, (1989).

[77] **G. Carlino et al.**, 1995 Forward-Backward Trigger Efficiency, Internal Report L3 Note 1951, CERN, (1996).

[78] **Y. Bertsch et al.**, The Second Level Trigger of L3 Experiment. 1. The Implementation, Internal Report LAPP-EXP-93.04, LAPP, (1993).
S.P. Beingessner et al., The Second Level Trigger of L3 Experiment. 2. The Event Selection, Internal Report LAPP-EXP-93.05, LAPP, 1993.

[79] **C. Dionisi et al.**, Nucl. Inst. Meth., **A336**, (1993) 78.

[80] **S. Banerjee** and **F. Bruyant**, The L3 EVENT Data Structure, Internal Report L3 Note 748, CERN, (1990).
J. Swain and **L. Taylor**, L3 Computing Guide, Preprint NUB-3065, Northeastern University Boston, (1993).

[81] **R. Brun et al.**, GEANT3 Users Guide, Preprint CERN DD/EE/84-1, (1984).

[82] **T. Sjöstrand**, Comp. Phys. Comm., **82**, (1994) 74.
T. Sjöstrand, PYTHIA 5.7 and JETSET 7.4 Physics and Manual, Preprint CERN-TH/7112-93, (1993); revised August 1995.

[83] **Jörg Wenninger**, Mesure de paramètres électro-faibles du Z^o avec la rèaction $e^+e^- \to e^+e^-(\gamma)$, Thèse de Doctorat n^0 2544, Université de Genève, (1992).

[84] **Gilbert Morand**, Développement et Utilisation du système de Moniteur au Xénon du Calorimètre électromagnétique de l'Expérience L3, Thèse de Doctorat n^0 2464, Université de Genève, (1991).
A. Bay et al., Nucl. Inst. Meth., **A321**, (1992) 119.

[85] **J.A. Bakken at al**, Nucl. Inst. Meth., **A254**, (1987) 535.
J.A. Bakken at al, Nucl. Inst. Meth., **A280**, (1989) 25.

[86] **J.H. Field**, Phys. Lett., **B323**, (1994) 432.
J.H. Field and **T. Riemann**, Comp. Phys. Comm., **94**, (1996) 53.

[87] **C. Cecchi at al.**, BGO Calibration at LEP II, Internal Report L3 Note 1892, CERN, (1995).

[88] **H. Akbari et al.**, Nucl. Inst. Meth., **A274**, (1989) 113.
H. Ma et al., Nucl. Inst. Meth., **A281**, (1989) 469.

[89] **S. Catani, Yu.L. Dokshitzer, M. Olsson, G. Turnock** and **B.R. Webber**, Phys. Lett., **B269**, (1991) 432;
S. Catani, Yu.L. Dokshitzer and **B.R. Webber**, Phys. Lett., **B285**, (1992) 291.

[90] **L3 Collab., M. Acciarri et al.**, Phys. Lett., **B398**, (1997) 223.

[91] **L3 Collab., M. Acciarri et al.**, Phys. Lett., **B407**, (1997) 419.

[92] **LEP Working Group**, LEP Energy Calibration in 1996, LEP Energy Group 97/01.

[93] **A.Weber**, How to Determine the W-Mass from the Mass Spectrum of the Decay Products, The Box Method, Internal Report L3 Note 2097, CERN, (1997).

[94] **L. Lönnblad** and **T. Sjöstrand**, Phys. Lett., **B351**, (1995) 293.
S. Jadach and **K. Zalewski**, W Mass Reconstruction from Hadronic Events in LEP-2: Bose Einstein Effect, CERN-TH/97-029L.

[95] **LEP electroweak Working Group and the SLD Heavy Flavour Group, D. Abbaneo et al.**, A Combination of Preliminary LEP and SLD electroweak Measurements and Constraints on the Standard Model, Preprint LEPEWWG/98-01 and ALEPH 98-037 PHYSICS 98-018 and DELPHI 98-45 PHY 774 and L3 note 2259 and OPAL Technical Note TN 541 and SLD Physics Note 68, CERN, 1998.

[96] **SLD Collaboration, G. Crawford**, talk presented at the XXXIIIth Rencontre de Moriond, Les Arcs, France, 15-21 March 1998.

[97] **C.Cecchi et al.**, Nucl. Inst. Meth., **A385**, (1997) 445.

[98] **M. Placidi** and **R. Rossmanith**, Nucl. Inst. Meth., **A274**, (1989) 79.

[99] **G.Altarelli, T.Sjöstrand**, and **F. Zwirner (eds)**, Report of the Working Group on Beam Energy Measurements at LEP, Proc. LEP2 Study. CERN Yellow Report 96-01, Vol. 1.

[100] **J. Antille et al.**, Phys. Lett., **B194**, (1987) 568.